Measurements of the associated production of a top quark pair and a Z boson with the ATLAS detector

Laurynas Mincė

Submitted in fulfilment of the requirements for
the Degree of Doctor of Philosophy

School of Physics and Astronomy
College of Science and Engineering
University of Glasgow

April 27, 2023

Abstract

This thesis presents measurements of the inclusive and differential cross-sections of a top quark pair produced in association with a Z boson with the ATLAS detector. The full LHC Run-2 dataset corresponding to an integrated luminosity of $139\,\text{fb}^{-1}$ collected during proton-proton collisions at a centre-of-mass energy of $\sqrt{s}$ =13 TeV is used in the measurements. The thesis focuses on the three-lepton final states of the $t\bar{t}Z$ system where only electrons or muons are considered. The measured inclusive cross-section is $\sigma(pp \rightarrow t\bar{t}Z) = 0.99 \pm 0.05\,(\text{stat.}) \pm 0.08\,(\text{syst.})\,\text{pb} = 0.99 \pm 0.10\,\text{pb}$. It is in good agreement with other experimental observations and the theoretical prediction of $\sigma_{t\bar{t}Z} = 0.86^{+0.07}_{-0.08}\,(\text{scale}) \pm 0.02\,(\text{PDF})\,\text{pb}$. The measurements of the differential cross-sections are performed using profile likelihood unfolding. A comprehensive set of eight observables is used to probe different aspects of the $t\bar{t}Z$ production. The differential cross-section in each observable is measured to be in good agreement with the theoretical prediction which uses the MADGRAPH5_AMC@NLO+PYTHIA8 Monte Carlo event generation. The measurements presented in this thesis achieve a significant improvement in precision with respect to the previous ATLAS measurements.

Declaration

I declare that this thesis is an original account of my own work, unless stated otherwise. The research was carried out in the Experimental Particle Physics group in the School of Physics and Astronomy at the University of Glasgow and has not been submitted for any other degree or qualification at this university or any other institution.

During my research, I was a member of the ATLAS collaboration at the LHC and, more broadly, a user of the facilities at CERN. My work would have been impossible if not for collaborations with thousands of ATLAS scientists, their work and expertise. Therefore, this thesis also contains discussions of the works of other people which are relevant to my own work. Chapters 1–7 are dedicated to the introduction of the theoretical background and the experimental apparatus as well as analysis tools and techniques where I did not contribute any work. The exception is Chapter 5 where my own work on the monitoring of the ATLAS high level muon trigger is documented. Chapters 8–10 present my work towards the measurements of the $t\bar{t}Z$ process which contributed to a publication and measurements which are under the internal review at the time of writing this thesis. Chapter 8 documents the measurement of the inclusive $t\bar{t}Z$ cross-section. My work on the three-lepton event selection optimisation is described in Section 8.4 and the remaining parts of the chapter outline the work of the analysis team. The content of Chapter 9 is the result of my own work except:

- Section 9.1 where the general strategy to the measurements is outlined.
- Section 9.3 where the three-lepton event selections are discussed.
- Section 9.4 where the event reconstruction techniques are described.

- Section 9.5 where the set of the observables and the initial binning selections were delivered by the analysis team. My own work is outlined in the latter part of the section.

In addition to my contributions declared above, I also contributed to the maintenance of the ATLAS software framework and technical support through my work as a Flavour-tagging liaison for the Top Quark working group. This is not documented in the thesis.

Laurynas Mincė

Acknowledgements

I would like to first thank my PhD supervisor Mark who guided my research and placed me in an excellent position to make significant contributions towards the ATLAS physics programme. I am very grateful for the time he took to answer numerous questions. I learned a great deal about the scientific approach to solving complex physics problems and technical challenges as well as effectively and professionally navigating the ATLAS collaboration. I would also like to thank Federica for her constant support and patient discussions from the first day of my PhD. I greatly benefited from her expertise and work. I am very grateful to my second supervisor Aidan who overlooked the progress of my PhD research and my undergraduate studies before that. He has provided invaluable support, guidance and advice since before I arrived at the University of Glasgow for the first time ten years ago.

I would like to acknowledge and thank Baptiste, Michal, Tom, Steffen, Tomas and all the members of the ATLAS $t\bar{t}Z$ analysis team. Their work and advice contributed to and enabled my work discussed in this thesis. It was a pleasure working with you and I only wish there were more opportunities to meet in person at CERN.

A big thank you to Tony, Craig, Sarah, Giuseppe, Jay, Mike, Chloe, Will, Jonathan J., Neil W. and the entire Experimental Particle Physics group for warmly welcoming me and answering my questions. Thank you, Sam and Gordon, for providing technical support and keeping the computing systems running. Thank you, Jill, for keeping track of the administrative side and organising all the travels.

A very big thank you to the Beans on Roast Coffee Club, its founding members, Adam, Conor, Dima, Dwayne, Lluis, Lojius and Neil M., and all its other members. We started the club in my first year of PhD and kept it going through it all. It provided not only caffeine boosts but also built friendships and great memories. The coffee breaks on Zoom were especially vital distractions during the pandemic.

The PhD would not have been the same without Adam, Bruno and David, lately known as the Writers' Club. It was great sharing the journey of the PhD together. Thank you, Jonathan T. and the Writers' Club for the company in the gym. It helped me stay sane in the last months of my PhD (and achieve some PRs).

Lastly, I want to thank my family for their unwavering support. Thank you for giving freedom to do my undergraduate studies at the University of Glasgow in the first place and for continuing to support and encourage me during my PhD. I firmly believe I would not have the opportunities I have and would not be where I am without your trust in me. Finally, I would like to thank my high school physics teacher Mrs. Vladislava Zinkienė who sparked my interest in physics through her passion and dedication to teaching physics.

To all the people mentioned here and many more who I met in the last four years, thank you all! I learned something new from each and every one of you.

Contents

Chapter 1

Introduction

The field of high energy physics seems, however subjectively, to be best poised for deciphering the origin of the natural world around us. The Standard Model of particle physics (SM) has been arguably the most successful theory describing our Universe down to 10^{-35} s after the Big Bang. Yet, a number of questions remain unanswered which suggest that the SM is not a complete theory. Some of the most advanced experimental setups are required to test the SM and search for the answers to the remaining questions. The European Organization for Nuclear Research, abbreviated as CERN[1], hosts a complex of particle accelerators and a myriad of experimental setups outside of Geneva (Switzerland). Its highest energy accelerator is the Large Hadron Collider (LHC) which provides high energy proton-proton, proton-ion and ion-ion collisions. Four particle physics experiments, including the ATLAS experiment (A Toroidal LHC Apparatus), are built around the LHC tunnel to study these collisions and probe the SM. It was my focus and endeavour of the last four years to make meaningful contributions towards the physics programme of the ATLAS collaboration. This thesis is an account of my studies, analyses and measurements predominantly focusing on the production of a top quark pair in association with a Z boson ($t\bar{t}Z$). The top quark plays a central role in the Standard Model and has been under scrutiny for almost 30 years. Due to how heavy the top quark is, details of its interactions with other fundamental particles have only come to light relatively recently thanks to the capabilities of the LHC. The $t\bar{t}Z$ process offers an opportunity to further improve our understanding of the top quark and the SM at large. It also presents a possibility to explore new physics beyond the Standard Model (BSM).

[1] The acronym originates from Conseil Européen pour la Recherche Nucléaire

The thesis is organised so that the first few chapters will provide a theoretical, experimental and analytical background which, for the most part, relies on the work of thousands of scientists in the ATLAS collaboration. The discussion then turns to the measurements of the $t\bar{t}Z$ process where most of the author's work is described. Therefore, Chapter 2 establishes the theoretical aspects of the Standard Model, with a particular focus on the top quark and the $t\bar{t}Z$ system. Chapter 3 turns to the experimental setup of the ATLAS detector. Analysis tools and techniques as well as the relevant statistical background are described in Chapter 4. The author's contributions to the development of the ATLAS trigger and data acquisition system are given in Chapter 5. Next, Chapters 6 and 7 establish some key components of the $t\bar{t}Z$ measurements performed with the ATLAS detector. Chapter 8 discusses the measurement of the inclusive $t\bar{t}Z$ cross-section and gives an account of the author's work in this analysis. Chapter 9 is dedicated to the discussion of the measurements of the differential $t\bar{t}Z$ cross-section where the majority of the author's work is. Finally, Chapter 10 summarises the work presented in the previous chapters and concludes this thesis.

Chapter 2

Theoretical background

2.1 The Standard Model

The Standard Model of particle physics is a quantum field theory which describes nature in terms of the fundamental matter particles and their interactions at the smallest scales. The theory was postulated in the 1960s and 1970s based on experimental observations and theoretical ideas primarily by the works of S. Glashow [1], S. Weinberg [2] and A. Salam [3], as well as M. Gell-Mann [4] and Y. Ne'eman [5]. At the core of the SM, there are twelve fundamental spin-half particles, called fermions, which interact via at least one of the three fundamental forces[1]: the strong force, the weak force or the electromagnetic (EM) force. An interaction between two of these fermions is interpreted as a result of an exchange of a force-carrying spin-one particle, called a boson.

The dynamics and kinematics of the SM are controlled by its Lagrangian which is required to obey the local $\mathrm{SU}(3) \times \mathrm{SU}(2) \times \mathrm{U}(1)$ gauge symmetry group. The three force fields and their associated spin-one particles are related to the terms of the symmetry group. The $\mathrm{SU}(3)$ term is associated with the strong force of quantum chromodynamics (QCD) and eight types of the spin-one gluon are generated. According to the SM, the weak and EM interactions are unified at sufficiently high energies. The $\mathrm{SU}(2) \times \mathrm{U}(1)$ term is a symmetry group of the unified electroweak (EWK) interaction which is associated with four spin-one bosons. The weak force is mediated by the $W^{\pm}$ and Z^0 gauge bosons while the photon, γ^0, is the mediator of the electromagnetic

[1] Gravity is not included in the SM. Due to its minuscule effects on the fundamental particles, it is appropriate to neglect it in high energy physics experiments.

interaction of quantum electrodynamics (QED). The $W^{\pm}$ gauge bosons are associated with the $\mathrm{SU}(2)$ term while the Z^0 gauge boson and the photon are generated from the transformations with the $\mathrm{SU}(2) \times \mathrm{U}(1)$ term.

The SM Lagrangian can only be gauge-invariant if the electroweak symmetry, $\mathrm{SU}(2) \times \mathrm{U}(1)$, is spontaneously broken, such that $\mathrm{SU}(2) \times \mathrm{U}(1) \rightarrow \mathrm{U}(1)_{\mathrm{EM}}$. A mechanism like this was proposed by P. Higgs [6], F. Englert and R. Brout [7], which is now known as the Higgs mechanism. The $W^{\pm}$ and Z^0 bosons are permitted to have masses in a gauge-invariant way determined from their interactions with the Higgs field. The Higgs mechanism was confirmed experimentally by the ATLAS and CMS collaborations independently with the discovery of the spin-0 Higgs boson in 2012 [8, 9]. Similarly to the $W^{\pm}$ and Z^0 gauge bosons, spin-half fermions are known to have non-negligible masses. Fermions interact with the Higgs field and gain mass via the Yukawa coupling. These masses are free parameters in the SM which means that they are not determined theoretically, but are measured experimentally. However, it is implied that a more massive fermion is characterised by a stronger Yukawa coupling.

The particle content of the SM is summarised in Table 2.1. The six quarks, which are arranged into three generations, are affected by all three fundamental forces and, in particular, carry a "colour" charge quantum number as a result of being susceptible to the strong force. Quarks are grouped into up- and down-type quarks within each generation and carry a fractional electric charge. The six leptons are grouped into three generations of electrically charged-neutral particle pairs. In contrast to quarks, leptons do not carry the colour charge and thus do not interact via the strong force. It is a convention to refer to charged leptons as leptons and their neutral partners as neutrinos. All fermions can interact via the weak force and only the electrically charged leptons are affected by the EM interactions. The previously discussed bosonic force carriers are also listed in the table. Finally, each fermion and boson has a corresponding anti-particle. An anti-particle is defined as a particle with its charge quantum numbers inverted, so-called charge conjugation, while all the other quantum numbers are unchanged. Therefore, electrically neutral particles are their own anti-particles. However, the antiparticles are not counted as unique components of the SM.

Table 2.1: A summary of the fundamental matter and force-carrying particles within the Standard Model as well as the Higgs boson [10].

	Generation	Particle	Symbol	Electric charge	Spin	Mass
Quarks	I	up	u	$+2/3$	$1/2$	2.2 MeV
		down	d	$-1/3$	$1/2$	4.7 MeV
	II	charm	c	$+2/3$	$1/2$	1.3 GeV
		strange	s	$-1/3$	$1/2$	93.4 MeV
	III	top	t	$+2/3$	$1/2$	172.7 GeV
		bottom	b	$-1/3$	$1/2$	4.2 GeV
Leptons	I	electron	e	-1	$1/2$	0.5 MeV
		electron neutrino	ν_e	0	$1/2$	< 1.1 eV
	II	muon	μ	-1	$1/2$	105.7 MeV
		muon neutrino	ν_μ	0	$1/2$	< 0.2 MeV
	III	tau	τ	-1	$1/2$	1.8 GeV
		tau neutrino	ν_τ	0	$1/2$	< 18.2 MeV
Bosons		gluon	g	0	1	0
		photon	γ	0	1	0
		Z boson	Z	0	1	91.2 GeV
		W boson	W	± 1	1	80.4 GeV
		Higgs boson	H	0	0	125.3 GeV

2.2 Top quarks and Z bosons

The top quark

The top quark was postulated to be a constituent of the predicted third generation of quarks by M. Kobayashi and T. Maskawa in 1973 [11]. It was finally discovered by the CDF [12] and D0 [13] collaborations at the Tevatron (Fermilab) in 1995. The mass of the top quark is currently measured as $(172.69 \pm 0.30)\,\text{GeV}$ [10] which is an average of the LHC and Tevatron measurements. The large value of the top quark mass corresponds to a lifetime of $\mathcal{O}(10^{-25}\,\text{s})$. This is one order of magnitude shorter than the average time it takes for a parton to hadronize, $\mathcal{O}(10^{-24}\,\text{s})$, thus allowing to study the top quark as the only "bare" quark. The top quark plays an important role in searches of new physics due to its large mass generated by a strong interaction with the Higgs field.

Top quarks are predominantly produced in quark-antiquark pairs through QCD gluon-gluon interactions at the LHC using proton-proton collisions. Gluon-gluon fusion is responsible for 90% of top-quark pair productions while the remaining 10% are produced via quark-antiquark annihilation. The most recent theoretical calculations estimate the production cross-section of the top-quark pair at $832^{+40}_{-46}\,\text{pb}$ at next-to-next-to-leading order (NNLO) precision in QCD with next-to-next-to-leading-logarithmic (NNLL) order corrections and assuming the centre-of-mass energy of 13 TeV [14]. This can be seen in Figure 2.1 where the theoretical prediction for proton-proton collisions is shown by a line with the green band. The figure shows an evolution of the $t\bar{t}$ cross-section theoretical calculations and experimental measurements as a function of the centre-of-mass energy. The experimental measurements are in good agreement with the prediction, shown in different markers.

Top quarks decay via the $t \to Wq$ electroweak process nearly 100% of the time, where the quark can be one of the three down-type quarks, d, s or b. The branching ratio is dominated by decay to a b-quark at 0.957 ± 0.034 [10] and hence only these decays are considered in the remainder of this thesis. The W boson undergoes a further decay. In the absolute majority of cases, a W boson decays into either a lepton-neutrino or quark-antiquark pair. Table 2.2 lists the dominant decay channels and their branching ratios of the W boson. Therefore, there are three decay channels that a top quark pair can decay by: hadronic, semi-leptonic and leptonic, listed in the decreasing order of the branching ratios. The leptonic $\tau\nu$ decay is problematic from an

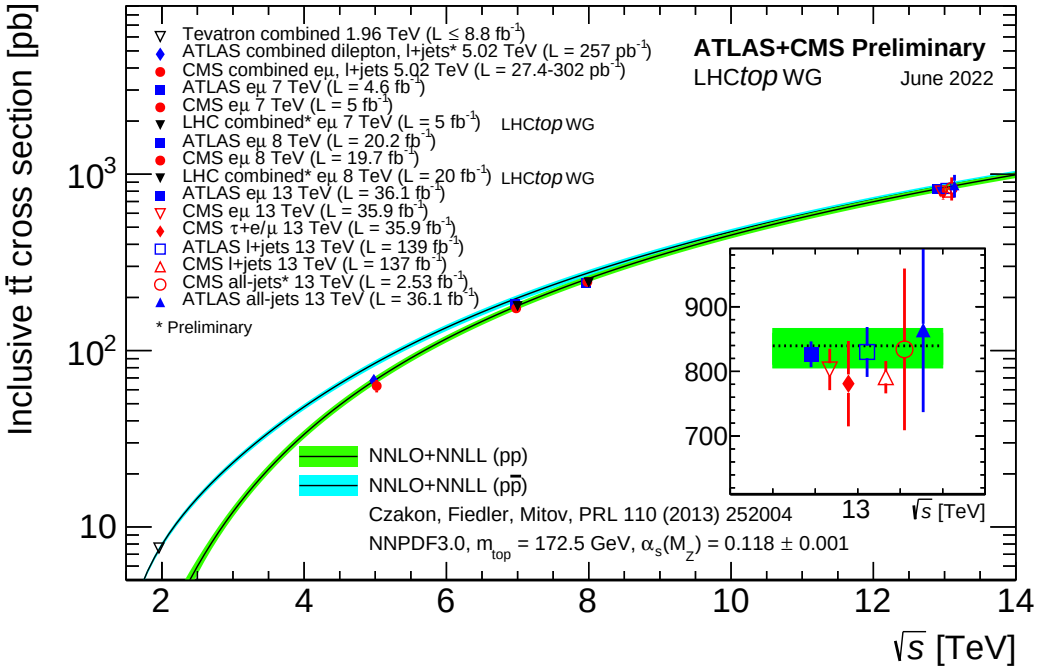

Figure 2.1: Summary of the measurements of the inclusive top quark pair production cross-section. The measurements are from the Tevatron and LHC experiments and correspond to different centre-of-mass energies. The theoretical calculations are shown at the NNLO + NNLL precision [15].

Table 2.2: A summary of the dominant decay channels of the W boson [10].

Channel	Decay		Branching ratio
Leptonic	$W \to$	$e\nu$	$(10.71 \pm 0.16)\,\%$
		$\mu\nu$	$(10.63 \pm 0.15)\,\%$
		$\tau\nu$	$(11.38 \pm 0.21)\,\%$
Hadronic	$W \to$	$q\bar{q}'$	$(67.41 \pm 0.27)\,\%$

Table 2.3: A summary of the dominant decay channels of the $t\bar{t}$ system. The final states with tau leptons ($\ell = \tau$) are excluded from the branching ratios.

Channel	Decay	Branching ratio
Hadronic	$t\bar{t} \to W^+bW^-\bar{b} \to q\bar{q}'bq''\bar{q}'''\bar{b}$	$\approx 45\,\%$
Semi-leptonic	$t\bar{t} \to W^+bW^-\bar{b} \to q\bar{q}'b\ell^-\bar{\nu}_\ell\bar{b}$	$\approx 29\,\%$
Leptonic	$t\bar{t} \to W^+bW^-\bar{b} \to \ell^+\nu_\ell b\ell'^-\bar{\nu}_{\ell'}\bar{b}$	$\approx 7\,\%$

experimental point of view because the tau lepton is not stable itself and decays inside the detector to hadrons or leptons. Reconstruction of such final states becomes too complicated for most measurements and the $W \to \tau\nu$ decays will be excluded from the analyses of this thesis. The $t\bar{t}$ decay channels are summarised in Table 2.3.

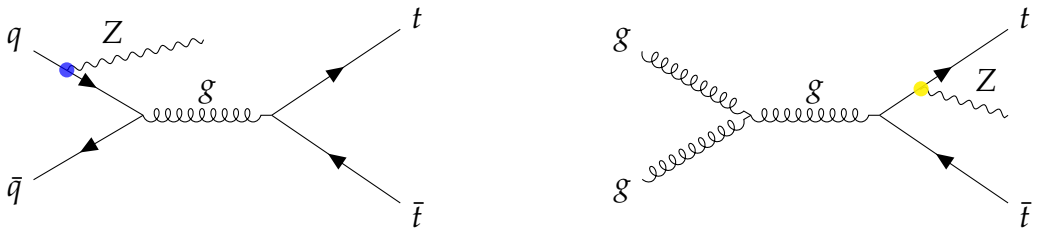

(a) Quark-antiquark annihilation. **(b)** Gluon-gluon fusion.

Figure 2.2: Leading order Feynman diagrams of the $t\bar{t}Z$ production.

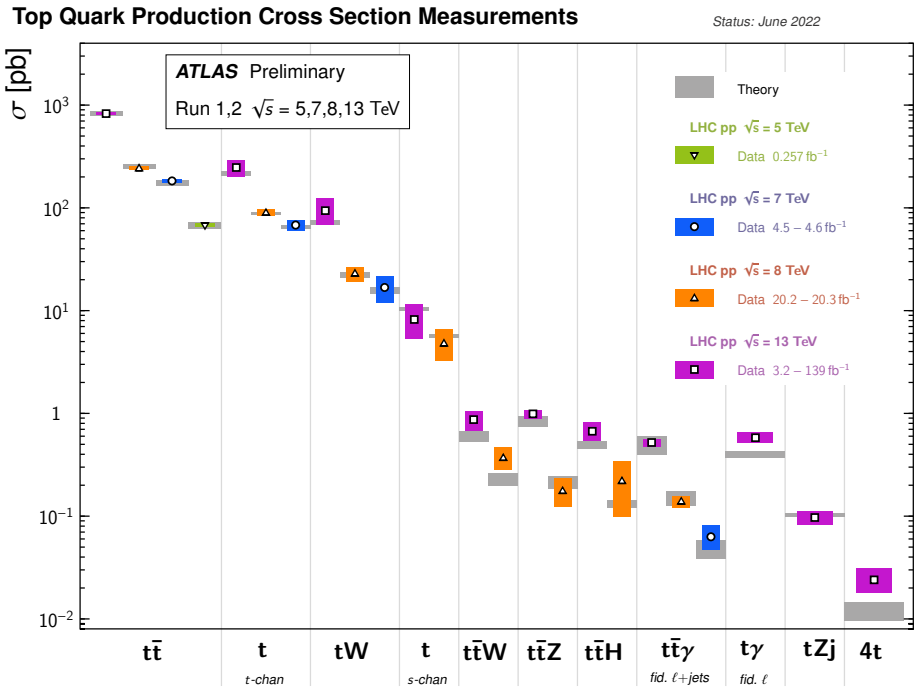

Figure 2.3: Summary of the total production-cross section measurements involving a top quark [15]. The purple $t\bar{t}Z$ marker shows the result presented in Chapter 8.

Top quark pair production in association with a Z boson

The production of a top quark pair in association with a Z boson ($t\bar{t}Z$) can be considered a higher order electroweak correction to the $t\bar{t}$ process, as shown in Figure 2.2. It is a rare occurrence which is $\mathcal{O}(10^3)$ less frequent than the inclusive $t\bar{t}$ production due to the presence of an electroweak vertex and the amount of additional energy required to produce a massive Z boson. A comparison of the $t\bar{t}Z$ production cross-section with other processes involving top quarks is shown in Figure 2.3. Currently, theoretical calculations estimate the $t\bar{t}Z$ production cross-section as:

$$\sigma^{\mathrm{SM}}_{t\bar{t}Z} = 0.86^{+0.07}_{-0.08}\,(\mathrm{scale}) \pm 0.02\,(\mathrm{PDF})\,\mathrm{pb}, \tag{2.1}$$

where up to next-to-leading order (NLO) in QCD and EWK precision, and next-to-next-to-leading-logarithmic (NNLL) corrections are used [16].

The $t\bar{t}Z$ system decays to final states which are commonly characterised by the number of leptons. They can be derived from Table 2.3 of the $t\bar{t}$ decays and Table 2.4 showing the decay channels of the Z boson. While a final state with no leptons is

Table 2.4: A summary of the dominant decay channels of the Z boson [10].

Channel	Decay		Branching ratio
Leptonic	$Z \to$	e^+e^-	$(3.3632 \pm 0.0042)\,\%$
		$\mu^+\mu^-$	$(3.3662 \pm 0.0066)\,\%$
		$\tau^+\tau^-$	$(3.3696 \pm 0.0083)\,\%$
		$\nu_\ell\bar{\nu}_\ell$	$(20.000 \pm 0.055)\,\%$
Hadronic	$Z \to$	$q\bar{q}'$	$(69.911 \pm 0.056)\,\%$

available theoretically and offers the largest branching ratio, the sensitivity is too low due to significant backgrounds. The measurements in this thesis will focus on the three-lepton (3ℓ) channel with semi-leptonic $t\bar{t}$ and leptonic Z boson decays, where only electrons and muons are considered.

Several top quark processes have similar multi-lepton final states and low rates of production, such as: $t\bar{t}W$, $t\bar{t}H$ and $t\bar{t}\gamma$. Accurate knowledge of the $t\bar{t}Z$ production cross-section, therefore, allows for the improvement of the measurements of these SM processes and searches of new physics with similar signatures. The $t\bar{t}Z$ process also features an electroweak top-Z coupling when the Z boson is radiated from the final state radiation (FSR), as in Figure 2.2b. The top-Z coupling is predicted by the SM, but has not been measured directly, and hence is not a well-constrained quantity. New physics effects could act to modify this coupling. Accurate measurements of the $t\bar{t}Z$ system can therefore constrain new physics models.

2.3 Beyond the Standard Model

Even though the Standard Model fits experimental data to a high degree of precision, there is a list of remaining questions that it does not explain. These questions give compelling hints for physics beyond the Standard Model. From the discussion about the SM in Section 2.1, one can identify several deficiencies of the theory already:

- If the SM is an all-encompassing description of the fundamental forces of nature, how can we incorporate gravity?

- Experimental evidence suggests that neutrinos are not massless and modifications of the SM are needed to explain this.
- The range of fermion masses, from 0.5 MeV to 172.7 GeV, varies widely between and within the generations.
- If antiparticles are identical to their particle counterparts except for their charges, the amount of matter-antimatter asymmetry observed in the universe is not sufficiently explained by the amount of CP violation in the SM.
- The SM does not explain the existence or nature of dark matter and dark energy.
- The mass of the Higgs boson is expected to be governed by new physics effects at a high energy scale Λ, which could be as high as the Planck mass $\mathcal{O}(10^{19}\,\text{GeV})$. However, the measured mass of the Higgs boson is 125 GeV and suggests that $\Lambda \approx \mathcal{O}(\text{TeV})$. This is known as the hierarchy problem.

A way to tackle these questions is by using an effective field theory (EFT). An assumption is made that the SM is a low energy approximation of an underlying theory which involves yet undiscovered physics. Such new physics effects are assumed to be beyond the energy reach of the LHC. The idea is then to parameterise an effective theory with a Lagrangian $\mathcal{L}_{\text{EFT}} = \mathcal{L}_{\text{SM}} + \mathcal{L}_{\text{BSM}}(\Lambda)$. The BSM Lagrangian $\mathcal{L}_{\text{BSM}}(\Lambda)$ is defined in terms of a set of dimension-d operators $\mathcal{O}_i$ with the associated Wilson coefficients C_i scaled by the energy scale of new physics Λ^{d-4}. The dimensions-5 operators violate the conservation of the lepton and baryon numbers [17], therefore the discussion will focus on the dimension-6 operators. The expected cross-section can be expanded for a given operator as follows:

$$\sigma = \sigma_{\text{SM}} + \frac{C}{\Lambda^2}\sigma^{(1)} + \frac{C^2}{\Lambda^4}\sigma^{(2)}, \tag{2.2}$$

where σ_{SM} is the SM cross-section, the second linear term corresponds to the interference between the SM and BSM while the third quadratic term is purely a BSM contribution. In this framework, a new physics discovery would appear as a non-zero Wilson coefficient, thus resulting in $\sigma \neq \sigma_{\text{SM}}$. A large number of EFT operators exist that probe different SM interactions. Figure 2.4 shows an example of distributions of the differential cross-section in the transverse momentum of a Z boson, $p_{\text{T}}(Z)$, in $t\bar{t}Z$ events for the Wilson coefficient C_{tG} of the chromo-magnetic dipole operator $\mathcal{O}_{tG}$ fixed to a value of 1 and the energy scale of $\Lambda = 1$ TeV. The SM cross-section is compared

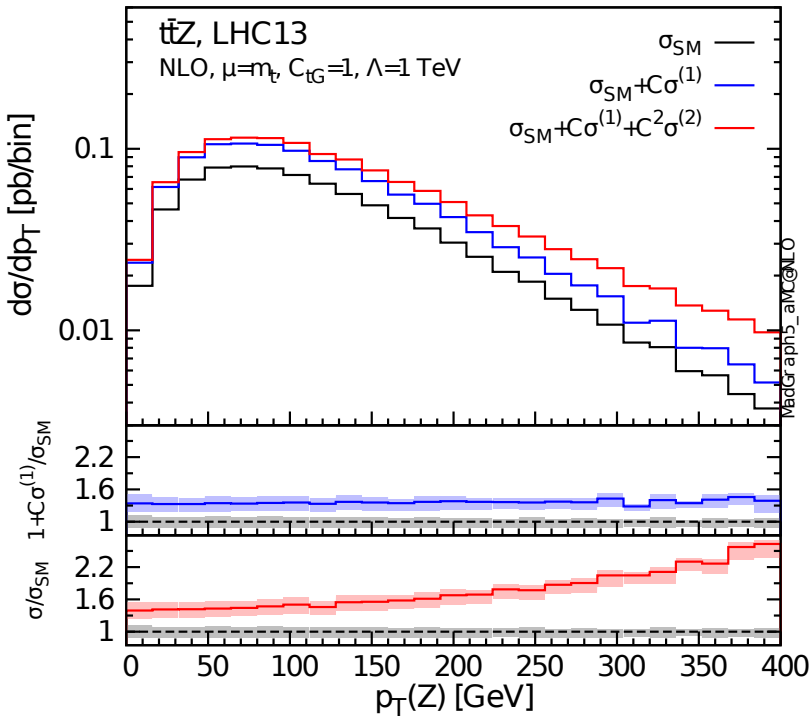

Figure 2.4: The $t\bar{t}Z$ differential cross-section distributions with respect to the transverse component of the Z boson momentum at NLO precision. The black line shows the SM prediction while the red (linear-only term) and blue (linear+quadratic terms) lines estimate new physics effects in an EFT framework [19].

to the expected cross-sections where only the linear or linear and quadratic terms are included. The total (integrated) cross-sections with both linear and linear & quadratic terms are markedly larger than the SM cross-section. This suggests that an EFT interpretation can alreadu be performed with the total cross-section to assess the BSM effects [18]. However, even more sensitivity is available from the differential cross-sections which are possible to measure with the LHC data from the 2015–2018 period. From Figure 2.4, new physics is predicted to be most likely at high energy spectrum when the linear & quadratic terms are included. Therefore if such BSM effects exist, measurements of the differential cross-section with respect to kinematic observables of the $t\bar{t}Z$ system, such as $p_{\mathrm{T}}(Z)$, would reveal progressively larger deviations from the SM expectation with the increasing energy.

Chapter 3

Experimental apparatus

The first particle accelerator was built by John D. Cockcroft and E.T.S. Walton at the Cavendish Laboratory in Cambridge (England) [20, 21] and dates back to the 1930s. Accelerator technology has been evolving substantially since. The LHC [22] at CERN is currently the state-of-the-art facility.

3.1 CERN accelerator complex

CERN hosts a number of accelerators capable of reaching different beam energies. These accelerators are used in a chain to gradually increase the energy of protons before reaching the LHC, all of which starts with a bottle of hydrogen gas. The hydrogen is stripped of its electrons in an electric field, leaving bare protons. These protons are injected into the LINear ACcelerator 2 (LINAC2) [23, 24] where they get accelerated to the energy of 50 MeV. A further boost in energy to 1.4 GeV is given in the Proton Synchrotron Booster (PSB) [25, 26]. The next accelerator in the chain is the Proton Synchrotron (PS) [27] which further accelerates protons to 25 GeV. The penultimate step in the acceleration chain is the Super Proton Synchrotron (SPS) [28] and is used to increase the energy of protons to 450 GeV. The protons are split into two beams upon their entry in the LHC which then circulate in the clockwise and anticlockwise directions. The LHC is designed to achieve an energy of 7 TeV per beam, or a centre-of-mass energy of $\sqrt{s} = 14$ TeV. An overview of the acceleration chain is shown in Figure 3.1.

Operation of the CERN accelerator complex during the 2015–2018 period, called Run-2, is relevant to the work presented in this thesis. During this period, the LHC

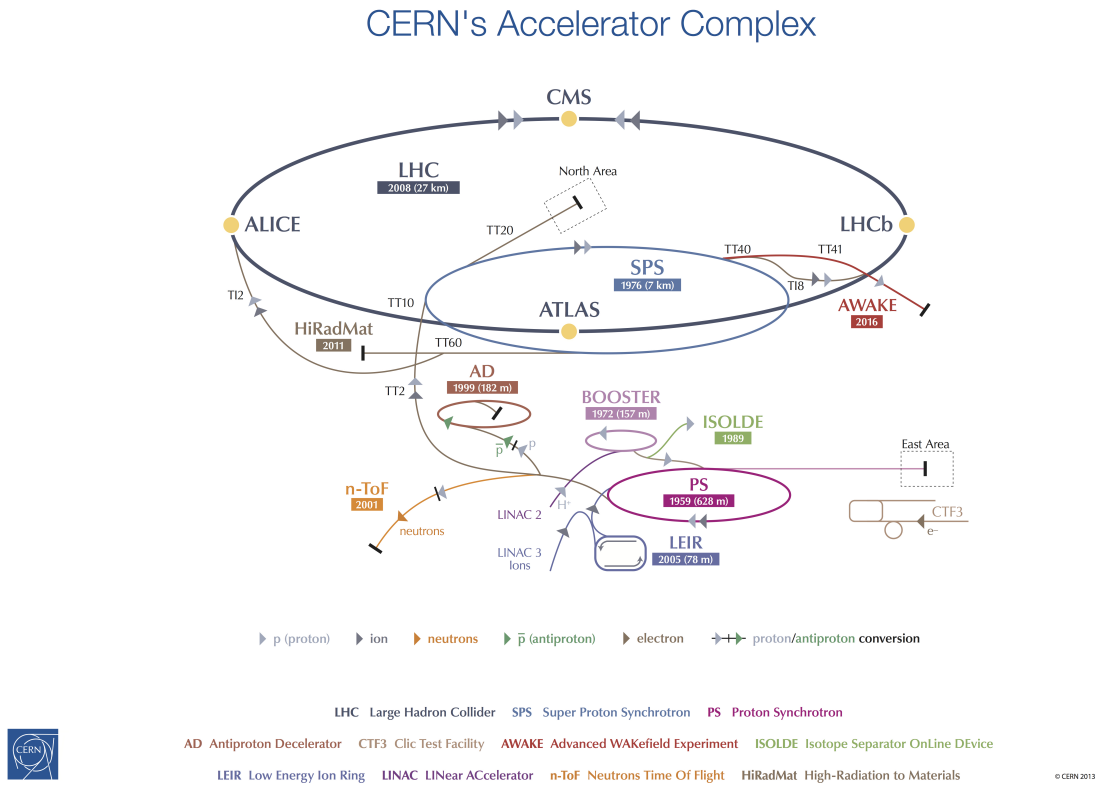

Figure 3.1: Schematic image of the CERN accelerator complex used in the LHC Run-2 [29].

reached $\sqrt{s} = 13\,\text{TeV}$ centre-of-mass energy. Since the end of Run-2, the LINAC2 accelerator has been decommissioned and replaced with LINAC4 [30] which now boosts negative hydrogen ions and strips off their two electrons at the exit. Finally, the LHC energy has been increased to $\sqrt{s} = 13.6\,\text{TeV}$ in the currently ongoing Run-3 data-taking period.

3.2 The Large Hadron Collider

The LHC is a synchrotron that accelerates and collides protons in a 27 km circumference tunnel initially built for and occupied by the Large Electron-Positron (LEP) collider [31]. The LHC started its operation on the 10th of September 2008 and remains the latest addition to the accelerator complex at CERN that is able to achieve collisions of protons at the highest centre-of-mass energy to date.

Often thought of as a circle, the LHC is actually an octagon made of eight straight sections which are connected with eight arcs each of a 3.7 m internal diameter. This shape was inherited from the LEP tunnel and imposes limits on the design of the LHC. In particular, the maximum beam energy is limited by the available magnet technologies that can handle the pre-defined curvature of the arcs. The LHC is instrumented with superconducting electromagnets which operate at a temperature below 2 K and provide magnetic fields larger than 8 T. The superconducting electromagnets are designed as twin-bore, or two-in-one, electromagnets to accommodate two rings with oppositely circulating beams of protons. The beams are bent using 1,232 dipole magnets. Moreover, protons in the beams are bundled into bunches and focused vertically and horizontally using 392 quadrupole magnets. Finally, proton-proton collisions are achieved by squeezing the bunches from the incoming beams together with the dedicated electromagnets. Table 3.1 gives a summary of some of the key LHC parameters used during Run-2.

Collisions occur at four dedicated interaction points (IP) around the LHC tunnel where the four main experiments are housed: A Large Ion Collider Experiment (ALICE) [32], A Toroidal LHC Apparatus (ATLAS) [33], Compact Muon Solenoid (CMS) [34] and Large Hadron Collider Beauty (LHCb) [35]. The ATLAS and CMS experiments are general-purpose detectors designed to cover a wide-ranging physics programme, from the discovery of the Higgs boson, to precision measurements of SM processes (such as $t\bar{t}Z$) to searches of new physics. The LHCb experiment is designed to make precision measurements of the b-quark physics and investigate the CP violation. The ALICE experiment focuses on studies of quark-gluon plasma created in heavy-ion collisions.

In contrast to collisions in classical mechanics, a well-defined cross-sectional area for a scattering event to occur does not exist in quantum mechanics. Rather, the colliding particles have to be "close enough" to each other, within some effective cross-sectional area, for a collision to occur via an exchange of a force-carrying particle. The rate of collisions can be characterized with the instantaneous luminosity [37]:

$$\mathcal{L}(t) = \frac{f N_1 N_2 N_b}{4\pi\sigma_x\sigma_y}, \tag{3.1}$$

where f is the frequency of collisions, N_i is the number of protons per bunch in beam i, N_b is the number of bunches and σ_x and σ_y are width and height, respectively, of

Table 3.1: Parameters of the LHC during Run-2 [36].

Parameter	Value
Circumference	26.659 m
Dipole operating temperature	1.9 K
Number of magnets	9,593
Number of main dipoles	1,232
Number of main quadrupoles	392
Number of RF cavities per beam	8
Nominal energy, protons	6.5 TeV
Number of bunches per beam	2,808
Number of protons per bunch (at start)	1.2×10^{11}
Number of turns per second	11,245
Number of collisions per second	1×10^{9}

the beams with a Gaussian profile. The LHC is designed to achieve an instantaneous luminosity of 10^{34} cm^{-2}s^{-1}. The integrated luminosity ($\int dt\mathcal{L}(t)$) is used to quantify the amount of data that is collected in a certain period of time. The inverse femtobarn (fb^{-1}) is the unit usually used to measure the integrated luminosity. Figure 3.2 shows the daily cumulative luminosity delivered to ATLAS for each year of the LHC operation.

3.3 The ATLAS experiment

The ATLAS detector is the largest particle detector ever built. Its cylindrical geometry measures 44 m in length and 25 m in diameter and weighs 7,000 tonnes. The LHC beampipe runs along the length of the centre of the detector with proton-proton collisions occurring roughly in the geometrical centre. The detector is organized in layers of sub-detector systems built in concentric layers around the beamline and each is designed to record different types of particles.

The innermost detector sub-system starts 3 cm away from the beam pipe and is designed to record the tracks of charged particles. Measurements of electromagnetic and hadronic showers are achieved with dedicated calorimeters which occupy the next

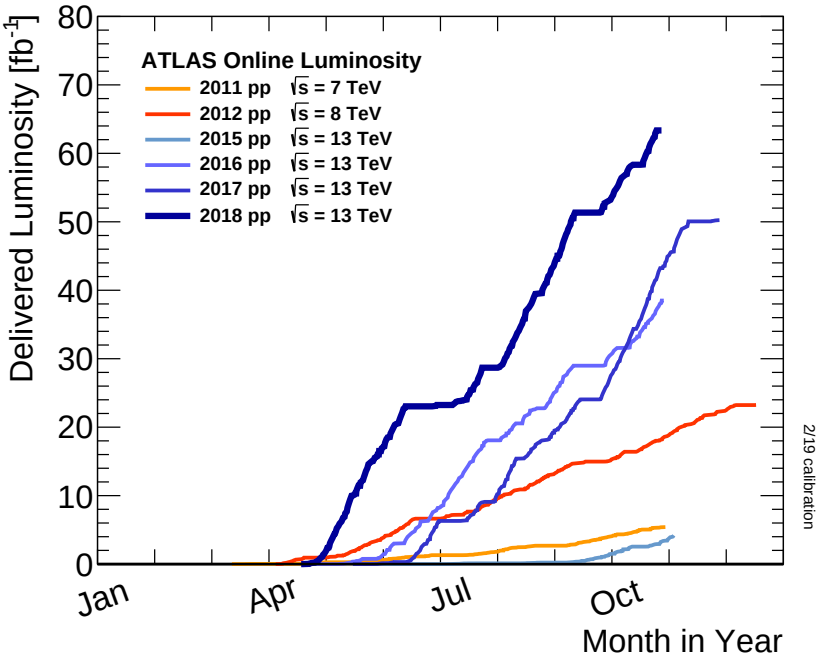

Figure 3.2: The daily cumulative luminosity delivered to ATLAS during stable beams and for high energy proton-proton collisions in the 2011–2018 period [38].

two layers. Lastly, the outermost layer is designed to make precision measurements of muon tracks. Two systems of superconducting magnets are housed in the detector to provide magnetic fields for the tracking sub-detectors. The ATLAS detector and its subsystems are split into a barrel and two endcap regions providing almost a full 4π coverage. The detector is illustrated in Figure 3.3, showing the overall scale of the experiment.

3.3.1 Coordinate system

A right-handed Cartesian coordinate system (x, y, z) is used to describe the ATLAS detector. The interaction point, which coincides with the geometrical centre of the detector, is defined as the origin. The positive x-axis points towards the centre of the LHC ring and the positive y-axis points upwards. The z-axis aligns with the beamline and is defined to be positive in the counterclockwise direction of the LHC tunnel (if viewed from above).

Given the cylindrical shape of the ATLAS detector, a cylindrical polar coordinate system (r, θ, ϕ) is also used. The distance from the beamline is measured with the

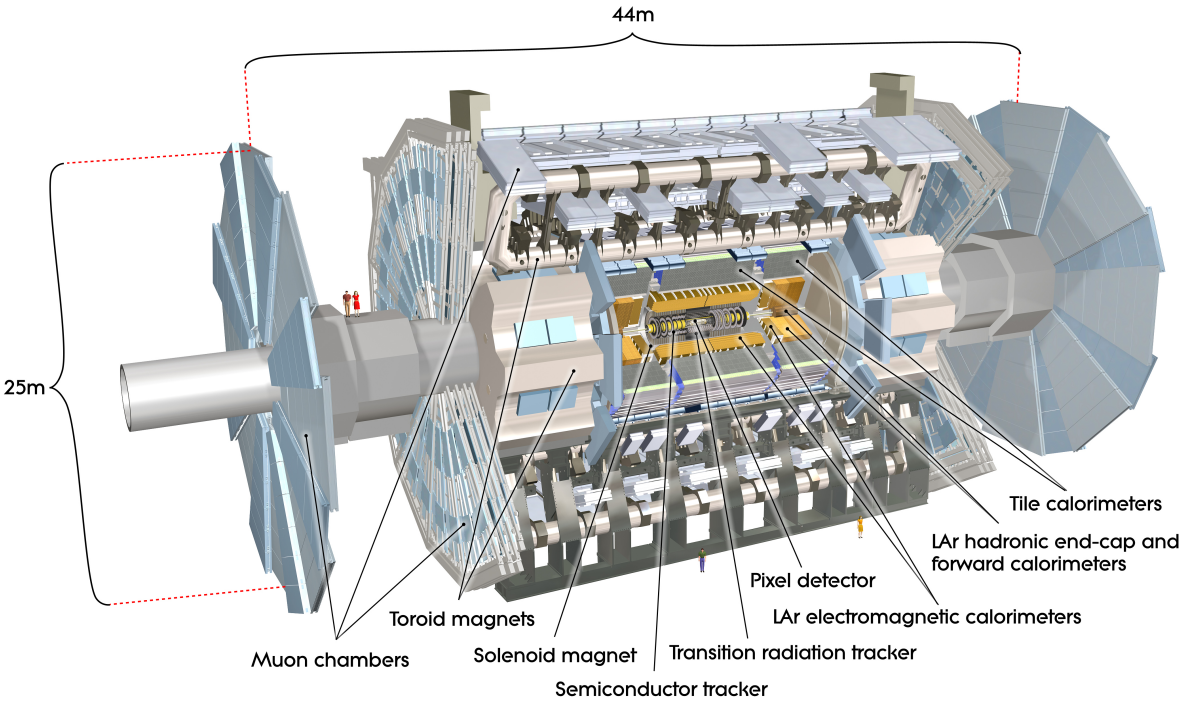

Figure 3.3: Computer generated image of the whole ATLAS detector [39]. Different parts of the detector are identified as well as two people are shown for scale.

radial coordinate, r. The azimuthal angle ϕ is defined as the angle around the z-axis and is in the $[-\pi, \pi]$ range. The polar angle θ is measured in the (x, z) plane and is defined as the angle from the positive z-axis.

It is usually preferable to use variables which are Lorentz invariant in the z direction. The transverse momentum of a particle is defined as $p_{\mathrm{T}} = \sqrt{p_x^2 + p_y^2}$, which is already an invariant quantity under boosts along the z-axis. However, the longitudinal momentum p_z changes under such Lorentz boosts and is, therefore, replaced with rapidity:

$$y = \frac{1}{2} \ln \left(\frac{E + p_z}{E - p_z} \right), \tag{3.2}$$

where E is the energy of a particle. Rapidity is not a Lorentz invariant variable itself, however, differences in rapidity are invariant under boosts in the z direction. For

highly energetic massless particles with $E \gg m$ rapidity simplifies to pseudorapidity:

$$\eta = -\ln\left(\tan\frac{\theta}{2}\right). \tag{3.3}$$

Since the polar angle is not a Lorentz invariant quantity, (pseudo)rapidity is a preferred variable. Based on the definition, η can take values in the $[-\infty, \infty]$ range where $\eta = 0$ is the transverse plane to the beamline while $|\eta| \to \infty$ implies the parallel direction. Finally, the distance between two objects in the $(\eta - \phi)$ plane is defined as

$$\Delta R = \sqrt{(\Delta\eta)^2 + (\Delta\phi)^2}. \tag{3.4}$$

3.3.2 Magnet system

The ATLAS detector operates two superconducting magnet systems [40] which are designed to provide magnetic fields for the two tracking sub-detectors. The central solenoid magnet [41] creates a 2 T magnetic field for the inner tracking detector. The second system uses three sets of eight toroidal magnets [42] to provide a magnetic field to the outer muon tracking detector. Each of the two endcap regions has a set of toroidal magnets, and a third toroid surrounds the barrel region. The endcap toroids create an average magnetic field of 1 T while the barrel magnet provides an average magnetic field of 0.5 T. Figure 3.4 depicts the two systems of magnets.

3.3.3 Inner detector

The Inner Detector (ID) [44, 45] is the innermost system of the ATLAS detector. It is a tracking detector designed to register a series of points along the path of a passing charged particle. These *hits* left by a particle are used to reconstruct its track. Due to the magnetic field of the central solenoid magnet, the detector records information of the direction and curvature of each track in order to determine the momentum and charge of a particle. An overview of the ID is shown in Figure 3.5.

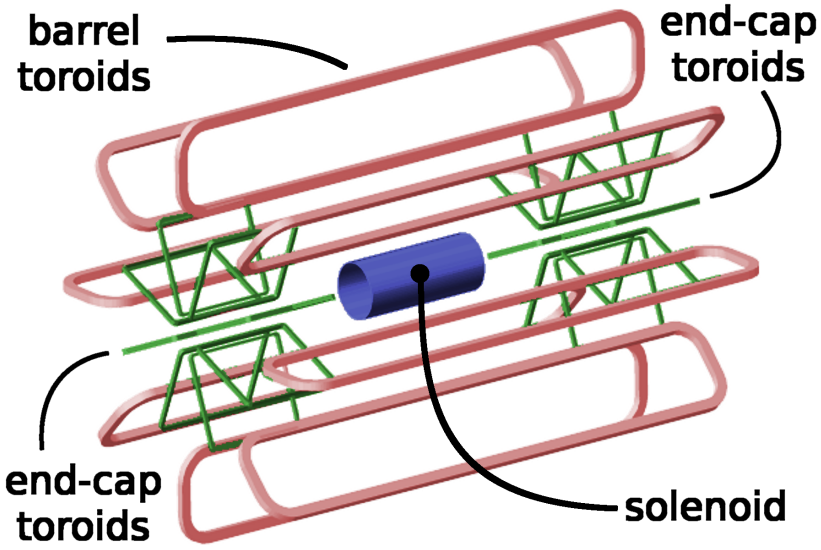

Figure 3.4: Computer generated image of the ATLAS magnet system [43].

Pixel detector

The Pixel detector [47, 48] is the innermost part of the ID. It consists of four layers of finely pixelated silicon sensors in the barrel region and three disk layers in the endcap regions. Charged particles induce electron-hole pairs in a silicon sensor which are then used to generate and record an electronic signal. Closest to the LHC beam pipe is the Insertable B-Layer (IBL) [49, 50, 51] which is designed to improve identification of secondary vertices[1] associated with the decays of B-hadrons. The IBL is built out of pixels of 50×250 µm^2 size while the remaining layers contain 50×400 µm^2 pixels. In total there are 92 million pixels in the detector covering approximately 1.9 m^2 area, a full azimuthal angle and $|\eta| < 3$. It achieves a 10 µm resolution in the orthogonal direction to the beamline and a 115 µm resolution along the beamline.

Semi-conductor tracker

The Semi-Conductor Tracker (SCT) [52] surrounds the pixel detector with modules of long silicon strip sensors. The SCT modules are arranged in four concentric cylindrical layers in the barrel region, $|\eta| < 1.4$, and nine planar discs in each endcap region, $1.4 < |\eta| < 2.5$. Each module contains two silicon strip sensors placed at a slight angle to allow a better spatial resolution. The SCT contains 4,088 modules of two-sided

[1] A secondary vertex occurs as a result of a particle decay or interactions. More on this in Section 4.1.1.

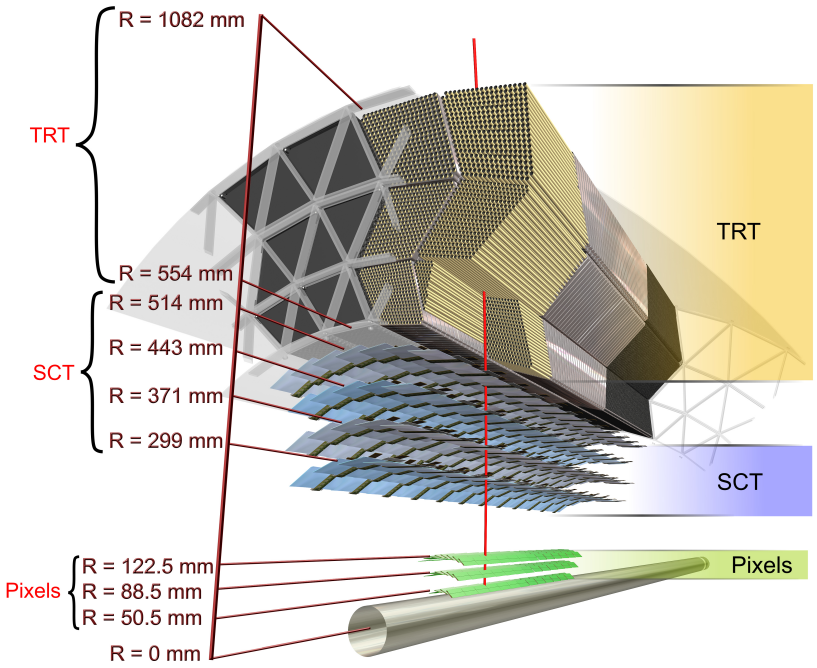

Figure 3.5: Computer generated image of the ATLAS Inner Detector [46].

silicon strip devices amounting to 60 m^2 of silicon. The detector is able to reach a resolution of 17 µm in the $(r - \phi)$ plane and 580 µm in the z direction.

Transition radiation tracker

The Transition Radiation Tracker (TRT) [53] is the final and largest layer of the ID which is used for particle tracking and pion-electron separation. The TRT is built using drift tubes with a diameter of 4 mm and a gold-plated tungsten wire with a diameter of 30 µm is stretched along the length of the tube. The drift tubes are filled with a mixture of Xe, O_2, and CO_2 gases. A passing charged particle ionises the gas and the resulting electrons drift towards the anode wire creating a signal. The drift tubes are arranged in 73 barrel layers and 122 layers in each endcap giving an average of 30–40 position measurements per track. The TRT is able to track charged particles in the $|\eta| < 2$ region with a spatial resolution of 130 µm in the $(r - \phi)$ plane. This is a notably worse resolution than the silicon-based detectors. However, the TRT improves the

tracking performance of the ID significantly, especially at high transverse momentum due to many position measurements [54]. Additionally, the TRT provides information to improve the discrimination between pions and electrons due to the difference in the amount of transition radiation generated by these particles.

3.3.4 Calorimeters

Calorimeters are devices that primarily measure the energy of charged and neutral particles by absorbing them. The ATLAS calorimeters [55] are strategically placed after the ID and designed to measure energies of electrons, photons and hadrons. These calorimeters are called sampling and are built from alternating layers of absorbing and active materials, where energy is measured in the active layers only. High-energy particles lose energy in a material by producing cascades of secondary lower-energy particles, referred to as showers. Electrons and photons lose energy via electromagnetic interactions with the material. In particular, bremsstrahlung is the dominant process for electrons above 10 MeV to lose energy in most materials, while photons predominantly lose energy via electron-positron pair production. The radiation length, X_0, of a material determines the frequency with which electromagnetic interactions occur in that material. The formation of hadronic showers is similar to that of electromagnetic cascades, but is governed by the strong force instead and is characterized by the nuclear interaction length, λ_I, of a material. For a typical material used in a calorimeter, λ_I is much longer than X_0.

Following the discussion above, calorimeters are able to identify particles. The fact that $X_0 \ll \lambda_I$ implies that electrons and photons interact before hadrons. As a result, ATLAS uses two types of calorimeters; the electromagnetic calorimeter followed by the hadronic calorimeter. Figure 3.6 shows the construction of the ATLAS calorimeter system which is described in the following text.

Electromagnetic calorimeter

The electromagnetic calorimeter (ECal) is a liquid argon (LAr) [57] and lead sampling calorimeter. The ECal operates by generating particle showers in the lead absorber layers and ionising the LAr active layers which then produce electronic signals. The calorimeter is designed to provide a consistent amount of material in all directions, corresponding to an interaction length of $22X_0$, and covers a pseudorapidity range of

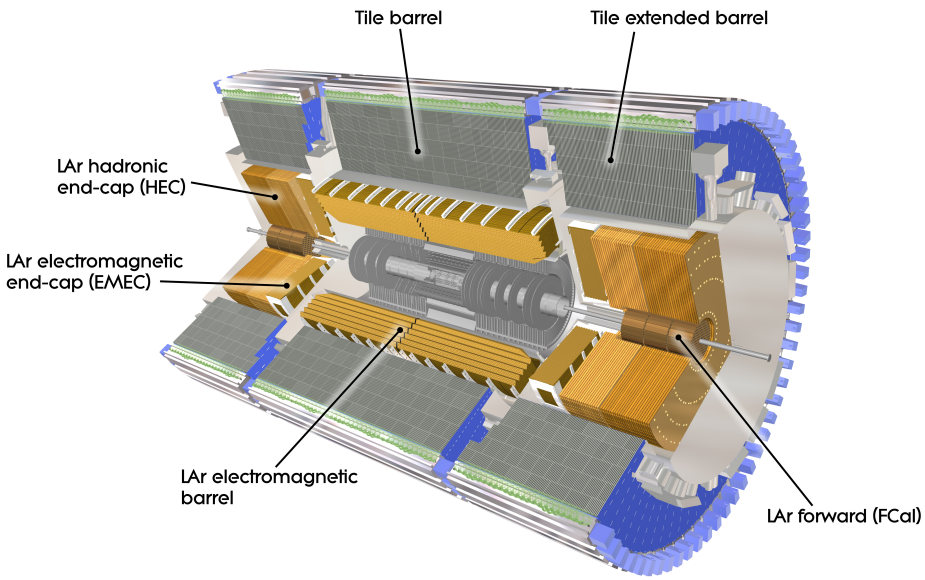

Figure 3.6: Computer generated image of the ATLAS calorimeters [56].

$|\eta| < 3.2$ and the full range of ϕ. The barrel region, $|\eta| < 1.475$, starts with a layer of LAr, called presampler, to measure the amount of energy lost in the ID. The main body of the barrel ECal contains three finely granulated layers to provide measurements of photons and electrons. The endcap regions, $1.375 < |\eta| < 3.2$, are coarser and use only two layers. The resolution of the ECal is parameterised as

$$\frac{\sigma_E}{E} = \frac{10\%\text{GeV}^{1/2}}{\sqrt{E}} \oplus 0.7\%, \tag{3.5}$$

where the first term is due to stochastic sampling fluctuations and the second term is a constant instrumental offset. The $\oplus$ symbol denotes a sum in quadrature.

Hadronic calorimeter

The hadronic calorimeter (HCal) adopts the LAr and scintillating tile [58] technologies in its active layers. The barrel region, $|\eta| < 1.7$, uses steel as the absorber and scintillating tiles as the active medium. Showers of hadrons interact with the plastic scintillator material and produce photons which are then converted into an electronic signal and read out. The endcap regions, $1.7 < |\eta| < 3.2$, induce showers of particles with a copper absorber and detect signals in LAr active layers. Similarly to the ECal,

the resolution of the HCal can be expressed as

$$\frac{\sigma_E}{E} = \frac{50\%\text{GeV}^{1/2}}{\sqrt{E}} \oplus 3\%. \tag{3.6}$$

Forward calorimeters

The Forward Calorimeter (FCal) covers the very-high range of pseudo-rapidity, $3.2 < |\eta| < 4.9$, in order to increase the precision of measuring missing transverse energy. The sampling is done using LAr while layers of copper and tungsten are used as absorbers. The FCal is segmented into three parts (based on the absorber material) where the first part is dedicated to the electromagnetic showers and the last two to the hadronic showers. The resolution of the FCal is:

$$\frac{\sigma_E}{E} = \frac{100\%\text{GeV}^{1/2}}{\sqrt{E}} \oplus 10\%. \tag{3.7}$$

3.3.5 Muon spectrometer

The Muon Spectrometer (MS) [59] is another tracking detector within ATLAS designed to measure tracks of muons. It is the outermost sub-detector system because muons are the only SM charged particles which are not absorbed by the calorimeters. The MS is organised into three layers. The barrel region is arranged in concentric cylindrical shells centred around the beamline while the endcaps form wheels, perpendicular to the z-axis. The precision tracking of muons is available in the $|\eta| < 2.7$ region where the muon track resolution varies with energy. For example, the transverse momentum of a 1 TeV muon is measured with a $\sigma(p_\text{T})/p_\text{T} = 10\%$ resolution.

The MS is also used as a hardware trigger in the $|\eta| < 2.4$ region. Figure 3.7 illustrates the MS within the ATLAS detector, including the superconducting toroidal magnets which provide the necessary magnetic field for the precision tracking of muons. Figure 3.8 is a schematic picture of how different parts of the MS are organised. Four detector technologies are used in the MS. The main subdetector is called the monitored drift tubes and is used in both the barrel and endcap regions. These subdetectors are complemented by the cathode strip chambers in the first layer of the endcap regions. The resistive plate chambers and cathode strip chambers are also used in the barrel and encap regions, respectively.

Monitored drift tubes

The Monitored Drift Tubes (MDTs) [62] are cylindrical tubes filled with a mixture of Ar and CO_2 gases. Each tube contains a tungsten wire running in the centre of the tube along its length. As a muon passes through a drift tube, it ionises the gas and the resulting electrons drift in the electric field towards the anode wire while the ions move towards the cathode tube to create a signal. The MDTs are used for the precision tracking of muons.

The drift tubes are arranged into chambers, each chamber contains two groups of drift tubes and each group has either three or four layers of tubes. All three layers of the MS in the barrel region are instrumented with MDTs covering the $|\eta| < 2.7$ range. In contrast, the MDTs in the innermost layers of the endcap regions cover a shorter pseudorapidity range of $|\eta| < 2.0$. The MDT technology has an excellent spatial resolution, with each chamber providing up to 30 µm precision and high tracking efficiency that is independent of the angle of incidence.

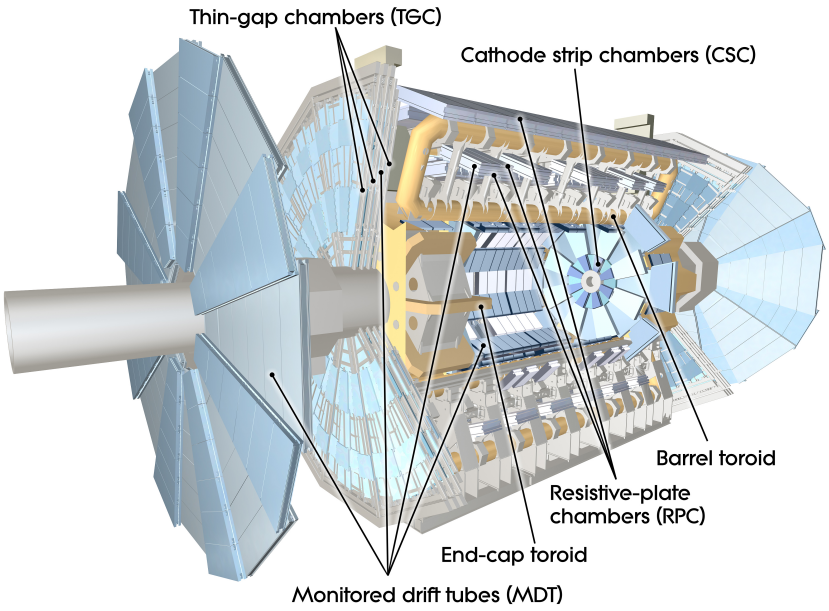

Figure 3.7: Computer generated image of the ATLAS muon spectrometer [60].

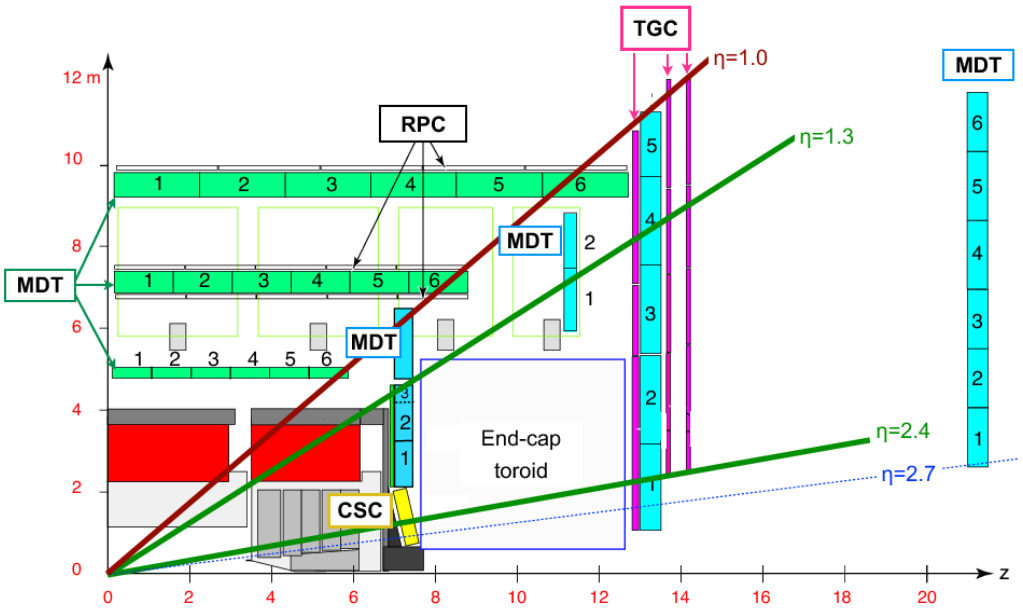

Figure 3.8: A schematic picture showing a quarter-section of the muon system in a plane containing the beam axis [61].

Cathode strip chambers

The Cathode-Strip Chambers (CSCs) [63] are multi-wire proportional counters with segmented cathode readout. The CSCs consist of two layers of resistive strip plates, which act as cathodes, and surrounding anode wires. A mixture of Ar and CO_2 gases is used to fill the gap between the plates. One layer of the cathode strips is oriented perpendicularly to the direction of the anode wires in order to provide a ϕ coordinate. The other layer is arranged parallel to the wires to provide the η measurement. Similarly to the MDTs, a passing muon ionises the gas, and the resulting electrons and ions drift towards the anode and cathode, respectively.

The CSCs are installed in the first endcap layer of the muon spectrometer to cover the high pseudorapidity range, $2.0 < |\eta| < 2.7$. The CSCs are able to handle particle flux up to $1000\,\mathrm{Hz/cm^2}$ in contrast to the MDTs which can only sustain a flux of up to $150\,\mathrm{Hz/cm^2}$. Thus, they complement the precision tracking of muons provided by the MDTs.

Resistive-plate chambers

The Resistive Plate Chambers (RPCs) [64] are gaseous detectors that are primarily used to provide trigger functionality for the MS. The RPCs consist of two parallel plates separated by a gap of the order of a few millimetres and filled with a mixture of $C_2H_2F_4$, Iso$-C_4H_1O$ and SF_6 gases. The RPCs are capable of handling high rates of particles in high-background environments. They cover a range of $|\eta| < 1.05$ in the barrel region and provide position resolution of 10 mm. The RPCs achieve a time resolution of 1 ns which is independent of the particle rate.

Thin-gap chambers

The Thin Gap Chambers (TGCs) [65] are multi-wire proportional chambers, much like the CSCs. The wire-to-cathode distance is smaller than the wire-to-wire distance in the TGCs, while these distances are equal in the CSCs. The TGCs are located in the endcap regions of the MS to extend the triggering functionality up to $|\eta| = 2.4$. They provide approximately the same time resolution as the RPCs while the spatial resolution is improved up to 2 mm.

3.4 Trigger system

The LHC provides proton bunch crossings every 25 ns in the ATLAS detector, which corresponds to a 40 MHz event rate or a stream of 60 TBs of data every second. It is not possible to read out and store such a massive rate of data from the computational point of view. Furthermore, it is expected that the majority of interesting physics phenomena lie in events containing high-momentum objects. Thus, rooted in the technical limitations and backed up by physics, the ATLAS collaboration has developed a two-level data filtering system, the Trigger and Data Acquisition (TDAQ) system. The TDAQ system uses custom-made electronics and software to reduce the data rate to about 2 GB/s which is then stored for physics analyses.

3.4.1 Level-1 trigger

The Level-1 (L1) trigger [66] is a hardware-based event selection system that uses reduced granularity information from the calorimeters and the RPCs and TGCs of the muon spectrometer. The L1 trigger is designed to process an event in less than 2.5 µs which is achieved by doing a coarse analysis of events. It identifies events potentially containing high-p_{T} leptons, jets or high missing transverse energy and uses this information to perform the first selection step[2]. Regions in the $(\eta - \phi)$ space where such high-energy activities are detected are called regions of interest (ROIs). The initial event rate is reduced to 100 kHz in L1 and is passed on to the second trigger stage.

3.4.2 High level trigger

The High-Level Trigger (HLT) [67] is a software-based trigger that receives full fine-granularity information of the events passing the L1 trigger. The HLT has 40,000 CPU cores at its disposal and 200 µs to make a decision by processing data in steps of increasingly more complex reconstruction algorithms. Such a sequence of algorithms is called a trigger *chain* and is designed to identify a particular type of a physics object, e.g. an electron or a muon. A large *menu* of trigger chains is selected based on the ATLAS physics programme and the needs of different physics analyses. To preserve the computational resources, an event is rejected by a trigger chain in the first instance it fails a reconstruction algorithm. However, such an event is not immediately discarded by the menu. Instead, it is further processed by all the chains in the same manner. An event which passes at least one of the chains is stored long-term for physics analyses. As a result, the HLT reduces the event rate to 1 kHz.

Muon high level trigger

The following is an illustration of an HLT chain using a muon-specific HLT chain as an example. High-level muon trigger chains start from ROIs within the MS and a fast reconstruction of muon tracks using trigger-specific algorithms. Muon tracks are reconstructed using relatively simple techniques such as local linear fits and look-up tables. This reduces the complexity of the algorithms and the execution time to $\mathcal{O}(\mathrm{ms})$.

[2] Identification of particles is not performed at this stage, it is done at a later stage (Chapter 4).

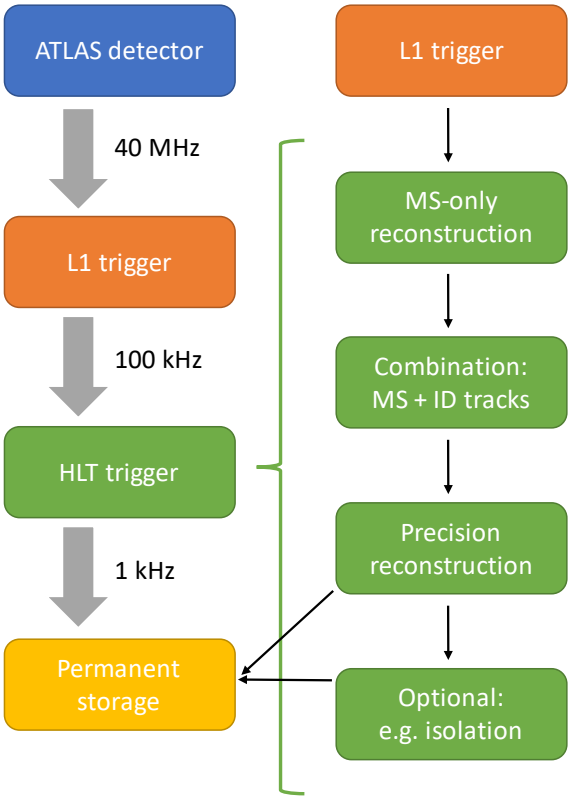

Figure 3.9: Overview of the ATLAS trigger system on the left with a more detailed breakdown of the muon HLT trigger on the right.

Next, muon tracks in the MS are combined with matching tracks in the ID using optimised look-up tables, and their p_{T} is estimated as a weighted average of the tracks. Finally, the precision reconstruction is applied to the events which pass the first two steps. Keeping to the ROIs, muon tracks are extrapolated *outside-in* from the MS to the ID using higher precision reconstruction algorithms. In cases when no ID track is matched to an MS track, the reverse, *inside-out*, procedure is performed where the unmatched ID tracks are extrapolated to the MS. Alternatively, the search of muon tracks can be extended to outside the ROIs for the full-scan (FS) reconstruction. Muon tracks can further be rejected based on other optional requirements such as isolation. A track is considered to be isolated if there are no other tracks within a specified volume around it. The ATLAS HLT trigger chains follow a naming convention that identifies the key characteristics of a chain. For example, the `HLT_mu20_iloose_L1MU15` chain picks out events containing at least one muon with $p_{\mathrm{T}} > 20$ GeV and satisfying loose isolation requirements; the last part in the string refers to the L1 trigger. Figure 3.9 summarises the discussion above.

Chapter 4

Analysis tools and techniques

4.1 Reconstruction of physics objects

The ATLAS detector is designed to detect products of proton-proton collisions based on their nature and interactions with the sub-detector materials. Figure 4.1 shows example paths of various particles traversing ATLAS. The output of the detector is a collection of electronic signals. To make sense of this information, the data has to be carefully processed, cleaned and reconstructed to form physics objects. The following sections will describe how the physics objects relevant for the measurements of the $t\bar{t}Z$ system are reconstructed using advanced analysis techniques.

4.1.1 Inner detector tracks, vertices and pileup

Charged particle tracks in the ID are reconstructed from charge depositions (hits) in the layers of the Pixel, SCT and TRT sub-detectors. Three-dimensional *space-points* of particle hits are used to create *track-seeds* in the Pixel and SCT sub-detectors. Track candidates are extrapolated from the track-seeds using a combinatorial Kalman filter [69], cleaned by resolving overlaps and rejecting incorrect combinations, and finally, extended to the TRT sub-detector. A detailed description of the reconstruction procedure is given in Ref. [70].

Each track is described by five parameters, $(d_0, z_0, \phi, \theta, q/p)$, and a reference point defined as the average position of the proton-proton interactions. The transverse impact parameter, d_0, is the distance of closest approach to the beamline in the $(r - \phi)$ plane, the longitudinal impact parameter, z_0, is the distance along the beamline

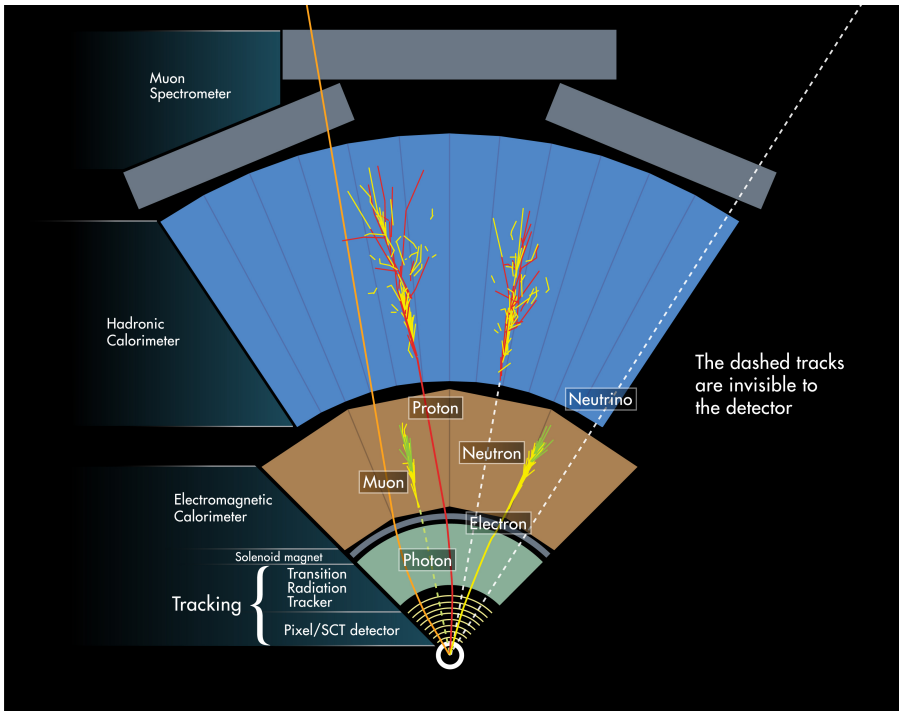

Figure 4.1: Schematic representation of interactions of various physics objects with the ATLAS detector [68].

between the point of closest approach and the reference point, ϕ is the azimuthal angle, θ is the polar angle and q/p is the ratio of charge to momentum. Tracks are required to pass several selection criteria, including $p_{\mathrm{T}} > 400\,\mathrm{MeV}$, $|\eta| < 2.5$, $|d_0| < 2\,\mathrm{mm}$ and $|z_0 \sin(\theta)| < 3\,\mathrm{mm}$.

Once the ID tracks have been established, they are extrapolated backwards to the beam interaction region. Locations where several tracks meet are called vertices and correspond to particle-particle interactions or particle decays. Each bunch crossing at the LHC produces a large number of low energy interactions which may be accompanied by a high transverse momentum hard-scattering interaction. The low energy interactions are collectively called pileup and lead to many vertices. The primary vertex (PV) is identified as a vertex with the largest $\sum p_{\mathrm{T}}^2$ over the associated tracks and is considered to be originating from the hard scatter. The remaining vertices are called secondary and are associated with the pileup events or decays of long-lived particles, such as B-hadrons.

4.1.2 Electrons

Electrons are reconstructed using the information from the electromagnetic calorimeter and the ID. Electromagnetic showers in the calorimeter are reconstructed with a topological clustering algorithm [71] which builds dynamic variable-size clusters and is able to recover low energy, $\mathcal{O}(100\,\text{MeV})$, bremsstrahlung photons. The clustering algorithm relies on the cell significance variable, defined as:

$$\zeta_{\text{cell}}^{\text{EM}} = \frac{|E_{\text{cell}}^{\text{EM}}|}{\sigma_{\text{noise,cell}}^{\text{EM}}}, \tag{4.1}$$

where $|E_{\text{cell}}^{\text{EM}}|$ is the absolute cell energy at the EM scale and $\sigma_{\text{noise,cell}}^{\text{EM}}$ is the expected cell noise. Topo-cluster formation is an iterative procedure. First, cells with $\zeta_{\text{cell}}^{\text{EM}} \geq 4$ are selected to seed *proto-clusters*. Proto-clusters expand by progressively collecting neighbouring cells with $\zeta_{\text{cell}}^{\text{EM}} \geq 2$ until no neighbouring cell meets the criterion. Lastly, the cell significance requirement is relaxed to $\zeta_{\text{cell}}^{\text{EM}} \geq 0$ in order to collect the remaining calorimeter cells neighbouring each proto-cluster. The output of this procedure is a collection of topo-clusters. The topo-cluster with the highest p_{T}, a minimum of 1 GeV energy and matching an ID track with at least four hits is selected as the seed of a super-cluster, as depicted in Figure 4.2. The remaining topo-clusters are examined for association with the super-cluster and are labelled as the *satellite* clusters if they meet the criteria. The above procedure is repeated on the remaining topo-clusters until the collection is exhausted. Each super-cluster with an associated track is considered to be a candidate electron whose energy is determined from the cluster energy.

The measurement of the cluster energy is calibrated using the $Z \to ee$ events in order to mitigate the differences between the data and Monte Carlo (MC) simulations [73, 74]. Corrections are applied to the data to improve the uniformity of the energy response, intercalibrate the different calorimeter layers and calibrate the absolute energy scale. The energy resolution corrections are applied to the MC simulation in order to correct the mismodelling.

The collection of calibrated electrons is refined based on the requirements for the electron p_{T}, η, and longitudinal and transverse impact parameters. The following selection is applied: $p_{\text{T}} > 7\,\text{GeV}$, $|\eta^{\text{clust}}| < 2.47$ except from $1.37 < |\eta^{\text{clust}}| < 1.52$, $|d_0/\sigma(d_0)| < 5.0$ and $|z_0 \sin(\theta)| < 0.5\,\text{mm}$. Electrons are further classified using the identification quality criteria [74]. A likelihood-based (LH) multivariate discrimi-

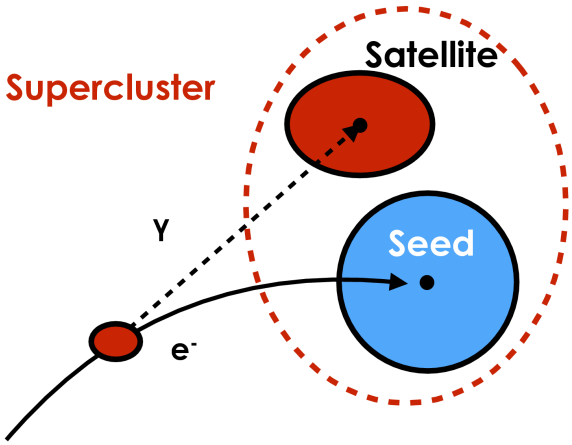

Figure 4.2: A schematic depiction of a supercluster consisting of the seed and a satellite topo-clusters originating from an electron and a photon, respectively [72].

nator [75] is used to assign an identification score to each candidate electron. Five thresholds on the identification score, called working points (WP) are calibrated by the ATLAS collaboration. They correspond to the different identification efficiencies of electrons, listed here in decreasing order of efficiency: `VeryLoose`, `Loose`, `LooseAndBLayer`, `Medium` and `Tight`. The `Medium` WP is used for the analysis selections presented in this thesis. Figure 4.3 shows efficiencies of the `Loose`, `Medium` and `Tight` WPs as functions of E_{T} and η.

4.1.3 Muons

Muons are charged particles which are reconstructed primarily using the MS and ID. Muons have minimal interactions with the calorimeters and, thus, can be detected in the MS. However, the calorimeters are also used in the reconstruction. The muon reconstruction procedure in the ID follows the same steps as any other charged particle. This section describes the reconstruction of muon tracks in the MS and the combined muon reconstruction.

Muon reconstruction in the MS

The reconstruction of a muon track in the MS starts with finding muon *segments*. A segment is defined as a track in a single layer of the MS. For the segments in the MDT

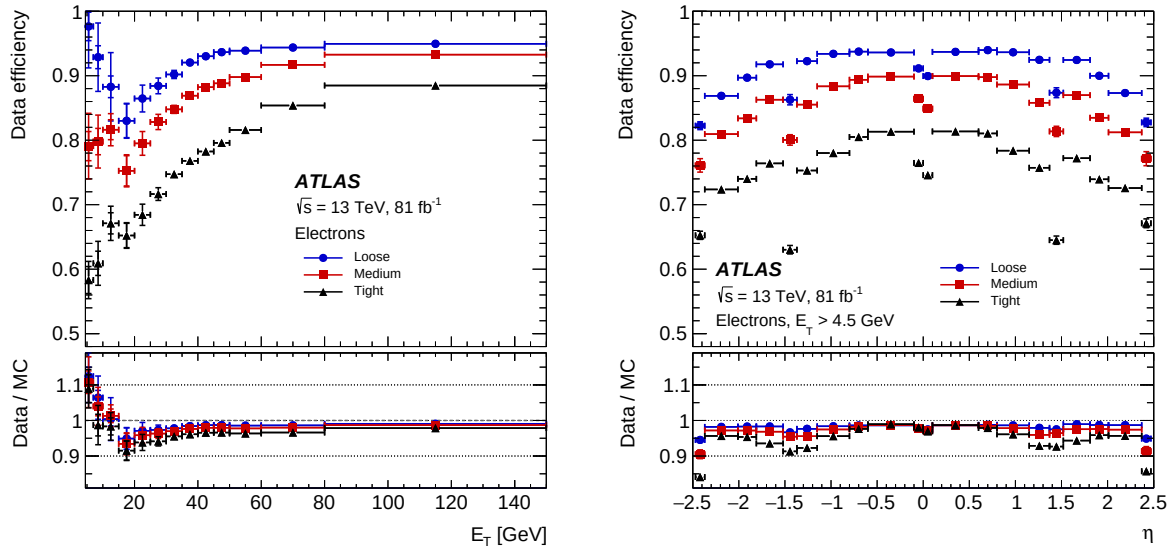

(a) **(b)**

Figure 4.3: The electron identification efficiency as a function of (a) E_{T} and (b) η for the `Loose`, `Medium` and `Tight` working points. The efficiencies are calculated from the data-to-simulation ratios using the $J/\psi \to ee$ and $Z \to ee$ events [74].

chambers, a Hough transform [76] is applied to find a straight-line fit along the hits in a single layer. In contrast, the CSC segments are built from a combinatorial search in the $(\eta - \phi)$ plane.

Once the segment search is completed, the segments in the middle layer are used as seeds and the MS tracks are built by matching a seed with segments in the inner and outer layers of the MS. Tracks are required to have at least two segments, except in the barrel-endcap transition region where a single high-quality segment is allowed to form a track. A global χ^2 fit is performed on the hits associated with each track candidate to define MS tracks.

Combined muon reconstruction

Information from the ID, MS and calorimeters can be combined in several ways to reconstruct muons. Four types of the reconstruction procedure are used by the ATLAS collaboration:

- Combined muon (CB) tracks are built from the independently reconstructed muon tracks in the ID and MS. These MS tracks are extrapolated inwards and

matched to ID tracks. An inside-out reconstruction is also available if the primary outside-in procedure does not find a match.

- Segment-tagged (ST) muons are defined as muon tracks where an ID track is matched with at least one MS segment.
- Calorimeter-tagged (CT) muons are muon tracks created from hits in the ID and energy deposits in the calorimeters. An ID track is reconstructed as a muon if it has a matching energy deposit in the calorimeter that is consistent with a minimum-ionizing particle.
- Extrapolated muons (ME) are reconstructed from the MS hits alone with a loose requirement for the track to be compatible with the interaction point. ME tracks are required to have hits in at least two layers of the MS, except from the forward region, $2.5 \geq |\eta| \geq 2.7$, where three layers are required.

The momentum scale and resolution of reconstructed muons are calibrated to correct the performance in simulation with respect to the data [77]. The CB muons are used to measure the correction factors in data using the $Z \to \mu\mu$ and $J/\psi \to \mu\mu$ events for the ID and MS separately. The calibrated muons are required to pass the standard $p_{\mathrm{T}} > 7\,\mathrm{GeV}$, $|d_0/\sigma(d_0)| < 3.0$ and $|z_0 \sin(\theta)| < 0.5\,\mathrm{mm}$ requirements.

Quality requirements are applied to the muon identification relying on the fact that non-prompt muon tracks in the ID often have a characteristic kink marking the point where a decay occurs. This results in a poor fit quality of the combined muon as the momentum measurements in the ID and MS are in disagreement. Three muon identification quality definitions, namely, `Loose`, `Medium`, `Tight`, are available [78]. Figure 4.4 shows the reconstruction and identification efficiencies of the `Tight`, `Medium` and `Loose` muons as functions of p_{T} and η. The default muon quality WP used by ATLAS and in the analyses discussed in this thesis is `Medium`.

4.1.4 Prompt lepton tagging

Prompt leptons are defined as electrons or muons which originate from the decays of W or Z bosons. Due to the small lifetimes of these bosons, prompt leptons are created near the interaction vertex. Non-prompt leptons, on the other hand, include leptons originating from the decays of hadrons containing b or c quarks which have larger lifetimes and can be measured experimentally. Lepton signatures can also be faked in

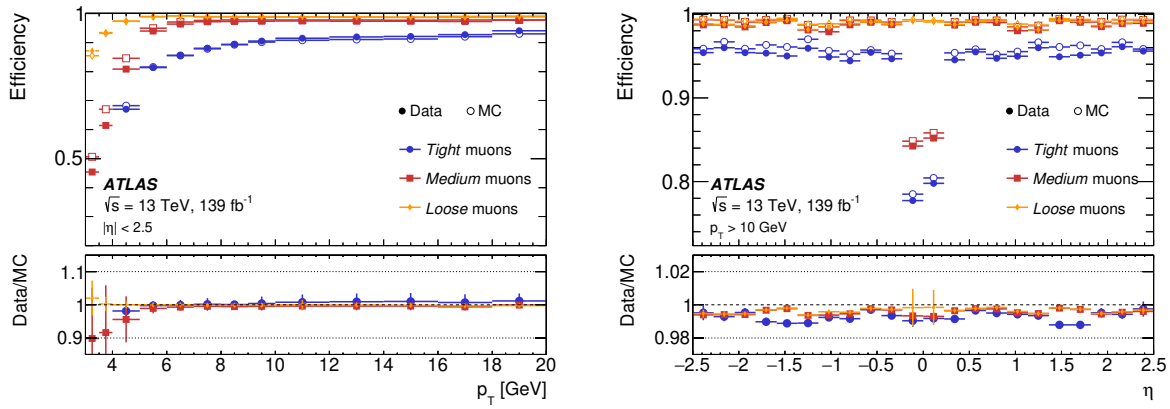

(a) **(b)**

Figure 4.4: Reconstruction and identification efficiencies of muons for the `Loose`, `Medium` and `Tight` working points as functions of muon (a) p_{T} and (b) η. The error bars indicate the statistical uncertainty in the efficiency while the ratio plots include systematic uncertainties as well [78].

processes such as photon conversions or meson decays. The following text will refer to both the non-prompt and fake leptons as the fake lepton background or fake leptons.

In addition to applying requirements on the lepton identification and impact parameters for the electron and muon reconstructions, lepton isolation requirements are also applied to reject fake leptons. Isolation of a lepton is calculated from the amount of detector activity in a cone of radius ΔR around it, excluding the lepton itself. The amount of the transverse energy, $E_{\mathrm{T}}^{\mathrm{varcone}}$, around a candidate lepton (charged or neutral) is measured in the calorimeter. Similarly, the scalar sum of the transverse momenta, $p_{\mathrm{T}}^{\mathrm{varcone}}$, around a charged candidate lepton is measured in the tracker. The ATLAS collaboration provides recommendations for the isolation working points using selection requirements on the aforementioned variables [74, 77].

Measurements of multi-lepton processes such as $t\bar{t}Z$ are susceptible to the fake lepton background and may benefit from a more efficient lepton isolation strategy than the cut-based approach. The prompt lepton veto (PLV) algorithm is a multivariate technique to tag prompt leptons and is based on a boosted decision tree (BDT) algorithm [79]. The isolation and lifetime variables are combined in the BDT model which is trained on $t\bar{t}$ events. The prompt lepton improved veto (PLIV) algorithm is a second iteration of the PLV algorithm. The PLIV algorithm aims to further increase the discriminating power between the prompt and fake leptons by adding dedicated isolation and lifetime variables for prompt lepton tagging. The ATLAS

collaboration recommends two PLV WPs, `PLVLoose` and `PLVTight`, and two PLIV WPs, `PLImprovedTight` and `PLImprovedVeryTight` [80]. These working points are calibrated to match the efficiencies in MC simulation with the data using $Z \to \ell\ell$ events.

4.1.5 Jets

Experimentally, partons are indirectly detected as cone-like cascades of secondary charged or neutral particles that are approximately collimated in the direction of the original partons. These cascades or showers of particles are called jets. They are reconstructed using dedicated clustering algorithms which are required to be infrared and collinear (IRC) safe [81]. An infrared-safe algorithm is one that is invariant upon adding additional soft radiation, e.g. a low-p_{T} particle. Collinear safety ensures that a jet reconstruction is invariant to the addition of a particle which is collinear to the jet. The sequential recombination anti-k_{T} jet clustering algorithm [82] is used by ATLAS. The algorithm groups clusters of energy deposits left by hadronic showers based on a distance between two entities i and j, d_{ij}:

$$d_{ij} = \min\left(\frac{1}{p_{\mathrm{T},i}^2}, \frac{1}{p_{\mathrm{T},j}^2}\right)\frac{\Delta R_{ij}^2}{R^2}, \tag{4.2}$$

and a distance between the entity i and the beam, d_{iB}:

$$d_{iB} = \frac{1}{p_{\mathrm{T},i}^2}, \tag{4.3}$$

where $\Delta R_{ij}^2 = (\phi_i - \phi_j)^2 + (y_i - y_j)^2$ is a separation between two entities in the $(y - \phi)$ space, p_{T} are their transverse momenta, R is an adjustable fixed-radius parameter set to $R = 0.4$.

The anti-k_{T} algorithm builds jets from topologically reconstructed energy clusters in the hadronic calorimeter. The topological clustering procedure is equivalent to that of the topo-cluster procedure described for electrons in Section 4.1.2. A cluster is considered to be a jet if its d_{iB} distance is smaller than any d_{ij} distance, otherwise a *pseudo-jet* is created by merging cluster i with another cluster j with the smallest value of d_{ij}. The algorithm continues to merge topo-clusters and pseudo-jets in this manner until all topo-clusters are reconstructed into jets.

A jet calibration procedure is applied to correct for the calorimeter response and differences arising between jets reconstructed from simulation and from the data [83]. Calorimeter energy deposits are measured on the energy scale consistent with purely electromagnetic interactions and therefore lead to hadronic jet energy lower than the true value. Jet energy scale (JES) corrections [84] are derived from MC simulations and *in-situ* measurements to restore the jet energy response to hadronic energy levels. Jet energy resolution (JER) corrections [85] are applied to account for the resolution differences in the data and the MC simulation. Jets originating from pileup are identified and rejected using a jet vertex tagger (JVT) [86, 87], a procedure which relies on a likelihood-based multivariate discriminant. Only the calibrated jets which pass a $p_{\mathrm{T}} > 25\,\mathrm{GeV}$ selection and are within $|\eta| < 2.5$ are accepted.

4.1.6 Jet flavour tagging

Jet flavour tagging, commonly referred to as b-tagging, is a procedure to label jets with respect to the flavour of the quarks they originate from. Three classes of jets are commonly used by ATLAS analyses: b-jets which originate from b-hadron decays, c-jets which contain c-hadrons and no b-hadrons, and light-flavour jets which contain neither b-hadrons nor c-hadrons. Since the top quark decays via the $t \to Wb$ process nearly 100% of the time, measurements of the $t\bar{t}Z$ system rely on efficiently identifying b-jets to reject backgrounds featuring c and light-flavour jets.

Low-level flavour tagging algorithms are based on properties of individual charged-particle tracks associated with a hadronic jet [88], secondary vertex finding [89] or a topological multi-vertex finding algorithm [90]. Outputs of the low-level algorithms are combined in high-level multivariate algorithms: a boosted decision tree based `MV2` algorithm or a deep feed-forward neural network (NN) based `DL1` algorithm [88].

The `MV2` algorithm uses kinematic properties of jets, p_{T} and $|\eta|$, in addition to the low-level variables to produce discriminants for b-, c- and light-flavour jets. The optimised `MV2c10` version of the `MV2` algorithm, which offers a more optimal balance between the c-jet and light-flavour jet rejections [91], is recommended for ATLAS analysis. Figure 4.5 shows the rejections of c- and light-flavour jets as a function of the b-tagging efficiency with the `MV2c10` algorithm.

The `DL1` algorithm is a successor to `MV2`. Aside from switching to the classification with a deep neural network, `DL1` uses the same input variables as the `MV2` algorithm

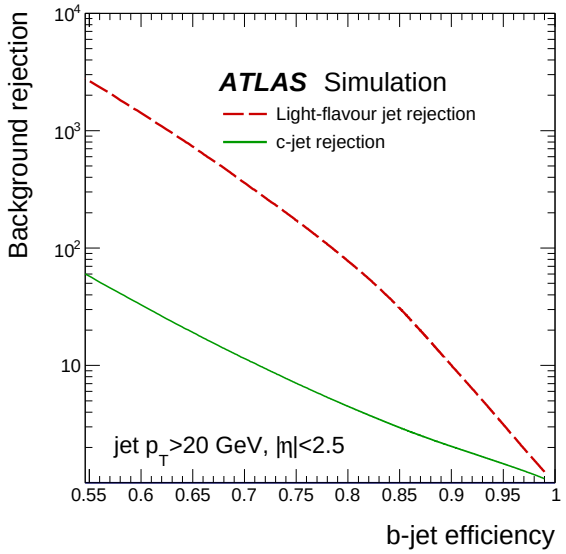

Figure 4.5: The light-flavour jet (red line) and c-jet (green line) rejection as a function of the b-jet tagging efficiency using the `MV2c10` algorithm [91].

and includes the `JetFitter` [90] c-tagging variables. The recommended version of the `DL1` algorithm for ATLAS analyses is `DL1r`. The performance of this version is improved by employing the output of a recurrent neural network which is designed to exploit the correlations between the impact parameters of tracks [92]. Figure 4.6 shows the light-flavour and c-jet rejections as a function of the b-tagging efficiency using the `MV2`, `DL1` and `DL1r` algorithms.

Both algorithms are calibrated by estimating the discrepancies between the tagging efficiencies in the data and simulated $t\bar{t}$ and Z+jets events [93]. The associated scale factors are derived as functions of jet p_{T} to match the simulation with the data. The ATLAS collaboration supports four flavour-tagging working points corresponding to the b-tagging efficiencies of 85%, 77%, 70% and 60%. The calibration procedure can be performed for each working point separately, called a fixed b-tagging, or as a function of the four b-tagging scores, called pseudo-continuous b-tagging (PCbT). With the former, jets can only be tagged with one of the four efficiencies which may be a limiting factor for an analysis. The latter allows to use more than one b-tagging working point in a single event selection and the associated uncertainties are propagated consistently. The PCbT approach will be discussed and demonstrated in more detail in Section 8.4. It is applied in both the inclusive and differential $t\bar{t}Z$ cross-section measurements.

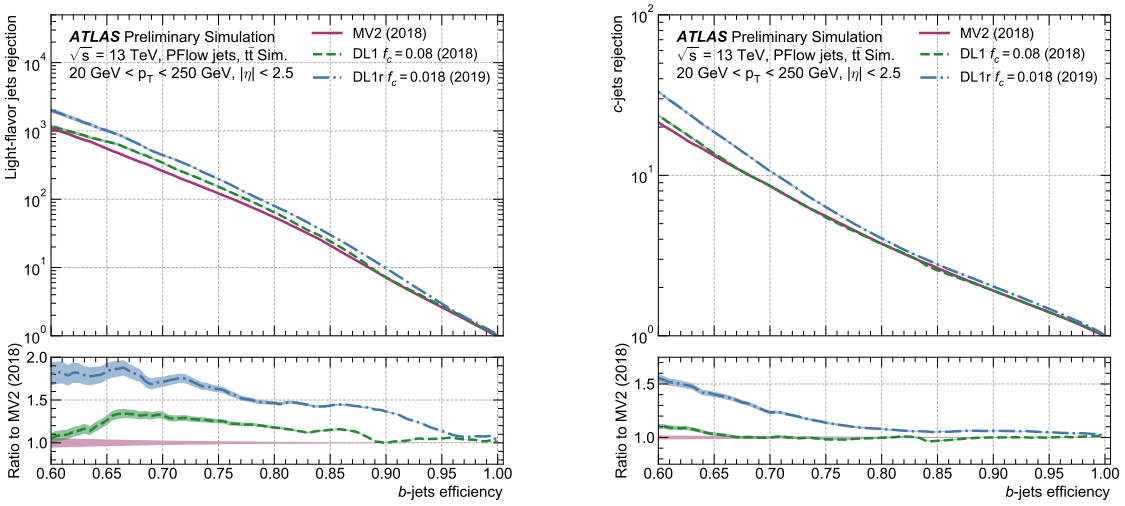

(a) **(b)**

Figure 4.6: Comparison of (a) the light-flavour jet and (b) c-jet rejection as a function of the b-tagging efficiency using the `MV2` (purple line), `DL1` (green line) and `DL1r` (blue line) algorithms [92].

4.1.7 Missing transverse energy

Conservation of momentum implies that the sum of the transverse momenta of all particles in a given collision event should be zero. However, experimentally this is usually not the case due to reconstruction inefficiencies of objects as well as due to the production of neutrinos in many SM processes which escape detection. The missing transverse energy, $E_{\mathrm{T}}^{\mathrm{miss}}$, is defined as the modulus of the negative vectorial sum of the transverse momenta:

$$E_{x,y}^{\mathrm{miss}} = \sum_{p} E_{x,y}^{\mathrm{miss},p} + E_{x,y}^{\mathrm{miss,soft}}, \tag{4.4}$$

where the sum is over all reconstructed objects in a given event and all terms which are not associated with any reconstructed objects are grouped into the second soft term [94].

4.2 Monte Carlo simulations

Most ATLAS analyses rely on using simulated data of physics processes as purely data-driven methods are not sufficient. Monte Carlo simulations are extensively used to model proton-proton interactions and the response of the ATLAS detector to the resulting physics objects. Figure 4.7 illustrates different parts of the MC event generation procedure that are discussed in the following sections.

4.2.1 Parton distribution functions

Protons are composite particles made of three valence quarks: two u-quarks and a d-quark. Additionally, a *sea* of virtual quark-antiquark pairs and gluons surround the valence quarks. Parton distribution functions (PDFs) model momentum distributions of partons inside a proton as well as other hadronic particles at different energy scales. Each parton inside a proton carries a fractional longitudinal momentum of the proton, x, where, at high energies, partons can be considered to be collinear with the parent proton. Moreover, the balance between the valence and sea quarks depends on the transfer of momentum, μ^2; the valence quarks are most dominant at low μ^2 values, as can be seen in Figure 4.8. A production cross-section of some process X from a proton-proton collision is then

$$\sigma_{pp\to X} = \sum_{i,j\in\{q,\bar{q},g\}} \int dx_1 \int dx_2 f_i(x_1,\mu^2) f_j(x_2,\mu^2) \hat{\sigma}_{ij}, \tag{4.5}$$

where i and j indices label the species of colliding particle, the functions $f_i(x_k,\mu^2)$ are the PDFs, which are measured experimentally, and $\hat{\sigma}_{ij}$ is a cross-section for quarks and/or gluons to produce the final state X.

4.2.2 Event generation

MC event generation consists of several sequential steps that address the phenomena illustrated in Figure 4.7. The event generation procedure creates a collection of physics objects for a particular physics process, e.g. $t\bar{t}Z$. It does not consider the effects of an experimental apparatus which is done in a separate simulation stage. This section briefly describes each step of the event generation procedure.

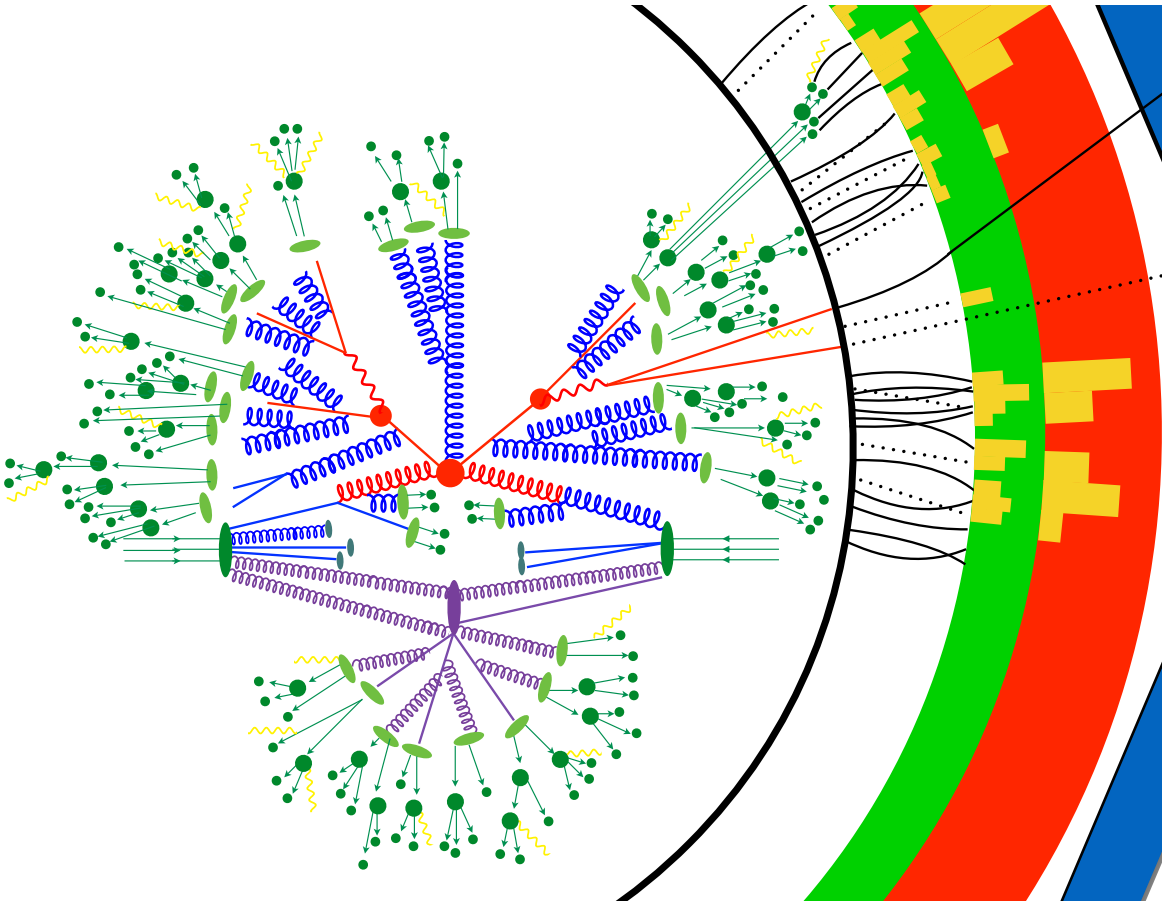

Figure 4.7: Schematic representation of the event generation procedure using Monte Carlo methods. The figure illustrates a simulation of the $gg \to t\bar{t} \to q\bar{q}b\mu\nu_\mu\bar{b}$ process. The incoming protons are shown as two dark green ovals with arrows pointing to the centre. The hard-scatter event is depicted in red where a $t\bar{t}$ pair is created. The parton shower is illustrated in blue which leads to the hadronisation processes in light green ovals. The dark green circles depict the final state stable particles where the yellow lines are photons. Multiple parton interactions are shown in purple and their decay products contribute to the underlying event. The right side of the figure depicts different layers of the ATLAS detector where the interactions between the final state particles and the detector sensors are simulated. The figure is taken from Ref. [95].

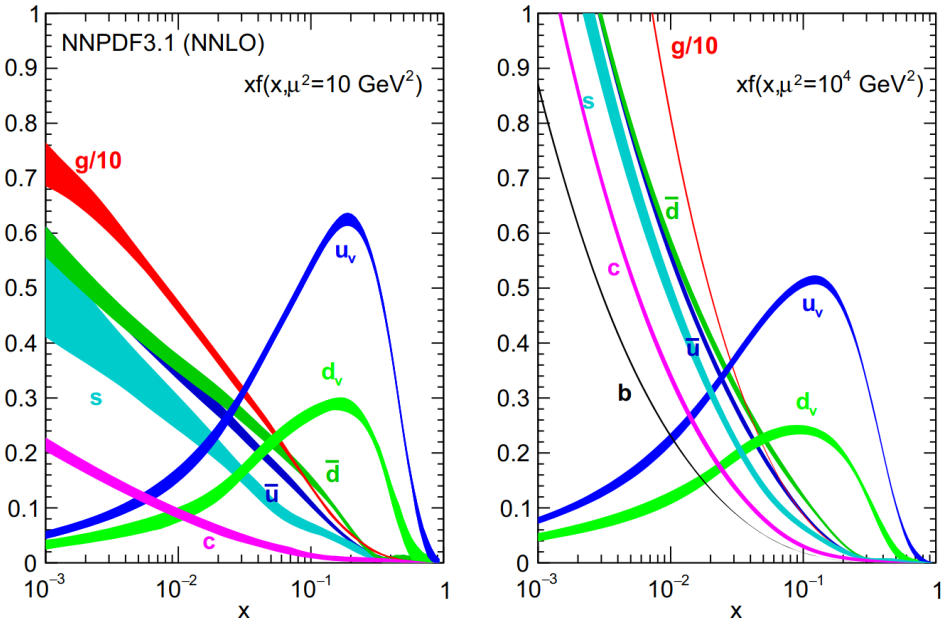

Figure 4.8: Parton distribution functions for the partons of a proton at a momentum transfer $\mu^2 = 10\,\text{GeV}^2$ (left) and $\mu^2 = 10^4\,\text{GeV}^2$ (right). Valence quarks are indicated with a subscript "v" [96].

Hard scattering

The hard-scatter part of the event generation is done by calculating matrix elements (ME) for a process of interest, e.g. $pp \to t\bar{t}Z$, using perturbation theory at a fixed order in the strong coupling constant α_s. The calculations are done to leading order (LO) or next-to-leading order (NLO) in α_s. LO represents a sum of Feynman diagrams for the process of interest with the fewest number of the strong interaction vertices. Higher order corrections, such as NLO, include extra loops/ legs in the diagrams, and, therefore, add additional powers of α_s. Since the collisions at the LHC occur between protons, parton distribution functions are used in the ME calculations to account for the probability of a parton being at the right energy for the hard scatter to occur.

Parton shower

A parton showering is the next step in the event generation procedure. Dedicated algorithms simulate the splittings of the initial hard-scatter particles into soft emissions [97]. For example, a parton produced in the hard scattering may split into two, separated by the angle θ and carrying momentum fractions z and $(1-z)$, respectively.

Parton showering starts at the hard scattering energy scale and continues until the emissions reach a cut-off energy scale of around 1 GeV.

Hadronisation

The cut-off energy scale of parton showers coincides with the colour confinement scale. Below this energy, partons are not allowed to be isolated and must form colourless bound states, called hadrons. The formation of hadrons, called hadronisation, is modelled in simulations and the model parameters are tuned to the experimental data. The Lund string model depicts hadronisation as splittings of quark-antiquark pairs which are connected by colour strings [98]. A string connecting a quark with an antiquark splits in half due to the asymptotic freedom property of QCD where the combined total energy of the two resulting hadrons is smaller than the initial energy. The evolution continues until the energy of the system is too low to proceed. The other approach to hadronisation is called the cluster model which is based on the concept of preconfinement [99] of partons from the parton shower. Gluons from the parton shower are first split into quark-antiquark pairs and then all quarks are grouped into colour-singlet clusters. The clusters are finally decayed into hadrons [100].

This stage of the event generation procedure is referred to as *particle-level* and gives a collection of leptons, photons and stable hadrons. Effects of the underlying event, defined in the following section, can also be included. These are detector-independent estimates of the true physical quantities, often used to make the differential cross-section measurements such as those presented in Chapter 9.

Underlying event

The event generation steps described above are not sufficient to fully approximate the experimental observations. In particular, lower energy interactions accompany the hard-scatter process. Such non-hard scattering interactions are collectively called the underlying event (UE). The UE can be composed of several effects, including the beam remnants and multiple parton interactions (MPI). The MPI occur when the transverse distance between the incoming protons is small enough and the overlap is large so that multiple partons can interact. The MC simulations account for the UE through dedicated models which are tuned using the experimental data.

Pileup

A simplified picture of proton-proton collisions at the LHC was used in the previous sections. Rather than trying to collide single protons, the LHC collides bunches of them to increase the chance of hard-scatter collisions. This results in 30–40 collisions per bunch crossing on average. Proton-proton collisions occurring in the same bunch crossing are called in-time pileup. Out-of-time pileup is defined to refer to additional proton-proton collisions occurring in bunch crossings just before or after the collision of interest and is due to the slower response of some parts of the electronics within the detector. The pileup effects are modelled by overlaying additional hard-scatter events onto the primary hard-scatter interaction and re-weighting them to match the average number of collisions per bunch crossing in data.

4.2.3 Software for event generation

General purpose MC event generators are software packages capable of performing each aspect of the event generation procedure. Examples of such generators are PYTHIA [101], HERWIG [102] and SHERPA [103]. PYTHIA is capable of generating LO matrix elements while HERWIG and SHERPA are NLO generators. Dedicated matrix element generators also exist and are used by the ATLAS collaboration. These generators specialise in the generation of matrix elements at leading and next-to-leading orders for multi-particle final states. MADGRAPH [104] and POWHEG [105] are common examples of these generators. Since they are not built to perform parton showering and hadronisation, the general purpose generators are interfaced with them. Ref. [97] gives an overview of the general purpose event generators used in the LHC experiments. The event generators which are used in the production of MC data samples relevant for the analyses of this thesis are listed in Chapter 6.

4.2.4 Detector simulation

The event generation procedure yields a collection of final state particles with the necessary kinematic information. To simulate the detector response and acceptance, the `Geant4` software package [106, 107] is used to build a detailed parameterisation of the ATLAS detector. The stable particles and jets from event generation are propagated outwards through the simulated detector in discrete time steps until they are absorbed

by a calorimeter, or they go out of the detector acceptance. The result of such simulation is a collection of simulated detector hits in the ID, MS and calorimeters.

The simulated detector hits are then digitised, transforming them into physical quantities such as voltage, time or position. At this point the MC simulation data can be passed to the same reconstruction of physics objects algorithms, as the real data is (Section 4.1), to form the detector-level (or reconstruction-level) collection of physics objects. The MC simulation procedure preserves information from different stages of the event generation which can be used as a reference to the detector-level data.

4.3 Parameter estimation

The maximum likelihood estimator (MLE) is applied to measure the inclusive and differential cross-sections in Chapters 8 and 9, respectively. Generally speaking, it determines values of the parameters which maximize a likelihood function $L(\theta)$ given a finite dataset. The likelihood function can be defined as follows:

$$L(\mathcal{D};\vec{\theta}) = \prod_{i=1}^{N} f(x_i;\vec{\theta}), \tag{4.6}$$

where the dataset $\mathcal{D} = (x_1, x_2, \ldots, x_N)$ consists of N independent identically distributed (i.i.d.) measurements of an observable x, e.g. the transverse momentum (p_{T}) of a particle. The i.i.d. condition implies that each x_i follows the same probability density function $f(x;\vec{\theta})$. A vector of the unknown model parameters $\vec{\theta} = (\theta_1, \theta_2, \ldots, \theta_M)$ is used here to indicate that the likelihood function is usually parameterised by a number of them. Such a likelihood function is considered to be a model and the MLE procedure determines values of the $\vec{\theta}$ parameters which maximise the likelihood of this model to match the dataset.

The product in the likelihood function of Equation 4.6 is generally transformed into a sum by applying a natural logarithm for computational convenience. Numerical techniques are then used to minimise the negative log-likelihood function to estimate its parameters. The `TRExFitter` analysis framework [108] is used for the cross-section measurements in this thesis which relies on the `Minuit` numerical minimisation algorithms [109]. The remaining sections of this chapter will outline the background for the statistical modelling and inference with the `TRExFitter` framework.

4.3.1 Profile likelihood fit

Datasets in the measurements of the high energy physics processes can grow very large making the statistical modelling with the likelihood approach computationally very expensive. It is also usually the case that we cannot reliably assume the mathematical form of the probability distribution function. Therefore, binned histograms are used, and the dataset becomes $\mathcal{D} = \vec{n} = (n_1, n_2, \ldots, n_N)$ where the number of bins is N and the number of entries in bin i, n_i, is expected to be distributed according to a Poisson distribution with the mean ν_i. Assuming that two types of events, signal and background, can exist, the expected number of events in bin i is defined as:

$$\nu_i = \mu \cdot S_i + B_i, \tag{4.7}$$

where μ is the signal strength parameter which measures the rate of the observed signal process $S_{\text{obs},i}$ with respect to the predicted value S_i such that $S_{\text{obs},i} = \mu \cdot S_i$. The expected background in each bin is B_i. Then, the likelihood function can be transformed into the extended likelihood function with binned data as follows:

$$L(\vec{n}; \mu, \vec{\theta}) = \prod_r^R \prod_i^N Pois(n_{i,r}; \mu S_{i,r}(\vec{\theta}) + B_{i,r}(\vec{\theta})), \tag{4.8}$$

where the $\prod_r^R$ factor allows for the splitting of the dataset into multiple orthogonal regions. This can be particularly useful in order to define a measurement strategy which uses the available statistics more efficiently (Chapter 8). The expected signal $S_{i,r}$ and background $B_{i,r}$ components are estimated from MC simulations and depend on a set of model parameters $\vec{\theta}$. The signal strength parameter μ is the parameter of interest (POI) and its estimate can be used to measure the inclusive cross-section, or the total rate of production, of the signal process. The remaining $\vec{\theta}$ parameters are separated from the POI since they are the nuisance parameters (NPs) of the model which account for the lack of our understanding about the precision of experimental procedures and theoretical predictions. Dedicated independent measurements are usually used to estimate these uncertainties and provide prior knowledge. Additional multiplicative factors can then be added to the likelihood function of the measurement at hand to constrain the associated nuisance parameters. The measurements in this thesis constrain the nuisance parameters with unit Gaussian distributions. In some cases, nuisance parameters are left as free parameters when the prior constraints are not known. For example, it is often possible to measure the rate of a dominant background

process as a nuisance parameter k directly in data. Here, an option to have multiple regions can be especially useful because a dedicated region where the background process is dominant may be possible to design. The likelihood function then becomes:

$$L(\vec{n};\mu,k,\vec{\theta}) = \prod_{r}^{R}\prod_{i}^{N} Pois(n_{i,r};\mu S_{i,r}(\vec{\theta}) + B_{i,r}(k,\vec{\theta}))\prod_{j}^{M} Gaus(\theta_j), \tag{4.9}$$

where the last product term represents the unit Gaussian constraints of each nuisance parameter. Nuisance parameters allow systematic uncertainties to be fully included in the likelihood function in a statistically consistent way. All possible systematic effects are accounted for by building the likelihood function out of template histograms representing nominal values and $\pm 1\sigma$ variations. It is possible to estimate the systematic uncertainties as constant normalisation factors, as variations in shape or both. The negative log-likelihood function is then minimised numerically to estimate the μ, k and $\vec{\theta}$ parameters to get best-fit values $\hat{\mu}$, $\hat{k}$ and $\hat{\hat{\theta}}$, respectively.

The measurements presented in this thesis are based on statistical models which are functions of various parameters, namely the POI and NPs. The NPs can be profiled with the conditional maximum likelihood estimate (CMLE) $\hat{\hat{\vec{\theta}}}(\mu)$ such that the profile likelihood becomes a function of POIs only. The CMLE fixes the value of the POI μ and estimates $\vec{\theta}$ parameters which maximise the likelihood function thereby allowing to select specific values of the NPs. The `TRExFitter` analysis package [108] allows such functionality and therefore the term "profile likelihood" is used.

4.3.2 Ranking of the nuisance parameters

The exact effects of the individual nuisance parameters on the POI are not known *a priori* and they are not obvious after the fit. A ranking of the nuisance parameters can be performed in terms of their impacts on the estimation of the POI. Given a nuisance parameter θ, its impact $\Delta\mu$ is measured as the difference between the POI value of $\hat{\mu}$ in the nominal fit and $\hat{\mu}_{\text{NP}}$ in the fit where the nuisance parameter is fixed:

- The pre-fit impact is evaluated by fixing a nuisance parameter to $\hat{\theta} \pm 1$. This is defined according to the prior unit Gaussian constraint of the nuisance parameter. The pre-fit impact is undefined for the nuisance parameters which are free parameters in the fit and do not have the associated prior constraints.

- The post-fit impact is evaluated by fixing a nuisance parameter to $\hat{\theta} \pm \Delta\hat{\theta}$, where $\Delta\hat{\theta} \leq 1$ is the uncertainty of $\hat{\theta}$ estimated in the nominal fit.

Large values of $\Delta\mu$ imply that the associated nuisance parameters contribute more significantly to the total uncertainty of the estimated POI. The pre-fit impact of a nuisance parameter may differ from its post-fit impact which implies that the fitting procedure is able to constrain this nuisance parameter further, i.e. $\Delta\hat{\theta} < 1$. The `TRExFitter` analysis package [108] implements such assessment of nuisance parameters in the form of a ranking plot for the POI.

4.3.3 Profile likelihood unfolding

Unfolding is a general term used to describe techniques which aim to remove experimental effects, such as resolution, efficiency and acceptance of a device, from data. This allows inferring the true underlying distributions of experimentally measured physics processes which can be compared with the theoretical predictions and other experiments. Figure 4.9 is an illustration of unfolding and how it relates to the experimental data and MC simulations.

Modelling of the detector effects

Measurements of the experimental data can be represented by the Fredholm integral equation [111]:

$$g(x) = \int R(x,y) f(y)\, dy, \tag{4.10}$$

where $g(x)$ is a detector-level distribution of an observable x, $f(y)$ is the corresponding truth-level distribution of an observable y, $R(x,y)$ is a kernel function, which encodes the smearing effects of the detector and is called the response matrix. An unfolding method aims to estimate the $f(y)$ distribution given $g(x)$ and $R(x,y)$. The $g(x)$ distribution is obtained from the experimental data while $R(x,y)$ is most often estimated from Monte Carlo simulations. To account for the discrete nature of the differential distributions, the above discussion can be represented in terms of histograms:

$$\vec{v} = R \cdot \vec{\tau}, \tag{4.11}$$

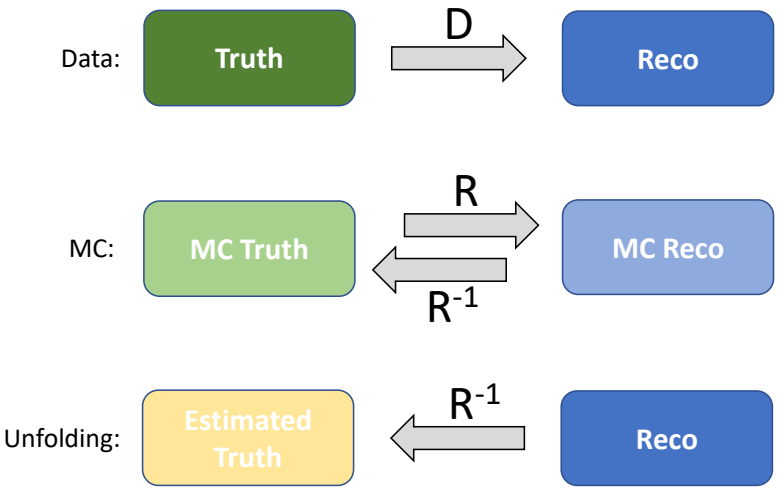

Figure 4.9: A depiction of the unfolding problem. Label D denotes the experimental apparatus which introduces smearing to the true spectrum, R represents an approximation of the experimental effects, as derived from the MC simulations, and R^{-1} is the inverse mapping of R which is obtained with an unfolding method. R^{-1} is used to infer the underlying true distribution of the experimental data. The figure is reproduced from Ref. [110].

where $\vec{\nu} = (\nu_1, \nu_2, \ldots, \nu_N)$ is a detector-level histogram, $\vec{\tau} = (\tau_1, \tau_2, \ldots, \tau_M)$ is the corresponding truth-level histogram. The truth-level distribution can then be estimated as follows:

$$\hat{\vec{\tau}} = R^{-1}\vec{\nu}, \tag{4.12}$$

where R^{-1} is an inverse of the response matrix, which is one of the main tasks of an unfolding algorithm[1]. The response matrix accounts for the resolution, efficiency and acceptance effects of an experimental apparatus. Therefore, it is defined as a product of the following parts:

- Migration matrix M_{ij} which models the finite resolution of the detector leading to smearing of the true distribution. For example, a lepton in an event with a true value of $p_{\mathrm{T}}^{\mathrm{true}}$ may be reconstructed as an event with a different value of p_{T}.
- Detector acceptance α^i is a bin-wise probability of a detector-level event in bin i to pass a truth-level selection of bin $j = i$. It accounts for events at detector-level

[1] Not all methods invert the response matrix directly.

which do not pass the fiducial definition for the cross-section under study:

$$\alpha^i = \frac{N^i_{\text{reco}} \cap N^i_{\text{truth}}}{N^i_{\text{reco}}}, \tag{4.13}$$

where $N^i_{\text{reco}} \cap N^i_{\text{truth}}$ is the number of detector-level events in bin i which also pass the truth-level selection in bin $j = i$ and N^i_{reco} is the number of detector-level events in bin i.

- Selection efficiency ϵ_j is a bin-wise probability of a truth-level event in bin j to pass the detector-level selection of bin $i = j$. For example, a truth-level event may not pass the detector-level selection:

$$\epsilon_j = \frac{N^j_{\text{reco}} \cap N^j_{\text{truth}}}{N^j_{\text{truth}}}, \tag{4.14}$$

where $N^j_{\text{reco}} \cap N^j_{\text{truth}}$ is the number of truth-level events in bin j which also pass the detector-level selection in bin $i = j$ and N^j_{truth} is the number of truth-level events in bin j.

The maximum likelihood estimator may be applied to infer the true distribution. Such an unfolding method is called profile likelihood unfolding (PLU) and is based on Equation 4.9 from the previous section:

$$L(\vec{n}; \vec{\mu}, \vec{\theta}, \vec{k}) = \prod_i^N Pois(n_i; S_i(\vec{\mu}, \vec{\theta}) + B_i(\vec{k}, \vec{\theta})). \tag{4.15}$$

The main difference in the likelihood function of PLU is that multiple parameters of interest are estimated. The POIs ($\vec{\mu}$) are signal strength parameters μ_j for each truth-level bin j of $\vec{\tau}$. The expected number of signal events in a detector-level bin i for each POI is represented by S_i such that:

$$S_i = \sum_j R_{ij} \tau_j \mu_j, \tag{4.16}$$

where the response matrix is defined using the components described above:

$$R_{ij} = \epsilon_j M_{ij} \alpha^i. \tag{4.17}$$

The remaining parts of the likelihood function for PLU are equivalent to those in the likelihood function of Equation 4.9. The post-fit vector of POIs is used to calculate the cross-sections in each truth-level bin j and derive the unfolded differential distribution. So far, the discussion focused on a single region with the corresponding response matrix. It is straightforward to include additional regions:

$$L(\vec{n};\vec{\mu},\vec{\theta},\vec{k}) = \prod_{r}^{R}\prod_{i}^{N} Pois(n_{i,r}; S_{i,r}(\vec{\mu},\vec{\theta}) + B_{i,r}(\vec{k},\vec{\theta})), \tag{4.18}$$

where each such region requires the corresponding response matrix which maps its detector-level distribution to the same truth-level distribution, and the POIs are fully correlated between the regions. Finally, the systematic uncertainties on the nuisance parameters can be directly included in the likelihood function with an additional penalty term, similarly to the standard profile likelihood fit:

$$L(\vec{n};\vec{\mu},\vec{\theta},\vec{k}) = \prod_{r}^{R}\prod_{i}^{N} Pois(n_{i,r}; S_{i,r}(\vec{\mu},\vec{\theta}) + B_{i,r}(\vec{k},\vec{\theta})) \prod_{p}^{P} Gaus(\theta_p), \tag{4.19}$$

where the systematic variations are given in the form of the unit Gaussian distributions. The procedure to account for the systematic variations is exactly the same for the uncertainties which affect the backgrounds. For the uncertainties affecting the signal process, an individual response matrix $R_r(\theta_p)$ is derived for each systematic variation θ_p in each region r and variations of the nominal signal distribution $S_{i,r}(\theta_p)$ are calculated:

$$S_{i,r} \rightarrow S_{i,r}(\theta_p) = \sum_{j} R_{ij,r}(\theta_p)\tau_j\mu_j. \tag{4.20}$$

The normalised differential cross-section measurement is performed by adding a normalisation factor for the total cross-section $\mu_{\text{tot.}}$. To maintain the same number of free POIs as the number of data points, the $\mu_{\text{tot.}}$ parameter replaces the POI associated with the last truth-level bin by default[2]. The remaining signal strength parameters are redefined as $\mu_j = \mu_{\text{norm.},j}\mu_{\text{tot.}}$ while the normalisation of the excluded bin k is:

$$\mu_{\text{norm.},k} = \frac{n_i}{n}\frac{1 - \sum_{i,i\neq k}^{n}\mu_{\text{norm.},i}}{n_k/n}, \tag{4.21}$$

[2]Any bin in the truth-level distribution can be replaced.

where n_i is the initial number of events in bin i and $n = \sum_i n_i$ is the total number of events. Finally, the cross-section of the excluded bin is the difference between the total cross-section and the sum of the cross-sections in the other bins. The `TRExFitter` analysis package [108] implements the PLU based on its profile likelihood functionality for measurements of total cross-sections. It is applied in Chapter 9 to perform the measurements of the differential $t\bar{t}Z$ cross-section.

4.3.4 Testing goodness-of-fit with χ^2

It is sometimes useful to evaluate the agreement between two distributions with a goodness-of-fit test. The χ^2 statistic will be used to assess the validation tests of the unfolding procedure in Chapter 9. In its simplest form, χ^2 is defined as:

$$\chi^2 = \sum_i \frac{(n_i - \mu_i)^2}{\sigma_i^2}, \tag{4.22}$$

where n_i is a measured value, μ_i is the corresponding true value and σ is the uncertainty associated with the measurement. Smaller values of χ^2 suggest a better agreement between the measured and true values. More generally, measurements can be correlated, and the χ^2 statistic is then calculated using the covariance matrix $C_{ij} = \overline{x}_i\overline{x}_j - \overline{x_i x_j}$ as follows:

$$\begin{aligned} \chi^2 &= \sum_{ij}(n_i - \mu_i)C_{ij}^{-1}(n_j - \mu_j) \\ &= \vec{n}^{\mathrm{T}} C^{-1}\vec{n}, \end{aligned} \tag{4.23}$$

where C^{-1} is the inverse of the covariance matrix and C_{ij}^{-1} is the $(i,j)^{th}$ element of it. The second line shows χ^2 as a vector equation, where $\vec{n}^{\mathrm{T}}$ is the transpose of $\vec{n}$.

Chapter 5

Monitoring of the high level muon trigger

The key role of the ATLAS Trigger and Data Acquisition system (introduced in Section 3.4) is to identify interesting physics events while removing the rest so that the data are collected at a manageable rate. Monitoring of the trigger system is therefore essential to ensure that the TDAQ operations are efficient and accurate. This chapter focuses on the monitoring of the HLT muon algorithms. The work discussed here is a part of a bigger effort to transition the ATLAS software framework to Run-3.

5.1 Towards multithreaded Athena

The ATLAS software framework, Athena [112], is based on the Gaudi framework [113] and covers all major data processing tasks from the high level trigger to analyses. One of the main technical challenges of Athena is the amount of computational power needed to process the experimental and simulation data. The new generations of central processing unit (CPU) designs are continuously increasing the density of cores but have low amounts of accessible run-time memory per core. This has the potential to exacerbate the problems of the ATLAS experiment since more data than ever will need to be processed in Run-3 and Run-4. Therefore, the ATLAS software has to take advantage of advanced CPU features to achieve the required performance.

The efficiency of the run-time memory usage was increased with the multiprocessing design of Athena, AthenaMP, for the Run-2 data taking period. In this approach, a CPU is able to process a task more efficiently by splitting it into several sub-tasks

while using the originally allocated amount of memory. However, multiprocessing is not a sufficient solution for Run-3/4, and transitioning to a fully multithreaded implementation of Athena, AthenaMT, was deemed most reasonable [114]. Multithreading allows to further increase the computational power with a more efficient use of the run-time memory by using multiple threads of a single CPU to process an event. At the time of writing this thesis, the transition to AthenaMT is finished and Run-3 has started. The implementation of AthenaMT required significant changes in the code which had to be ensured to be thread-safe.

5.2 Online monitoring in offline algorithms

The HLT relies on two types of data reconstruction algorithms: *online* and *offline*. The online reconstruction is HLT-specific, fast and lower precision, designed to be used during the data taking periods when the ATLAS experiment is on-line. The offline algorithms (Section 4.1) are primarily designed to be used outside the TDAQ system and are less constrained by the computational time which allows for more precise reconstructions. One of the specifications for the design of AthenaMT is an improved integration of the offline reconstruction algorithms in TDAQ. In particular, the offline reconstruction algorithms should be run directly in the HLT, keeping the trigger performance close to the offline reconstruction.

Typically, monitoring is done by producing histograms of the HLT outputs and comparing them with respect to a previously validated set of analogous histograms. Discrepancies from the reference may indicate problems in the TDAQ system. This section focuses on the discussion about the monitoring of the offline reconstruction algorithms for the muon HLT operations of Run-3.

5.2.1 Monitoring of the online and offline algorithms

Monitoring of the online trigger operations is required to be done in parallel with the trigger in order to identify issues as soon as possible. Additionally, the majority of events are rejected by the HLT and monitoring them at later stages is impossible. Therefore, such monitoring is embedded in the online reconstruction algorithms. On the other hand, monitoring of the offline reconstruction can be done sequentially to the reconstruction and is therefore disjoint from the reconstruction procedure. The offline-

reconstructed data is stored for further processing and can be validated with an offline monitoring algorithm. Since the offline reconstruction algorithms can be run directly in the HLT of AthenaMT, they need to have monitoring functionality. Furthermore, these monitoring tools should be implemented such that they are enabled during HLT operations and stay inactive during the offline reconstruction runs.

5.2.2 Monitored observables

The performance of muon HLT operations is assessed by monitoring a selection of reconstructed muons as a set of histograms. The types of reconstructed muons and the associated observables are based on the previously used Run-2 monitoring. The MS segments and MS tracks, which are reconstructed using the information from the MS alone, are monitored in addition to the extrapolated muons, combined muon tracks and ID tracks, which are defined in Section 4.1.3. Each type of muon is monitored with respect to four observables, p_{T}, η, ϕ, and N (the number of muons). The MS segments are generally not bent enough by the magnetic field to determine their p_{T} and, therefore, are not monitored with respect to this observable. Additionally, monitoring of the pseudorapidity against transverse momentum (η vs. p_{T}) of the ID tracks and the azimuthal angle against pseudorapidity (ϕ vs. η) of the MS tracks are implemented. Observables relating to the reconstruction performance, such as χ^2 between the MS and ID tracks, are not included because these are not measurements of the HLT performance directly. In addition, such more complex measurements would increase the computational time which is a scarce resource in the trigger operations. The selection of observables above gives a sufficient overview of the operational stability of the HLT which is in-line with the monitoring implementation during Run-2 and keeps the compute resources under control.

5.2.3 Results

The implementation and performance of the muon HLT monitoring in the offline reconstruction algorithms were tested throughout the development process with dedicated trigger validation tests. The monitoring histograms that are presented in this section were produced in the trigger validation framework using MC simulated $t\bar{t}$ events.

Figure 5.1 shows the monitoring histograms for the MS segments. These histograms show all segments found in each event, including those which were not used in extrapolations to MS tracks. The pseudorapidity of an MS segment is calculated using the angle of the segment from the beamline, rather than the interaction point. Additionally, MS segments are reconstructed as straight lines due to the lack of their bending in the MS. This therefore may lead to values of pseudorapidity that exceed the expected detector acceptance for reconstructed muons. This is noticeable in Figure 5.1b where some MS segments exceed the MS $|\eta| < 2.7$ acceptance. Therefore, the tails of the distribution at large values of η are understood and not considered to be problematic.

The transverse momentum, pseudorapidity and azimuthal angle histograms for the MS tracks are shown in Figure 5.2. The MS tracks are defined using the MS segments (Section 4.1.3) and, therefore, the histograms contain a subset of all MS segments. This can be seen when comparing Figure 5.2 with Figure 5.1 where the number of events is larger. Histograms of the ID tracks are shown in Figure 5.3, the ME tracks in Figure 5.4 and the CB tracks in Figure 5.5. The pseudorapidity distributions for all these monitored muons are seen to have a sharp reduction in tracks around zero. This is consistent with the MS system which has a "dead" region used for cabling around $|\eta| = 0$. Therefore, these and other histograms are seen to show expected and consistent performance indicating no issues. Following these tests, the online muon monitoring in offline algorithms was included in the muon HLT validation framework.

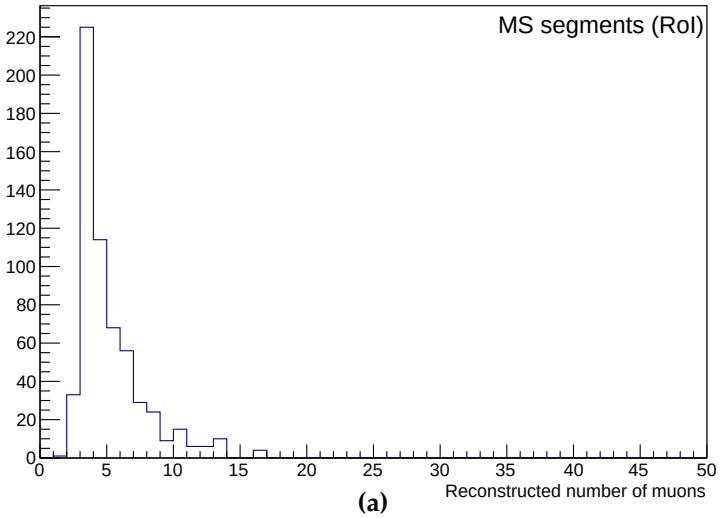

(a)

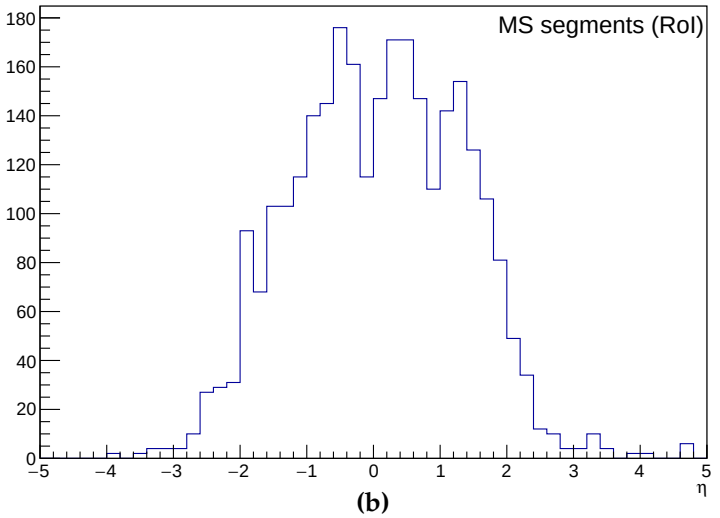

(b)

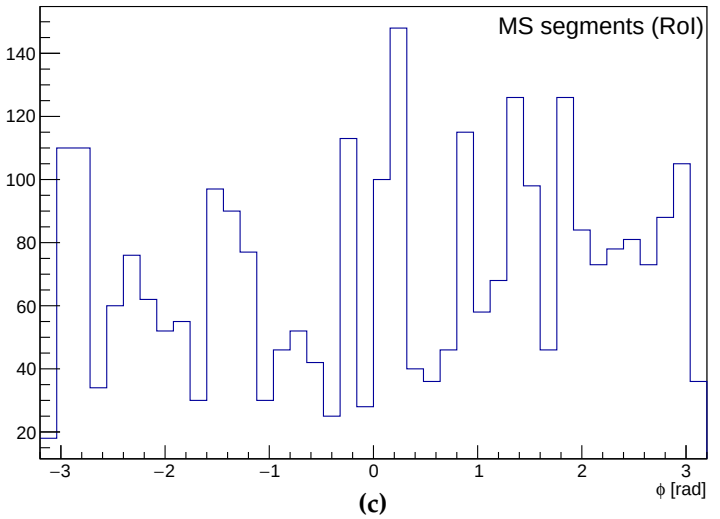

(c)

Figure 5.1: Monitoring histograms of the MS segments.

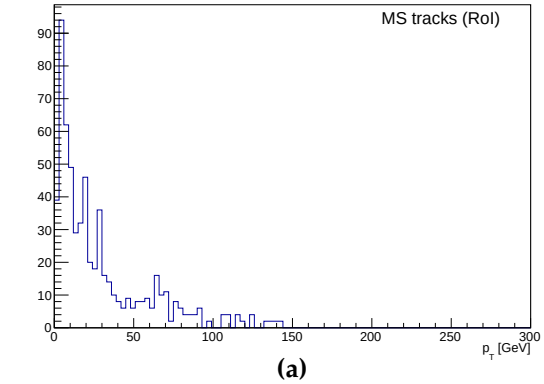

(a)

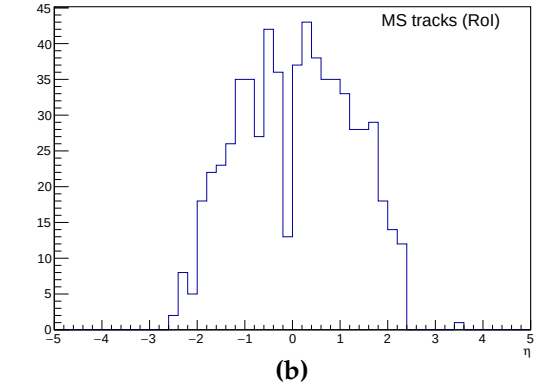

(b)

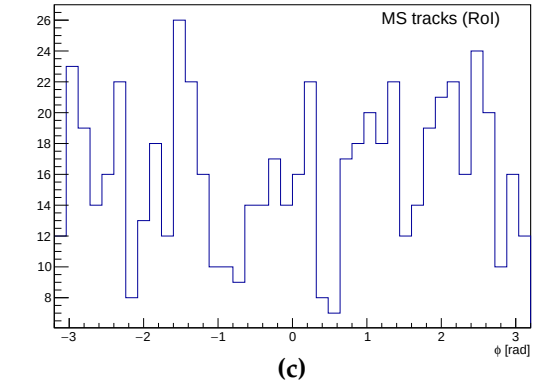

(c)

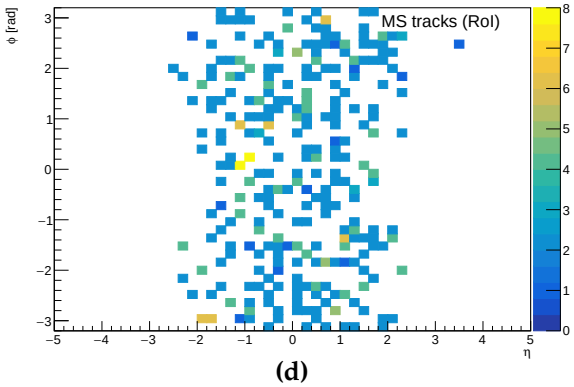

(d)

Figure 5.2: Monitoring histograms of the MS tracks.

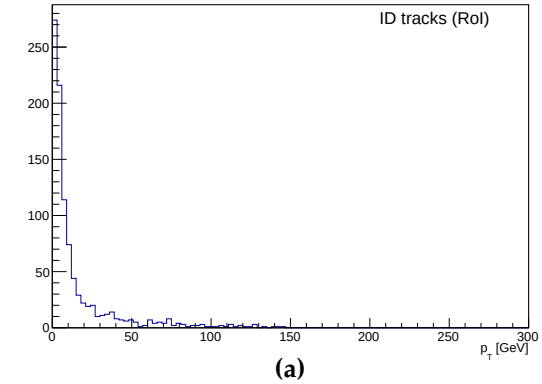

(a)

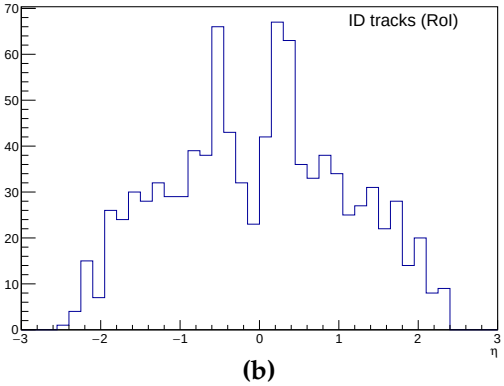

(b)

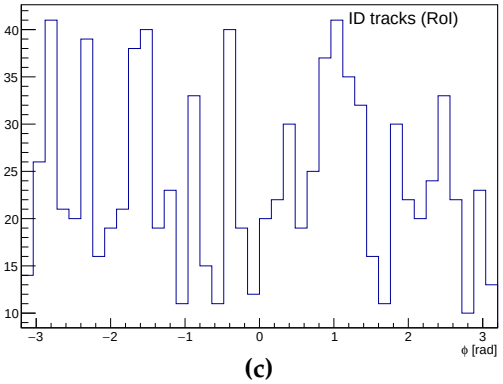

(c)

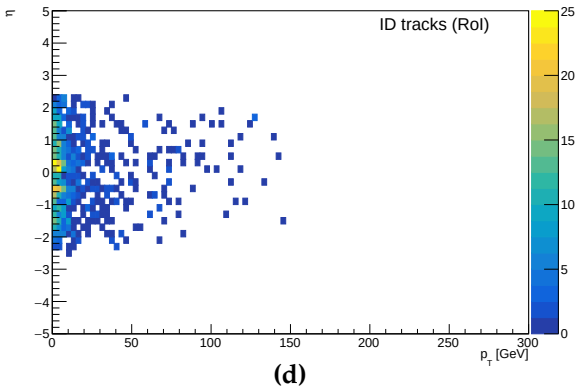

(d)

Figure 5.3: Monitoring histograms of the ID tracks.

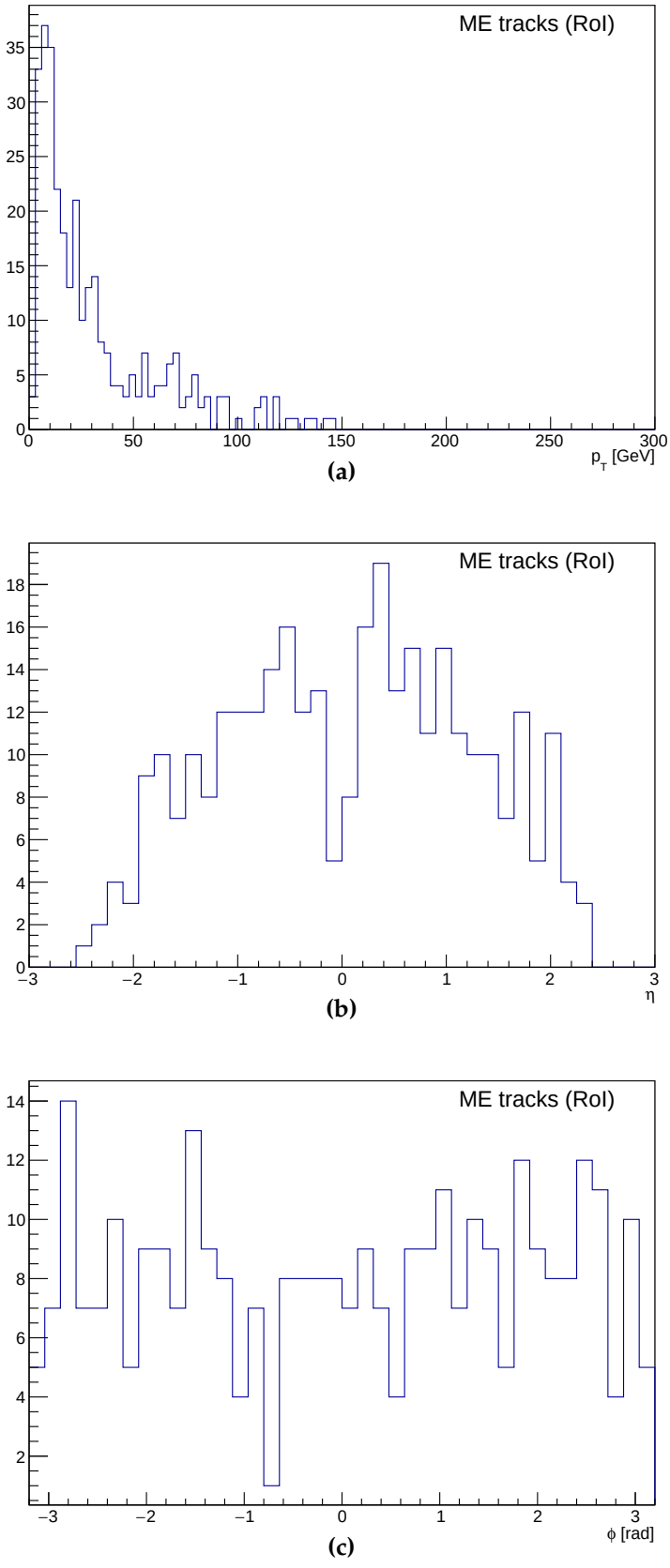

Figure 5.4: Monitoring histograms of the ME tracks.

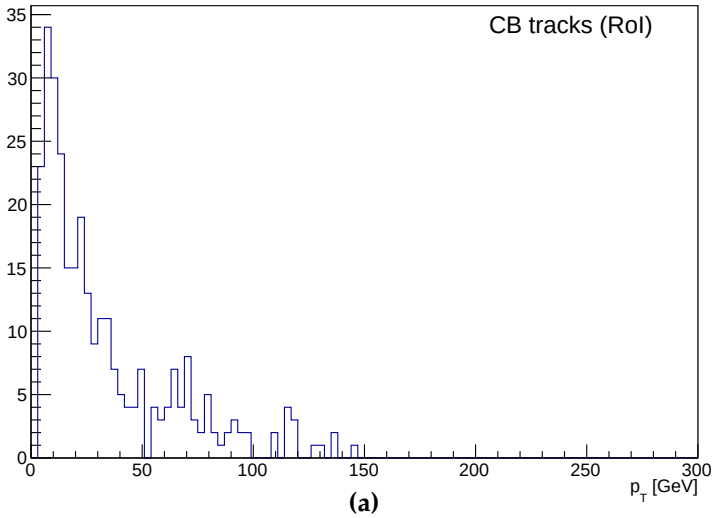

(a)

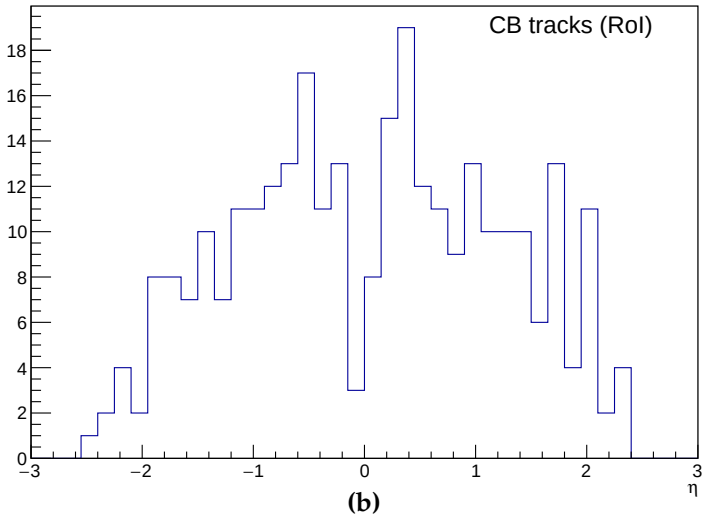

(b)

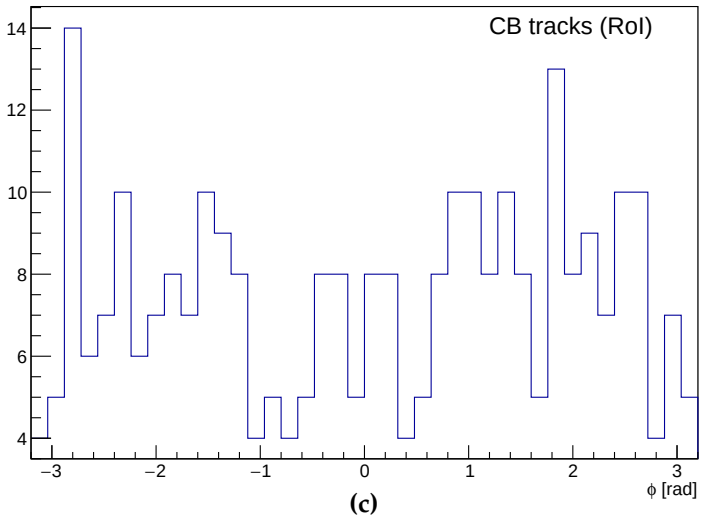

(c)

Figure 5.5: Monitoring histograms of the CB tracks.

5.3 Truth-based muon efficiency monitoring

The parallelisation of multithreaded TDAQ/Athena is significantly more challenging to develop than the multiprocess parallelisation. Multiple tasks can be executed concurrently on separate CPU threads while sharing the same pool of heap memory. This makes it challenging to schedule tasks, as only one thread is allowed to write to a memory address at a time, and other threads should not access that memory address while it is currently being written. Therefore, careful validation of the HLT within the AthenaMT development is needed. A commonly used validation procedure is the monitoring of the trigger efficiencies. Such efficiencies measure how well the trigger algorithms perform with respect to a reference. This section will focus on an implementation of an efficiency calculation and a monitoring algorithm designed with the transition to the parallelisation of multithreaded TDAQ/Athena in mind.

5.3.1 Offline reconstruction-based efficiencies

As offline reconstruction algorithms are more complex due to fewer restrictions on computing resources, compared to the online trigger algorithms, they are considered to be a good reference. They are commonly used to measure the efficiencies of the trigger operations. The aim of monitoring such reconstruction-based efficiencies is to ensure that the trigger software finds muons that are also reconstructed in the offline algorithms and used in physics analyses. A reconstruction-based efficiency is defined as follows:

$$\epsilon_{\text{reco}} = \frac{\text{offline muons} \in \text{trigger muons}}{\text{offline muons}}, \tag{5.1}$$

where the numerator is the number of reconstruction-level muons matched to the triggered muons.

As mentioned previously, the ATLAS HLT system incorporates offline reconstruction algorithms in the precision stages of the trigger chains. Monitoring reconstruction-based efficiencies using the same reconstruction algorithm in the trigger and offline reconstructions can potentially overestimate the trigger performance. For example, a faulty reconstruction algorithm can miss a muon in both the trigger and the offline reconstruction, yielding the trigger efficiency of 100%. Similarly, possible detector issues would not be identified leading to poor quality of the collected data. As the

adoption of the offline software becomes more integrated with the transition to the multithreaded Athena framework, issues with the monitoring of the reconstruction-based efficiencies could be amplified. The remainder of this section will introduce and discuss an alternative measure of efficiency that could help to mitigate the potential pitfalls of reconstruction-based efficiencies.

5.3.2 Truth-based efficiencies

Truth-based efficiencies measure the accuracy of a trigger algorithm with respect to MC simulations. Muons in the MC truth record, called truth muons, are matched to the muons selected by the trigger. A truth-based efficiency of a trigger chain is defined as follows:

$$\epsilon_{\text{truth}} = \frac{\text{truth muons} \in \text{trigger muons}}{\text{truth muons}}, \tag{5.2}$$

where the numerator is the number of truth muons that can be matched to muons selected by the trigger. These are referred to as truth-matched muons. The MC truth record is considered to be absolute, making the truth-based efficiency an absolute measure. Truth-based efficiencies are useful in the validation stages of the HLT where MC simulation data are available. They are complementary to those made using techniques such as the tag-and-probe method [115] where discrepancies between data and simulation can be probed. The truth-based efficiencies can be used to explore differences between different simulation setups, but they cannot be measured during the data acquisition periods since they are not defined for experimental (real) data.

The addition of the truth-based muon efficiency monitoring was motivated by the fact that the HLT framework was undergoing significant changes in preparation for Run-3. A thorough validation of these changes was needed to ensure that the new framework was ready for deployment. The remaining sections of this chapter will discuss an implementation of the truth-based muon efficiency monitoring. Efficiency is usually reported as a function of an object p_{T}. In addition to the p_{T}, these efficiencies were implemented as functions of η and ϕ observables.

5.3.3 Truth matching procedure

The distance between a truth muon and a trigger muon in the $(\eta - \phi)$ space, $\Delta R = \sqrt{(\Delta\eta)^2 + (\Delta\phi)^2}$, is used as the criterion to define a truth-matched muon. Since multiple muons may be reconstructed by the trigger in a single event, the pair with the smallest ΔR separation is selected as matched. The expectation is that the separation between the matching truth and trigger muons is small. Therefore, only the truth-trigger muon pairs which pass the $\Delta R < 0.1$ selection cut are considered in the matching procedure. Figure 5.6 confirms the choice of the selection cut where a distribution of ΔR for the pairs of truth and trigger muons is shown. The histogram shows the distribution of all truth-trigger muon pairs without the ΔR selection cut. The majority of truth-trigger muon pairs which pass the selection cut are concentrated in the first bin indicating that the majority of pairs have minuscule angular separations, as expected. Furthermore, there is a large difference between the pairs failing the cut ($\Delta R > 0.5$) and those that pass it ($\Delta R < 0.1$). This implies that the ΔR selection cut is not correlated with the truth-based efficiency and is a reasonable choice.

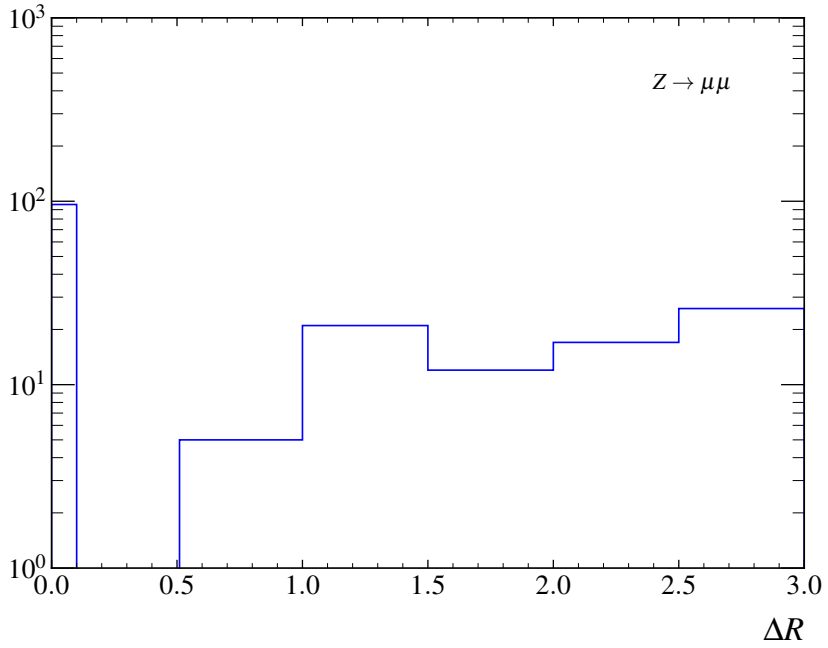

Figure 5.6: The distributions of angular separations between the truth muons and matching `HLT_mu26_ivarmedium` (Run-2) trigger muons using $Z \to \mu\mu$ events.

5.3.4 Results

The truth-based efficiency monitoring is implemented to be compatible with the Run-2 and Run-3 trigger chains. The performance of the monitoring tool is demonstrated using $Z \to \mu\mu$ events and three muon HLT chains which are defined for the Run-3 validation of the TDAQ system:

1. `HLT_mu26_ivarmedium_L1MU20`,
2. `HLT_mu50_L1MU20`,
3. `HLT_mu60_0eta105_msonly_L1MU20`.

Each trigger chain selects events with at least one muon. The chains are listed in the increasing order of the p_{T} threshold on the muons, namely 26 GeV, 50 GeV and 60 GeV. The first chain looks for muons that also satisfy the `Medium` isolation requirements while the third chain only selects events with muons in the $|\eta| < 1.05$ region. Each trigger chain requires that the events pass the L1 trigger.

Figure 5.7 shows the efficiency of the `HLT_mu26_ivarmedium_L1MU20` trigger chain as a function of the selected muon observables. The p_{T} distribution in Figure 5.7a has a reasonable shape and expected characteristics. Firstly, the first non-empty bin in the distribution corresponds to the 26 GeV cut on muon p_{T} imposed by the chain. The truth-based algorithm is implemented in such a way that efficiencies would show up in lower-p_{T} bins if present as well. This acts as an extra validation of the muon HLT chains because muons in the truth record may have transverse momenta below the trigger-chain threshold. The distribution of efficiencies with respect to pseudo-rapidity in Figure 5.7b demonstrate a reasonable performance. The distribution has the characteristic reduction in performance near $|\eta| = 0$ and $|\eta| = 1$ where the MS is not fully instrumented. In contrast to the p_{T} distribution, the truth-based efficiencies with respect to η and ϕ observables are only monitored using the truth muons which pass the p_{T} threshold of the trigger chain of interest. This is done to avoid artificially reducing the efficiencies. Figure 5.7c shows the distribution of efficiencies with respect to ϕ. The observed irregularities of the distribution around $\phi = -2$ rad are associated with the support structures of the ATLAS detector and at $\phi = -1$ rad is a statistical fluctuation. The performance of the `HLT_mu50_L1MU20` trigger chain in terms of the truth-based efficiencies is summarised in Figure 5.8 and that of the `HLT_mu60_0eta105_msonly_L1MU20` trigger chain is shown in Figure 5.9.

The truth-based muon monitoring was used by the ATLAS collaboration to validate the development and transition of the HLT framework into the multithreaded architecture. For each new release, the HLT validation framework was used to produce truth-based efficiencies and compare them with the previous validation run. At the time of writing this thesis, AthenaMT is fully operational. The truth-based efficiencies provided a valuable input in achieving this milestone and will continue to add value to the future development of the muon HLT framework.

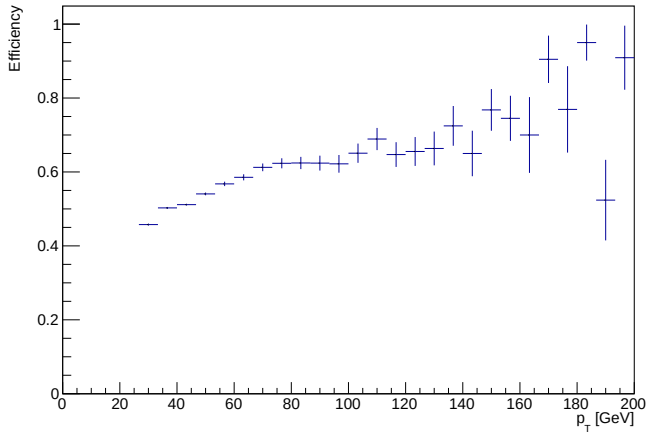

(a)

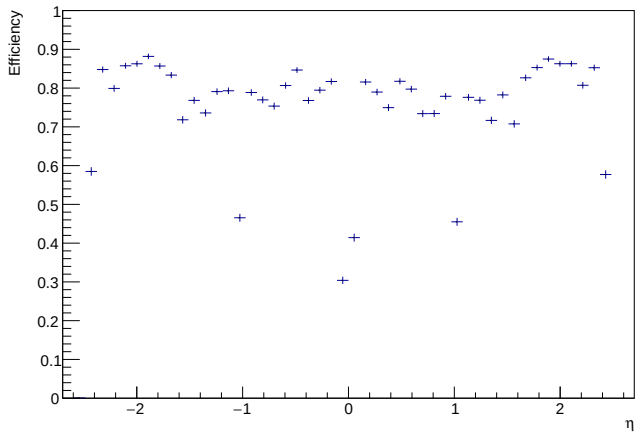

(b)

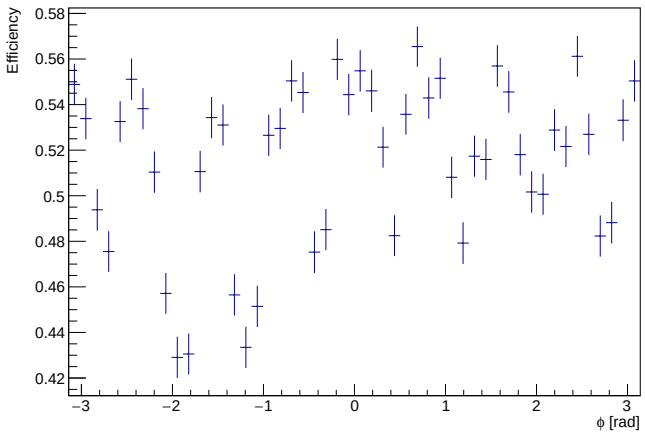

(c)

Figure 5.7: Truth-based efficiencies of the `HLT_mu26_ivarmedium_L1MU20` (Run-3) trigger chain.

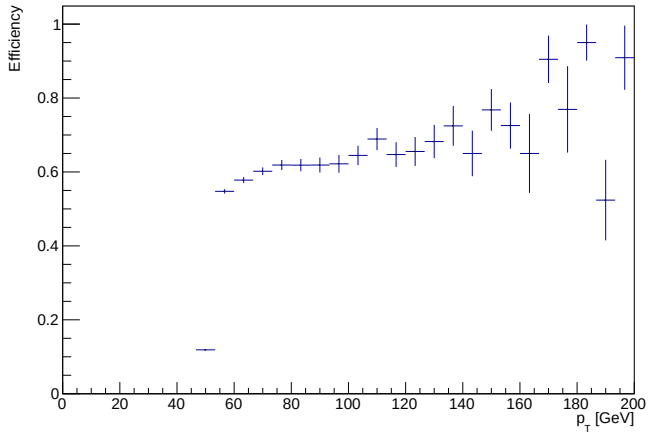

(a)

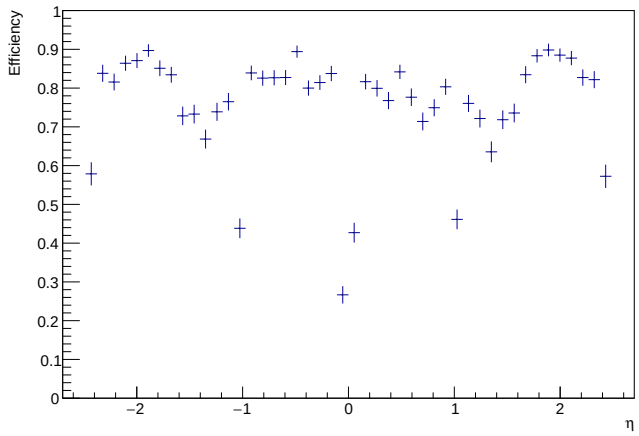

(b)

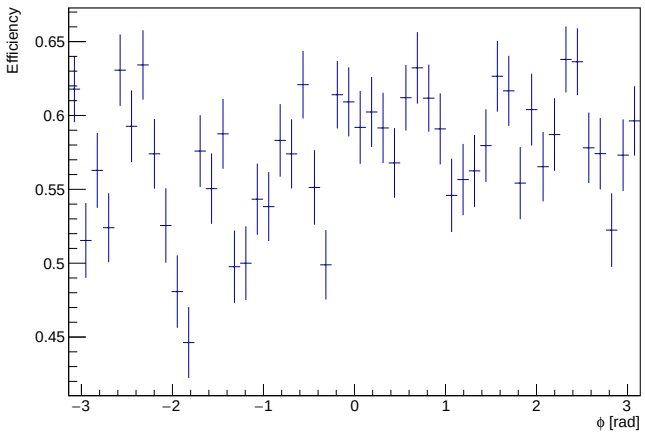

(c)

Figure 5.8: Truth-based efficiencies of the `HLT_mu50_L1MU20` (Run-3) trigger chain.

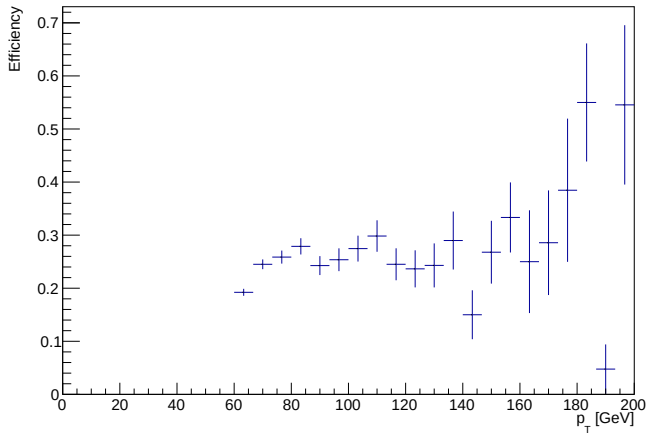

(a)

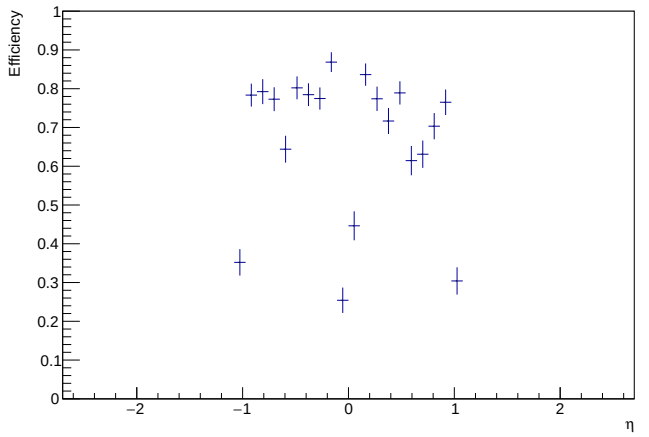

(b)

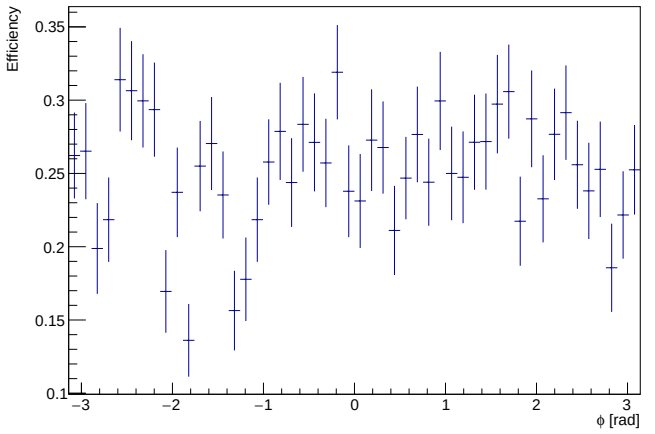

(c)

Figure 5.9: Truth-based efficiencies of the `HLT_mu60_0eta105_msonly_L1MU20` (Run-3) trigger chain.

Chapter 6

Prediction of the Standard Model processes

6.1 Signal processes

The nominal sample The production of a top-quark pair in association with a leptonically decaying Z boson is modelled using the MADGRAPH5_AMC@NLO generator [104]. The generator uses the `NNPDF3.0NLO` PDF set [116] and provides matrix elements at NLO precision. PYTHIA parton showering and hadronization [101] is interfaced with the MADGRAPH generator.

Alternative samples A few alternative approaches to generating the $t\bar{t}Z$ signal process are used in order to evaluate the theoretical uncertainties of the signal prediction:

1. **SHERPA 2.2.1**: The SHERPA 2.2.1 generator [103] at NLO precision and its default parton shower is used along with the `NNPDF3.0NLO` PDF set.
2. **SHERPA 2.2.11**: A newer version of the SHERPA 2.2.1 generator, SHERPA 2.2.11 [103], is used.
3. **MADGRAPH + HERWIG**: The MADGRAPH5_AMC@NLO generator interfaced with the HERWIG parton showering and hadronisation [117].
4. **MADGRAPH + PYTHIA A14**: A variation of the `A14` tune [118] parameters in the nominal event generation setup.

6.2 Backgrounds

A number of the Standard Model processes have similar final states to the $t\bar{t}Z$ signal process. Such processes are thus considered to be backgrounds which obscure measurements of the relevant signal process. Background processes are grouped into two categories in the three-lepton $t\bar{t}Z$ channel: the prompt lepton background and the non-prompt/ fake lepton background.

6.2.1 Prompt lepton background

The prompt lepton background collects processes which contain at least three real leptons in the final state. Leptons are called real if they originate from the W or Z boson decays. The backgrounds are estimated from the Monte Carlo simulations or using data-driven approaches.

Diboson The diboson background consists of the WZ+jets and ZZ+jets processes. The WZ+jets process with both vector bosons decaying leptonically, $WZ \to \ell\ell\ell\nu$, is dominant in the three-lepton channel. Diboson processes are simulated using the SHERPA 2.2.2 generator with the `NNPDF3.0NNLO` PDF set. Events with zero or one additional parton are simulated at NLO while events with two or three partons are simulated at the LO precision.

Single top-quark with vector bosons The tWZ and tZq processes are major irreducible $t\bar{t}Z$ backgrounds due to the closely matched three-lepton final states. The main differentiating characteristic between these backgrounds and the $t\bar{t}Z$ final state is the number of b-jets. Both processes are simulated at NLO with the MADGRAPH5_AMC@NLO generator using the `NNPDF3.0NNLO` PDF set interfaced to PYTHIA for the parton shower and hadronisation.

Top-quark pair with a W or H boson Small contributions to the overall background come from top-quark pair production in association with a W or Higgs boson, $t\bar{t}W$ and $t\bar{t}H$, respectively. Both background processes are simulated at NLO with the MADGRAPH5_AMC@NLO generator using the `NNPDF3.0NNLO` PDF set and the `A14` tune of PYTHIA parton shower for the inclusive cross-section measurement. The $t\bar{t}W$

process is instead simulated using the SHERPA generator and its default parton shower for the differential cross-section measurements.

Other Several other processes have very small contributions to the prompt lepton background. Production of a top-quark pair in association with another top quark, four-tops or three vector bosons are included among these backgrounds. Such small backgrounds are grouped together into a sample called "other", with an exception in the differential cross-section measurements where the $t\bar{t}t\bar{t}$ sample is left separate. As with other backgrounds, these processes are generated with the MADGRAPH, SHERPA or PYTHIA generators at LO or NLO.

6.2.2 Fake lepton background

The non-prompt/ fake lepton background occurs when physics objects are incorrectly identified as leptons leading to a fake trilepton final state. The dominant sources of the fake lepton background are the production of the top-quark pairs and W or Z boson in association with heavy-flavour hadrons, $t\bar{t}$, W+jets and Z+jets, respectively. Other sources include photon conversions, meson decays or light-jet signatures mimicking leptons. The inclusive cross-section measurement employs a fully data-driven method to estimate fake lepton contributions to the overall background, called the matrix method, while the differential cross-section measurements use a semi-data-driven method, called the fake factor method.

Matrix method

A data-driven method, the matrix method [119, 120], can be used to estimate the size of the fake lepton background. The method relies on two types of data selections: the standard selection, referred to as *tight*, and the standard selection with looser lepton definitions, referred to as *loose*. The tight selection results in the N_{T} number of events while the loose selection gives N_{L} number of events. It is assumed that the number of events can be split into the "real" and "fake" parts so that the corresponding efficiencies can be measured in control regions:

$$\epsilon_{\mathrm{real}} = \frac{N_{\mathrm{T}}^{\mathrm{real}}}{N_{\mathrm{L}}^{\mathrm{real}}} \qquad \epsilon_{\mathrm{fake}} = \frac{N_{\mathrm{T}}^{\mathrm{fake}}}{N_{\mathrm{L}}^{\mathrm{fake}}}, \tag{6.1}$$

where $N_{\mathrm{T}}^{\mathrm{real}}$ and $N_{\mathrm{T}}^{\mathrm{fake}}$ are the numbers of real- and fake-lepton events, respectively, in the tight selection and, similarly, $N_{\mathrm{L}}^{\mathrm{real}}$ and $N_{\mathrm{L}}^{\mathrm{fake}}$ are the numbers of real- and fake-lepton events in the loose selection. The objective of the matrix method is to estimate $N_{\mathrm{T}}^{\mathrm{fake}}$ which is achieved by solving a system of linear equations, given measured N_{L}, N_{T} and the above efficiencies:

$$N_{\mathrm{L}} = N_{\mathrm{L}}^{\mathrm{real}} + N_{\mathrm{L}}^{\mathrm{fake}} \qquad N_{\mathrm{T}} = \epsilon_{\mathrm{real}} N_{\mathrm{L}}^{\mathrm{real}} + \epsilon_{\mathrm{fake}} N_{\mathrm{L}}^{\mathrm{fake}}. \tag{6.2}$$

The number of linear equations scales with the number of leptons in the system as 2^{N_ℓ} since the number of fake and real efficiencies grows to account for different combinations of fake leptons.

The inclusive $t\bar{t}Z$ cross-section measurements discussed in Chapter 8 use the maximum likelihood matrix method [121]. The maximum likelihood approach is applied to estimate the real- and fake-lepton efficiencies in the dedicated control regions for electrons and muons separately. The control regions separate the events into ee, $e\mu$ and $\mu\mu$ events, and a simultaneous fit is performed to measure the fake efficiencies.

Fake factor method

A semi-data-driven method, the fake factor method, is used to estimate the contributions of fake leptons in the trilepton signal regions for the differential $t\bar{t}Z$ cross-section measurements in Chapter 9. The Monte Carlo truth record is used to define four MC templates using the origin and type of leptons. Three of the templates target the dominant sources of fake leptons: electrons from heavy-flavour decays (F-e-HF) or from other sources (F-e-Other) and muons from heavy-flavour decays (F-μ-HF). The remaining fake-lepton events are grouped into the "F-Other" template.

Three control regions, CR-$t\bar{t}$-e, CR-$t\bar{t}$-μ and CR-Z-e, are defined to isolate the dominant components of fake-lepton events. The control regions closely follow the kinematic selection requirements of the signal regions, in particular keeping the same criteria for the lepton p_{T}, N_{jets} and $N_{b-\mathrm{jets}}$. The orthogonality with the signal regions is ensured by requiring one of the three leptons to not satisfy the identification and isolation requirements used for the signal leptons, resulting in a loose lepton. The CR-$t\bar{t}$-e and CR-$t\bar{t}$-μ control regions require no OSSF lepton pairs and the loose lepton is required to be part of the same-sign lepton pair. These requirements lead to regions

highly enriched in the $t\bar{t}$ process which isolates contributions of fake leptons from heavy-flavour decays. The events are then categorised into the two regions by the flavour of the loose lepton. The CR-Z-e aims to isolate the "F-e-Other" fake-lepton events by selecting events with exactly three electrons, one of which is a loose electron as before. An OSSF lepton pair is required in this region and events with $E_{\mathrm{T}}^{\mathrm{miss}} > 80\,\mathrm{GeV}$ are vetoed. Therefore, the CR-Z-e region primarily selects events with a Z boson and a fake lepton. A summary of the fake control region definitions is given in Table 6.1. Table 6.2 shows observed and expected event yields in the fake factor control regions.

Table 6.1: Definition of the three-lepton fakes control regions.

Variable	**Preselection**		
N_ℓ $(\ell = e, \mu)$	$= 3$ (of which $= 1$ loose non-tight)		
p_{T} (ℓ_1, ℓ_2, ℓ_3)	$> 27,\ 20,\ 15$ GeV		
Sum of lepton charges	± 1		
N_{jets} $(p_{\mathrm{T}} > 25\,\mathrm{GeV})$	≥ 3		
$N_{b-\mathrm{jets}}$	≥ 1@85%		
	CR-$t\bar{t}$-e	**CR-$t\bar{t}$-μ**	**CR-Z-e**
Lepton flavours	no OSSF pair (loose lepton is an electron)	no OSSF pair (loose lepton is a muon)	OSSF pair (exactly 3 electrons)
$E_{\mathrm{T}}^{\mathrm{miss}}$	—	—	$< 80\,\mathrm{GeV}$

The normalisation (fake) factors of the three dominant fake-lepton sources, $\mathcal{N}_{\text{F-}e\text{-HF}}$, $\mathcal{N}_{\text{F-}e\text{-other}}$ and $\mathcal{N}_{\text{F-}\mu\text{-HF}}$, are estimated from data using a maximum likelihood estimator. A two-bin b-jet multiplicity distribution is used to perform the template fits in the CR-$t\bar{t}$-e and CR-$t\bar{t}$-μ. The 6-bin transverse mass of the W boson, m_{T}^{W}, distribution is fitted in the CR-Z-e. Figure 6.1 shows these distributions before the fit. The normalisation of the "F-Other" category is fixed and is assigned a 50% normalisation uncertainty. Additional non-closure normalisation uncertainties of 20% and 10% are applied on fake electron and muon templates, respectively, in the signal regions. These uncertainties account for the amount of non-closure observed in the dedicated study of the Fake Factor method for the $t\bar{t}Z$ analysis [122].

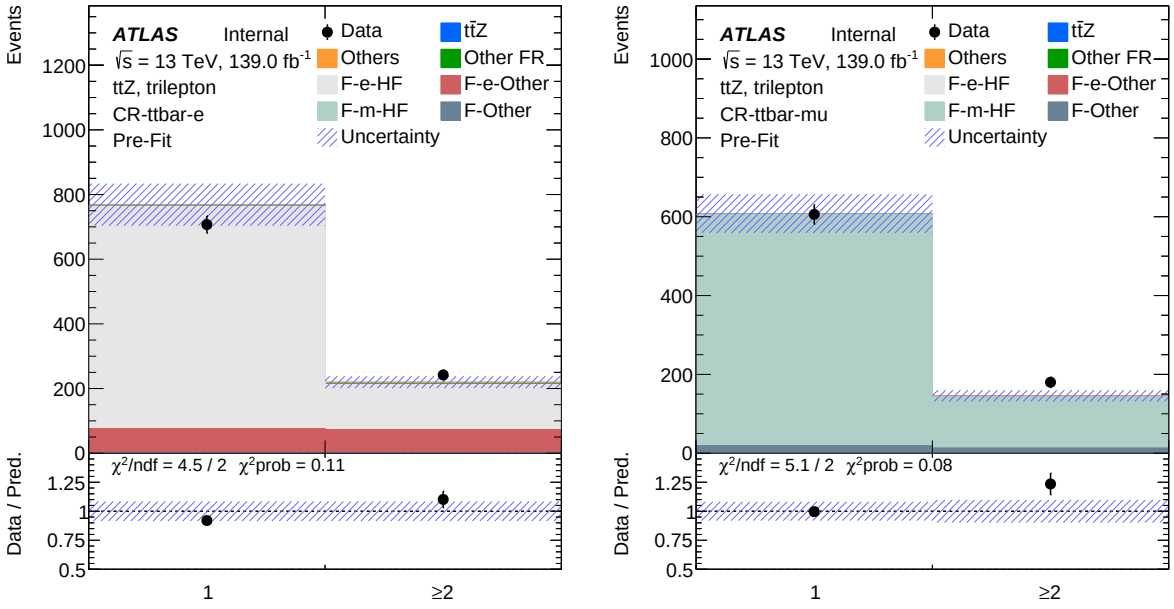

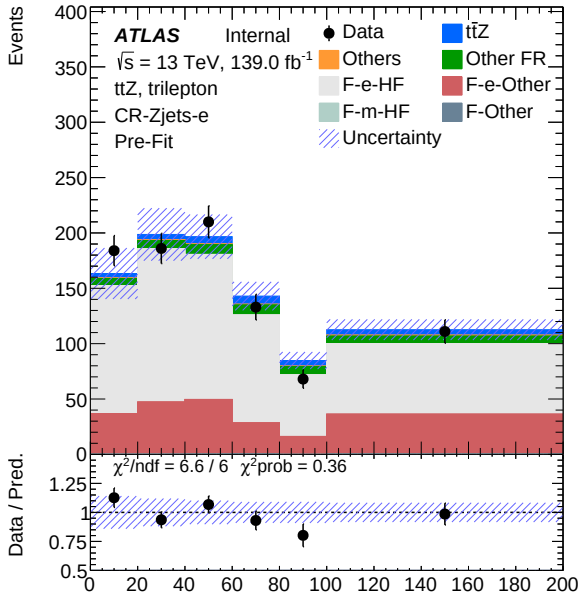

Figure 6.1: Distributions of the b-jet mulitiplicities in the (a) CR-$t\bar{t}$-e and (b) CR-$t\bar{t}$-μ fake control regions, and of m_{T}^{W} in the (c) CR-Z-e region before the fit.

Table 6.2: Expected and observed event yields in the fake factor control regions using the dataset of a 139 fb^{-1} integrated luminosity. The errors include statistical and systematic uncertainties before the fit which are described in Section 7.

	CR-$t\bar{t}$-e	CR-$t\bar{t}$-μ	CR-Z-e
$t\bar{t}Z$	2.6 ± 0.7	0.71 ± 0.29	33.0 ± 7.0
$t\bar{t}W$	2.5 ± 1.3	1.3 ± 0.7	1.2 ± 0.6
$t\bar{t}H$	4.4 ± 0.4	2.28 ± 0.23	3.12 ± 0.33
Other FR	2.5 ± 1.3	0.9 ± 0.4	45.0 ± 23.0
F-e-HF	830.0 ± 70.0	0.0 ± 0.0	600.0 ± 60.0
F-e-Other	146.0 ± 10.0	0.16 ± 0.04	214.0 ± 25.0
F-μ-HF	0.24 ± 0.09	720.0 ± 60.0	0.0 ± 0.0
F-Other	1.6 ± 0.8	31.0 ± 16.0	0.8 ± 0.5
Total	990.0 ± 80.0	750.0 ± 60.0	900.0 ± 90.0
Data	949	786	892

Chapter 7

Systematic uncertainties

The $t\bar{t}Z$ analysis is performed using complex procedures which are obscured by a number of measurement uncertainties. The uncertainties which are not caused by random statistical fluctuations are called systematic uncertainties. They are further split into experimental and theoretical systematic uncertainties. This chapter will define the systematic uncertainties used in the $t\bar{t}Z$ measurements of this thesis. The effects of these uncertainties on the measurements will be presented and discussed in Chapters 8 and 9.

7.1 Experimental uncertainties

The experimental systematic uncertainties account for our limited understanding of the precision with which the ATLAS detector is able to perform measurements of the $t\bar{t}Z$ system. Generally speaking, the uncertainties are derived from the dedicated calibration measurements and data-to-MC comparisons. The relevant sources of the experimental uncertainties are outlined in this section. Each source is usually associated with a number of different factors which lead to multiple nuisance parameters.

Luminosity The dedicated LUCID-2 detector [123] is used to measure and calibrate the luminosity during the data-taking periods. The total integrated luminosity of $139\,\text{fb}^{-1}$ for the LHC Run-2 period has an uncertainty of 1.7% [124].

Pileup reweighting The number of proton-proton collisions per bunch crossing is modelled in the simulation and needs to be corrected to match the data. The pileup reweighting procedure derives scale factors to mitigate these differences and the associated uncertainty is propagated to the analyses.

Jet energy scale and resolution The calibration of the jet energy scale is performed using dijet, multijet and Z/γ+jet events, as outlined in Section 4.1.5. The majority of the jet energy scale uncertainties are due to the *in situ* measurements and are propagated to the $t\bar{t}Z$ analyses using the prescription of Ref. [83]. The jet energy resolution is measured in data and its dependence on the jet p_{T} is parameterised in the calibration procedure. The differences in resolution between the simulation and data are corrected by smearing the resolution in the simulation where it exceeds the resolution in the data. The residual uncertainties in the resolution are propagated to the $t\bar{t}Z$ analyses by smearing the jet energies in the simulation with a Gaussian function [83].

Jet vertex tagger The jet vertex tagging efficiency is measured in data using the tag-and-probe method with the $Z \to \mu\mu$ +jets events [86]. The associated systematic uncertainty is derived by comparing the JVT efficiencies in the MC simulation samples of different event generators. These uncertainties are relevant because the method of propagating the efficiency measurements to the analysis needs both the JVT efficiency measurement in the data and the simulation.

Flavour-tagging efficiencies The performance of the flavour-tagging algorithms, `MV2c10` and `DL1r`, is evaluated in terms of the b-tagging efficiency as well as efficiencies of rejecting c- and light-flavour jets. The calibration procedure is performed using $t\bar{t}$ and Z+jets events, which is discussed in more detail in Section 4.1.6. The associated uncertainties are estimated as variations in the tagging efficiencies and correspond to the pseudo-continuous b-tagging calibration [93]. The eigenvector decomposition is used to derive a set of orthogonal uncertainty components which are propagated to the $t\bar{t}Z$ analyses.

Lepton efficiencies The selection efficiencies of lepton reconstruction, identification, isolation and trigger procedures, as described in Section 4.1, are measured in data using $Z \to \ell\ell$ and $J/\psi \to \ell\ell$ events with tag-and-probe methods [75, 78]. Scale factors

are derived to match the selection efficiencies in the simulation to data. The associated systematic uncertainties of the scale factors are derived as variations in the efficiency calculations and propagated to the $t\bar{t}Z$ analyses.

Lepton momentum scale and resolution The calibration procedures of leptons are outlined in Section 4.1.2 for electrons and Section 4.1.3 for muons. The associated systematic uncertainties are propagated to the analyses of this thesis.

Missing transverse energy The reconstruction of $E_{\mathrm{T}}^{\mathrm{miss}}$, as outlined in Section 4.1.7, is limited by the ability to accurately measure p_{T} of the soft and hard terms in an event. The uncertainties associated with the energy scale and resolution of leptons and jets are propagated to the estimation. The systematic uncertainty on the soft term is derived from the data and MC simulation comparison using $Z \to \mu\mu$ events without any jets [94]. The resulting systematic uncertainties account for the scale and resolution of the $E_{\mathrm{T}}^{\mathrm{miss}}$ soft term.

7.2 Theoretical uncertainties

Theoretical systematic uncertainties primarily originate from the approximations in the MC event generation which lead to making various free choices. Uncertainties are propagated to the measurements by applying variations to the nominal choice of parameters such as renormalisation, factorisation or resummation scales. Alternative MC event generators are also considered for several processes to evaluate the modelling uncertainties.

$t\bar{t}Z$ signal

Renormalisation and factorisation scales The renormalisation, μ_R, and factorisation, μ_F, scale variations are applied to account for the missing higher-order terms in the perturbative QCD calculations. The uncertainties are derived by scaling the nominal values of the μ_R and μ_F parameters individually and/or simultaneously by factors of 2 and 0.5. This leads to seven variations in total, referred to as a 7-point variation.

PDF uncertainties The PDF4LHC prescription [125, 126] is followed to account for the uncertainties in the derivation of the nominal `NNPDF3.0NLO` PDF set. These uncertainties originate from the experimental measurements and perturbative QCD calculations which are used in the derivation. Additionally, the alternative `PDF4LHC` PDF set is used to account for the uncertainty originating from the choice of the nominal PDF set.

Parton showering A choice of the parton showering algorithm, such as PYTHIA8 in the nominal signal sample, inevitably introduces an uncertainty. An alternative signal sample which uses the same MADGRAPH5_AMC@NLO matrix element generator but a different showering algorithm, HERWIG7, is used as a variation to the nominal sample to estimate this uncertainty.

Modelling of ISR Uncertainties for the initial state radiation (ISR) modelling are estimated from an alternative signal sample. The alternative sample is derived by varying the `Var3c` parameter of the `A14` tune and is otherwise equivalent to the nominal signal sample. The `Var3c` parameter corresponds to the variation of the α_s constant in the ISR.

Diboson + jets background

The WZ+jets and ZZ+jets backgrounds are separated into the b-, c- and light-flavour processes based on the flavours of the additional jets using the truth-level information. Consequently, the systematic uncertainties are applied as separate nuisance parameters for each component and are uncorrelated from each other.

Renormalisation and factorisation scales Uncertainties on the choice of the μ_R and μ_F parameters are applied in the same way as for the $t\bar{t}Z$ signal sample.

PDF uncertainties The uncertainty associated with the derivation of the nominal `NNPDF3.0NNLO` PDF set is applied following the standard PDF4LHC prescription [125, 126]. The uncertainty due to the choice of the nominal PDF set is accounted for using the central values of the `CT14` [127] and `MMHT14` [128] PDF sets as variations of the

nominal PDF set. An uncertainty on the scale of the α_s constant is accounted for as a variation in the nominal value.

Merging & resummation scales and recoil scheme Variations of the merging and resummation scales as well as the recoil scheme are included to account for the uncertainties in the matching between the matrix elements and the parton shower [126]:

- The Catani-Krauss-Kuhn-Webber (CKKW) merging scheme [129] is used to prevent double-counting of additional partons which are produced by the ME generator and the parton shower algorithm. The associated uncertainty is a variation of the nominal merging scale below which additional partons are added by the parton shower.
- The QSF resummation scale is a choice of an order in perturbative calculations of the parton shower evolution at which the remaining terms are summed to all orders in α_s. A variation to the nominal scale is applied to model the uncertainty.
- The uncertainty on the choice of the recoil scheme is evaluated by using an alternative CSSKIN scheme [130] as a variation to the nominal `MEPS@NLO` prescription [129, 131, 132, 133] used in the generation of the diboson samples.

Cross-section normalisation Uncertainties on the normalisation of the WZ+jets and ZZ+jets background cross-sections are applied for each b-, c- and light-flavour component which are derived from the data-MC comparisons using the $Z + b/c$ events or derived from data directly [134]. The $WZ/ZZ + b/c$ processes are applied 50% and 30% uncertainties, while the $WZ/ZZ + l$ backgrounds are assigned 15% and 30% uncertainties, respectively. When a background process is estimated directly from data, the corresponding constant normalisation uncertainty is omitted.

tZq background

Renormalisation and factorisation scale Uncertainties on the choice of the μ_R and μ_F parameters are applied in the same way as for the $t\bar{t}Z$ signal sample.

PDF uncertainties The uncertainty associated with the derivation of the nominal `NNPDF3.0NNLO` PDF set and the uncertainty due to the choice of this set are applied

following the standard procedure, which is used for the $t\bar{t}Z$ signal sample and is recommended by PDF4LHC [125].

Parton showering The tZq parton shower uncertainty is estimated using an alternative MADGRAPH5_AMC@NLO + HERWIG7 sample.

Modelling of ISR Uncertainties for the initial state radiation (ISR) modelling are estimated by varying the `Var3c` parameter of the `A14` tune while keeping the rest of the configuration equivalent to the nominal tZq sample.

Cross-section normalisation A 30% uncertainty is applied in the inclusive cross-section measurement, motivated by the dedicated measurements [135, 136]. The differential cross-section measurements use a 14% uncertainty instead which is based on a newer measurement by the ATLAS collaboration [137].

tWZ background

Renormalisation and factorisation scale Uncertainties on the choice of the μ_R and μ_F parameters are applied in the same way as for the $t\bar{t}Z$ signal sample.

PDF uncertainties The uncertainty associated with the derivation of the nominal `NNPDF3.0NNLO` PDF set and the uncertainty due to the choice of this set are applied following the standard procedure, which is used for the $t\bar{t}Z$ signal sample and is recommended by PDF4LHC [125].

Modelling A modelling uncertainty is derived from a comparison of the nominal tWZ sample which is generated using the `DR1` diagram removal scheme and an alternative sample produced with the `DR2` scheme [138]. This uncertainty is based on the studies in Ref. [134].

$t\bar{t}H$ background

Cross-section normalisation and PDF choice A normalisation uncertainty of $^{+5.8\%}_{-9.2\%}$ on the NLO cross-section is taken from Ref. [139]. An additional uncertainty of $\pm 3.6\%$ is applied to account for the choice of the PDF set in the $t\bar{t}H$ sample. This uncertainty is retained from the previous $t\bar{t}Z$ and $t\bar{t}W$ analysis [140].

Other background processes

Minor background processes Samples such as $t\bar{t}W$, $t\bar{t}t$, VH, VVV, etc. have very small contributions to the overall event yield. These samples are applied a conservative normalisation uncertainty of 50%.

The $t\bar{t}t\bar{t}$ background process A parton shower uncertainty on the $t\bar{t}t\bar{t}$ background process is considered for the differential cross-section measurements. An alternative MADGRAPH5_AMC@NLO+HERWIG7 sample is used to derive the uncertainty.

Chapter 8

Measurements of the inclusive cross-section

The measurement of the inclusive (or total) $t\bar{t}Z$ production cross-section is an important test of the Standard Model. Precise knowledge of this cross-section in the observed data tests the precision of the perturbative calculations used in the theoretical predictions and could reveal new physics effects. The $t\bar{t}Z$ production is a rare SM process which has not been fully explored. The analysis of the full LHC Run-2 dataset offers an opportunity to improve the precision of the previous measurements [140, 141].

8.1 Analysis strategy

The $t\bar{t}Z$ cross-section is measured using events containing three and four leptons in the final state, where only electrons or muons are considered. The full Run-2 dataset of proton-proton collisions at the centre-of-mass energy of $\sqrt{s} = 13\,\text{TeV}$ corresponding to an integrated luminosity of $139\,\text{fb}^{-1}$ is used. The signal efficiency and background contributions are estimated from the MC samples and using the data-driven matrix method, which is described in Section 6. The experimental and theoretical systematic uncertainties from Section 7 are considered in the measurement. Full details of the measurement can be found in the corresponding publication [134] by the ATLAS collaboration.

The inclusive cross-section measurement in the three-lepton channel is the main focus of this chapter since it offers optimal performance. This multi-lepton final state preserves a reasonable number of the signal events while backgrounds can be

efficiently rejected. Section 8.2 describes the high-level definitions of the reconstructed physics objects and outlines the three-lepton event pre-selection. Section 8.3 defines the control region which is used to constrain one of the main backgrounds in the optimisation study and the main analysis. Section 8.4 discusses the optimisation study which is performed by the author in order to define optimal event selection criteria for the measurement of the three-lepton $t\bar{t}Z$ inclusive cross-section. Section 8.5 outlines the final three-lepton signal regions and Section 8.6 discusses the final results of the inclusive cross-section measurement.

8.2 Pre-selection of data

8.2.1 Object definitions

The analysis of the three-lepton $t\bar{t}Z$ channel relies on the reconstruction of electrons, muons and jets. The baseline reconstruction techniques and requirements are described in Section 4.1. This section defines requirements that are specific for the inclusive cross-section measurement:

- **Electrons:** The `MediumLH` likelihood-based identification and the `FCTight` isolation requirements are used to select electrons.
- **Muons:** The `Medium` quality and `FCTightTrackOnly` isolation requirements are used to select muons.
- **Jets:** The anti-k_{T} jet algorithm with the $R = 0.4$ distance parameter and topological clusters as inputs is used to reconstruct jets (Section 4.1.5). The `MV2c10` b-tagging algorithm is applied to identify jets which contain b-hadrons using pseudo-continuous efficiency b-tagging working points (Section 4.1.6).

8.2.2 Pre-selection of the three-lepton events

The $t\bar{t}Z$ system can result in three-lepton final states when the Z boson and a W boson from one of the top quarks decay leptonically. At leading order, two jets are expected from the decay of the remaining W boson as well as two other jets which originate

from the b-quarks of the top quark decays. The event pre-selection criteria are defined to identify the signal events with such signatures.

Exactly three isolated leptons (electrons or muons) are required in each event to ensure orthogonality with the other $t\bar{t}Z$ final states. At least one pair of opposite-sign same-flavour (OSSF) leptons which have an invariant mass within 10 GeV of the Z boson mass, $m_Z = (91.1876 \pm 0.0021)$ GeV [10], is required to reconstruct on-shell Z bosons. If more than one pair of OSSF leptons are present, the pair with the closest mass to the Z boson is selected. Additionally, each OSSF pair is required to have the invariant mass larger than 10 GeV to remove low-mass resonances. Leptons are sorted in the increasing p_{T} order, namely the leading, subleading and third leptons. Minimum transverse momentum requirements are applied on the leptons; the leading lepton is required to have $p_{\mathrm{T}} > 27$ GeV while the subleading and third leptons with $p_{\mathrm{T}} > 20$ GeV are selected. The leading lepton p_{T} selection is limited by the ATLAS lepton triggers where events with at least one 26 GeV lepton are required. The p_{T} selection is relaxed for the remaining two leptons to achieve a higher signal efficiency. Table 8.1 summarises these requirements. The pre-selection does not efficiently suppress the dominant WZ+jets, tZq, tWZ backgrounds. Additional selection requirements and a dedicated measurement in a control region are therefore used to improve the background rejection and reduce the associated uncertainties. The following two sections will discuss the corresponding techniques and Section 8.5 gives the final event selection.

Table 8.1: Summary of the pre-selection of the three-lepton $t\bar{t}Z$ events.

Variable	**Pre-selection**
$N_\ell(\ell = e, \mu)$	$= 3$
	≥ 1 OSSF pair with $\lvert m_{\mathrm{OSSF}} - m_Z \rvert < 10$ GeV
	for all OSSF combinations $m_{\mathrm{OSSF}} > 10$ GeV
$p_{\mathrm{T}}(\ell_1, \ell_2, \ell_3)$	$\geq 27, 20, 20$ GeV

8.3 Definition of the control region

A region in the three-lepton $t\bar{t}Z$ phase-space can be defined where the dominant process is the WZ+jets background while the $t\bar{t}Z$ signal contribution is minimal. This control region is called 3ℓ-WZ-CR since the estimation of the WZ+jets background is more powerful than that of the signal process. The definition of the control region is based on the three-lepton $t\bar{t}Z$ pre-selection and additionally requires events with at least three jets in total. The events are further required to have no b-tagged jets which are identified with the b-tagging efficiency of 85%. This requirement in particular suppresses the signal process and any other background process featuring a b-hadron initiated jet in the final state. The summary of the 3ℓ-WZ-CR control region definition is given in Table 8.2.

Table 8.3 shows the expected yields of each SM process and the observed yield in the data in the 3ℓ-WZ-CR control region. The WZ+jets background is dominant, and the highest contribution is from the $WZ + l$ final state due to the veto of the events containing b-tagged jets. The $t\bar{t}Z$ process is sufficiently suppressed in the region, corresponding to 2.5% of the total event yield. The fake lepton background is estimated via the matrix method, which is described in Section 6.2.2. The normalisation of the $WZ + l$ background and the associated uncertainty can therefore be reliably measured in the data sample of this control region.

Table 8.2: Summary of the event selection in the three-lepton control region of the inclusive $t\bar{t}Z$ cross-section measurement.

Variable	**Pre-selection**
$N_\ell(\ell = e, \mu)$	$= 3$
	≥ 1 OSSF pair with $\lvert m_{\text{OSSF}} - m_Z \rvert < 10\,\text{GeV}$
	for all OSSF combinations $m_{\text{OSSF}} > 10\,\text{GeV}$
$p_{\text{T}}(\ell_1, \ell_2, \ell_3)$	$\geq 27, 20, 20\,\text{GeV}$
	3ℓ-WZ-CR
N_{jets}	≥ 3
$N_{b-\text{jets}}$	$= 0$ @ 85%

Table 8.3: Event yields in the 3ℓ-WZ-CR control region. The uncertainties include statistical uncertainties of the MC prediction and systematic uncertainties.

Process	3ℓ-WZ-CR
$t\bar{t}Z$	43.8 ± 11.3
$WZ + l$	1156.8 ± 368.9
$WZ + b$	16.7 ± 10.0
$WZ + c$	234.5 ± 103.0
ZZ+jets	131.8 ± 21.4
tWZ	13.3 ± 1.2
tZq	9.1 ± 3.5
$t\bar{t}X(W/H)$	1.8 ± 0.38
Fake leptons	86.1 ± 43.3
Other	12.4 ± 6.4
Total SM	1706.3 ± 395.3
Data	1569

8.4 Optimisation of signal regions

The pre-selection criteria of the three-lepton $t\bar{t}Z$ signal events are not efficient enough to suppress backgrounds and additional requirements on jets are needed. This optimisation study focuses on defining signal regions in terms of the number and definitions of b-tagged jets using PCbT[1], which was introduced in Section 4.1.6. For the $t\bar{t}Z$ measurements, it is expected to improve the suppression of a dominant WZ+jets background and the associated systematic uncertainties with respect to the previous measurements [140].

The selection efficiency of the $t\bar{t}Z$ events is highly dependent on the b-tagging efficiency due to the presence of two jets originating from b-hadrons at leading order. It may be more optimal to use a couple of signal regions with varying b-tagging efficiencies to achieve a higher overall efficiency. For example, a signal region with one b-tagged jet has the event selection efficiency $\epsilon_{1b} \approx 2\epsilon_b(1-\epsilon_b)\epsilon_c$, where ϵ_b is a b-tagging efficiency and ϵ_c is the efficiency of all cuts apart from ϵ_b. On the other hand, a signal region with two b-tagged jets has the selection efficiency $\epsilon_{2b} \approx \epsilon_b^2\epsilon_c$.

[1] pseudo-continuous b-tagging

This implies that using the same b-tagging efficiency in both regions will result in a smaller overall efficiency in the region with two b-tagged jets. Similarly, the number of incorrectly b-tagged jets is proportional to ϵ_{mistag} and $\epsilon^2_{\text{mistag}}$ for regions with one and two b-tagged jets, respectively. Therefore, the number of b-tagged jets carries a discriminating power itself which suppresses the background rate from processes without b-jets more in a two b-tagged jet region compared to a region with one b-tagged jet, using the same b-tagging efficiency. The goal of this optimisation study is to find a signal region or a combination of them where a choice of the number of b-tagged jets and the associated b-tagging efficiencies minimise the uncertainty on the measurements of the inclusive $t\bar{t}Z$ cross-section.

The optimisation study is performed using the Asimov dataset which is an MC simulation dataset corresponding to a total integrated luminosity of $139\,\text{fb}^{-1}$ for proton-proton collisions at the centre-of-mass energy of $\sqrt{s} = 13\,\text{TeV}$. The Asimov dataset assumes the SM production rate of the $t\bar{t}Z$ process. The background is estimated from the dominant WZ+jets and ZZ+jets processes, grouped into the diboson sample, as well as the fake lepton background and the $t\bar{t}W$ process. The fake lepton background is estimated from the MC simulation directly and the matrix method is not applied here. This likely leads to an underestimation of fake leptons, however, the effect is mitigated by relative comparisons that are used to make final conclusions of this optimisation study.

8.4.1 Definitions of signal regions

The event pre-selection criteria from Section 8.2.2 are used to define signal regions by adding additional requirements on the number of b-tagged jets and their tagging efficiencies. Each signal region vetoes events with less than four jets in total. The leading b-tagged jet is defined as a jet which is tagged with the lowest efficiency working point in a given event while the subleading b-tagged jet is a jet tagged with the second lowest efficiency working point in the same event. The PCbT approach allows not only the use of different WPs between the regions but also between the leading and subleading b-tagged jets.

Sixteen variations of the three-lepton event selection are defined using either a single signal region or two orthogonal signal regions which do not overlap with the control region defined in Section 8.3. Figure 8.1 illustrates several of the options. The

x-axis refers to the leading b-tagged jet WP and the subleading b-tagged jet WP is shown on the y-axis. Figure 8.1a depicts a selection which is used as the baseline of the optimisation study. The remaining three diagrams illustrate how PCbT can be used to design different combinations of orthogonal signal regions. In particular, Figures 8.1c and 8.1d show that, given a signal region with two b-tagged jets, a scan can be performed by gradually opening the b-tagging acceptance of the signal region with one b-tagged jet. It is essential to preserve orthogonality between the regions in each combination. This is achieved by explicitly adding a lower limit on the efficiency of the subleading b-tagged jet in 1b signal regions. For example, the 1b@60%[77%] + 2b@70%70% label should be read as an event selection using two signal regions, 1b and 2b, where the leading and subleading b-tagged jets in the 2b region pass the WP of 70% while the 1b region requires the leading b-tagged jet to pass the WP of 60% and vetoes events where the subleading b-tagged jet is tagged with the efficiency lower than 77% thus ensuring orthogonality. This nomenclature is used in the presentation of the expected results in Section 8.4.3.

8.4.2 Systematic uncertainties

A subset of the systematic uncertainties, which are discussed in Chapter 7, are used in this PCbT analysis. The majority of the systematic uncertainties cancel out when deriving relative comparisons between different definitions of the signal regions using the PCbT approach or have negligible effects. However, the PCbT approach can limit the contribution from the WZ+jets background thereby limiting the impact of the otherwise large associated systematic uncertainties. The $t\bar{t}Z$ signal yield may also be affected in this approach. Such effects may vary between different signal region definitions significantly. The following are the systematic uncertainties included in the study:

- Luminosity: one of the most dominant uncertainties which affects all MC samples.
- WZ +1b and WZ +2b: constant uncertainties of 12.5% are applied to the diboson sample in each signal region separately. These uncertainties account for the different event compositions of the signal and control regions. The 3ℓ-WZ-CR control region is dominated by the $WZ + l$ process while the signal regions are estimated to have a relatively larger contribution from the $WZ + b$ process.

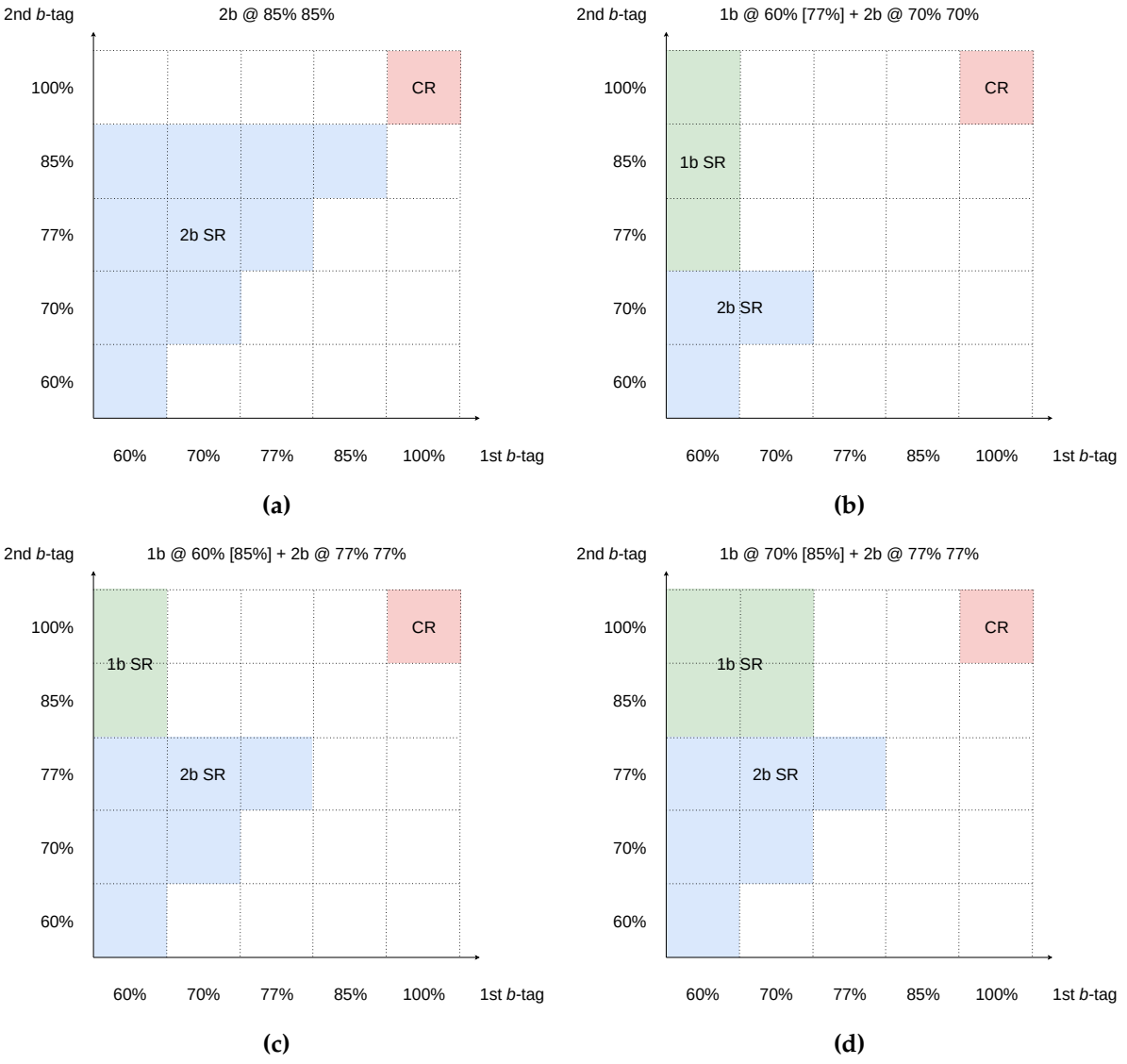

Figure 8.1: Illustrations of three-lepton signal regions where each subfigure corresponds to a single event selection. The x-axis indicates the definition of the leading b-tagged jet and the subleading b-tagged jet is defined on the y-axis.

- b-tagging efficiency scale factors: one of the most dominant systematic uncertainties which are significantly affected by the definitions of the b-tagged jets.

8.4.3 Expected results

A profile likelihood fit is performed to estimate expected statistical and total uncertainties of the inclusive $t\bar{t}Z$ cross-section measurement for each PCbT selection. Accordingly, the likelihood function is defined using either one or two signal regions and includes the 3ℓ-WZ-CR control region (Section 8.3) which are parameterised by the number of events. The selection criterion for the number of jets in the control region is tightened here to ≥ 4 jets to match the signal regions. The estimation of the normalisation factor for the $WZ + l$ background is driven by the control region in the combined fit of the signal and control regions.

Figure 8.2 shows expected event yields before the fit for the signal and background processes. It illustrates the effects of applying different b-tagging WPs in definitions of signal regions. Figures 8.2a, 8.2b and 8.2c are examples of $1b$ signal regions used in the optimisation study. The $1b$@70%[77%] selection (Figure 8.2a) has the largest acceptance of the three examples where the leading b-tagged jet passes the medium tightness WP of 70% and events containing a subleading b-tagged jet below the 77% efficiency are vetoed. The second region tightens the selection of the leading b-tagged jet by switching to the lowest efficiency WP of 60%. The acceptance is further reduced in the third selection where only one 60% b-tagged jet is allowed. Similarly, three $2b$ signal regions, where the selection is tightened from left to right, are shown in Figures 8.2d, 8.2e and 8.2f. The first region shows the event composition of the selection which is considered the reference point of this optimisation. In both sets of regions, the total count of events decreases with the tightening of selections at the cost of both the signal and background events. However, the background processes, and in particular the diboson background, are consistently reduced at a higher rate than the signal process in the three examples of the $2b$ signal regions. In the case of $1b$ signal regions, the same observation can be made where a selection accepts at least 1 b-tagged jet. It is seen that vetoing events with more than 1 b-tagged jets (Figure 8.2c) reverses the outcome and more signal events are rejected than the background.

Sixteen three-lepton event selections are tested and the expected uncertainties on the measured $t\bar{t}Z$ cross-section for each PCbT selection are shown in Table 8.4.

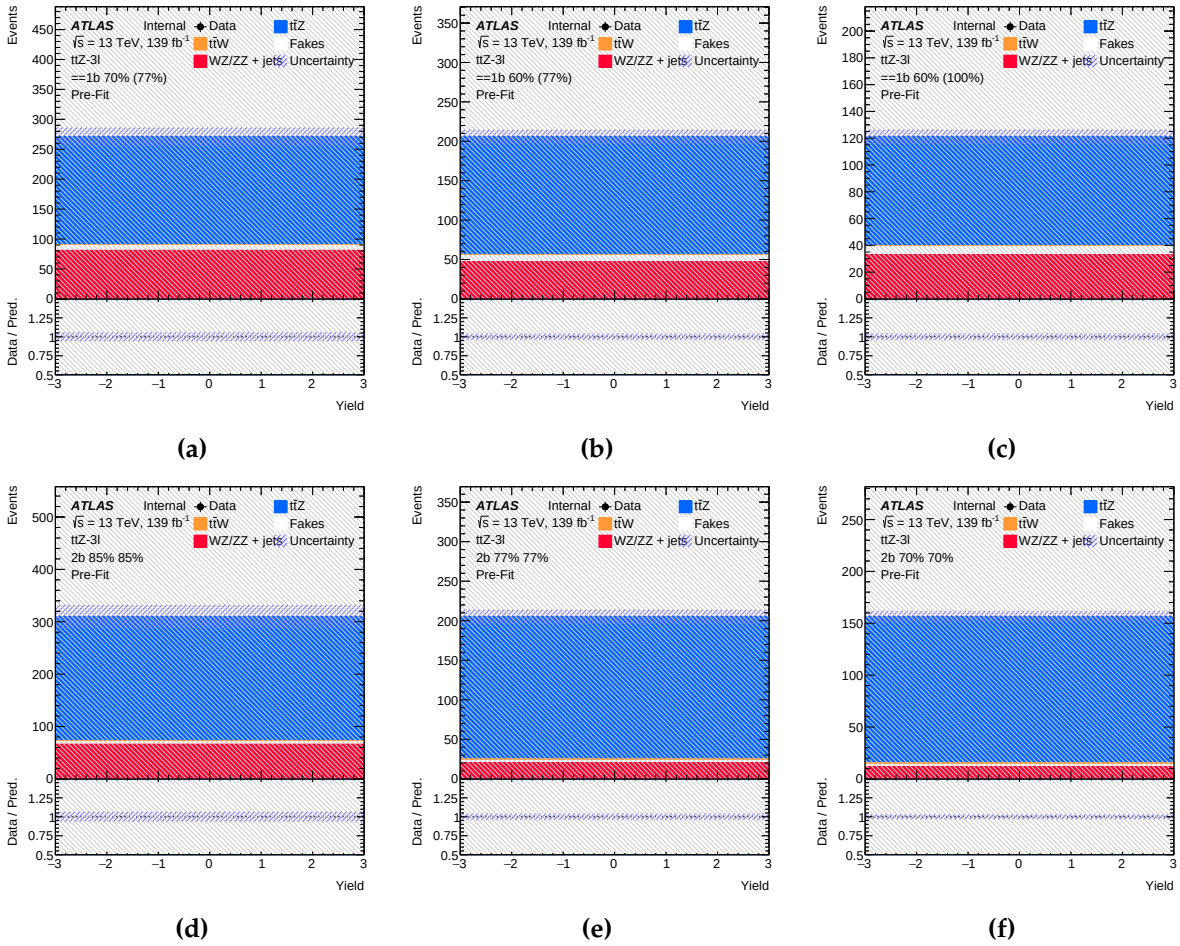

Figure 8.2: Event decomposition of the (a) 1b @ 70% [77%], (b) 1b @ 60% [77%], (c) 1b @ 60% [100%], (d) 2b @ 85% 85%, (e) 2b @ 77% 77% and (f) 2b @ 70% 70% signal regions. The signal event selection efficiency is reduced from the (a) to (c) subfigure and from the (d) to (e) subfigure.

Three of the selections are defined as a single $2b$ or $\geq 1b$ signal regions and the remaining thirteen options are orthogonal combinations of $1b$ and $2b$ signal regions. The $2b$@85%85% event selection, shown on the last row, is considered the baseline and the remaining options are compared with respect to it. The last two columns of Table 8.4 show the $t\bar{t}Z$ signal, S, and total background, B, yields, respectively. Three options, namely 7., 8. and 9., stand out from the point of view of the total uncertainty. These are the only options with the total estimated uncertainty below 8%. Option 13. gives the largest signal yield, however the background yield is also largest.

Table 8.4: Summary of expected uncertainties on the signal strength using different combinations of $1b$- and $2b$-tagged jets signal regions. The uncertainties are estimated using the profile likelihood method. All setups include the 3ℓ-WZ-CR control region. The last two columns show pre-fit signal (S) and background (B) event yields.

	Signal Regions	Stat. unc. [%]	Total unc. [%]	S	B
1.	$1b$ @ 70% [85%] + $2b$ @ 77% 77%	6.54	8.71	324.2	108.3
2.	$1b$ @ 70% [85%] + $2b$ @ 70% 77%	6.55	8.55	321.3	106.3
3.	$1b$ @ 70% [77%] + $2b$ @ 70% 70%	6.57	8.45	321.4	106.2
4.	$1b$ @ 77% [85%] + $2b$ @ 77% 77%	6.69	9.36	342.5	160.2
5.	$1b$ @ 60% [85%] + $2b$ @ 77% 77%	6.57	8.13	300.0	76.0
6.	$1b$ @ 60% [85%] + $2b$ @ 70% 77%	6.58	8.00	297.1	74.0
7.	$1b$ @ 60% [77%] + $2b$ @ 70% 70%	6.64	7.92	291.0	71.4
8.	$1b$ @ 60% [85%] + $2b$ @ 60% 77%	6.66	7.89	287.1	70.1
9.	$1b$ @ 60% [70%] + $2b$ @ 60% 60%	6.69	7.97	287.0	70.2
10.	$1b$ @ 60% [100%] + $2b$ @ 70% 85%	6.57	8.40	305.3	81.6
11.	$1b$ @ 70% [100%] + $2b$ @ 70% 85%	6.57	8.89	321.3	106.4
12.	$1b$ @ 70% [100%] + $2b$ @ 85% 85%	6.79	10.90	334.5	137.4
13.	$1b$ @ 85% [100%] + $2b$ @ 85% 85%	7.34	12.30	361.1	316.5
14.	$1b$ @ 77%	7.01	11.90	342.5	160.1
15.	$2b$ @ 77% 77%	8.02	9.56	180.2	25.1
16.	$2b$ @ 85% 85%	7.66	12.40	237.1	72.8

Figure 8.3 compares the fifteen alternative selections with respect to the baseline option (red line) in terms of the total uncertainty (green diamond markers), signal yields (dark red square markers) and the total uncertainty (blue circle markers). Nega-

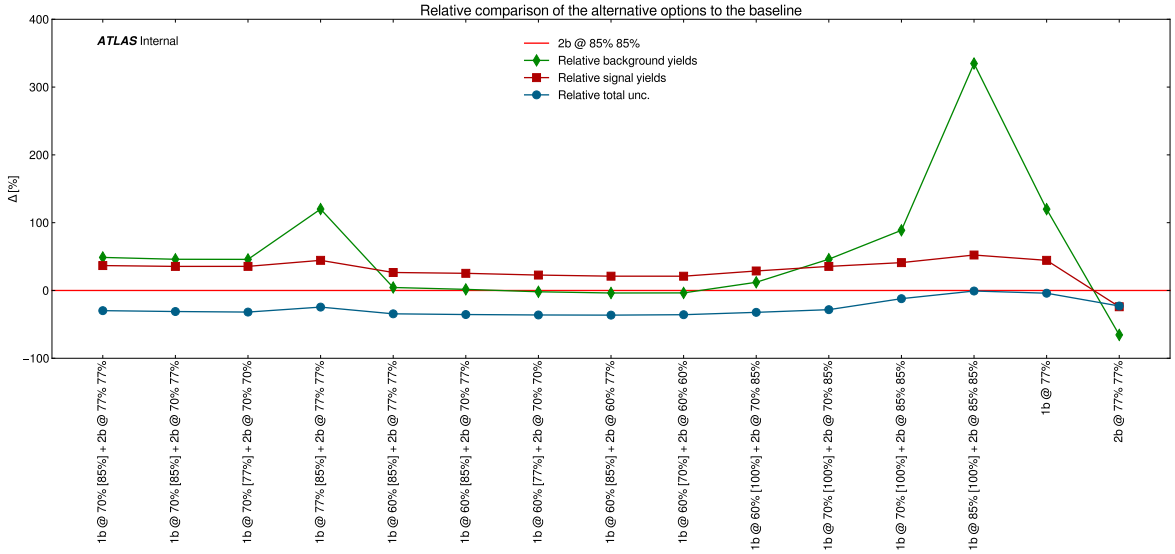

Figure 8.3: Comparison of the alternative selection relative to the baseline 2b@85%85% selection with respect to the background yield (green), signal yield (dark red) and total uncertainty (blue).

tive values refer to a reduction in the quantity using the alternative option. Generally, the total uncertainty and the background yield are desired to be reduced as much as possible while the signal yield increased. The 2b@77%77% selection stands out as the one with the largest suppression of the background. However, the signal yield is also reduced with respect to the nominal and, therefore, this option is not considered further. On the other hand, the 1b@77%[85%] + 2b@77%77%, 1b@77% and 1b@85%[100%] + 2b@85%85% options offer the best improvements in the signal yield, however, the background yields are amplified significantly, beyond the acceptable amount. The six selections in the middle region of the figure are the most reasonable: the signal yields are improved by 26–29% relative to the baseline and the background contributions remain at a similar level. Most significantly, the relative reduction in the total uncertainty is estimated to be in the 32–35% range. The 1b@60%[77%] + 2b@70%70% combination of signal regions is considered to be the most optimal among these options based on prioritising the improvements in the signal yield and total uncertainty equally.

Figure 8.4a shows a ranking of the nuisance parameters in the baseline 2b@85%85% selection and Figure 8.4b in the optimized 1b@60%[77%] + 2b@70%70% selection. The ranking plots are produced according to the prescription of Section 4.3.2 using the `TRExFitter` framework. The impact of a nuisance parameter on the POI is shown

as an empty rectangle with blue and cyan borders before the fit while the post-fit impact is depicted with a solid rectangle. The nuisance parameters are shown as black markers with horizontal error bars representing the associated post-fit uncertainties. All nuisance parameters associated with systematic uncertainties have initial central values of 0 while the free-floating normalisation factor is centred at 1. The central values are not shifted in the fit since the Asimov dataset is used in the estimations. The optimised selection reduces the impacts of nuisance parameters significantly. The first component of the b-tagging efficiency scale factors associated with the light-flavour jet mistagging ranks highest in both setups. However, the optimized selection reduces the impact of this systematic uncertainty by a factor of 3. The impact of the second component is reduced to a negligible effect. The optimised selection is less sensitive to the light-jet mistagging uncertainties since a relatively low overall b-tagging efficiency is achieved giving a high light-flavour jet rejection, as shown in Figure 4.5. The impact of the WZ2b systematic uncertainty is reduced even more, by a relative factor of 7. A minor reduction in the post-fit impact of the WZ1b uncertainty is seen due to a constraining power of the Asimov dataset on the associated nuisance parameter. Lastly, the impact of the uncertainty associated with the free-floating $WZ + l$ normalisation factor is halved in the optimised setup. Therefore, the performance of the optimised event selection using the two signal regions with the PCbT approach is expected to yield significant improvements in the final $t\bar{t}Z$ inclusive cross-section measurement.

8.5 Three-lepton signal regions

The final three-lepton event selection and the corresponding signal regions are defined using the event pre-selection from Section 8.2.2 and the results of the optimisation study. The pre-selected events are separated into two orthogonal signal regions following the conclusions of the optimisation study. The regions are primarily differentiated by the number of b-tagged jets, 1b and 2b, and the total number of jets is adjusted for each signal region. Each jet is required to pass the $p_{\mathrm{T}} > 25\,\mathrm{GeV}$ selection as before. The 2b signal region is defined by selecting events with two b-tagged jets where both jets are required to pass the WP of 70%. At least three jets in total are required in this signal region. The 1b signal region is defined next to select events with at least one b-tagged jet. The leading b-tagged jet is required to pass the WP of 60%. Events where additional jets are tagged with an efficiency lower than 77% are vetoed in order to not overlap with the 2b signal region. The requirement on the total number of jets

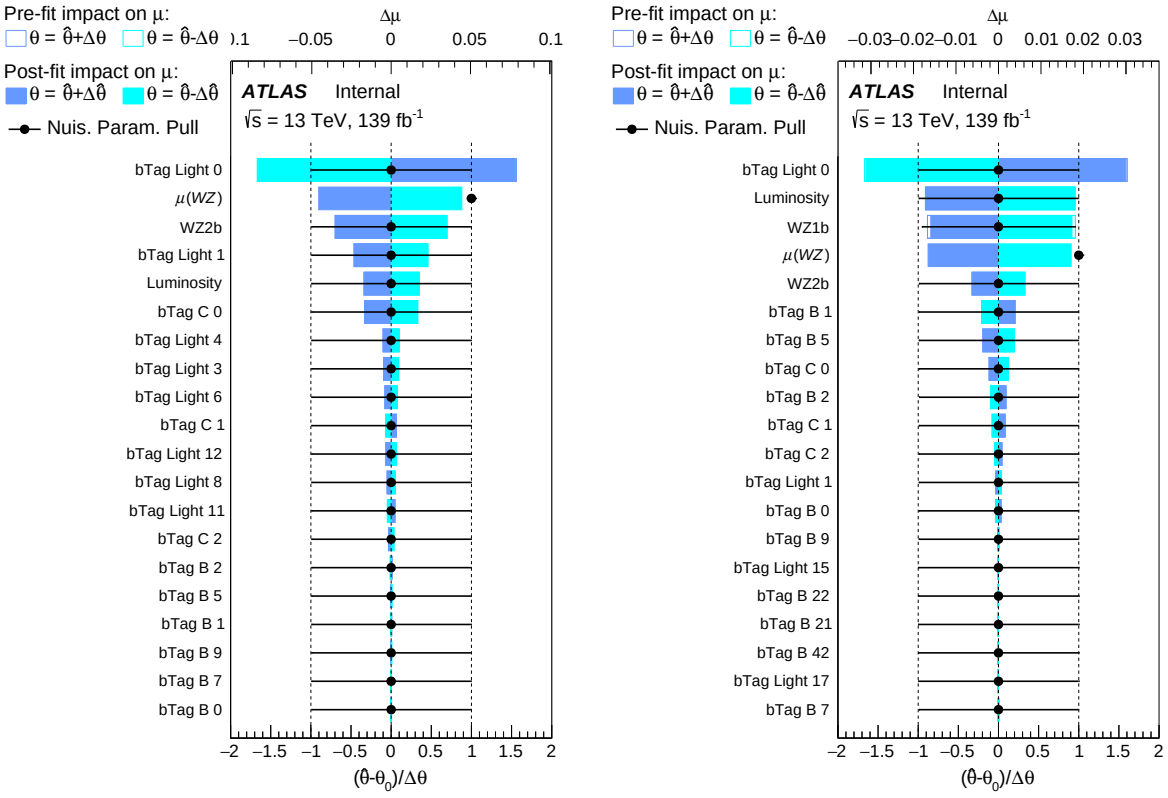

(a) $2b$@85%85% + 3ℓ-WZ-CR **(b)** $1b$@60%[77%] + $2b$@70%70% + 3ℓ-WZ-CR

Figure 8.4: Ranking of the systematic uncertainties with respect to their impact on the parameter of interest using Asimov data.

Table 8.5: Summary of the event selection in the three-lepton signal regions.

Variable	**Pre-selection**	
$N_\ell(\ell = e, \mu)$	$= 3$	
	≥ 1 OSSF pair with $\lvert m_{\text{OSSF}} - m_Z \rvert < 10\,\text{GeV}$	
	for all OSSF combinations $m_{\text{OSSF}} > 10\,\text{GeV}$	
$p_{\text{T}}(\ell_1, \ell_2, \ell_3)$	$\geq 27, 20, 20\,\text{GeV}$	
	3ℓ-Z-$1b4j$-PCBT	**3ℓ-Z-$2b3j$-PCBT**
N_{jets} ($p_{\text{T}} > 25\,\text{GeV}$)	≥ 4	≥ 3
$N_{b-\text{jets}}$	≥ 1	≥ 2
$(b^{\text{1st}}_{\text{tag}}, b^{\text{2nd}}_{\text{tag}})$	$(= 60\%, \geq 70\%)$	$(\leq 70\%, \leq 70\%)$

is retained from the optimisation study ($\geq$ 4 jets) in this signal region to ensure a reasonable rejection of background events where only one b-tagged jet is present. The overall selection efficiency is improved with respect to the previously used selection by including events with only one b-tagged jet because of the limited b-tagging efficiency. The two signal regions are labelled 3ℓ-Z-$1b4j$-PCBT and 3ℓ-Z-$2b3j$-PCBT and the selection criteria are summarised in Table 8.5.

8.6 Observed results

The measurement of the total inclusive $t\bar{t}Z$ cross-section is performed by combining the signal and control regions of the three-lepton channel with the four-lepton channel targeting the $t\bar{t}Z$ final state with four isolated leptons. The four-lepton channel is divided into four signal regions and has a dedicated 4ℓ-ZZ-CR control region to measure the $ZZ + l$ background normalisation from data, similarly to the $WZ + l$ background in the 3ℓ channel. More details about the four-lepton channel can be found in Ref. [134]. The measurement is performed using the profile likelihood approach where the likelihood function is a product of the 3ℓ and 4ℓ likelihood functions. The systematic uncertainties, which are constrained with unit Gaussian distributions in the likelihood function, are fully correlated where they apply to both channels. In addition to the signal strength parameter of interest, $\mu_{t\bar{t}Z}$, the normalisation factors associated

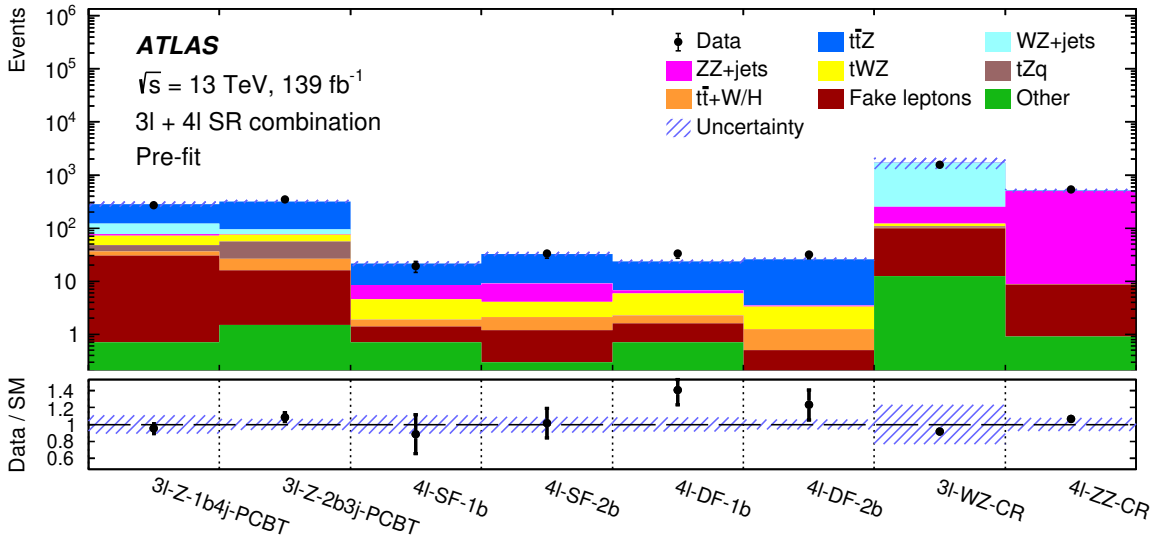

Figure 8.5: Post-fit event yields which are observed in data and MC simulations in the three-lepton and four-lepton signal and control regions [134]. Statistical and systematic uncertainties of the total SM prediction are shown by the blue striped band.

with the light-flavour components of the WZ+jets and ZZ+jets backgrounds, $\mathcal{N}_{WZ+l}$ and $\mathcal{N}_{ZZ+l}$, are free-floating parameters.

The data is compared with the results of the combined measurement in the regions of each channel in Figure 8.5. The signal strength parameter is measured to be:

$$\mu_{t\bar{t}Z} = 1.19 \pm 0.06\,(\text{stat.}) \pm 0.10\,(\text{syst.}). \tag{8.1}$$

The three-lepton channel dominates the combined measurement, however, the values in the individual 3ℓ, 4ℓ and combined fits are compatible, as can be seen in Table 8.6. The total inclusive $t\bar{t}Z$ cross-section measurement is derived from the combined $t\bar{t}Z$ signal strength estimation:

$$\sigma(pp \to t\bar{t}Z) = 0.99 \pm 0.05\,(\text{stat.}) \pm 0.08\,(\text{syst.})\,\text{pb} = 0.99 \pm 0.10\,\text{pb}. \tag{8.2}$$

The result is in good agreement with the SM prediction of $0.86^{+0.07}_{-0.08}\,(\text{scale}) \pm 0.02\,(\text{PDF})$ pb [16] at next-to-leading order calculations in QCD and electroweak precision with next-to-next-leading-logarithmic corrections.

The rankings of individual nuisance parameters are shown in Figure 8.6. The top 20 uncertainties with the largest impact on the parameter of interest are listed. The

Table 8.6: Measured signal strength, $\mu_{t\bar{t}Z}$, parameter obtained from the individual 3ℓ and 4ℓ channels as well as in the combined fit [134]. The uncertainties include statistical and systematic sources.

Channel	$\mu_{t\bar{t}Z}$
Three-lepton (3ℓ)	$1.17 \pm 0.07\,(\text{stat.})^{+0.12}_{-0.11}\,(\text{syst.})$
Four-lepton (4ℓ)	$1.21 \pm 0.15\,(\text{stat.})^{+0.11}_{-0.10}\,(\text{syst.})$
Combined (3ℓ + 4ℓ)	$1.19 \pm 0.06\,(\text{stat.}) \pm 0.10\,(\text{syst.})$

tWZ modelling uncertainty is ranked the highest while the second-highest $t\bar{t}Z$ parton shower uncertainty has a closely matched impact. The uncertainties can be grouped by type and their impacts on the measurement can be estimated in a similar way to the ranking of the individual nuisance parameters. Table 8.7 summarises such impacts of the grouped uncertainties. The dominant sources of systematic uncertainties are associated with the $t\bar{t}Z$ parton shower, the modelling of the tWZ background and jet flavour-tagging.

The $t\bar{t}Z$ inclusive cross-section was previously measured by the ATLAS and CMS collaborations using subsets of the Run-2 data. The ATLAS collaboration used $36.1\,\text{fb}^{-1}$ of integrated luminosity [140]:

$$\sigma^{\text{ATLAS}}_{t\bar{t}Z} = 0.95 \pm 0.08\,(\text{stat.}) \pm 0.10\,(\text{syst.})\,\text{pb} = 0.95 \pm 0.13\,\text{pb}, \tag{8.3}$$

where the dominant sources of uncertainty were due to the modelling of backgrounds (5.3%), modelling of the signal (4.9%) and flavour-tagging (4.2%). The CMS collaboration measured this cross-section using $77.5\,\text{fb}^{-1}$ of integrated luminosity at:

$$\sigma^{\text{CMS}}_{t\bar{t}Z} = 0.95 \pm 0.05\,(\text{stat.}) \pm 0.06\,(\text{syst.})\,\text{pb} = 0.95 \pm 0.08\,\text{pb}, \tag{8.4}$$

where the uncertainties associated with the lepton selection efficiencies (4%), the WZ+jets background (3%) and $t\bar{t}X(W/H)$ background (2%) were dominant [141]. All measurements are in agreement with each other and with the theoretical prediction. The current measurement achieves a relative improvement of 27% with respect to the previous ATLAS measurement. However, it is not as precise as the CMS measurement, where the modelling uncertainties of the $t\bar{t}Z$ process are significantly smaller than in the ATLAS measurement.

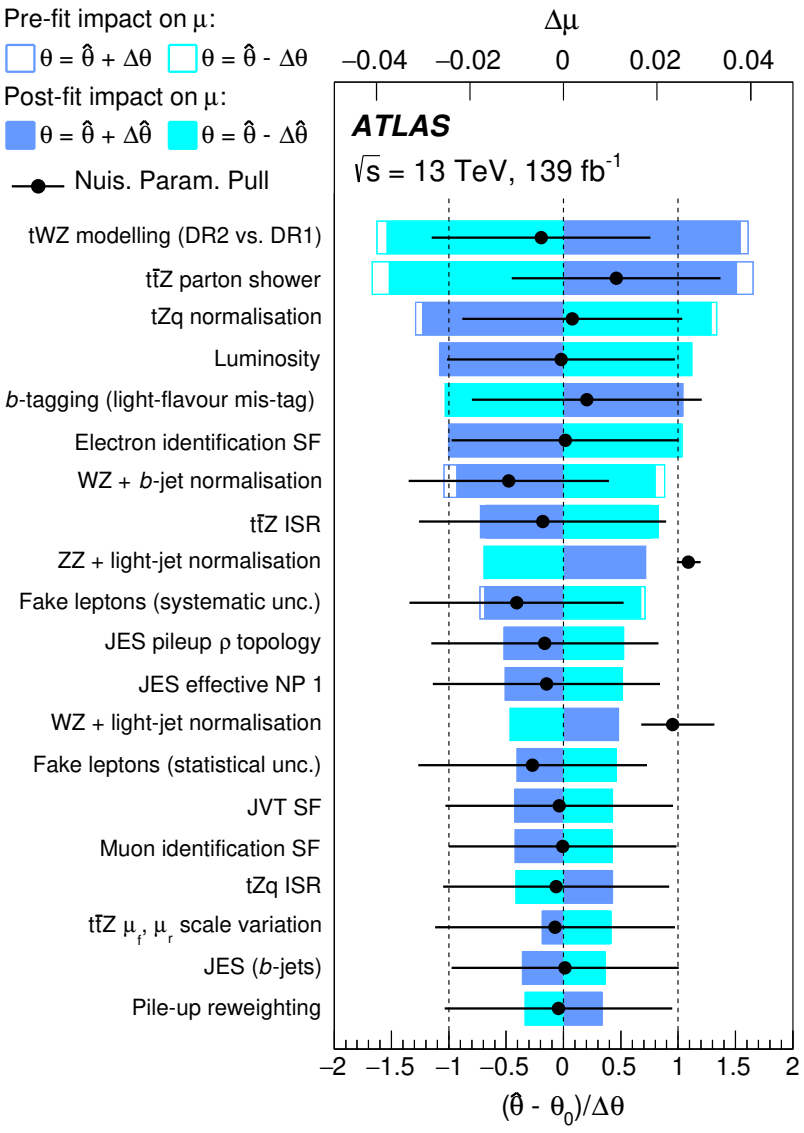

Figure 8.6: Ranking of the individual uncertainties in the combined (3ℓ+4ℓ) measurement [134].

Table 8.7: Impacts of grouped uncertainties on the measured inclusive $t\bar{t}Z$ cross-section from the combined (3ℓ+4ℓ) fit [134].

Uncertainty	$\Delta\sigma_{t\bar{t}Z}/\sigma_{t\bar{t}Z}$ [%]
$t\bar{t}Z$ parton shower	3.1
tWZ modelling	2.9
b-tagging	2.9
WZ/ZZ+jets modelling	2.8
tZq modelling	2.6
Lepton	2.3
Luminosity	2.2
Jets + $E_{\mathrm{T}}^{\mathrm{miss}}$	2.1
Fake leptons	2.1
$t\bar{t}Z$ ISR	1.6
$t\bar{t}Z$ μ_F and μ_R scales	0.9
Other backgrounds	0.7
Pile-up	0.7
$t\bar{t}Z$ PDF	0.2
Total systematic	8.4
Data statistics	5.2
Total	10

Chapter 9

Measurements of the differential cross-section

The differential cross-section of the $t\bar{t}Z$ process is measured as a function of various physical observables which probe different aspects of the system. Our understanding of the $t\bar{t}Z$ process may then be expanded by exploring its production rate at, for instance, different energies of the Z boson or angles between the Z boson and one of the top quarks as a distribution rather than a single number (from the inclusive cross-section measurement). The measurements presented in this chapter are part of an ongoing physics analysis by the ATLAS Collaboration [122].

9.1 Analysis strategy

The $t\bar{t}Z$ differential cross-section is measured using events with exactly three leptons (electrons or muons) in the final state. The full Run-2 dataset of proton-proton collisions at the centre-of-mass energy of $\sqrt{s}$ =13 TeV corresponding to an integrated luminosity of 139 fb^{-1} is used. The measurements are performed using the method of profile likelihood unfolding (Section 4.3.3). The signal and background processes are estimated as described in Chapter 6. All systematic uncertainties from Chapter 7 are included in the final measurements. The strategy of this analysis is developed to improve the previous $t\bar{t}Z$ cross-section measurements [134]. For instance, a new approach to unfolding is used, the lepton selection is optimised and a deep neural network is applied to the event selection.

The PLU method replaces the previously used Iterative Bayesian Unfolding (IBU) [142] technique. There are several advantages to the PLU method. It is straightforward to combine multiple analysis regions (this was shown to reduce the experimental uncertainties in Chapter 8), channels or even analyses as long as the event selections are not overlapping. Uncertainties associated with background processes can be estimated directly in data without prior assumptions. Furthermore, systematic uncertainties are naturally included in the measurement as nuisance parameters of the likelihood function and can be constrained by fitting to the data. Finally, an implementation of the PLU in the `TRExFitter` framework [108] allows having a coherent analysis strategy for the measurements of the inclusive and differential cross-sections.

The measurements of the differential $t\bar{t}Z$ cross-section are performed by unfolding the detector-level quantities (Section 4.2.4) to particle-level. The particle-level quantities are defined using the Monte Carlo truth information after the hadronisation step in the event generation procedure (Section 4.2.2). This leaves final-state stable particles (leptons, photons and hadrons) with mean lifetime $> 30\,\text{ps}$, which are detector-independent estimates of physics processes. Leptons are required to be prompt, meaning they do not originate from decays of hadrons or (u, d, s, c, b) quarks. Four-momenta of photons which do not originate from hadrons and are within $\Delta R \leq 0.1$ from a muon or electron are added to the lepton momenta (lepton dressing). Jets are reconstructed using the anti-k_{T} algorithm with a radius parameter of $R = 0.4$ using all stable particles (Section 4.1.5), excluding the selected leptons and the associated photons as well as neutrinos originating from the Z boson or top-quark decays. A particle-level jet is identified as a b-jet using the ghost-matching procedure [143]. A ghost particle is a Monte Carlo simulated particle which is assigned an infinitesimal transverse momentum but leaving the angular information unchanged. The jet reconstruction procedure using the anti-k_{T} algorithm is repeated using the ghost particles as inputs instead of the previously used topo-clusters. The resulting jets of ghost particles contain particle-level information which can be matched with the jets above to identify particle-level b-jets. Finally, missing transverse energy is defined as a sum of the transverse momenta of all neutrinos which do not originate from hadron decays.

The MC event generation gives access to the full phase-space, however, the experimental setup of the ATLAS detector has limited coverage in terms of the geometrical acceptance or hardware and software performance. An attempt to extrapolate the experimental quantities to regions where the detector is not able to make any observa-

tions introduces model dependency to the measurement. Therefore, it is important to define a particle-level fiducial volume which is highly overlapping with the real detector and make measurements within that volume. Two variations of the particle-level fiducial volume for the three-lepton $t\bar{t}Z$ measurements are used in the upcoming discussion and will be defined where this is relevant.

The chapter is organised into sections, starting with the presentation of the study performed by the author to pick optimal criteria for the selection criteria of leptons (Section 9.2). Section 9.3 outlines the event selection at detector- and particle-levels which are used in the sections following it. Section 9.4 describes aspects of the techniques which are used to reconstruct top quarks as well as W and Z bosons in the three-lepton $t\bar{t}Z$ events. Section 9.5 motivates and defines the observables which are used in the measurements of the differential cross-section and discusses a study, which was performed by the author, aimed at defining histograms of the differential observables. Validation of the profile likelihood unfolding method is performed in Section 9.6 by the author to ensure the absence of bias. Finally, the author's measurements of the differential cross-section are presented and discussed in Section 9.7.

9.2 Optimisation of lepton identification and isolation

An in-depth study is performed to optimise lepton identification and isolation requirements for the differential cross-section measurements. The three-lepton $t\bar{t}Z$ channel is susceptible to the non-prompt lepton background which can be mitigated with an appropriate choice of the lepton identification and isolation requirements. The selection criteria associated with the lepton p_{T} thresholds may also be improved. However, there is a trade-off between high efficiency and increased background as the lepton p_{T} threshold is reduced. Therefore, the study aims to select optimal electron and muon identification and isolation working points, as well as test alternative lepton p_{T} selections.

Three electron identification (El ID), eight electron isolation (El Iso), and fourteen muon isolation (Mu Iso) WPs are considered in the study. Muon identification quality is kept at the `Medium` WP since that is the recommendation of the ATLAS collaboration and no gain is expected from a different WP. Table 9.3 summarises the available working points as well as the lepton p_{T} cuts. In the following text, a choice of an El ID,

Table 9.1: Summary of the available electron identification (El ID), isolation (El Iso) and muon isolation (Mu Iso) WPs as well as lepton p_{T} cuts which are tested in the optimisation analysis.

El ID	El Iso	Mu Iso	Lepton p_{T} cuts [GeV]
LooseAndBLayerLH	FCTight	PflowTight_FixedRad	27, 20, 20
MediumLH	FCLoose	PflowTight_VarRad	27, 20, 15
TightLH	FCHighPtCaloOnly	PflowLoose_FixedRad	27, 20, 10
	PLVTight	PflowLoose_VarRad	27, 15, 15
	PLVLoose	HighPtTrackOnly	27, 15, 10
	PLITight	TightTrackOnly_FixedRad	27, 10, 10
	PLIVeryTight	TightTrackOnly_VarRad	
	Gradient	Tight_FixedRad	
		Loose_FixedRad	
		Loose_VarRad	
		PLVTight	
		PLVLoose	
		PLITight	
		PLIVeryTight	

El Iso, Mu Iso and lepton p_{T} cuts is referred to as a *lepton definition*. A total of 2,016 different lepton definitions are possible.

The optimisation study is performed in two steps. First, a group of lepton definitions is pre-selected based on their performance with respect to a few basic metrics. This allows to significantly reduce the number of potential lepton definitions. In the second step, the differential cross-section is measured for each pre-selected definition. The expected uncertainties of these measurements are then used to assess the lepton definitions.

9.2.1 Pre-selected lepton definitions

The performance of each lepton definition can be reasonably estimated using a set of metrics, such as the $t\bar{t}Z$ signal yield (S), the total background yield (B), and the yield of the MC fake lepton background (F). The signal yield is important because differential measurements of the $t\bar{t}Z$ process are limited by statistics, as demonstrated in the

Table 9.2: The definitions of the three-lepton signal regions that are used in the optimisation of the lepton definitions analysis.

Variable	3ℓ-Z-$1b4j$	3ℓ-Z-$2b3j$
$N_\ell(\ell = e, \mu)$	$= 3$	
	≥ 1 OSSF pair with $\lvert m_{\text{OSSF}} - m_Z \rvert < 10\,\text{GeV}$	
	for all OSSF combinations $m_{\text{OSSF}} > 10\,\text{GeV}$	
$p_{\text{T}}(\ell_1, \ell_2, \ell_3)$	$\geq 27,\ [20, 15, 10],\ [20, 15, 10]\,\text{GeV}$	
N_{jets}	≥ 4	≥ 3
$N_{b-\text{jets}}$	≥ 1	≥ 2
$(b^{\text{1st}}_{\text{tag}}, b^{\text{2nd}}_{\text{tag}})$	$(= 60\%, \geq 70\%)$	$(\leq 70\%, \leq 70\%)$

previous analyses [134]. Additional metrics are derived to inform the pre-selection of lepton definitions better:

- Signal significance $\sigma = \text{S}/\sqrt{\text{B}}$.
- Modified signal significance $\sigma_{\text{F}} = \text{S}/\sqrt{\text{S} + \text{B} + (\text{F}/2)^2}$, which accounts for the uncertainty in the estimation of the fake lepton background from MC simulations. This is based on the previous inclusive cross-section measurement [134].
- Signal purity $\text{P} = \text{S}/(\text{S} + \text{B})$.

Each metric is calculated using the three-lepton $t\bar{t}Z$ events selected following the requirements of the inclusive cross-section measurement (Section 8.5). Two orthogonal signal regions, 3ℓ-Z-$1b4j$ and 3ℓ-Z-$2b3j$, are defined where the requirements for the p_{T} of leptons are modified for each lepton definition accordingly. Table 9.2 summarises this selection.

The baseline electrons are defined with the `MediumLH` identification and `FCTight` isolation WPs while muons are defined with the `Medium` quality and `PflowTight_FixedRad` isolation WPs. The lepton p_{T} cuts are set to 27, 20, 20 GeV. This definition is selected to match the previous measurements of the differential $t\bar{t}Z$ cross-section as closely as possible and is characterised by the S = 371.5, B = 185.2, F = 21.3, $\sigma = 27.3$, $\sigma_{\text{F}} = 14.4$ and P = 0.7 values. All options with a signal yield below the baseline value are rejected since the previous measurements were already limited by the statistics. The remaining options are further compared with the baseline definition to pre-select a reasonable

number of definitions. Table 9.3 summarises this pre-selection, where Definition 0 is the baseline option. Definition 1 has the largest signal yield, a relative increase of 68%, however, its modified signal significance is extremely low due to a very large fake lepton background. Definitions 2 and 3 are the best with respect to the signal significance, offering a large improvement in the yield of the signal events. However, the fake lepton background is increased by 85-130% relative to the baseline and the overall background is comparatively large. Definitions 4 and 5 are the best with respect to the modified signal significance, where up to 12% relative improvement in this metric is expected. Definition 6 is selected as the best with respect to purity, however other definitions are at the same or similar levels. Definition 7 vetoes the fake lepton background best and reduces it by 63% relative to the baseline. However, the signal yield is not expected to improve. Definition 8 is selected by first requiring that the fake lepton background is smaller than the baseline and vetoing all definitions which use a PLIV WP[1]. This definition is then picked from the remaining options which gives the highest increase in the signal yield. Lastly, Definitions 9-12 are additional choices based on discussions with the analysis team.

9.2.2 Expected performance of the pre-selected lepton definitions

The pre-selected lepton definitions are assessed by unfolding the associated distributions of the signal and background events with the PLU method. The expected precision of the differential cross-section is the main criterion used to select the optimal definition. The detector-level 3ℓ-Z-$1b4j$ and 3ℓ-Z-$2b3j$ signal regions are combined with the 3ℓ-WZ-CR control region from Section 8.3. The event selection requirements with respect to the lepton p_{T} thresholds are defined according to each pre-selected lepton definition. The normalisation factor for the $WZ + l$ background, $\mathcal{N}_{WZ+l}$, is measured in the fit thanks to the control region.

The differential cross-section is measured as a function of the transverse momentum of the Z boson, p_{T}^{Z}. It is defined by reconstructing a Z boson as a 4-momentum sum of a pair of OSSF leptons and the corresponding histogram is defined to have 7 bins with variable bin widths according to the previous measurement of the differential $t\bar{t}Z$ cross-section [134]. The definition of the fiducial volume closely matches the detector-level selection. Exactly three leptons with $p_{\mathrm{T}}(\ell_1, \ell_2, \ell_3) > 27, 20, 20\,\mathrm{GeV}$ are required.

[1] At the time of this study, the PLIV WPs were not calibrated.

Table 9.3: Definitions of lepton objects that are tested in the differential cross-section measurements. The following metrics are used to pre-select these lepton definitions: the signal yield (S), the total background yield (B), the yield of the MC fake lepton background (F), the signal significance (σ), the modified signal significance (σ_F) which takes into account a discrepancy in the MC fake lepton estimation, and the signal purity (P).

	El ID, El Iso, Mu Iso	$p_T(\ell_1, \ell_2, \ell_3)$	S	B	F	σ	σ_F	P
0.	MediumLH, FCTight, PflowTight_FixedRad	27, 20, 20	371.5	185.2	21.3	27.3	14.4	0.7
1.	LooseAndBLayerLH, FCLoose, Loose_VarRad	27, 10, 10	624.9	680.3	394.7	23.9	3.1	0.5
2.	LooseAndBLayerLH, PLVLoose, PLVLoose	27, 20, 15	496.2	273.7	49.1	29.9	13.4	0.6
3.	MediumLH, PLVLoose, PLVLoose	27, 15, 15	477.48	255.4	39.4	29.9	14.3	0.6
4.	LooseAndBLayerLH, PLITight, PLITight	27, 20, 15	415.6	201.0	13.7	29.3	16.1	0.7
5.	MediumLH, PLITight, PLITight	27, 15, 15	402.5	192.0	10.6	29.0	16.1	0.7
6.	LooseAndBLayerLH, PLITight, PLITight	27, 20, 20	378.3	177.4	9.5	28.4	15.7	0.7
7.	TightLH, PLITight, PLITight	27, 20, 15	372.5	174.9	7.9	28.2	15.7	0.7
8.	MediumLH, PLVLoose, PLVLoose	27, 20, 20	416.7	204.9	20.4	29.1	15.5	0.7
9.	MediumLH, PLVLoose, PLITight	27, 15, 15	444.7	227.1	26.6	29.5	15.3	0.7
10.	MediumLH, PLVTight, PLVLoose	27, 20, 15	432.4	220.2	24.9	29.1	15.2	0.7
11.	MediumLH, PLVTight, PLVTight	27, 20, 15	398.7	195.1	16.4	28.5	15.5	0.7
12.	MediumLH, PLVTight, PLVTight	27, 15, 15	399.9	196.3	16.8	28.6	15.5	0.7

At least one OSSF lepton pair with $|m_{\ell\ell} - m_Z| < 10\,\text{GeV}$ is required to be present. At least three jets with $p_T > 25\,\text{GeV}$ are required, including at least one ghost-matched b-jet.

The signal and background processes are modelled using MC simulations (Chapter 6), including the fake lepton background. This is considered to be a reasonable assumption for the purposes of this study since the absolute number of events cancels out when relative comparisons are made. The Asimov dataset corresponding to a total integrated luminosity of $139\,\text{fb}^{-1}$ is used in the estimations. A subset of the systematic uncertainties listed in Chapter 7 are included in the fit. An uncertainty of 50% is considered on the estimation of the fake lepton background [134] since different lepton definitions yield varying levels of this background. The amount of background contributions varies between the pre-selected lepton definitions in general, hence uncertainties on the cross-sections of the dominant background processes are applied too. The tZq background is assigned a 30% uncertainty while the $WZ + b$ and $WZ + c$ processes are assigned 50% and 30% uncertainties, respectively. Additionally, a reduced set of flavour-tagging uncertainties are included in the fit. In particular, the uncertainties associated with the first ten components of the b-, c- and light-flavour tagging scale factors are used. Finally, the pileup reweighting and the luminosity uncertainties are considered.

Table 9.4 is a summary of the differential measurements using each pre-selected lepton definition. The statistical and total uncertainties are shown for 3 of the 7 POIs as well as their averages. The baseline definition (Definition 0) has an average expected uncertainty of 21.0 % in each bin, where the statistical uncertainty contributes 19.0 % on average. The best performance is expected with Definition 2 where an average expected uncertainty of 19.5 % is estimated with the statistical uncertainty contributing 16.5 %. This corresponds to a relative improvement of 7 % and 13 % of the total and statistical uncertainties, respectively. Alternatively, Definition 3 is expected to have a relative improvement of 11 % with respect to the baseline definition and the total uncertainty is estimated at the same 19.5 % level as Definition 2. Definition 8 is closely related to Definition 3 and the main difference is in the lepton p_T thresholds. While Definition 3 tests loose 27, 15, 15 GeV lower bounds, Definition 8 is more conservative at the 27, 20, 20 GeV thresholds. The latter definition is expected to provide a reasonable improvement of 5.6 % in the statistical uncertainty and of 4.7 % in the total uncertainty with respect to the baseline configuration. The majority of the other definitions are estimated to have a total uncertainty up to 21 % with the statistical

uncertainty contributing up to 19 %. Only Definition 1 is estimated to have an overall poorer performance; it is expected to achieve a relative improvement of 8% in the statistical uncertainty, however, the associated total uncertainty deteriorates by 12% due to the large total and fake lepton backgrounds. In addition, this and the other definitions using the `LooseAndBLayerLH` electron identification WP are expected to underestimate the impact of the fake lepton background more significantly and should correspond to a larger assumed uncertainty than 50%. Therefore, all definitions using the `LooseAndBLayerLH` WP are not considered further. Similarly, all definitions including the `PLITight` WP are removed due to the lack of reasonable improvements over the other definitions.

As a result of this study the `MediumLH` electron identification, `PLVLoose` electron isolation and `PLVLoose` muon isolation working points are selected. These criteria correspond to Definitions 3 and 8. The lepton p_{T} thresholds are selected independently because those of Definition 3 are considered to be too loose while those of Definition 8 are too tight. These thresholds are set to 27, 20, 15 GeV by relaxing the third lepton p_{T} with respect to Definition 8. It is expected that this lepton definition will achieve a more reasonable signal acceptance in the final measurements thus improving statistical uncertainties. The backgrounds are not expected to increase significantly and therefore impacts of the systematic uncertainties should stay at a similar level to Definition 8.

9.3 Event selection

9.3.1 Detector-level selection

The final detector-level event selection and signal regions for the three-lepton $t\bar{t}Z$ differential cross-section measurements are presented in Table 9.5. The event preselection is based on the previous measurements and has several changes. A single requirement of at least one b-tagged jet is applied, where the `DL1r` b-tagging efficiency WP of 85% is used. At least 3 jets passing the $p_{\mathrm{T}} > 25$ GeV threshold are required in each event.

A deep neural network (DNN) classification model [144] is designed and trained to assign three labels to each event. The labels are defined as probabilities for an event to originate from $t\bar{t}Z$, tZq and WZ production, where tZq and WZ are domi-

Table 9.4: Summary of the expected differential cross-section uncertainties for each pre-selected lepton definition. The table lists statistical and total uncertainties of the POIs corresponding to the 1st, 4th and 7th bins of the particle-level distribution. The last two columns show average uncertainties of all POIs for each lepton definition.

	El ID, El Isol, Mu Isol, p_{T}	Bin 1 [%]		Bin 4 [%]		Bin 7 [%]		Avg. [%]	
		Stat.	Total	Stat.	Total	Stat.	Total	Stat.	Total
0.	MediumLH, FCTight, PflowTight_FixedRad, [27, 20, 20]	26.0	29.0	14.5	16.5	22.0	22.5	19.0	21.0
1.	LooseAndBLayerLH, FCLoose, Loose_VarRad, [27, 10, 10]	24.5	39.0	13.0	17.0	19.5	20.5	17.5	23.5
2.	LooseAndBLayerLH, PLVLoose, PLVLoose, [27, 20, 15]	22.0	26.5	13.0	15.5	21.0	21.0	16.5	19.5
3.	MediumLH, PLVLoose, PLVLoose, [27, 15, 15]	22.5	26.5	13.0	15.5	21.0	22.0	17.0	19.5
4.	LooseAndBLayerLH, PLITight, PLITight, [27, 20, 15]	24.0	27.0	13.5	15.5	21.5	23.0	18.0	20.0
5.	MediumLH, PLITight, PLITight, [27, 15, 15]	24.0	27.0	14.0	15.5	22.0	23.0	18.5	20.0
6.	LooseAndBLayerLH, PLITight, PLITight, [27, 20, 20]	25.0	28.0	14.5	16.5	22.0	23.0	19.0	20.5
7.	TightLH, PLITight, PLITight, [27, 20, 15]	25.5	28.0	14.5	16.5	22.5	23.5	19.0	21.0
8.	MediumLH, PLVLoose, PLVLoose, [27, 20, 20]	23.5	27.0	13.5	15.5	22.0	23.0	18.0	20.0
9.	MediumLH, PLVLoose, PLITight, [27, 15, 15]	23.0	27.0	13.5	15.5	21.0	22.0	17.5	20.0
10.	MediumLH, PLVTight, PLVLoose, [27, 20, 15]	25.0	28.0	14.5	16.5	22.0	23.0	19.0	20.5
11.	MediumLH, PLVTight, PLVTight, [27, 20, 15]	25.0	28.0	14.5	16.0	22.0	23.0	18.5	20.5
12.	MediumLH, PLVTight, PLVTight, [27, 15, 15]	25.0	28.0	14.5	15.5	22.0	23.0	18.5	20.5

Table 9.5: Definition of the three-lepton signal regions.

Variable	**Preselection**		
N_ℓ $(\ell = e, \mu)$	$= 3$		
	≥ 1 OSSF lepton pair with $\lvert m_{\ell\ell}^{Z} - m_Z \rvert < 10\,\text{GeV}$		
	for all OSSF combinations: $m_{\text{OSSF}} > 10\,\text{GeV}$		
$p_\text{T}\,(\ell_1, \ell_2, \ell_3)$	$> 27,\ 20,\ 15\,\text{GeV}$		
$N_\text{jets}\,(p_\text{T} > 25\,\text{GeV})$	≥ 3		
$N_{b-\text{jets}}$	$\geq$ 1@85%		
	SR-3L-ttZ	**SR-3L-tZq**	**SR-3L-WZ**
DNN-tZ output	< 0.43	≥ 0.43	—
DNN-diboson output	< 0.27	< 0.27	≥ 0.27
$N_{b-\text{jets}}$	—	—	$\geq$ 1@60%

nant background processes in the three-lepton regions. Figure 9.1 shows the event decompositions for output distributions of each discriminator. The impact of each input variables on each output label are shown in Figure 9.2. Overall, highly ranked variables are the transverse momentum of the leading jet ($\text{Jet}_1 p_\text{T}$), the sum of the transverse momenta of the leptons (H_T) and the leading b-tagging score (leading b-tag WP).

The pre-selected events are divided into three orthogonal regions according to the classification outputs of the DNN model and the signal sensitivity. The SR-3L-$t\bar{t}Z$ region is defined to contain events which are most probable to be $t\bar{t}Z$ while the SR-3L-tZq region contains events where the tZq DNN probabilities are largest. The SR-3L-WZ is similarly characterised to contain events predominantly classified as the WZ process. At least one b-tagged jet using the tightest 60% WP is required to enhance the $WZ + b$ background relative to the $WZ + l$ process in this region.

9.3.2 Particle-level selection

The three-lepton $t\bar{t}Z$ event selection at particle-level closely matches the detector-level selection. Exactly three leptons with $p_\text{T}(\ell_1, \ell_2, \ell_3) > 27,\ 20,\ 15\,\text{GeV}$ are required where

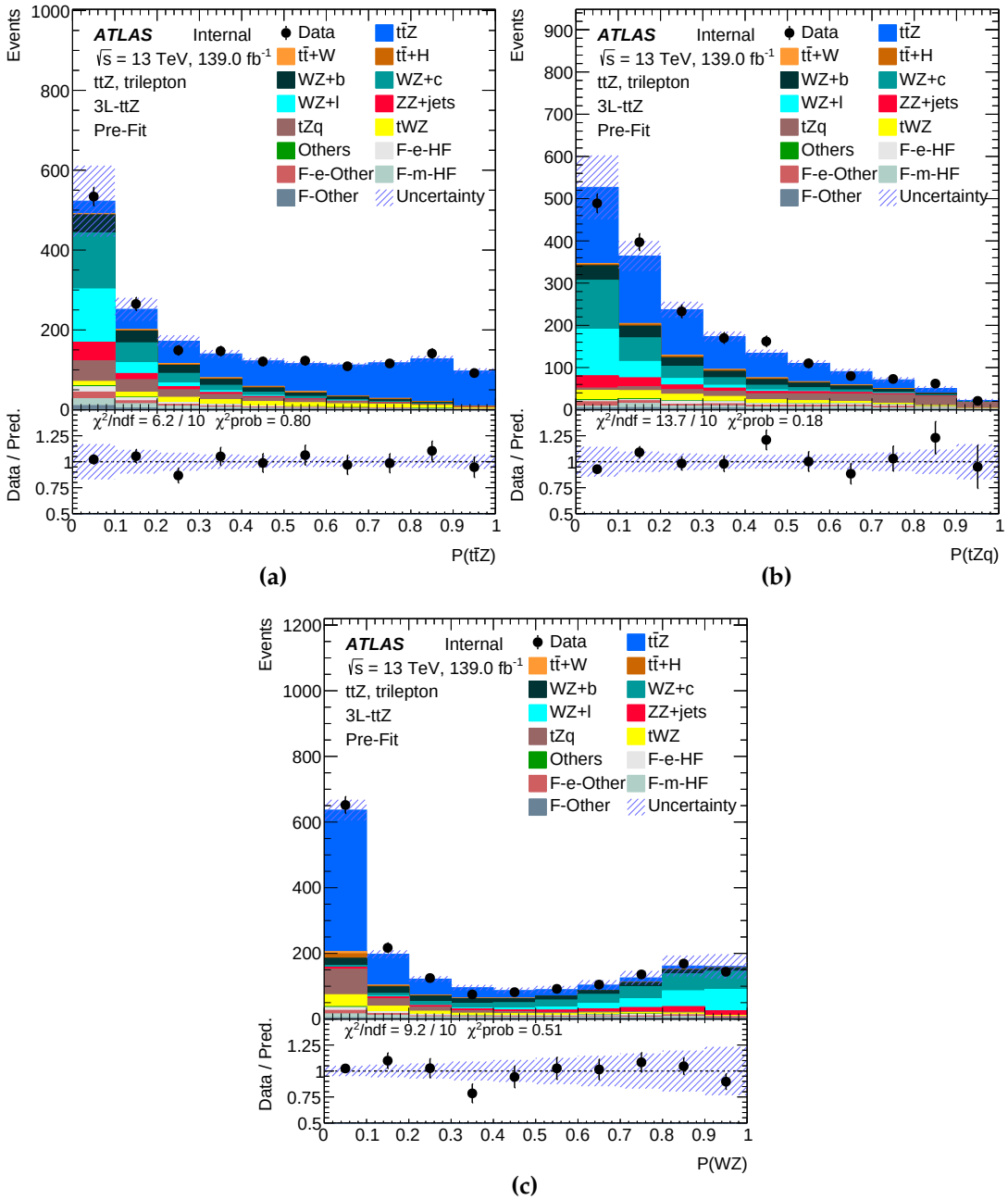

Figure 9.1: Distributions of the output discriminants.

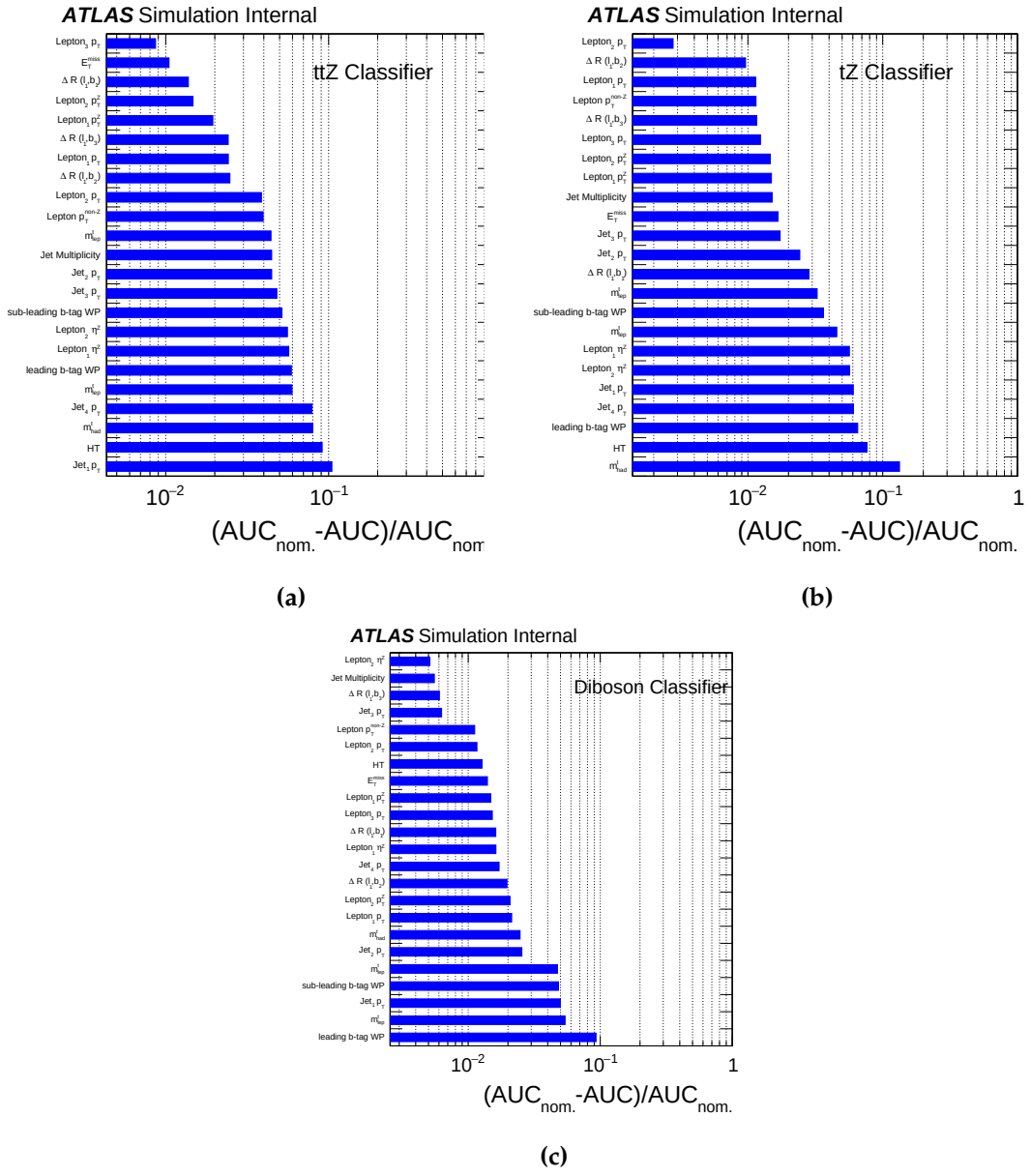

Figure 9.2: Ranking of the input variables by their importance in the DNN model for each output discriminant.

at least one OSSF lepton pair with $|m_{\ell\ell} - m_Z| < 10\,\text{GeV}$ is present. At least three jets with $p_\text{T} > 25\,\text{GeV}$ are required, including at least one ghost-matched b-hadron.

9.4 Event reconstruction

The measurements of the differential $t\bar{t}Z$ cross-section can be performed to explore the kinematics of the top quarks and the Z boson. A reconstruction algorithm is needed to associate the jets and leptons in the final states with the top quarks and the Z boson. The transverse momentum of the Z boson (p_T^Z) was introduced earlier which is trivially reconstructed as a 4-momentum sum of a pair of opposite-sign same-flavour leptons with a closely matching invariant mass to the Z boson. Other observables may be harder to define due to a more involved reconstruction procedure.

The three-lepton final state of the $t\bar{t}Z$ system features semi-leptonic $t\bar{t}$ decays. At leading order, one of the top quarks decays leptonically (leptonic top quark), $t \to bW \to b\ell\nu$, while the other is a hadronic top quark, $t \to bW \to bq'\bar{q}$. The $t\bar{t}$ system is reconstructed in two steps starting with the leptonic top quark reconstruction. The hadronic top quark reconstruction follows and is restricted by the results of the first step. Both reconstruction procedures are described below in more detail and apply to the detector- and particle-levels.

The reconstruction of the leptonic top quark requires knowledge of 4-momenta of the corresponding lepton, neutrino and b-jet. The information about the leptons and b-jets is available from the experimental setup, however, neutrinos escape undetected. The opposite-sign same-flavour lepton pair is selected first to reconstruct the Z boson. The remaining lepton is considered to be originating from a top quark. The `DL1r` flavour-tagging algorithm is used to identify the jets originating from b-hadron decays at detector-level (Section 9.3). At most two, leading and sub-leading (Section 8.4), b-tagged jets are considered in the event reconstruction. The ghost-matching procedure is used to identify jets originating from b-hadrons at particle-level, and the two highest p_T jets are considered. Information about neutrinos is not available at detector-level and an assumption is made that majority of the missing transverse energy in a three-lepton $t\bar{t}Z$ event is due to the neutrino. Therefore, the transverse momentum of the neutrino, p_T^ν, is approximated as E_T^miss and the associated azimuthal direction is considered to be the azimuthal angle of the missing transverse energy, ϕ^miss. This leaves the longitudinal momentum of the neutrino, p_z^ν, an unknown. A quadratic equation is

derived from the fact that the squared sum of the lepton and neutrino 4-momenta should be equal to the squared invariant mass of the W boson, 80.379 GeV [10]:

$$A\left(p_z^\nu\right)^2 + B\left(p_z^\nu\right) + C = 0, \tag{9.1}$$

where A, B and C depend on the measured lepton- and MET-kinematic quantities. The p_z^ν is found from the discriminant ($\Delta = B^2 - 4AC$) of the quadratic equation. If no real solution exists ($B^2 < 4AC$), the $E_{\mathrm{T}}^{\mathrm{miss}}$ can be decreased in steps of 100 MeV until a single solution for p_z^ν is found. This is done analytically by solving another quadratic equation which yields $B^2 = 4AC$. The leptonic top quark is reconstructed by combining the $\ell\nu$ pair (or pairs if two solutions for p_z^ν exist) with a b-jet. The b-jet which gives the smallest $\Delta R(\ell\nu, b\text{-jet})$ separation is selected. Finally, if two real p_z^ν solutions exist (which result in two leptonic top quark reconstruction options), the reconstructed top quark masses ($m_{b\ell\nu}$) are evaluated using an idealised $m_{b\ell\nu}$ distribution. This distribution is defined from the simulation data and represents a perfect reconstruction of the top quarks. An interpolation procedure is performed to assign an output weight for the two reconstructed leptonic top quarks, and the one with the higher weighting is selected [134].

Hadronic top quarks are reconstructed from a hadronically decaying W and a b-jet. The reconstruction is trivial for events with three jets in total. In such cases, either the second b- or one of the light-jets is considered to be out of the acceptance and the top quark is reconstructed from the remaining jets. In a more general case of events with at least four jets, invariant masses of pairs of light-jets are interpolated using a reference distribution and a multi-hypothesis test is applied to determine the most compatible pair of jets with the W boson.

9.5 Differential cross-section observables

The differential cross-section measurements are performed with respect to eight observables which are defined in Table 9.6. In addition to probing the $t\bar{t}Z$ production vertex, these observables are also suitable to test the modelling of MC generators and are sensitive to new physics effects.

Table 9.6: Summary of the observables used for the differential cross-section measurement.

Variable	Definition
p_{T}^{Z}	Transverse momentum of the Z boson; [GeV].
$\lvert y^{Z}\rvert$	Absolute rapidity of the Z boson.
$\cos(\theta_{Z}^{\star})$	Angle between the direction of the Z boson in the detector reference frame and the direction of the negatively charged lepton in the rest frame of the Z boson.
N_{jets}	Number of selected jets with $p_{\mathrm{T}} > 25\,\mathrm{GeV}$ and $\lvert\eta\rvert < 2.5$.
$H_{\mathrm{T}}^{\mathrm{leps}}$	Sum of the transverse momenta of all the signal leptons; [GeV].
$\lvert\Delta\phi(Z, t_{\mathrm{lep}})\rvert$	Absolute azimuthal separation between the Z boson and the top (anti-top) quark featuring the $W \to \ell\nu$ decay; [rad/π].
$\lvert\Delta y(Z, t_{\mathrm{lep}})\rvert$	Absolute rapidity difference between the Z boson and the top (anti-top) quark featuring the $W \to \ell\nu$ decay.
$p_{\mathrm{T}}^{\ell,\text{non-}Z}$	Transverse momentum of the lepton which is not associated with the Z boson; [GeV].

As already established, the $t\bar{t}Z$ process is a rare phenomenon with low available statistics. It is therefore necessary to carefully select a definition of the histograms associated with each observable. The histograms are defined in terms of the number of bins and their widths. The following text will refer to such a choice as a *binning*. In general, the largest number of bins is desired that can sustain reasonable statistical uncertainties and a stable unfolding procedure. The latter can be expected if a given binning yields a diagonal migration matrix.

A two-step procedure has been established to choose a binning for each observable individually. In the first step, an automated algorithm is used to study the observables and propose several options of binnings for each of them. The algorithm is carried over from the previous measurements of the $t\bar{t}Z$ differential cross-section and is documented in Refs. [145, 122]. The Iterative Bayesian Unfolding procedure is used to estimate the differential cross-section in the signal region enhanced with the $t\bar{t}Z$ events (SR-3L-$t\bar{t}Z$) only. The Asimov dataset is unfolded and the resulting statistical uncertainties are required to be below 30% for a binning to be viable.

The second step of the binning procedure validates the proposed solutions from the first step using the profile likelihood unfolding method. The likelihood function includes all three signal regions, SR-3L-$t\bar{t}Z$, SR-3L-tZq and SR-3L-WZ, as well as the control regions enhanced in the fake lepton background (Section 6.2.2). The nuisance

parameter associated with the $WZ + b$ background process is set to be a free parameter, $\mathcal{N}_{WZ+b}$, in the fit along with the $\mathcal{N}_{\text{F-}e\text{-HF}}$, $\mathcal{N}_{\text{F-}e\text{-Other}}$ and $\mathcal{N}_{\text{F-}\mu\text{-HF}}$ normalisation factors of the fake lepton background. All systematic uncertainties are included in the likelihood function except from the theoretical CKKW, QSF and CSSKIN uncertainties of the diboson samples. The Asimov dataset which corresponds to a total integrated luminosity of $139\,\text{fb}^{-1}$ is used to measure the expected performance. The diagonality of each migration matrix and the expected uncertainties are assessed to make the final decision.

Table 9.7 is a summary of the selected binnings for the differential observables. The table also shows averaged diagonal migration matrix elements and averaged total uncertainties of the POIs. The averaging of the migration matrices is done across all three signal regions to account for the less populated SR-3L-tZq and SR-3L-WZ regions. The number of bins for the N_{jets} observable is limited by the fact that the three-lepton $t\bar{t}Z$ system is characterised with 4 jets at leading order. A higher count of jets is possible and is included in the last two bins with up to 10 jets in total. A reasonable binning solution is not possible with a larger number of bins. The 5- and 6-bin histograms are selected for the $|\Delta y(Z, t_{\text{lep}})|$ and $|\Delta\phi(Z, t_{\text{lep}})|$ observables, respectively. These observables are limited by resolution as reflected in the corresponding migration matrices which show a degree of non-diagonality. Approximately 65% of the events are found in the diagonal elements of the migration matrices for the $|\Delta y(Z, t_{\text{lep}})|$ observable on average and 64% for the $|\Delta\phi(Z, t_{\text{lep}})|$ observable. However, the total uncertainties are expected to be well below the 30% mark and, therefore, these binnings are considered reasonable. The $p_{\text{T}}^{\ell,\text{non-}Z}$ observable is similarly limited in resolution, especially at low p_{T}. The 5-bin solution is obtained by reducing the granularity of a 6-bin histogram in this low-energy range. The 8-bin configuration of the p_{T}^{Z} observable is achieved by manually adjusting the last three bins provided by the automated algorithm from the first step. The adjustment is done to add an extra bin at high-p_{T} in order to achieve better sensitivity in this range where new physics effects can be expected. The remaining histograms of observables are expected to yield highly diagonal migration matrices (above 90%) with the associated total uncertainties smaller than 20%. The $|y^{Z}|$ observable has the most diagonal migration matrices and can be associated with a 9-bin histogram.

Table 9.7: Final bin ranges of the histograms associated with each differential observable. The <MMs> column shows the average value of the diagonal migration matrix element across the three signal regions for each observable. The <Tot. unc.> column shows the average total uncertainty of all POIs for each observable.

Observable	Bins	Bin Ranges	<MMs>	<Tot. unc.>
p_{T}^{Z} [GeV]	8	[0, 60, 100, 140, 180, 230, 280, 350, 1000]	92%	18.8%
$\lvert y^{Z}\rvert$	9	[0, 0.125, 0.275, 0.425, 0.6, 0.775, 0.95, 1.175, 1.45, 2.5]	96%	17.6%
$p_{\mathrm{T}}^{\ell,\text{non-}Z}$ [GeV]	5	[0, 35, 55, 80, 120, 500]	94%	14.9%
$\lvert\Delta y(Z, t_{\mathrm{lep}})\rvert$	5	[0, 0.25, 0.6, 1.05, 1.55, 5]	65%	22.1%
$\lvert\Delta\phi(Z, t_{\mathrm{lep}})\rvert$ [rad/π]	6	[0, 0.16, 0.44, 0.66, 0.82, 0.93, 1]	64%	23.7%
$H_{\mathrm{T}}^{\mathrm{leps}}$ [GeV]	8	[50, 130, 165, 195, 230, 275, 330, 405, 800]	92%	18.4%
N_{jets}	4	[2.5, 3.5, 4.5, 5.5, 10.5]	63%	22.0%
$\cos\theta_{Z}^{*}$	8	[-1, -0.75, -0.5, -0.25, 0, 0.25, 0.5, 0.75, 1]	92%	18.0%

9.6 Validation of the unfolding method

Three validation tests are presented in the current section. They check if the PLU application to the measurements of the $t\bar{t}Z$ differential cross-section is unbiased and gives a reliable estimate of the true distribution. For each test, the systematic uncertainties are not included in the model.

9.6.1 Bias due to the dataset

The closure test validates that the unfolding procedure is able to recover the underlying physics of a statistically independent dataset. The nominal MC signal sample is split into two independent datasets pseudo-randomly. The splitting is based on the event ID number where even and odd numbers are separated into training and testing datasets. The training dataset is used to derive the response matrix while the testing dataset is considered to be the pseudo-data which is unfolded. The test is evaluated by comparing the closure of the unfolded distribution to the particle-level distribution of the testing dataset. This is done by measuring and comparing χ^2 between the unfolded data and the particle-level distributions of the training and testing datasets. The test is passed if the χ^2 of the testing dataset is smaller than that of the training dataset.

The results of the test are shown in Figures 9.3 and 9.4 where each observable is unfolded to particle-level. The brown line is the particle-level distribution of the training sample. As expected, minor fluctuations are introduced to the particle-level distributions of the testing sample, which is considered to be the true distribution, shown by the pink line. The PLU method is unbiased if the unfolded data is in a reasonable agreement with the corresponding true distribution. The unfolded data of each observable show minor deviations from its true distribution. This can be seen in the ratio of prediction-to-data plots where the differences are contained within 5% for most observables, and up to 10% for the $|\Delta\phi(Z, t_{\text{lep}})|$ observable. In all cases, the deviations are negligible with respect to the expected statistical uncertainties. Table 9.8 shows the χ^2 agreement (Section 4.3.4) between the unfolded distribution and each particle-level distribution where only the statistical uncertainties of the datasets are considered. Better agreement is seen between the unfolded test data and the particle-level distribution of the test sample than between the unfolded test data and the particle-level distribution of the training sample. Therefore, the closure test is passed showing no significant bias in the PLU estimator.

Table 9.8: Summary of the χ^2 agreement between the unfolded data and the particle-level distributions of the training and testing samples used in the closure test.

Observable	Train χ^2	Test χ^2
$\cos(\theta^{\star}_{Z})$	0.097	0.046
$\lvert\Delta\phi(Z, t_{\text{lep}})\rvert$	0.188	0.120
$\lvert\Delta y(Z, t_{\text{lep}})\rvert$	0.064	0.029
N_{jets}	0.081	0.037
$p_{\text{T}}^{\ell,\text{non-Z}}$	0.074	0.043
$H_{\text{T}}^{\text{leps}}$	0.135	0.078
$\lvert y^{Z}\rvert$	0.122	0.045
p_{T}^{Z}	0.096	0.062

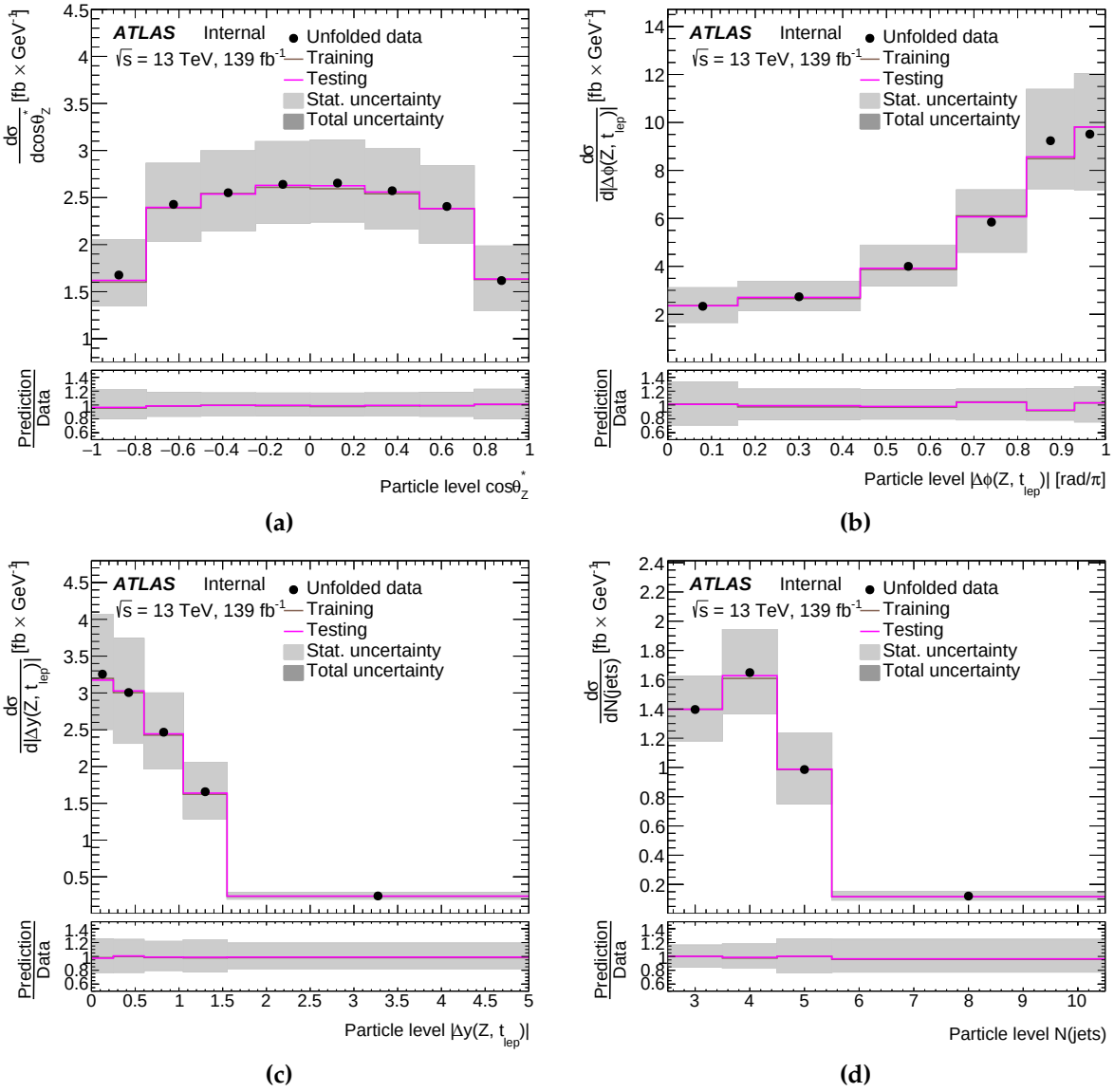

Figure 9.3: Results of the closure test for the (a) $\cos(\theta^{\star}_{Z})$, (b) $|\Delta\phi(Z, t_{\text{lep}})|$, (c) $|\Delta y(Z, t_{\text{lep}})|$ and (d) N_{jets} observables. The distribution in pink corresponds to particle-level of the unfolded dataset and the brown line shows particle-level of the dataset used to derive unfolding corrections. The bottom panel shows ratios between the particle-level distribution of the training and testing datasets with the unfolded data, respectively.

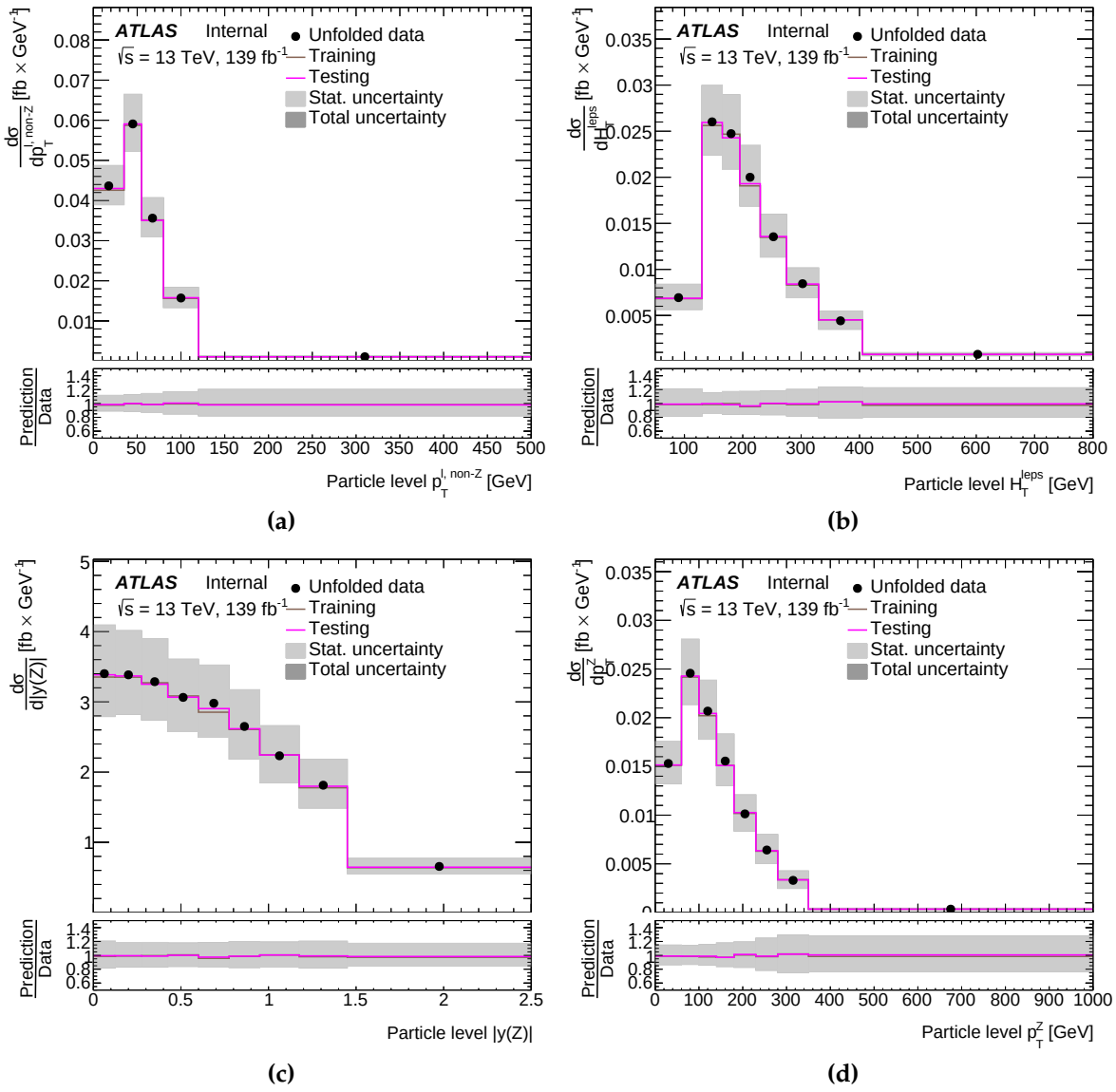

Figure 9.4: Results of the closure test for the (a) $p_{\mathrm{T}}^{\ell,\text{non-}Z}$, (b) $H_{\mathrm{T}}^{\text{leps}}$, (c) $|y^{Z}|$ and (d) N_{jets} observables. The distribution in pink corresponds to particle-level of the unfolded dataset and the brown line shows particle-level of the dataset used to derive unfolding corrections. The bottom panel shows ratios between the particle-level distribution of the training and testing datasets with the unfolded data, respectively.

9.6.2 Bias due to statistical fluctuations

A validation test is performed to ensure that the PLU method is not biased by statistical fluctuations in the dataset. The ability of PLU to recover the true distribution and to correctly estimate statistical uncertainties are validated. This test relies on the Monte Carlo pseudo-experiments. Initially, the unfolding corrections are derived from the full nominal MC signal sample and the nominal Asimov dataset is unfolded. This is followed by a series of pseudo-experiments where a Poisson distribution is used to smear the nominal Asimov dataset. For each detector-level bin, a Poisson distribution is defined with the mean value set to the expected number of events in that bin of the nominal distribution. Random values from the corresponding distributions are sampled and used to create a smeared pseudo-dataset. Finally, the nominal unfolding corrections are used to unfold the smeared dataset and the estimated values for each POI are saved. Such pseudo-experiments are repeated 5,000 times and the test is evaluated by comparing the nominal results with the averaged outcomes of all pseudo-experiments.

The estimated POIs of the pseudo-experiments are summarised in histograms such as those for the unfolding validation of the p_{T}^{Z} distribution in Figure 9.5. The distribution of POIs corresponding to Bin 2 (high-statistics bin) is shown in Figure 9.5a, Bin 5 (medium-statistics bin) in Figure 9.5b and Bin 8 (low-statistics bin) in Figure 9.5c. The high- and medium-statistics bins are approximately Gaussian (shown in red line) centred around 1 while the distribution in the low-statistics bin is slightly skewed compared to a Gaussian distribution. This is an expected feature since the Poisson distribution is asymptotically equivalent to the Gaussian only at large numbers of events. The Gaussian fit is performed for visualisation purposes and is not used to evaluate the pseudo-experiments with respect to the initial nominal unfolding.

The test is evaluated by checking the agreement of the mean of the pseudo-experiments in each bin ($\mu^{i}_{\mathrm{fitted}}$) with the value of 1. PLU ability to accurately estimate the statistical uncertainties is evaluated by comparing the root-mean-squared error of the pseudo-experiments for each POI ($\sigma^{i}_{\mathrm{fitted}}$) with the uncertainties estimated in the nominal unfolding. The results of the pseudo-experiments are summarised in Figure 9.6. Minor deviations of the mean values from 0 are observed for each observable. This is attributed to low statistics associated with the $t\bar{t}Z$ system which is a limiting factor in general. The estimations of statistical uncertainties in the pseudo-experiments are in good agreement with the nominal values for all observables. Therefore, no

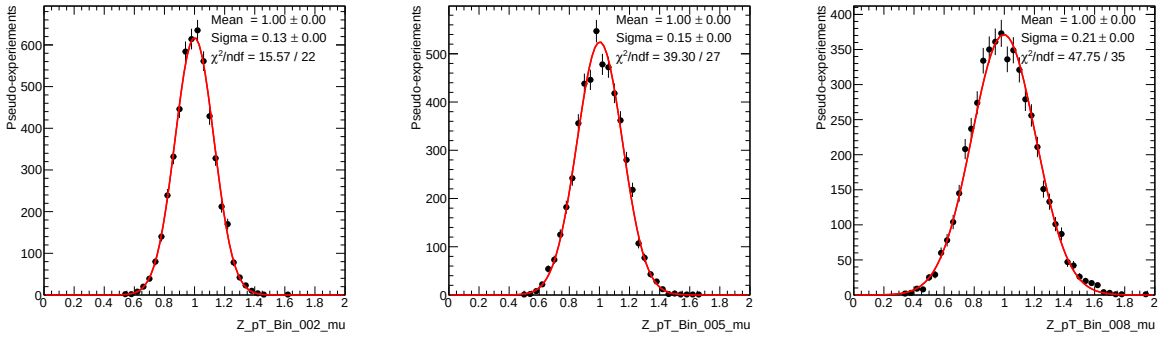

(a) POI: Bin 2 **(b)** POI: Bin 5 **(c)** POI: Bin 8

Figure 9.5: Distributions of pseudo-experiments for the second, fifth and eight bins of the p_{T}^{Z} distribution.

significant bias is observed in the validation and the PLU method is considered to pass the test.

9.6.3 Bias due to the model

The last test, referred to as the stress test, aims to verify that the unfolding technique is not biased by the shape of the distribution used to derive the unfolding corrections. While the modelling uncertainties of the nominal MC event generator are covered by the theoretical systematic uncertainties in Chapter 7, the stress test validates the statistical aspect. For example, new physics phenomena are expected to modify the high-energy spectrum. Given a p_{T}^{Z} distribution, this would appear as an excess in the unfolded distribution at high-p_{T} of the Z boson with respect to the particle-level distribution modelled by the MC generator. Hence, a change in the shape of the distribution. Therefore, it is essential to confirm that the PLU is able to recover the true underlying distribution in the experimental data.

The test is performed by re-weighting the nominal signal prediction both at detector- and particle-levels using a linear function $f(x)$, where x is a measured observable at particle-level. We perform a stress test where f is a function of p_{T}^{Z}:

$$f(p_{\mathrm{T}}^{Z}) = 1 + p_{\mathrm{T}}^{Z} \cdot k. \tag{9.2}$$

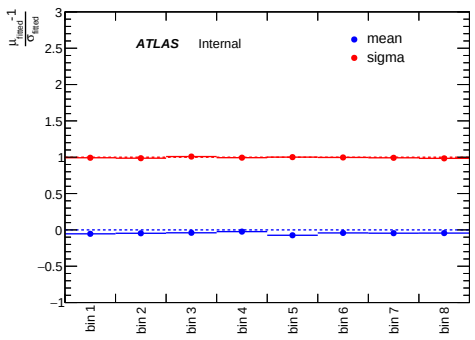

(a) $\cos(\theta^{\star}_{Z})$

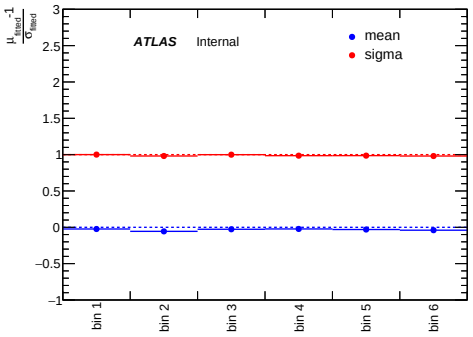

(b) $|\Delta\phi(Z, t_{\text{lep}})|$

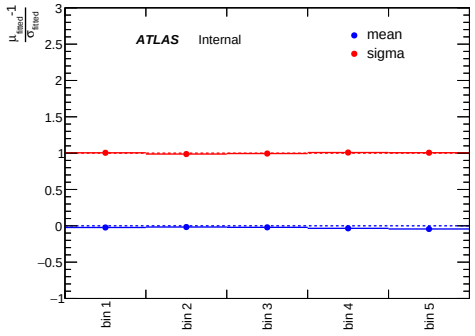

(c) $|\Delta y(Z, t_{\text{lep}})|$

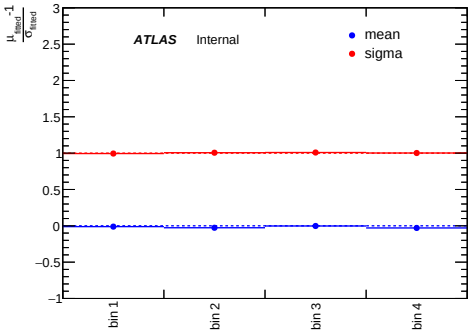

(d) N_{jets}

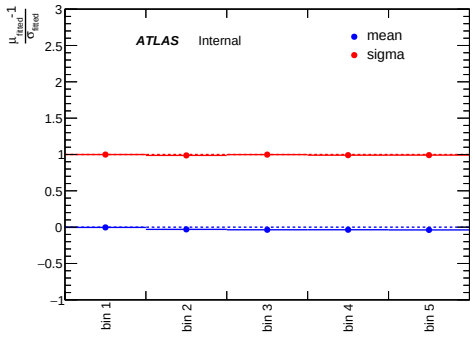

(e) $p_{\text{T}}^{\ell,\text{non-}Z}$

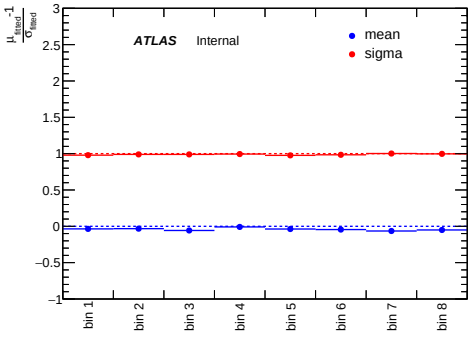

(f) $H_{\text{T}}^{\text{leps}}$

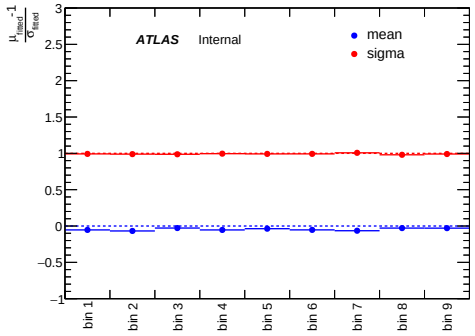

(g) $|y^{Z}|$

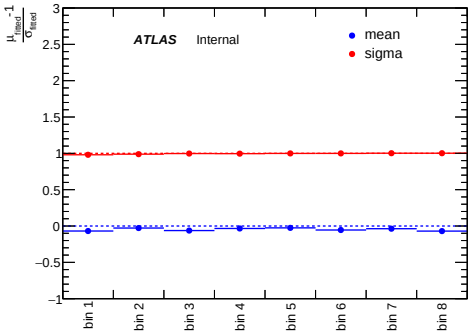

(h) p_{T}^{Z}

Figure 9.6: Summary of the validation using 5,000 pseudo-experiments for each observable. Blue markers indicate the arithmetic mean of the pseudo-experiments compared to the nominal measurements of the POIs using the Asimov data. Red markers are RMS errors of pseudo-experiments relative to statistical uncertainties of the nominal unfolding.

The parameter k is a constant that tunes the strength of the weight at high p_{T} and can be adjusted to change the strength of the test. Values of k are selected so that the events with $p_{\mathrm{T}}^{Z} = 1000\,\mathrm{GeV}$ receive an additional 0.75, 1.50 or 2.00 weight. The weights are chosen to be deliberately large to demonstrate that the procedure is unbiased even in extreme cases. This results in three different testing samples where a reduction in the $t\bar{t}Z$ signal is emulated in the first case. The remaining two testing samples emulate an increase in the signal at high p_{T} range by up to 50% and 100% with respect to the nominal sample. A pseudo-data sample is built by combining each re-weighted signal sample with the background samples. The unfolding corrections needed for the response matrix are derived from the nominal signal sample without the $f(p_{\mathrm{T}}^{Z})$ re-weighting. The pseudo-data is then unfolded and the stress test is assessed by comparing the unfolded pseudo-data with the re-weighted particle-level distribution. The results of the stress test of PLU using the p_{T}^{Z} distribution at particle-level are summarised in Figure 9.7. As for the closure test, the stress test is passed if the unfolded pseudo-data is in agreement with the corresponding particle-level distribution, shown as the pink line. The stress test is passed at all three strengths of re-weighting for the p_{T}^{Z} observable. The expected precision of the measurement is sufficiently high to discern the particle-level distribution of the $f(p_{\mathrm{T}}^{Z} = 1000\,\mathrm{GeV}) = 2.00$ testing sample from that of the nominal training sample, and the stress test is considered to be reasonably strong to be conclusive.

The remaining observables are unfolded to particle-level using the same three re-weighted pseudo-data samples. Results for each remaining observable are shown in Figures 9.8 and 9.9. Only the unfolded distributions using the strongest re-weighting are displayed. The unfolded pseudo-data is seen to have minor deviations from the associated particle-level shape which are significantly smaller than the expected statistical uncertainties. Table 9.9 summarises the stress test results in terms of the χ^2 agreement between the unfolded pseudo-data and the corresponding re-weighted particle-level distribution for each observable. Low values of χ^2 indicate that the underlying distribution is recovered successfully. Therefore, any potential bias is found to be negligible and the stress tests for each observable are considered to be passed.

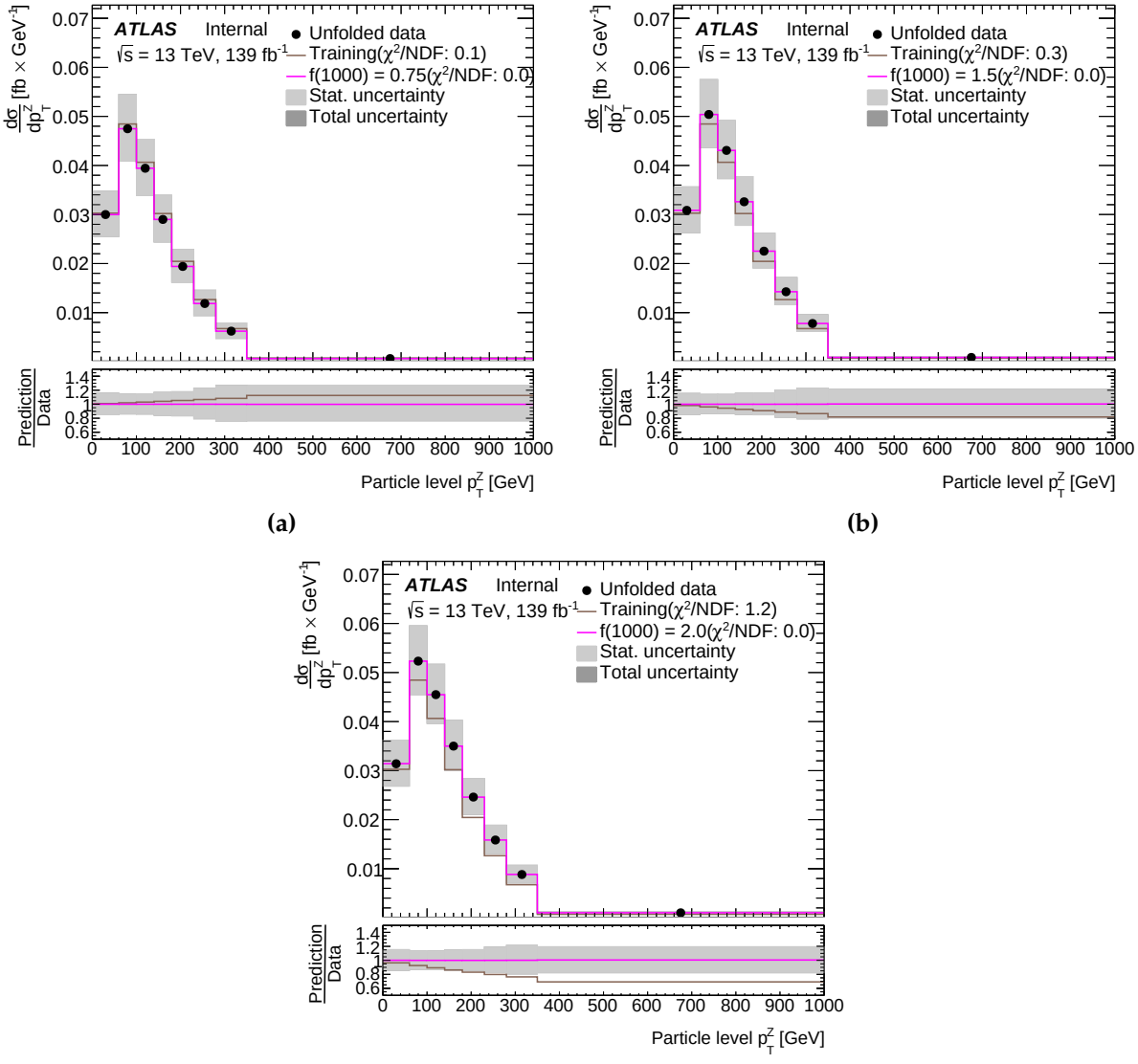

Figure 9.7: Summary of the stress tests where the p_{T}^{Z} observable is unfolded using the pseudo-data that was re-weighted using the particle-level p_{T}^{Z} distribution. Three values of linear scale factors are used: (a) 0.75, (b) 1.50 and (c) 2.00 for events with $p_{\mathrm{T}}^{Z} = 1000\,\mathrm{GeV}$.

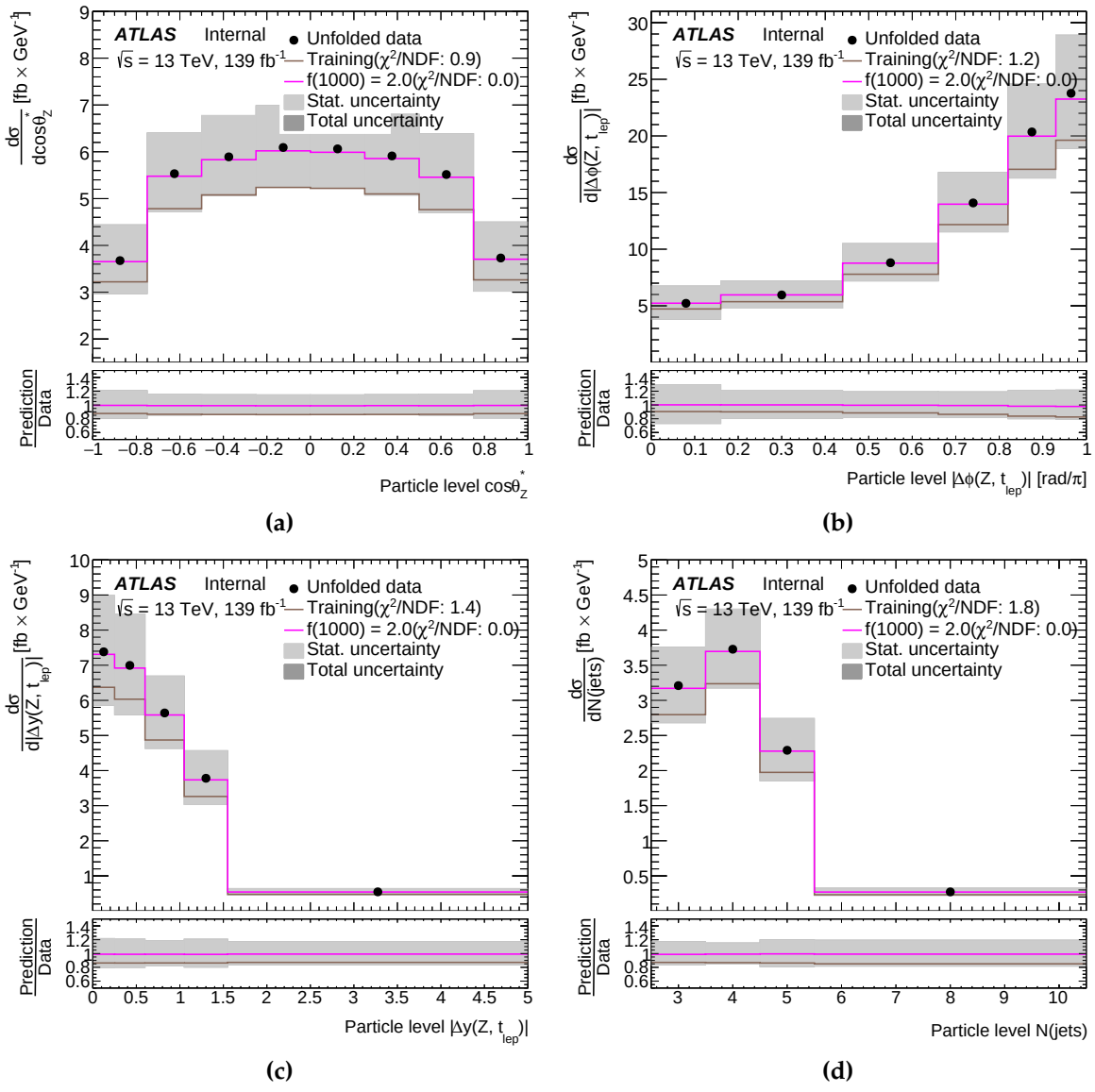

Figure 9.8: Summary of the stress tests where the (a) $\cos(\theta^{\star}_{Z})$, (b) $|\Delta\phi(Z, t_{\text{lep}})|$, (c) $|\Delta y(Z, t_{\text{lep}})|$ and (d) N_{jets} observables are unfolded using the pseudo-data that was re-weighted using the particle-level p^{Z}_{T} distribution. The strengths of re-weighting are set to up to 100% increase for events with $p^{Z}_{\text{T}} = 1000\,\text{GeV}$.

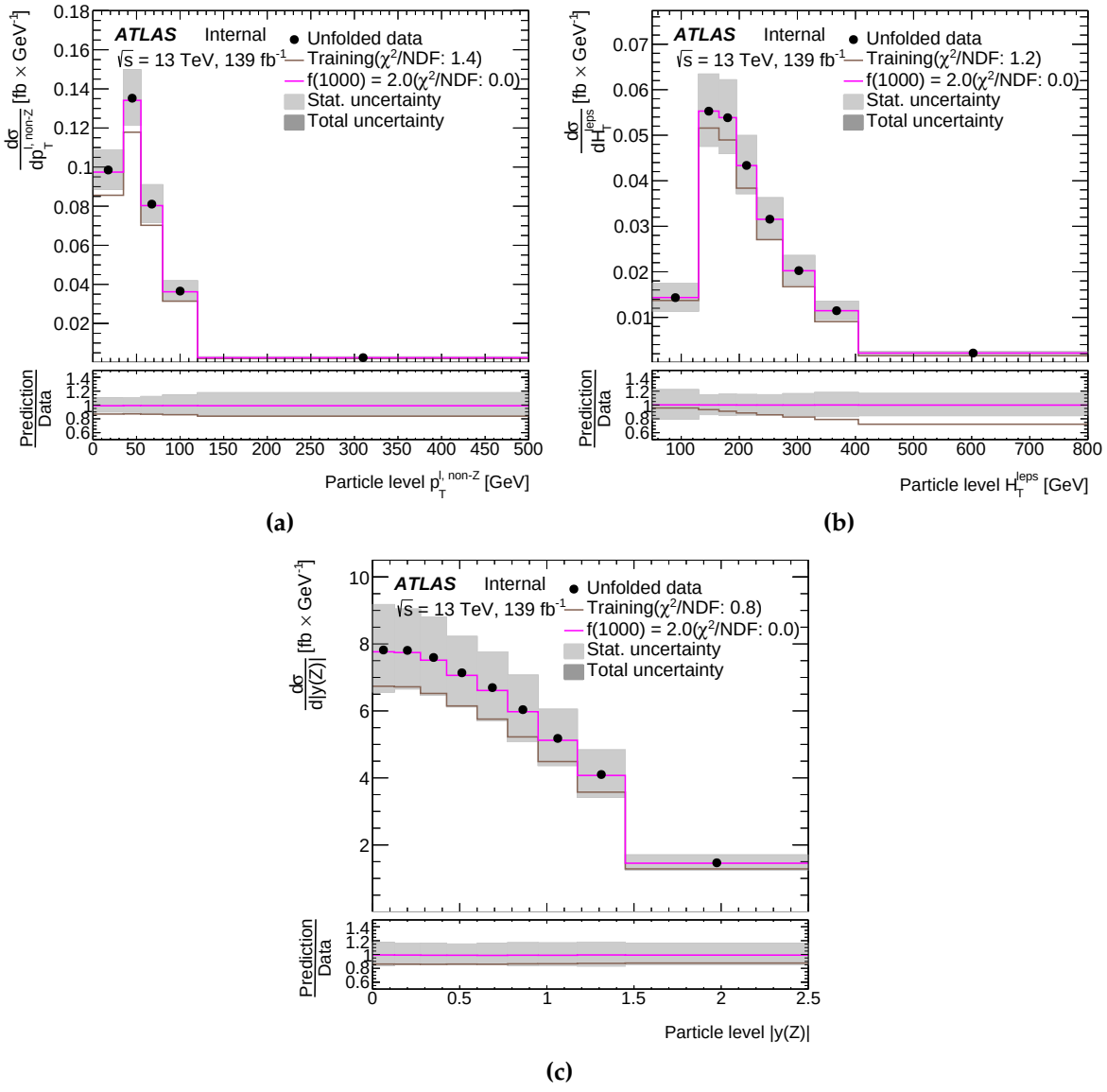

Figure 9.9: Summary of the stress tests where the (a) $p_{\mathrm{T}}^{\ell,\text{non-}Z}$, (b) $H_{\mathrm{T}}^{\text{leps}}$and (c) $|y^{Z}|$ observables are unfolded using the pseudo-data that was re-weighted using the particle-level p_{T}^{Z} distribution. The strengths of re-weighting are set to up to 100% increase for events with $p_{\mathrm{T}}^{Z} = 1000\,\mathrm{GeV}$.

Table 9.9: Summary of the χ^2 agreement between the unfolded pseudo-data and the particle-level distributions of the re-weighted samples used in the stress test. Only the statistical uncertainty of the dataset is considered.

Observable	-25%	+50%	+100%
p_{T}^{Z}	0.0001	0.0002	0.0008
$\cos(\theta_{Z}^{\star})$	0.0031	0.0108	0.0403
$\lvert\Delta\phi(Z, t_{\mathrm{lep}})\rvert$	0.0041	0.0146	0.0539
$\lvert\Delta y(Z, t_{\mathrm{lep}})\rvert$	0.0031	0.0110	0.0407
N_{jets}	0.0023	0.0076	0.0283
$p_{\mathrm{T}}^{\ell,\text{non-}Z}$	0.0029	0.0097	0.0363
$H_{\mathrm{T}}^{\mathrm{leps}}$	0.0000	0.0001	0.0003
$\lvert y^{Z}\rvert$	0.0028	0.0099	0.0372

9.7 Observed results

The measurements of the differential $t\bar{t}Z$ cross-section are performed by combining the three-lepton signal regions (Section 9.3) and the fake-lepton control regions (Section 6.2.2) using the profile likelihood unfolding method. The normalisation factors associated with the $WZ + b$, Fakes-e-HF, Fakes-μ-HF and Fakes-e-Other processes, $\mathcal{N}_{WZ+b}$, $\mathcal{N}_{\text{F-}e\text{-HF}}$, $\mathcal{N}_{\text{F-}\mu\text{-HF}}$, $\mathcal{N}_{\text{F-}e\text{-Other}}$, respectively, are free parameters. The full model of systematic uncertainies is included in the measurement (Chapter 7). The majority of the systematic uncertainies affect both the signal and background processes; they are assumed to be correlated across the processes.

The corrections of the selection efficiency for each observable in each signal region are shown in Figures 9.10, 9.11 and 9.12. The average scale of these corrections are $\approx 30\,\%$ in the SR-3L-$t\bar{t}Z$ region, $\approx 10\,\%$ in the SR-3L-tZq region and $\approx 3\,\%$ in the SR-3L-WZ region. The scale of the efficiencies is generally low across all regions due to detection inefficiencies, such as the reconstruction of leptons or b-tagging. The variation of the average efficiency between the signal regions is a reflection of the amount of the signal events in each detector-level region. Efficiency distributions of the p_{T}^{Z}, $p_{\text{T}}^{\ell,\text{non-}Z}$ and $H_{\text{T}}^{\text{leps}}$ observables are seen to have similar "ramp-up and plateau" shapes in the SR-3L-$t\bar{t}Z$ and SR-3L-WZ regions while the shape is inverted in the SR-3L-tZq region. The N_{jets} observable is characterised by a similar shape in the SR-3L-$t\bar{t}Z$ region while the SR-3L-tZq and SR-3L-WZ regions show efficiency reduction with the increasing number of jets. In both cases, this is attributed to the performance of the DNN selection. It tends to classify the high-p_{T} and high jet multiplicity events to the SR-3L-$t\bar{t}Z$ region over the SR-3L-tZq region where a low number of such events is expected. The remaining observables show approximately flat distributions of efficiencies.

The detector acceptance corrections for each observable are shown in Figures 9.13, 9.14 and 9.15. The scale of the acceptances is generally high, in the range from 75% to 92%, because the fiducial volume is defined to be similar to the detector selection. The mean scale of acceptances in the SR-3L-$t\bar{t}Z$ region tends to the 90% mark while the SR-3L-tZq and SR-3L-WZ are characterised by 80% acceptances approximately. The most significant shape variation is seen for the N_{jets} observable where the acceptance is relatively lower for events with three jets and quickly ramps up for a higher count of jets. The event selection at both particle- and detector-levels require that all jets pass the $p_{\text{T}} > 25\,\text{GeV}$ threshold. Particle-level events with a lower count of jets which pass

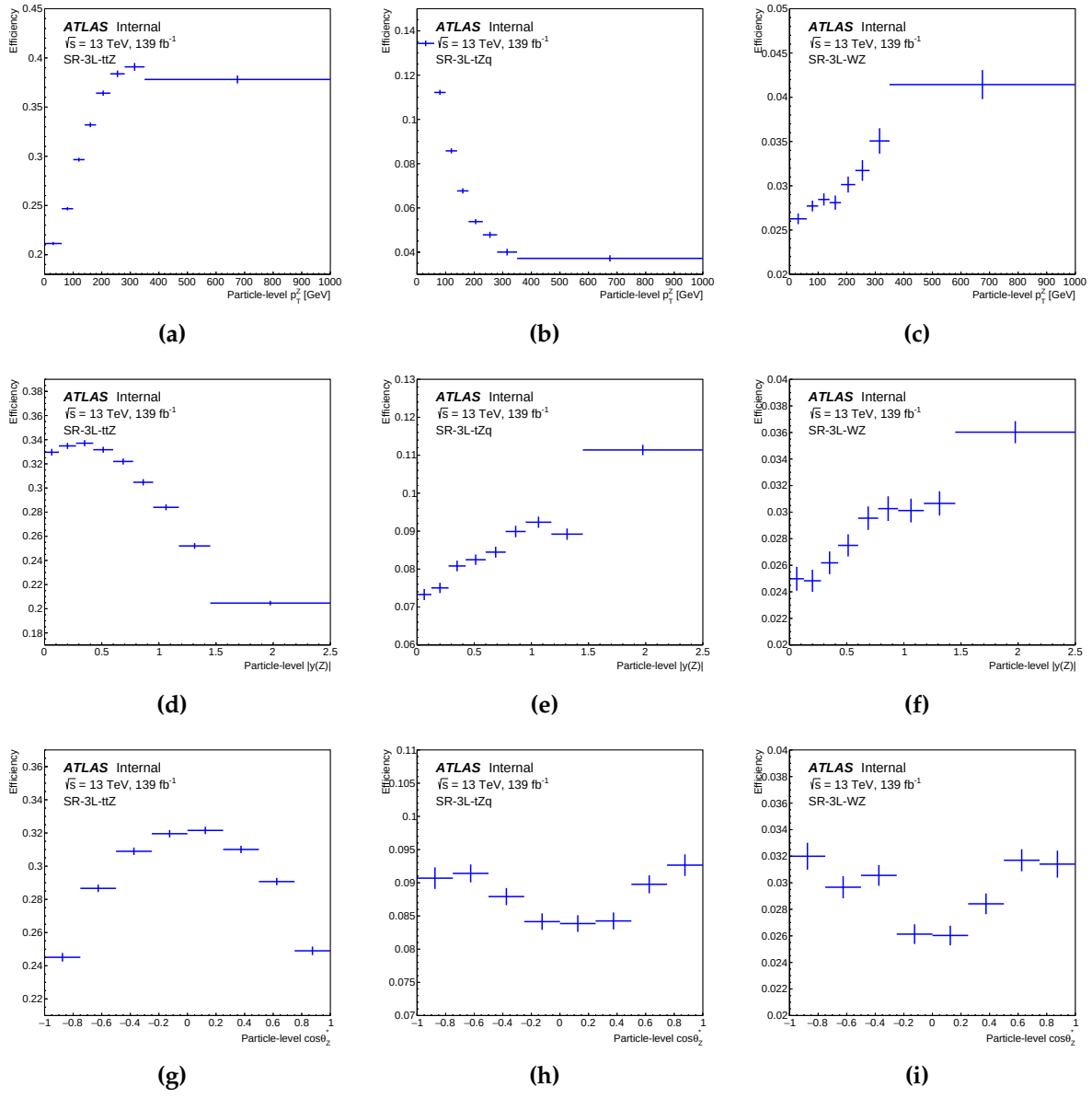

Figure 9.10: Selection efficiency corrections for the p_{T}^{Z}, $|y^{Z}|$ and $\cos\left(\theta_{Z}^{\star}\right)$ observables from top in the SR-3L-$t\bar{t}Z$, SR-3L-tZq and SR-3L-WZ regions from left.

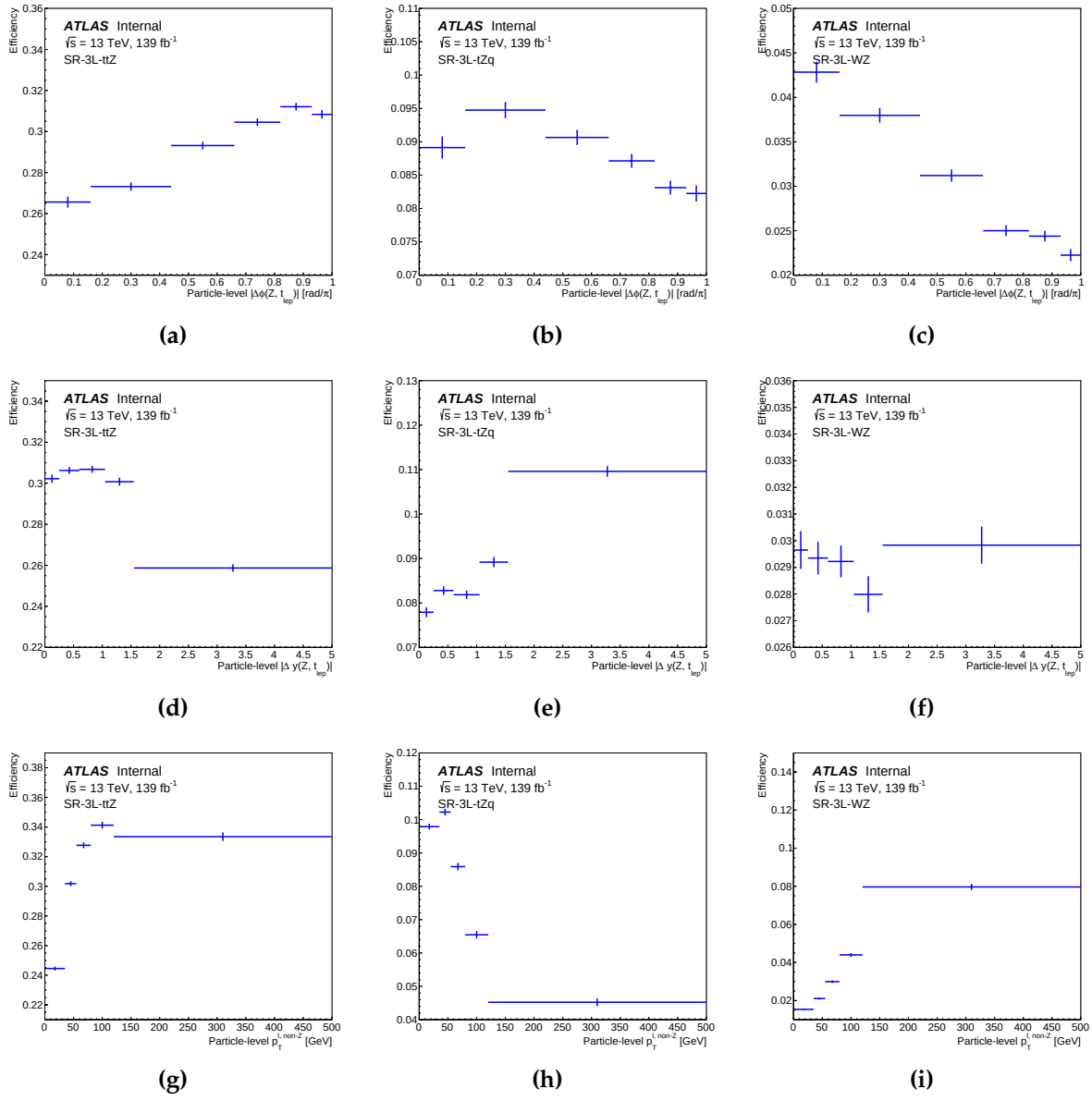

Figure 9.11: Selection efficiency corrections for the $|\Delta\phi(Z, t_{\text{lep}})|$, $|\Delta y(Z, t_{\text{lep}})|$ and $p_{\text{T}}^{\ell,\text{non-}Z}$ observables from top in the SR-3L-$t\bar{t}Z$, SR-3L-tZq and SR-3L-WZ regions from left.

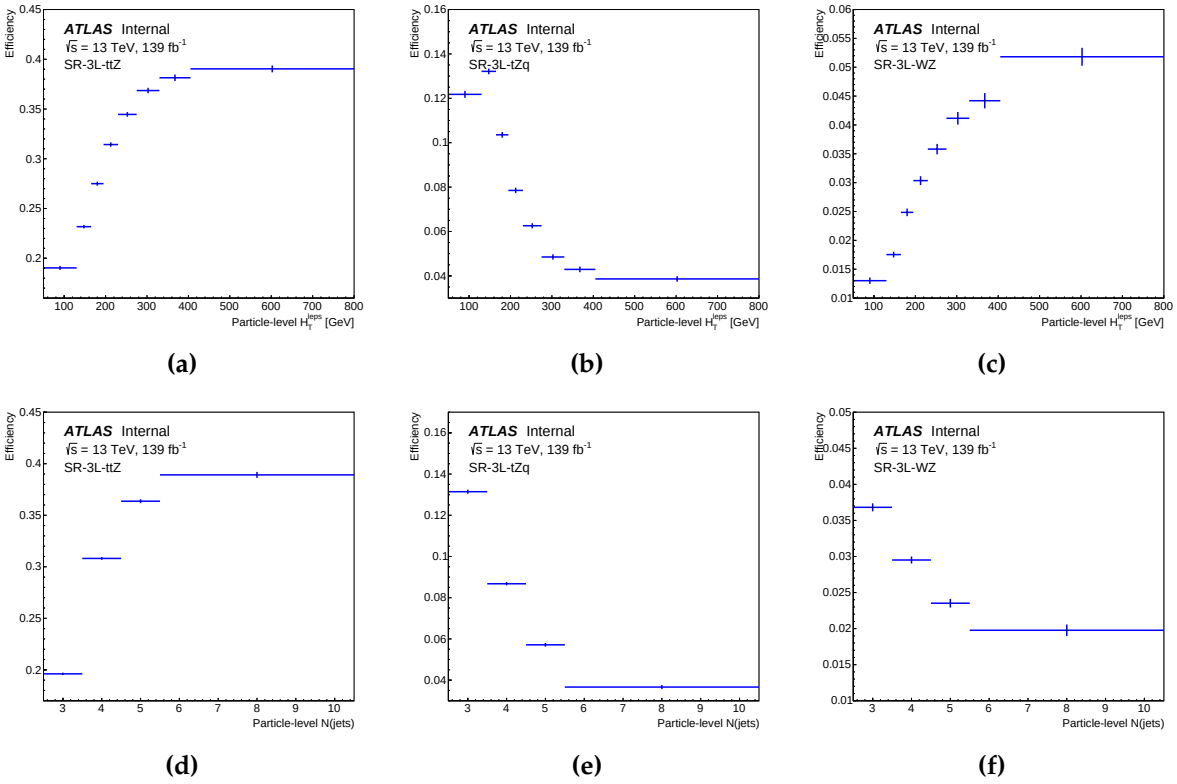

Figure 9.12: Selection efficiency corrections for the $H_{\mathrm{T}}^{\mathrm{leps}}$ and N_{jets} observables from top in the SR-3L-$t\bar{t}Z$, SR-3L-tZq and SR-3L-WZ regions from left.

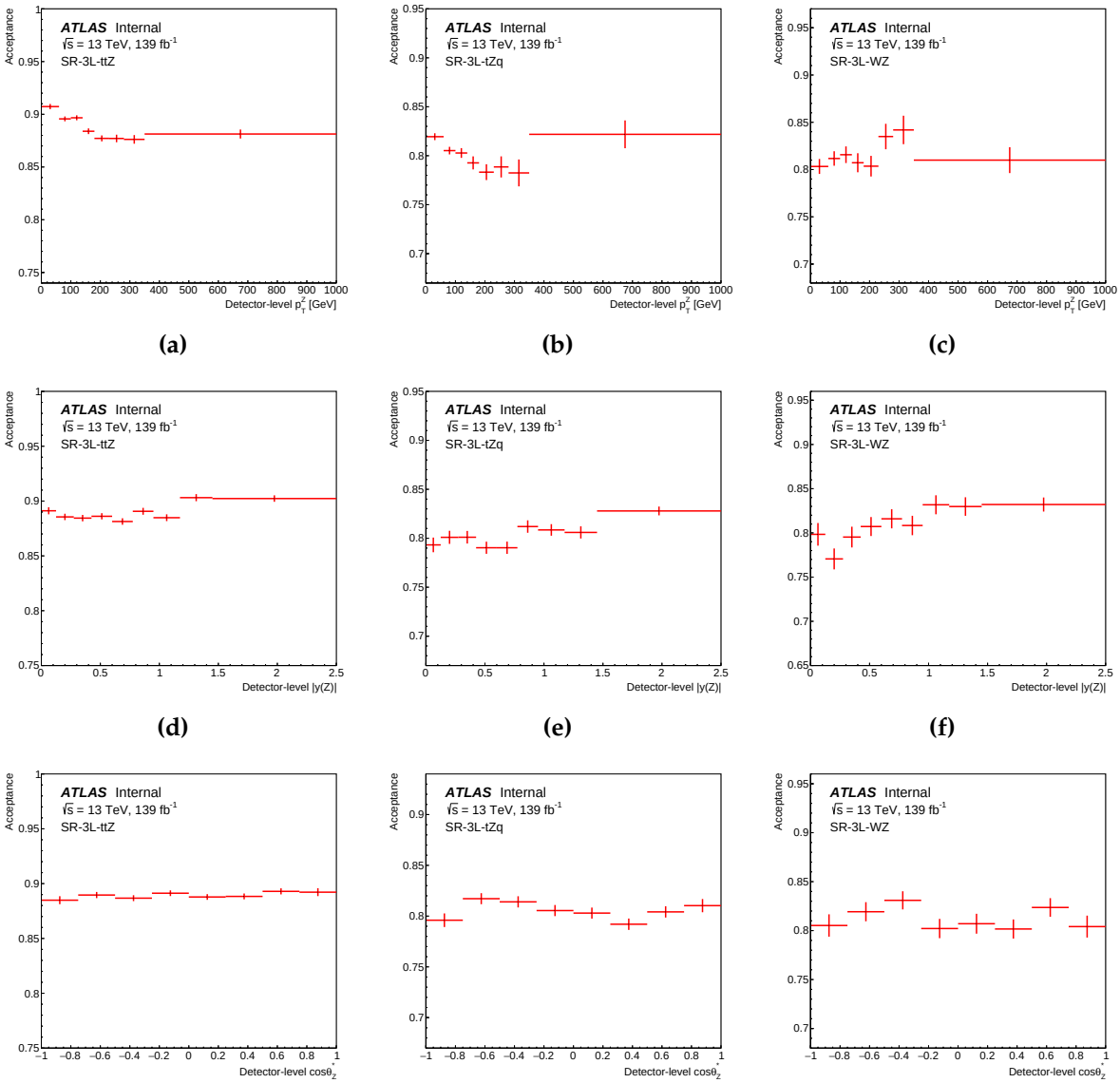

Figure 9.13: Detector acceptnce corrections for the p_{T}^{Z}, $|y^{Z}|$ and $\cos(\theta_{Z}^{\star})$ observables from top in the SR-3L-$t\bar{t}Z$, SR-3L-tZq and SR-3L-WZ region from left.

the p_{T} threshold may contain additional jets just below this cut-off. The associated detector-level events are more likely to contain a larger number of jets where the jets below the threshold at particle-level migrate to above the threshold at detector-level. Therefore, the acceptance at lower jet multiplicities is reduced. The majority of the remaining observables have reasonably flat acceptance distributions across each signal region.

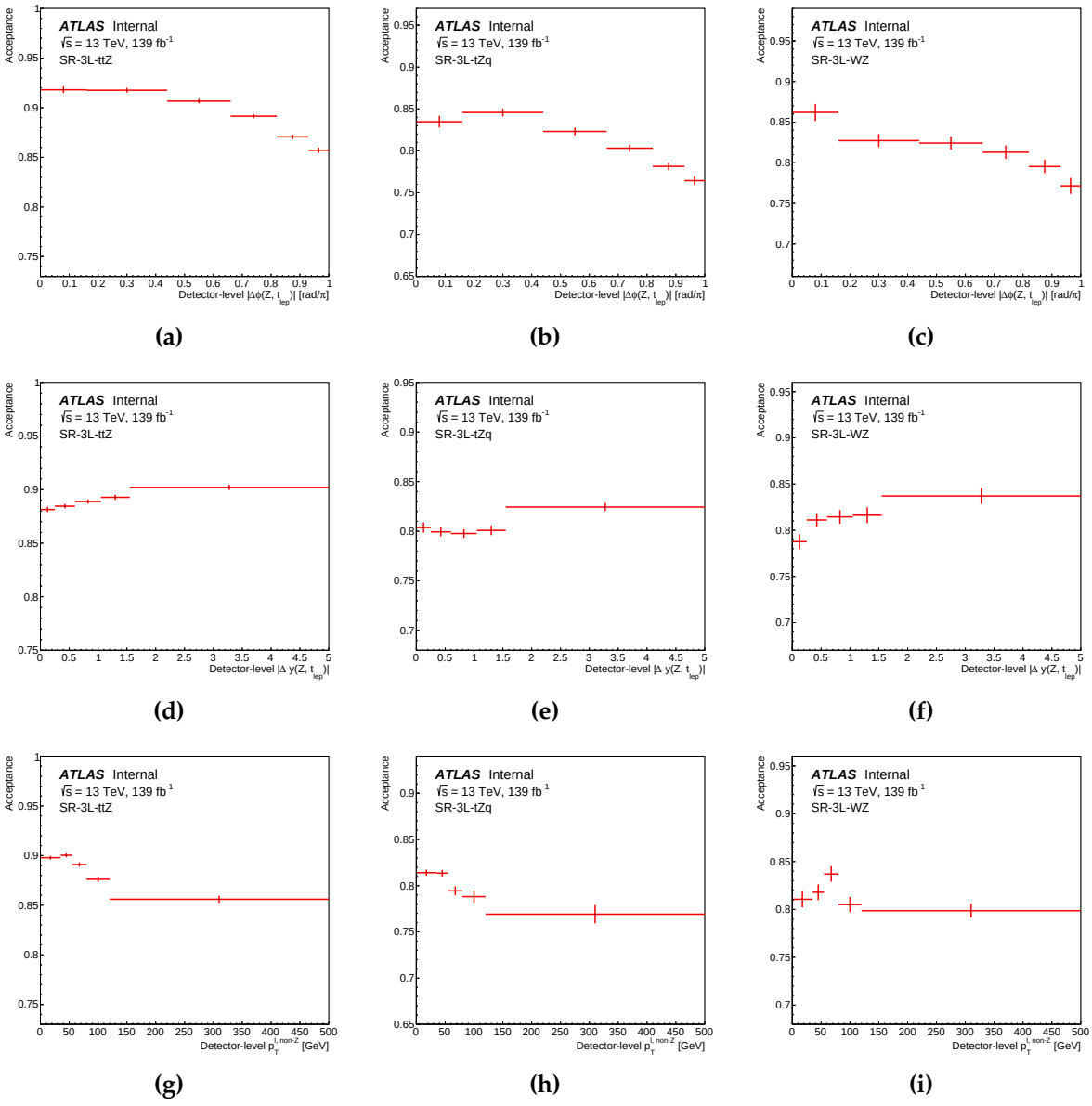

Figure 9.14: Detector acceptnce corrections for the $|\Delta\phi(Z, t_{\text{lep}})|$, $|\Delta y(Z, t_{\text{lep}})|$ and $p_{\text{T}}^{\ell,\text{non-}Z}$ observables from top in the SR-3L-$t\bar{t}Z$, SR-3L-tZq and SR-3L-WZ region from left.

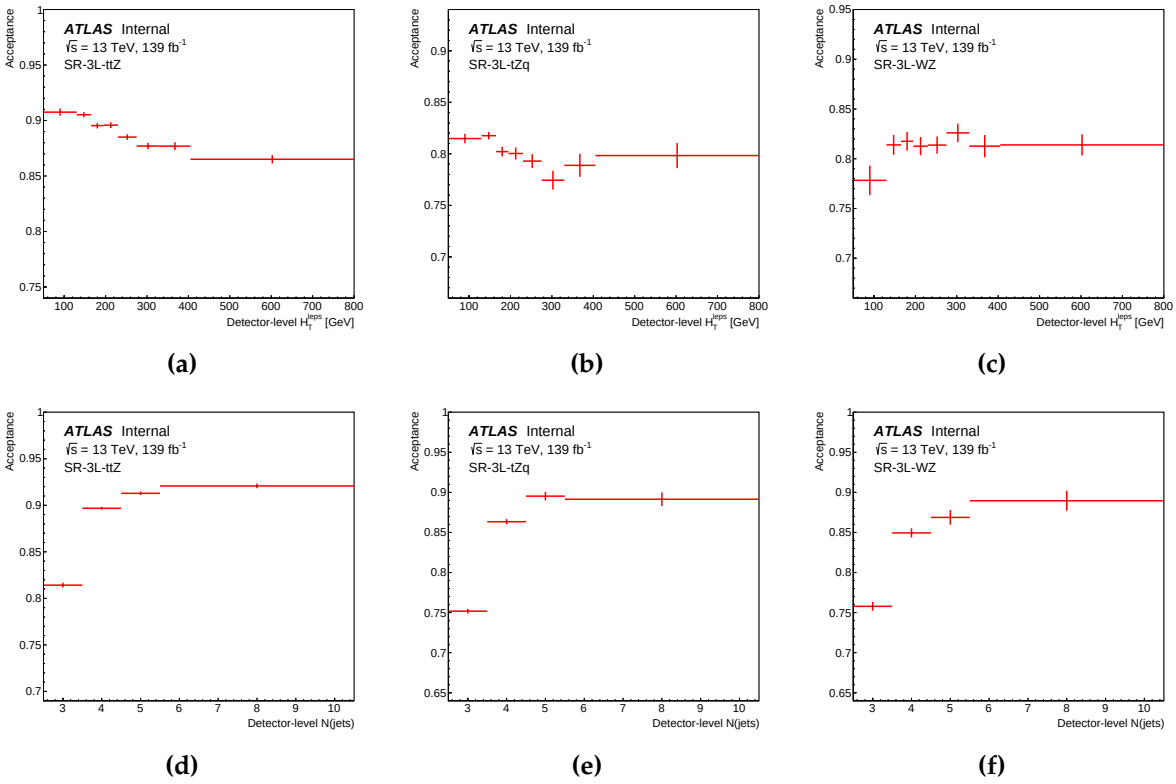

Figure 9.15: Detector acceptnce corrections for the $H_{\mathrm{T}}^{\mathrm{leps}}$and N_{jets} observables from top in the SR-3L-$t\bar{t}Z$, SR-3L-tZq and SR-3L-WZ region from left.

The majority of the migration matrices are highly diagonal, maintaining the diagonality which was achieved in the choice of binning study for each observable (Section 9.5). Strong diagonality of some matrices leads to off-diagonal bins with very few events which have overall negative MC weights. Such bins are shown in white colour and correspond to a negative event yield which was checked to be minor. The unfolding procedure corrects these bins by making an assumption that the actual number of events is 1×10^{-6}. The least diagonal matrices are obtained for the $|\Delta\phi(Z, t_{\text{lep}})|$, $|\Delta y(Z, t_{\text{lep}})|$ and N_{jets} observables. The migration matrices of the SR-3L-tZq and SR-3L-WZ signal regions tend to show higher migrations to neighbouring bins reducing their diagonality, however, at least 60% of events are maintained in the diagonal elements of the SR-3L-$t\bar{t}Z$ matrices. Overall, the migration matrices are considered to be reasonable as shown in Figures 9.16, 9.17 and 9.18.

Table 9.10 lists the contributions of the signal and background processes to the total number of events in each detector-level signal region. The observed data yield for each region is also shown, and the uncertainties include statistical and systematic sources. The overall agreement between the total prediction and data is good. The SR-3L-$t\bar{t}Z$ region contains the most amount of the signal events and its purity is highest at $\approx$ 75%. The dominant background in this region is the tWZ process. The SR-3L-tZq region is the second best in terms of the signal yield and the purity, which is $\approx$ 37%. As expected, the dominant background is the tZq process which contributes approximately 90 events and the second highest background is coming from the WZ+jets process. Lastly, the SR-3L-WZ region has the worst purity of $\approx$ 26% and the signal yield of 45 events is smaller than the event count of the dominant WZ+jets background at 65 events. As designed, the $WZ + b$ background process is the largest with respect to the $WZ + c$ and $WZ + l$ processes as well as overall. Figures 9.19, 9.20 and 9.21 compare the modelling of the signal and background events with respect to the data using each differential observable for each signal region. As in the table, the uncertainty bands include the effects of statistical and systematic uncertainties. The modelling is observed to be reasonable in general. A few disagreements between the observed data and the model are seen where the data-MC ratio is larger than two standard deviations, for example in Figure 9.19g. This is considered to be a statistical fluctuation since the overall modelling is shows a good data-MC agreement within the uncertainty bands.

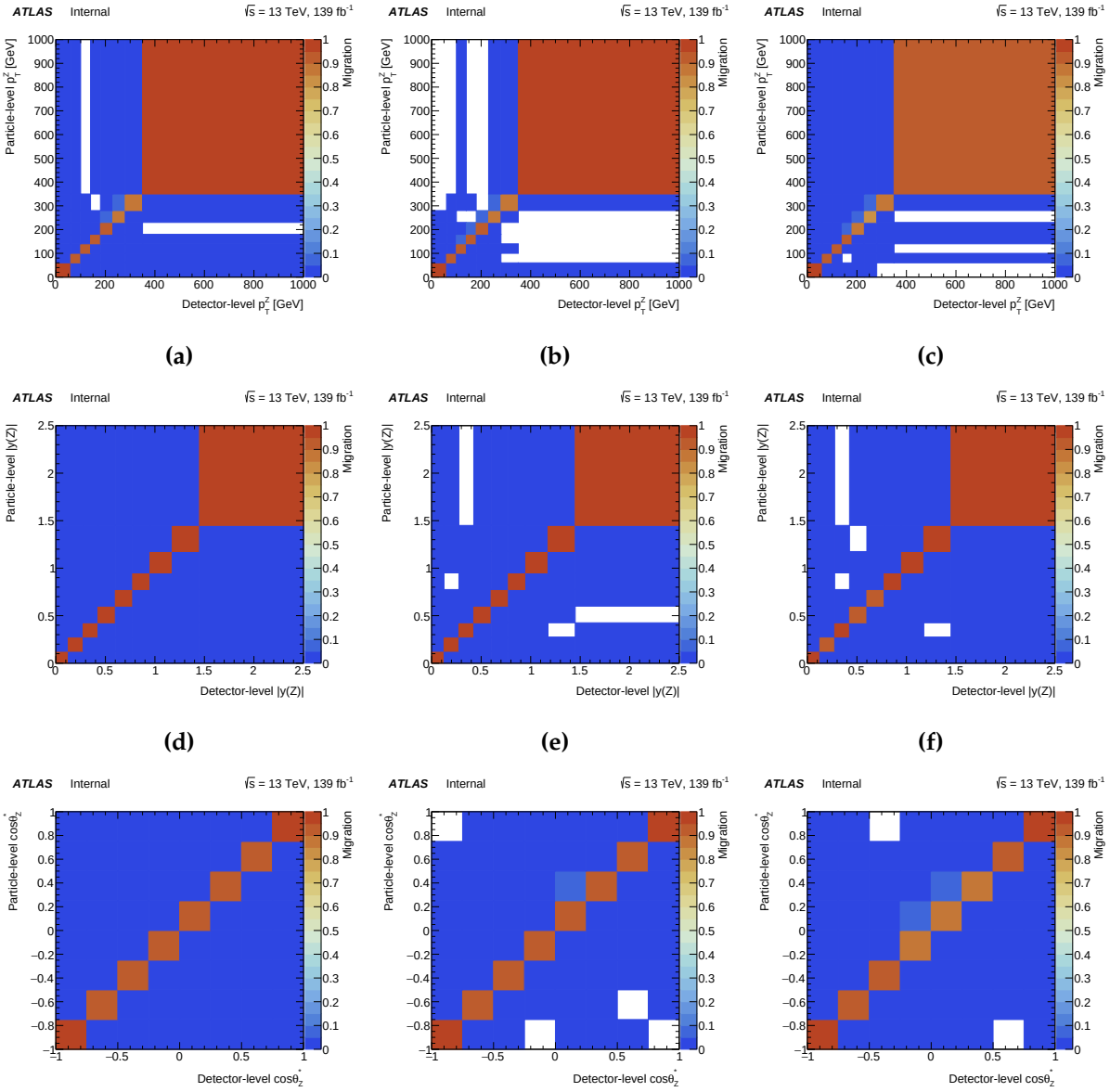

Figure 9.16: Migration matrices of the p_{T}^{Z}, $|y^{Z}|$ and $\cos(\theta_{Z}^{\star})$ observables from top to bottom for the SR-3L-$t\bar{t}Z$, SR-3L-tZq and SR-3L-WZ regions from left to right.

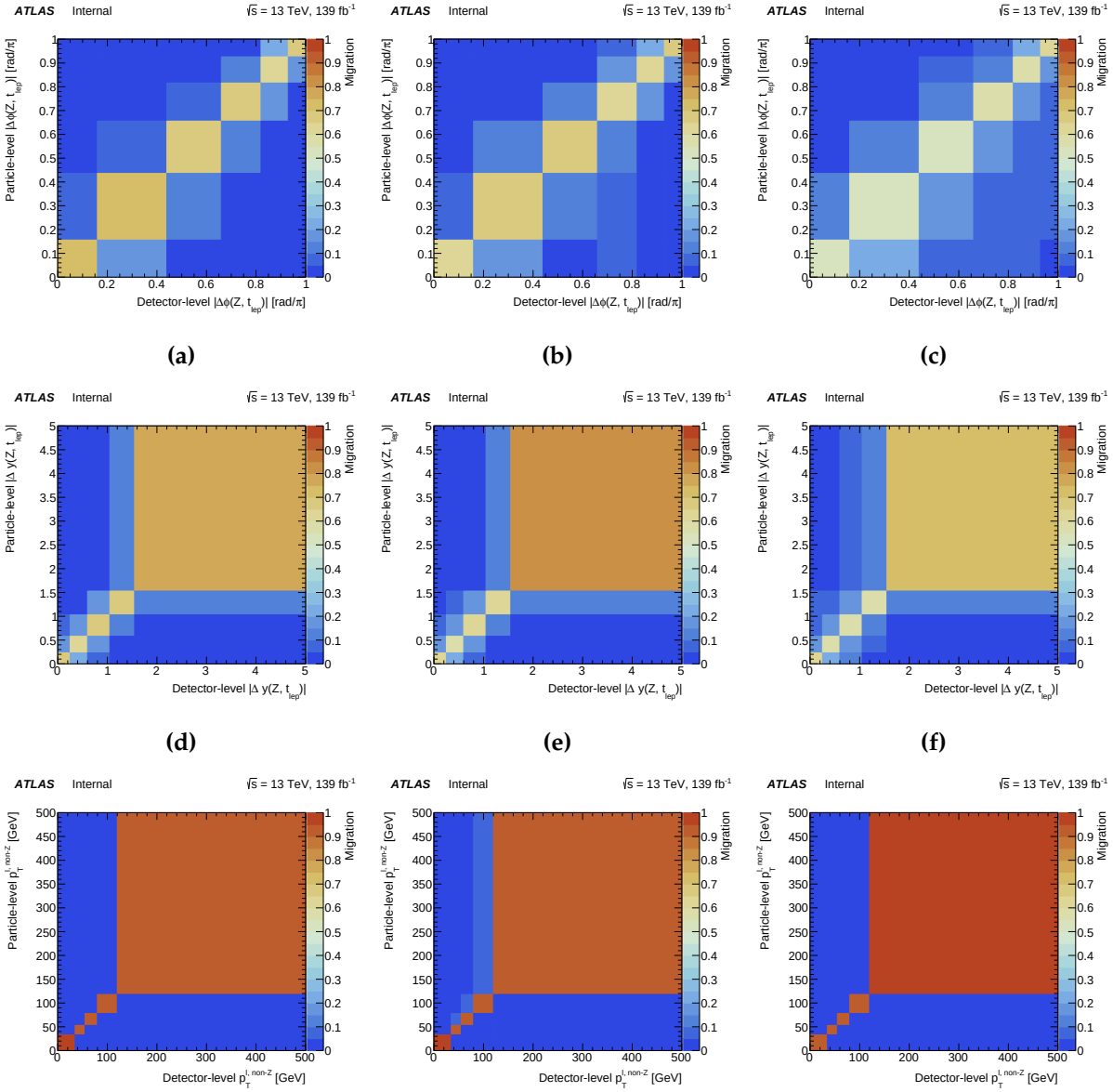

Figure 9.17: Migration matrices of the $|\Delta\phi(Z, t_{\text{lep}})|$, $|\Delta y(Z, t_{\text{lep}})|$ and $p_{\text{T}}^{\ell,\text{non-}Z}$ observables from top to bottom for the SR-3L-$t\bar{t}Z$, SR-3L-tZq and SR-3L-WZ regions from left to right.

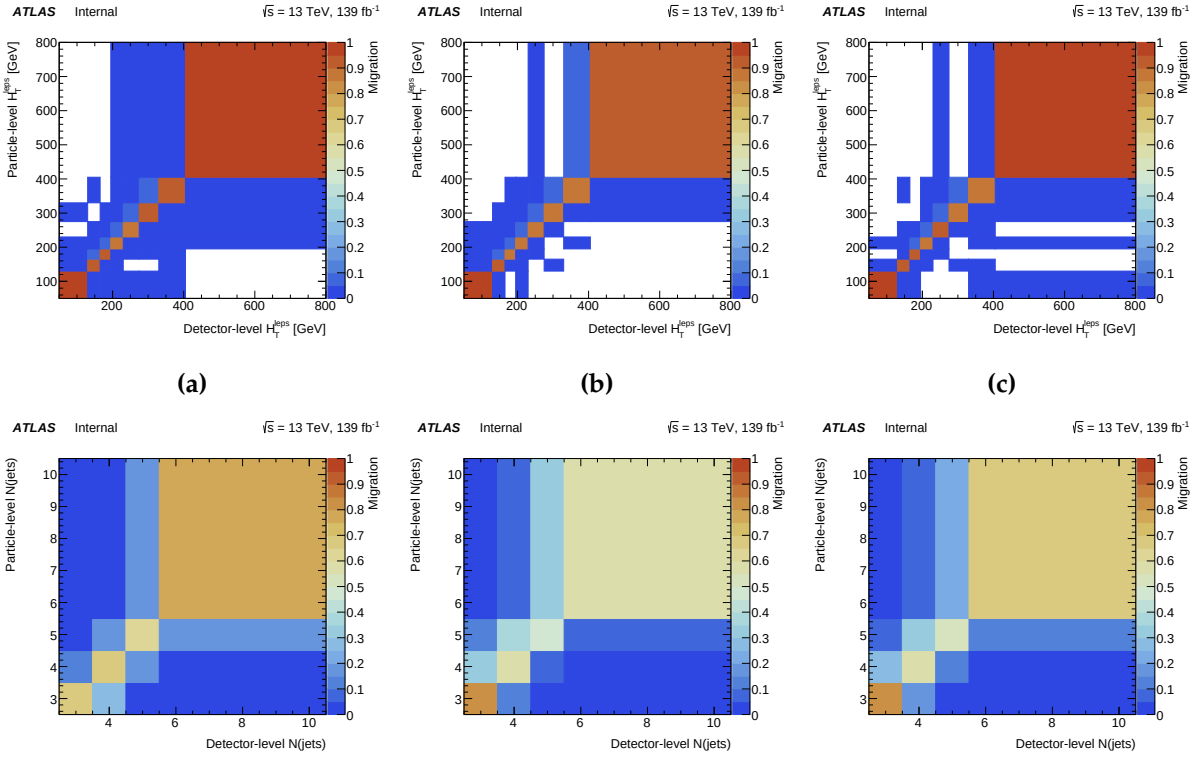

Figure 9.18: Migration matrices of the $H_{\mathrm{T}}^{\mathrm{leps}}$ and N_{jets} observables from top to bottom for the SR-3L-$t\bar{t}Z$, SR-3L-tZq and SR-3L-WZ regions from left to right.

Table 9.10: Yields of the signal and background processes in the model before the fit as well as the observed number of events in data for each signal region. Statistical and systematic uncertainties are shown.

Sample	SR-3L-$t\bar{t}Z$	SR-3L-tZq	SR-3L-WZ
$t\bar{t}Z$	424.0 ± 18.0	139.0 ± 8.0	45.8 ± 2.3
$t\bar{t}W$	4.3 ± 2.2	5.2 ± 2.6	2.1 ± 1.1
$t\bar{t}H$	11.7 ± 1.2	6.5 ± 0.6	1.43 ± 0.16
$WZ + b$	23.0 ± 6.0	30.0 ± 8.0	51.0 ± 14.0
$WZ + c$	9.0 ± 4.0	12.0 ± 5.0	13.0 ± 5.0
$WZ + l$	1.2 ± 0.6	1.8 ± 0.8	1.7 ± 0.8
$ZZ + b$	4.4 ± 2.6	7.0 ± 4.0	7.0 ± 4.0
$ZZ + c$	1.0 ± 0.5	1.3 ± 0.6	0.9 ± 0.4
$ZZ + l$	0.39 ± 0.15	0.47 ± 0.17	0.25 ± 0.11
tZq	20.0 ± 5.0	90.0 ± 22.0	12.0 ± 7.0
tWZ	42.0 ± 8.0	25.9 ± 3.4	19.0 ± 4.0
F-e-HF	5.0 ± 1.1	13.2 ± 2.8	4.3 ± 1.0
F-e-Other	8.3 ± 1.8	15.3 ± 3.3	6.7 ± 1.8
F-m-HF	6.7 ± 0.8	17.6 ± 2.1	5.0 ± 1.4
F-Other	2.8 ± 1.5	4.5 ± 2.3	2.4 ± 1.3
$t\bar{t}t\bar{t}$	1.56 ± 0.07	0.266 ± 0.025	0.128 ± 0.017
Other	1.7 ± 0.9	1.2 ± 0.7	1.3 ± 1.0
Total	568.0 ± 27.0	371.0 ± 28.0	174.0 ± 18.0
Data	569	388	175

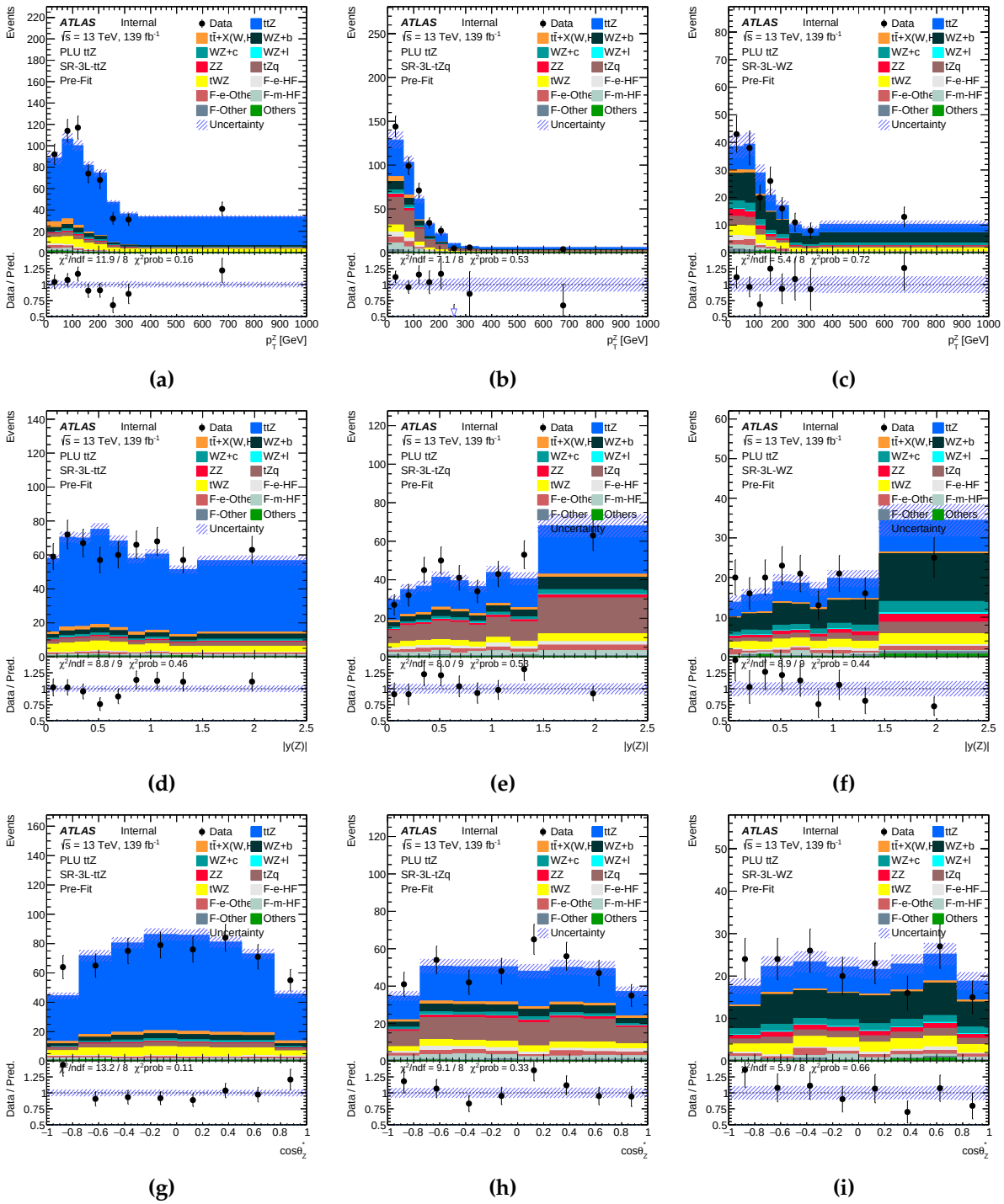

Figure 9.19: Distributions of the p_{T}^{Z}, $|y^{Z}|$ and $\cos(\theta_{\mathrm{Z}}^{\star})$ observables top to bottom at the detector level for the SR-3L-$t\bar{t}Z$, SR-3L-tZq and SR-3L-WZ regions left to right before the fit. Decompositions of the signal and background processes are shown in different colours.

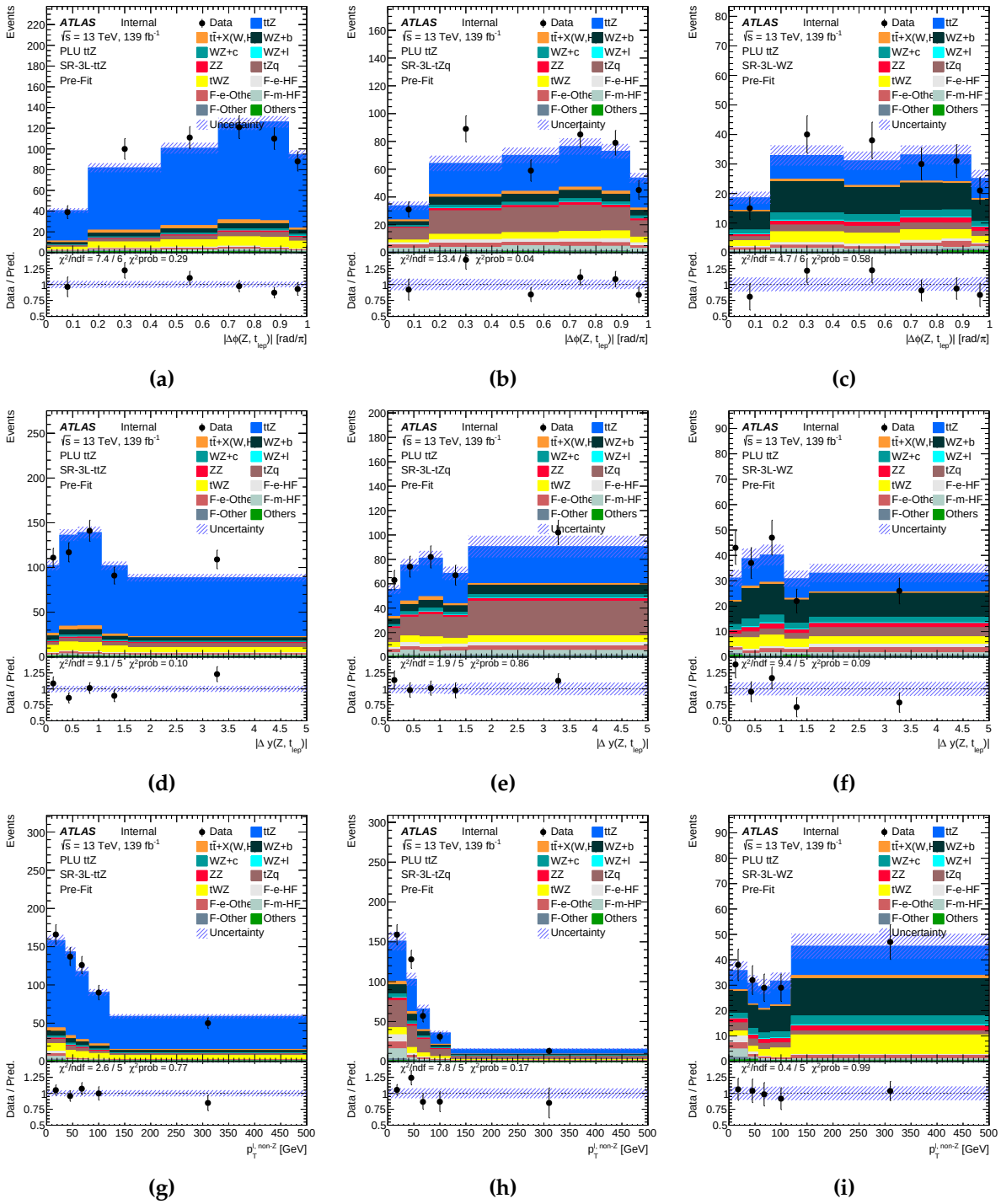

Figure 9.20: Distributions of the $|\Delta\phi(Z, t_{\text{lep}})|$, $|\Delta y(Z, t_{\text{lep}})|$ and $p_{\text{T}}^{\ell,\text{non-}Z}$ observables top to bottom at the detector level for the SR-3L-$t\bar{t}Z$, SR-3L-tZq and SR-3L-WZ regions left to right before the fit. Decompositions of the signal and background processes are shown in different colours.

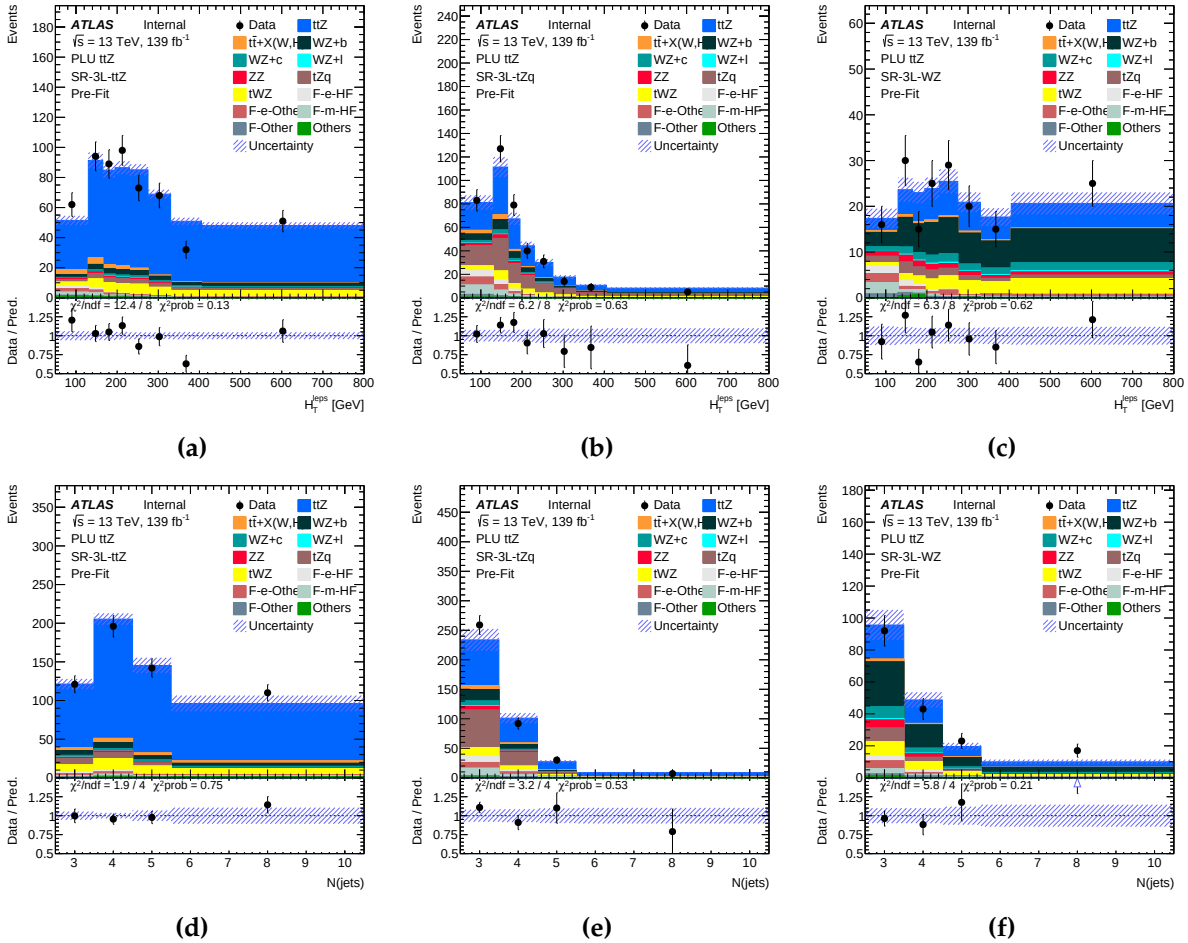

Figure 9.21: Distributions of the $H_{\mathrm{T}}^{\mathrm{leps}}$ and N_{jets} observables top to bottom at the detector level for the SR-3L-$t\bar{t}Z$, SR-3L-tZq and SR-3L-WZ regions left to right before the fit. Decompositions of the signal and background processes are shown in different colours.

The impact of the nuisance parameters, which include the systematic uncertainties and free-floating normalisation factors of background processes, on the measurements is assessed using ranking plots (Section 4.3.2). The rankings of nuisance parameters are produced for each parameter of interest separately using the same approach as for the inclusive cross-section measurement. The following text will discuss the impact of nuisance parameters on the measurements with respect to the p_{T}^{Z}, $|\Delta y(Z, t_{\mathrm{lep}})|$ and N_{jets} observables. These observables are considered to reflect the impact of nuisance parameters on the three-lepton $t\bar{t}Z$ cross-section measurements in general.

Figure 9.22 ranks the impacts of nuisance parameters on the differential cross-section measurements using the p_{T}^{Z} observable. The first row of Figures 9.22a, 9.22b and 9.22c show the rankings for the POIs associated with Bin 1, Bin 4 and Bin 8 of the distribution, respectively, in the absolute cross-section measurement. These bins correspond to the low-, medium- and high-p_{T} bins containing different event compositions. Systematic uncertainties associated with the choice of the renormalisation and factorisation scales on the $t\bar{t}Z$ signal sample (ttZ_muR_muF), the jet energy scale (JET Pileup RhoTopology) and the tWZ background modelling (tWZ modelling (DR1 vs. DR2)) are ranked highest in Bins 1, 4 and 8, respectively. The normalisation factors associated with the fake lepton backgrounds rank consistently high for each POI, however, their impact on the POI is reduced with increasing p_{T}^{Z}. This is expected since the fake lepton background is less significant at higher p_{T}. None of the nuisance parameters are significantly constrained. Some nuisance parameters are seen to be pulled from their initial central values which is induced by the fit in the control regions of the fake lepton background. The pulls are not considered to be significant. The second row of Figures 9.22d, 9.22e and 9.22f show ranking plots for the normalised cross-section measurement where the POI associated with the last bin is replaced with the POI of the total cross-section. The normalisation of the cross-section significantly reduces the impacts of the nuisance parameters on each POI and the majority of the experimental systematic uncertainties cancel out. This can be seen in the comparison of the total cross-section ranking plot (Figure 9.22f) with the ranking plots of the absolute cross-section measurement. The uncertainty associated with the modelling of the parton shower in the $t\bar{t}Z$ signal process is seen to rank highest. Figure 9.23 shows ranking plots for three of the POIs corresponding to the differential cross-section in $|\Delta y(Z, t_{\mathrm{lep}})|$. As for p_{T}^{Z}, the nuisance parameters are ranked for the absolute (Figures 9.23a, 9.23b and 9.23c) and normalised (Figures 9.23d, 9.23e and 9.23f) measurements. Similar rankings of the nuisance parameters are found in these measurements and the systematic uncertainties are not constrained in the fit. The pulls of the nuisance parameters

are caused by the control regions of the fake lepton background. Lastly, ranking plots of the nuisance parameters for the differential cross-section in N_{jets} are shown in Figure 9.24. The uncertainties related to the tZq process are seen to rank high in the first two bins of the distribution, corresponding to the region of a low jets multiplicity. This is attributed to the event composition, especially in the SR-3L-tZq and SR-3L-WZ regions, where tZq background is dominant. The ranking plot of the last bin, corresponding to $N_{\text{jets}} \geq 6$, is found to be in agreement with the differential cross-section in the other observables. In general, most dominant systematic uncertainty sources are from the choice of the renormalisation and factorisation scales in the $t\bar{t}Z$ signal process, modelling uncertainties and jet energy scale for each observable.

The measurements of the differential $t\bar{t}Z$ cross-section at particle-level in the three-lepton channel are presented in Figures 9.25–9.32. The distributions of the unfolded data are shown in black data points with the associated statistical and total uncertainties drawn as light-grey and dark-grey bands, respectively. The particle-level distribution of the nominal MADGRAPH5_AMC@NLO+PYTHIA8 signal sample is included in the plots as a blue line, labelled as MG5aMC@NLO+Pythia8. Each figure shows the absolute differential cross-section on the left and the corresponding normalised distribution on the right.

Figure 9.25 shows the absolute and normalised differential cross-sections in p_{T}^{Z}. The unfolded data are in good agreement with the particle-level distributions in both cases. The measurement precision is primarily limited by the statistical uncertainty, hence the total uncertainty does not cover each unfolded data point. The deviations are consistent with the previously observed data-MC agreement in Figures 9.19a, 9.19b and 9.19c. The unfolding validation (Section 9.6), especially the pseudo-experiments, did not uncover these deviations because they are on the tail end of the distribution while the pseudo-experiments were averaged. The first three bins in the unfolded data of the absolute cross-section (Figure 9.25a) are observed to have relatively larger contributions from the systematic uncertainties to the total uncertainty. This is explained by the fact that the background yield is largest in these bins and the associated systematic uncertainties are accordingly more relevant. The effects of these systematic uncertainties are seen to be cancelled out in the normalised cross-section distribution (Figure 9.25b), as expected.

The unfolded $|\Delta y(Z, t_{\text{lep}})|$ distribution in Figure 9.29 is observed to have relatively larger bin-to-bin fluctuations compared to the other observables. It is a combined effect of having the migration matrices with non-negligible off-diagonal elements and

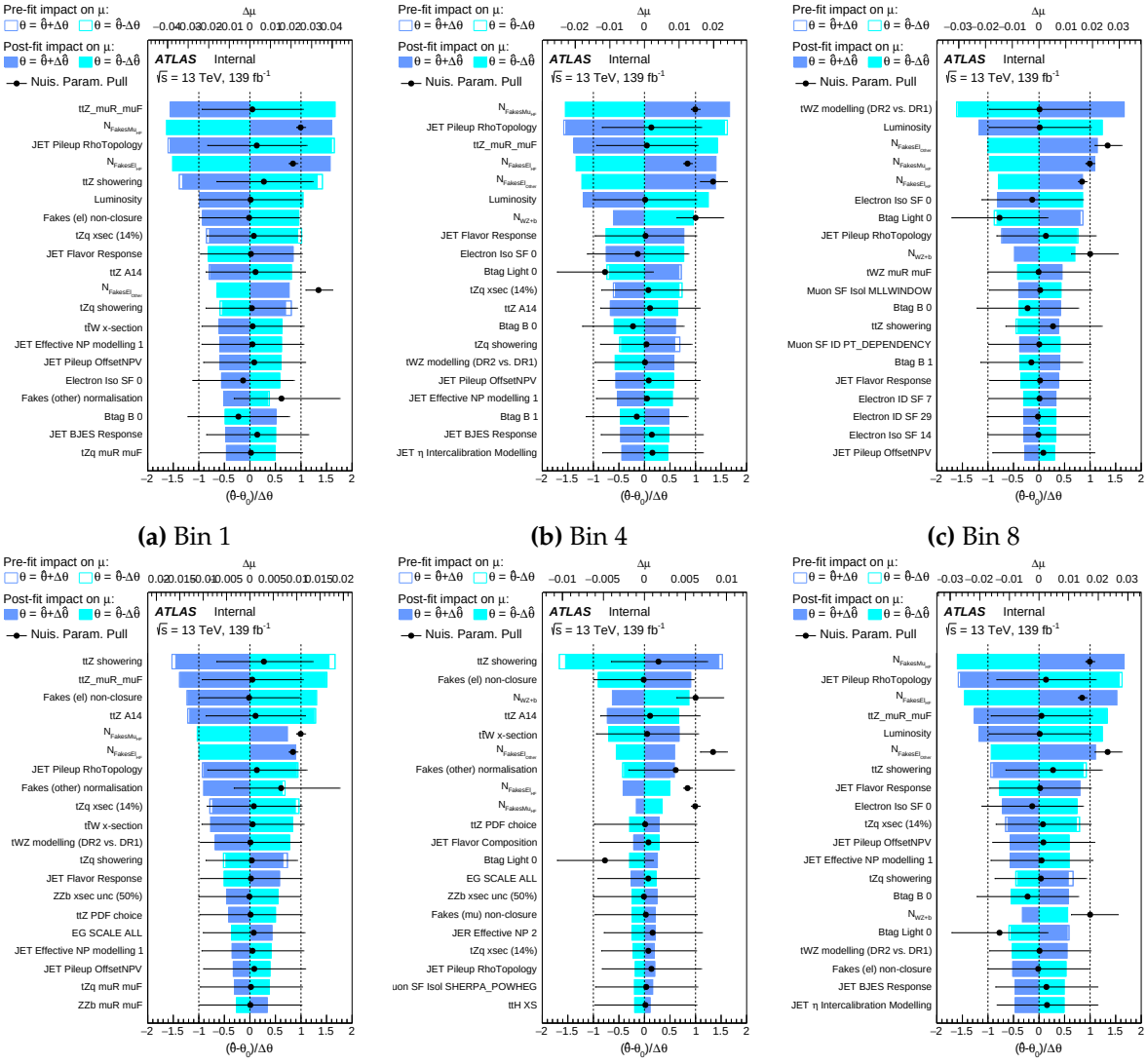

(a) Bin 1 **(b)** Bin 4 **(c)** Bin 8

(d) Bin 1 **(e)** Bin 4 **(f)** Total cross-section

Figure 9.22: Ranking plots of the nuisance parameters in the absolute (a –c) and normalised (d – f) differential cross-section measurements using the p_{T}^{Z} observable. Rankings for three of eight POI are shown which represent low-, medium- and high-p_{T} bins in the unfolded distribution. Subfigure (f) shows the total cross-section POI which replaces Bin 8 in the normalised cross-section.

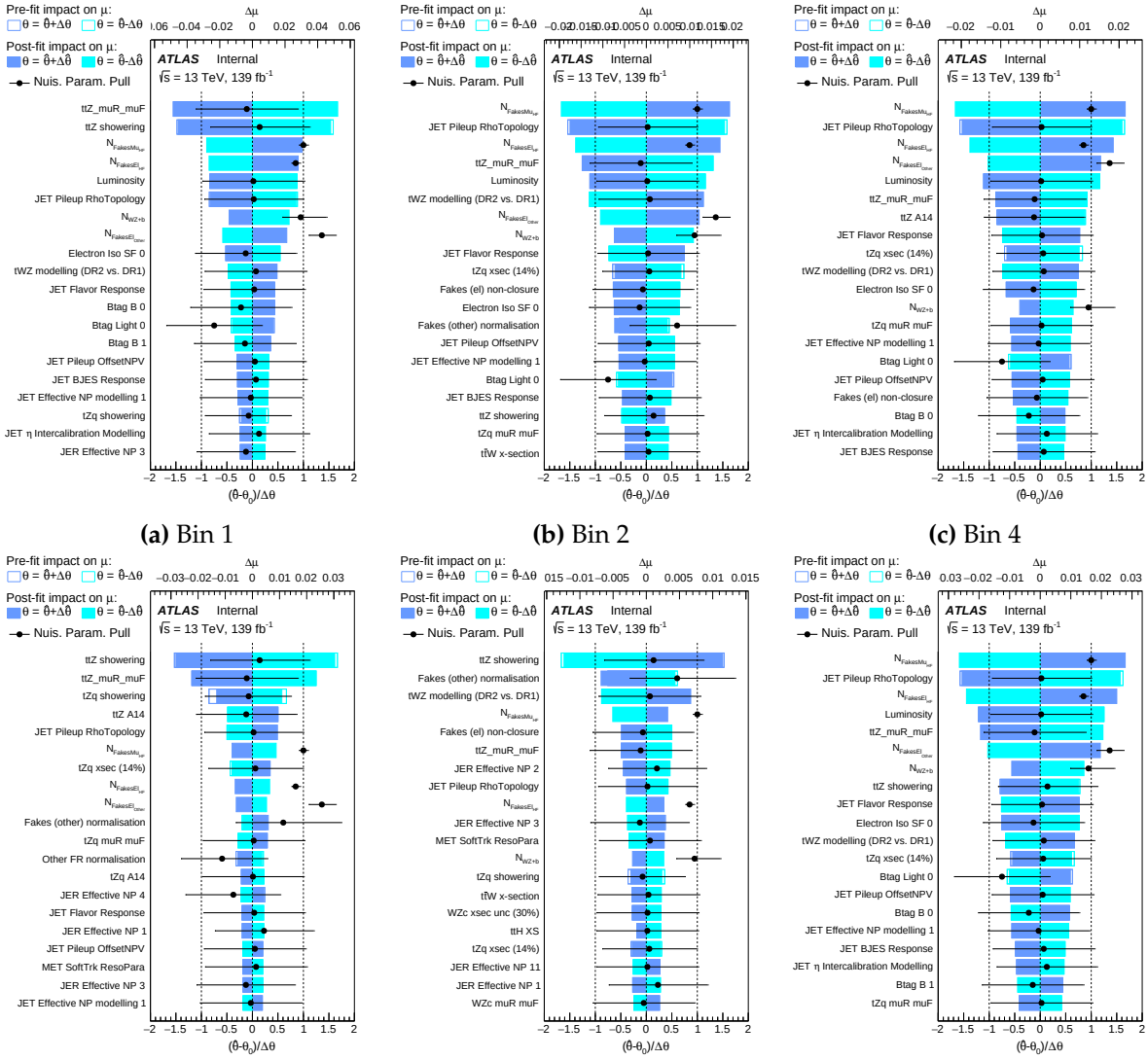

(a) Bin 1 **(b)** Bin 2 **(c)** Bin 4

(d) Bin 1 **(e)** Bin 2 **(f)** Total cross-section

Figure 9.23: Ranking plots of the nuisance parameters in the absolute (a – c) and normalised (d – f) differential cross-section measurements using the $|\Delta y(Z, t_{\text{lep}})|$ observable. Rankings for three of five POI are shown. Subfigure (f) shows the total cross-section POI which replaces Bin 5 in the normalised cross-section.

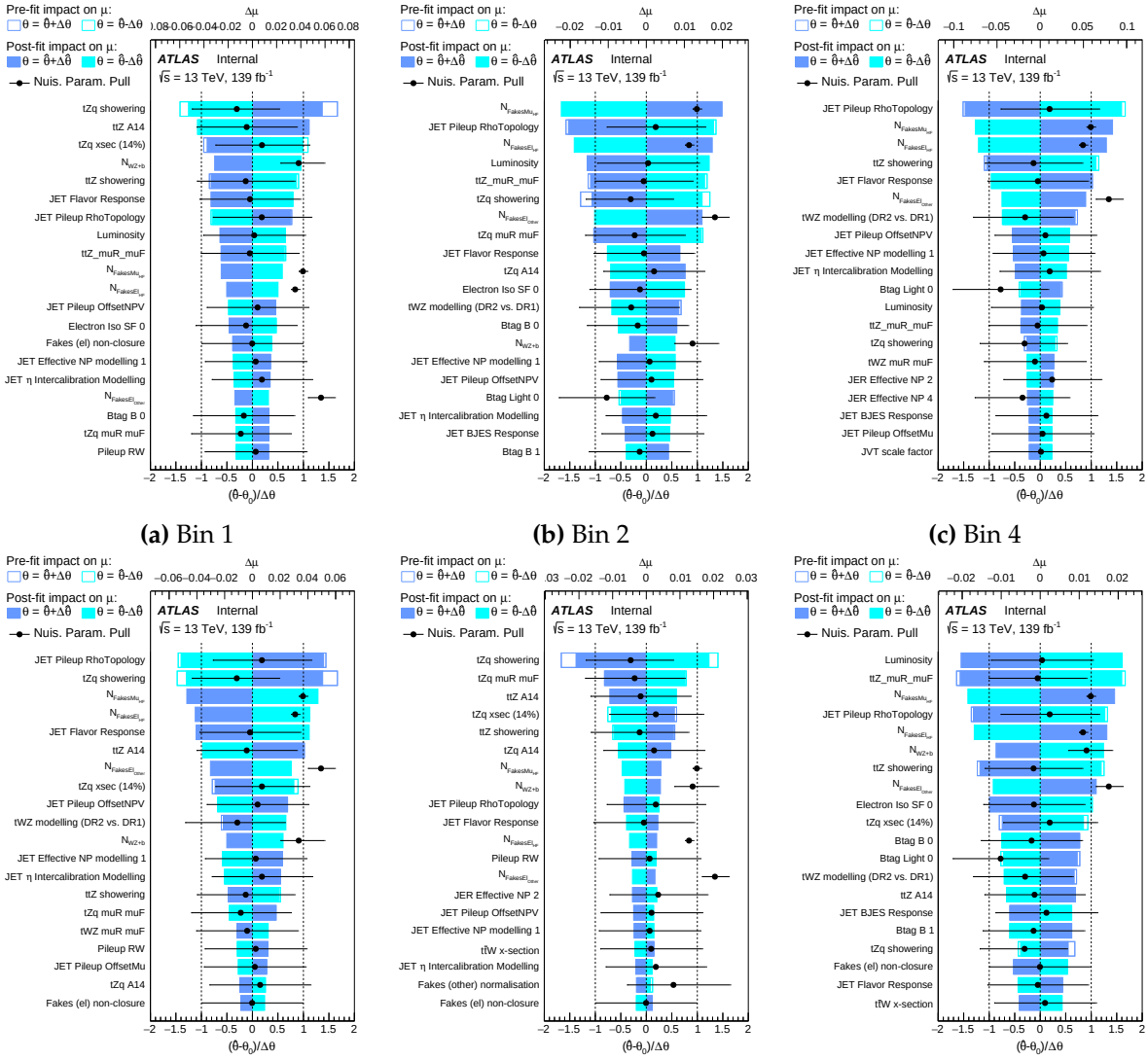

(a) Bin 1 **(b)** Bin 2 **(c)** Bin 4

(d) Bin 1 **(e)** Bin 2 **(f)** Total cross-section

Figure 9.24: Ranking plots of the nuisance parameters in the absolute (a – c) and normalised (d – f) differential cross-section measurements using the N_{jets} observable. Rankings for three of four POI are shown. Subfigure (f) shows the total cross-section POI which replaces Bin 4 in the normalised cross-section.

the detector-level distributions with minor data-MC disagreements. The associated migration matrices were shown to have the majority of the events migrate from the diagonal elements to the nearest off-diagonal elements (Figures 9.17d, 9.17e and 9.17f). The detector-level distributions were seen to display a degree of anti-correlation between the data-MC agreements of the neighbouring bins (Figures 9.20d, 9.20e and 9.20f). These disagreements are amplified by the migration matrices which result in fluctuations in the unfolded data. The observed fluctuations are considered to be reasonable given the model.

Figure 9.32 shows the absolute and normalised differential cross-sections in N_{jets}. The agreement between the unfolded data and prediction is reasonable. The total average uncertainty is approximately 20% and is slightly reduced in the normalised cross-section, as expected. The cross-sections in the first bin of the unfolded distributions in both the absolute and normalised measurements are estimated to have relatively larger systematic uncertainties where the main contributing systematic uncertainty is the modelling of the tZq showering. The remaining unfolded distributions are observed to be reasonably stable across the spectra. The measurements are estimated to have total uncertainties of up to 40% in a few cases and around 20% in most. The measurements are limited by statistical uncertainties in all cases, similarly to the previous measurements [134].

It is not straightforward to compare the current measurements with the results of the previous analysis primarily due to the different numbers of bins used for the same observables. The improved $t\bar{t}Z$ signal acceptance allows having a higher number of bins in these measurements. An approximate comparison can be made for the p_{T}^{Z} observable where the number of bins is increased from seven to eight, but none of the bins has the same edges. The previous measurement of the absolute cross-section in p_{T}^{Z} has a total uncertainty of 40% in the first bin and 27% on average. In contrast, the current measurement estimates an uncertainty of 17% on the cross-section in the first bin and an average uncertainty of 20%. None of the uncertainties in the current measurement exceeds 32%. Therefore, a relative improvement of 58% in the precision is observed in the first bin and 27% on average. It is important to note that the previous analysis performed this measurement using three- and four-lepton events. It is therefore expected that the current measurement will improve the precision further upon adding four-lepton events. Overall, the precision is significantly improved in the current measurements of the differential $t\bar{t}Z$ cross-section.

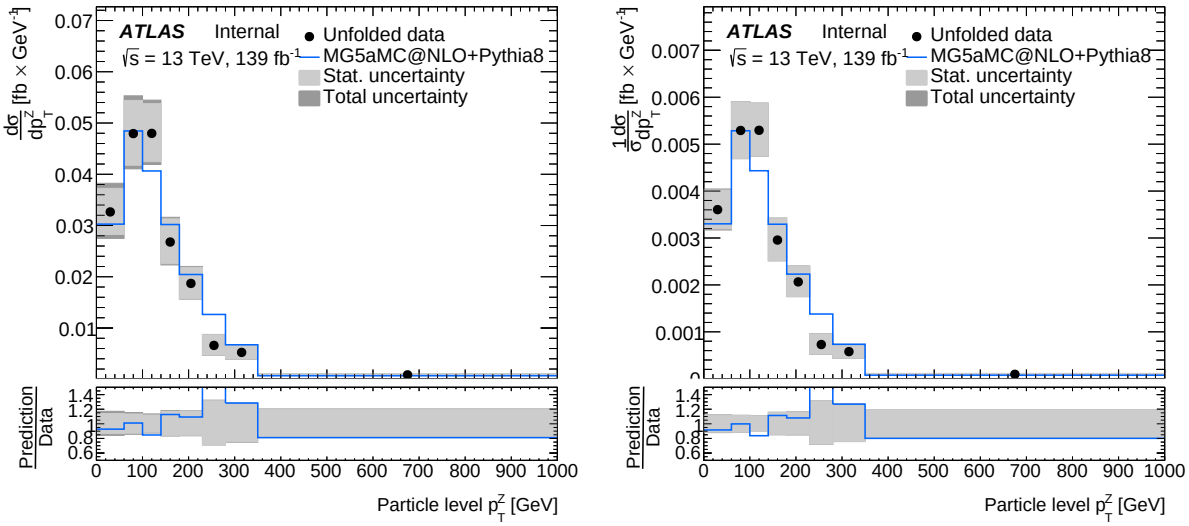

(a) **(b)**

Figure 9.25: Particle-level (a) absolute and (b) normalised differential cross-sections as a function of p_{T}^{Z}. The light-grey bands show statistical uncertainties while the dark-grey bands are the total uncertainty. The agreement with the nominal MADGRAPH4_AMC@NLO + PYTHIA8 prediction is shown in the bottom panel.

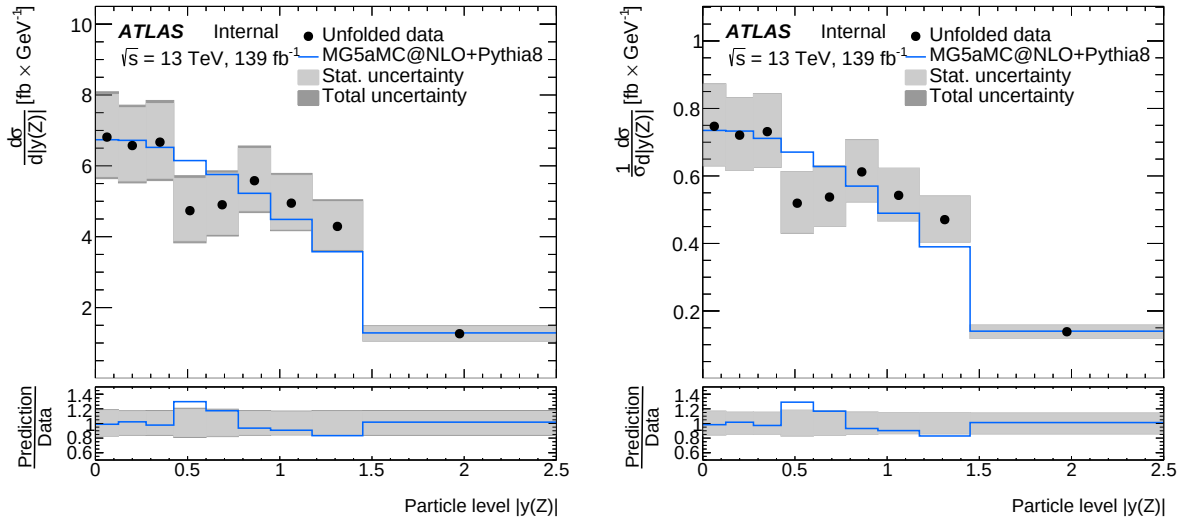

(a) **(b)**

Figure 9.26: Particle-level (a) absolute and (b) normalised differential cross-sections as a function of $|y^{Z}|$. The light-grey bands show statistical uncertainties while the dark-grey bands are the total uncertainty. The agreement with the nominal MADGRAPH4_AMC@NLO + PYTHIA8 prediction is shown in the bottom panel.

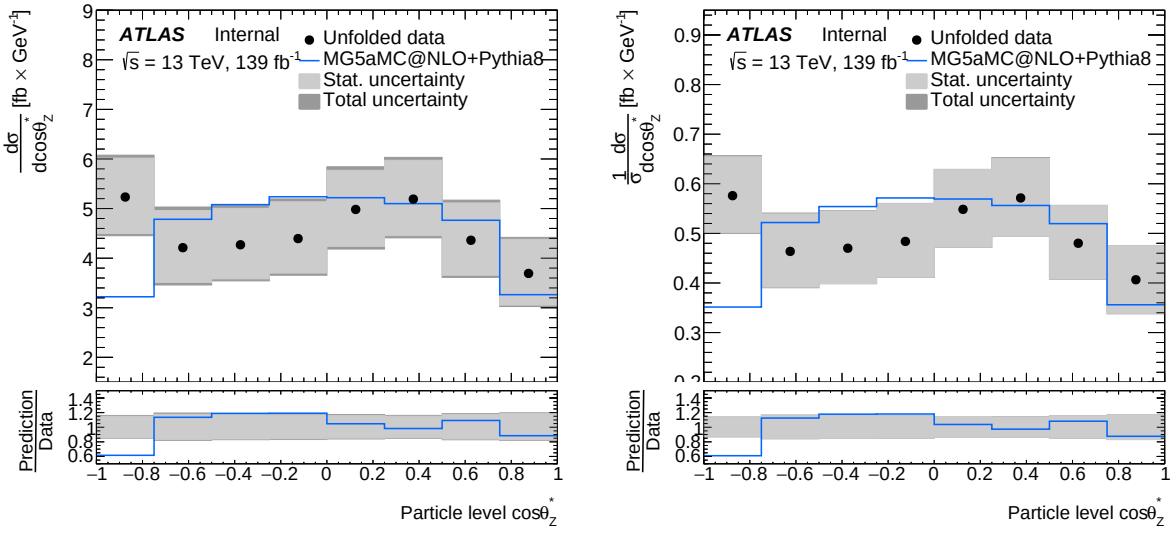

(a) (b)

Figure 9.27: Particle-level (a) absolute and (b) normalised differential cross-sections as a function of $\cos(\theta^{\star}_{Z})$. The light-grey bands show statistical uncertainties while the dark-grey bands are the total uncertainty. The agreement with the nominal MADGRAPH4_AMC@NLO + PYTHIA8 prediction is shown in the bottom panel.

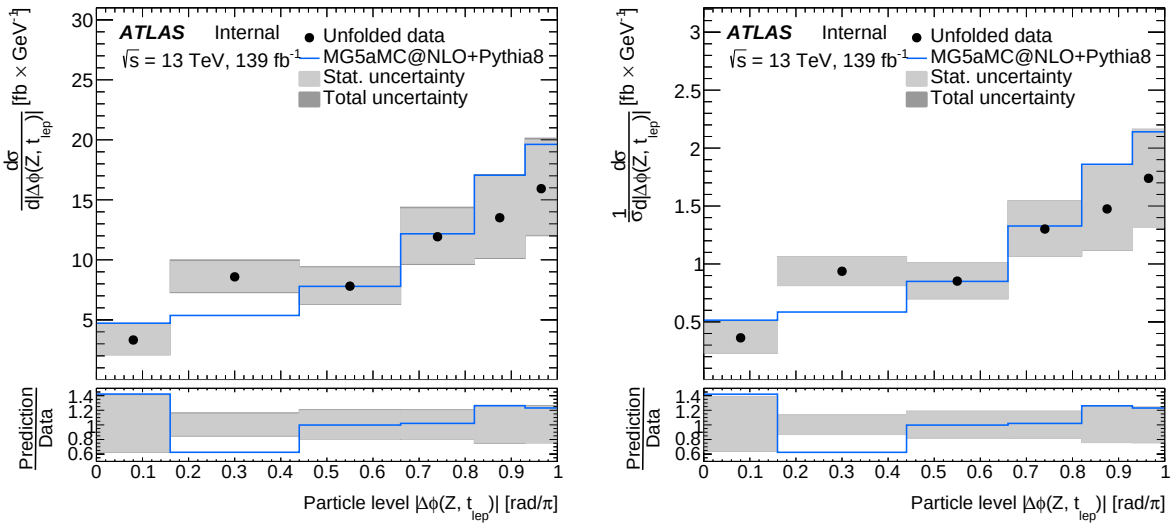

(a) (b)

Figure 9.28: Particle-level (a) absolute and (b) normalised differential cross-sections as a function of $|\Delta\phi(Z, t_{\text{lep}})|$. The light-grey bands show statistical uncertainties while the dark-grey bands are the total uncertainty. The agreement with the nominal MADGRAPH4_AMC@NLO + PYTHIA8 prediction is shown in the bottom panel.

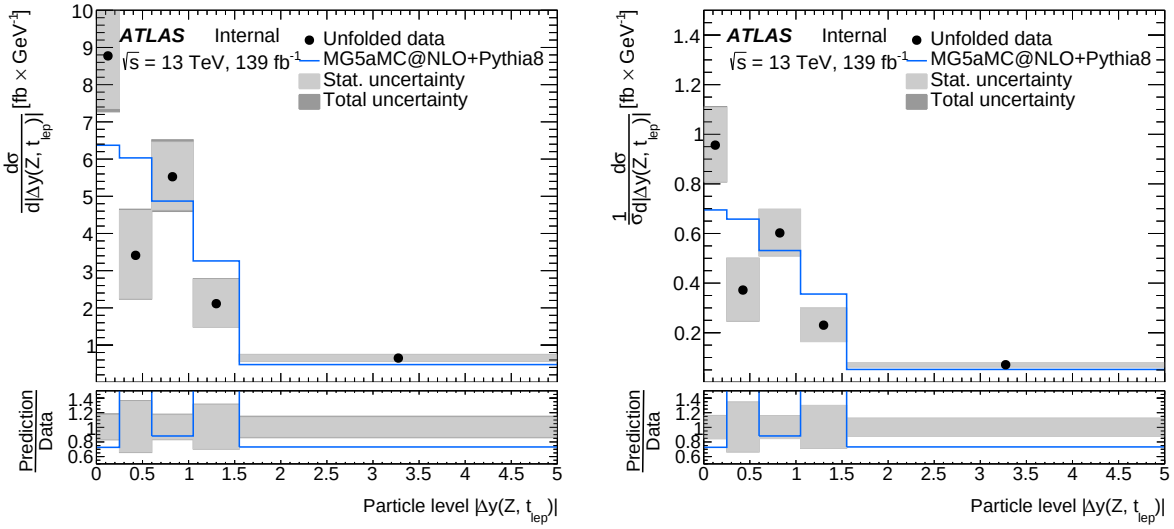

(a) **(b)**

Figure 9.29: Particle-level (a) absolute and (b) normalised differential cross-sections as a function of $|\Delta y(Z, t_{\text{lep}})|$. The light-grey bands show statistical uncertainties while the dark-grey bands are the total uncertainty. The agreement with the nominal MADGRAPH4_AMC@NLO + PYTHIA8 prediction is shown in the bottom panel.

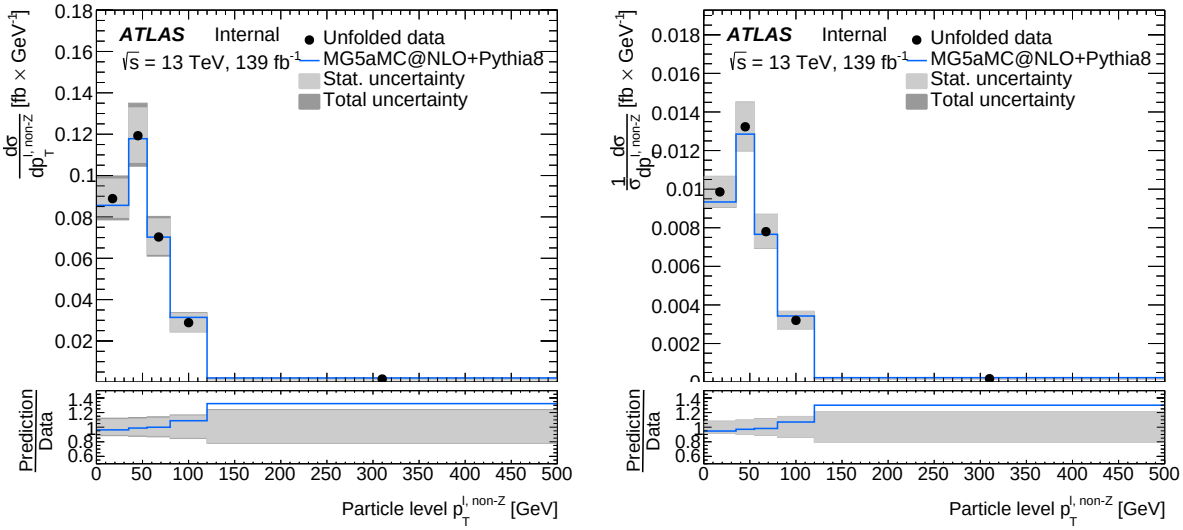

(a) **(b)**

Figure 9.30: Particle-level (a) absolute and (b) normalised differential cross-sections as a function of $p_{\text{T}}^{\ell,\text{non-}Z}$. The light-grey bands show statistical uncertainties while the dark-grey bands are the total uncertainty. The agreement with the nominal MADGRAPH4_AMC@NLO + PYTHIA8 prediction is shown in the bottom panel.

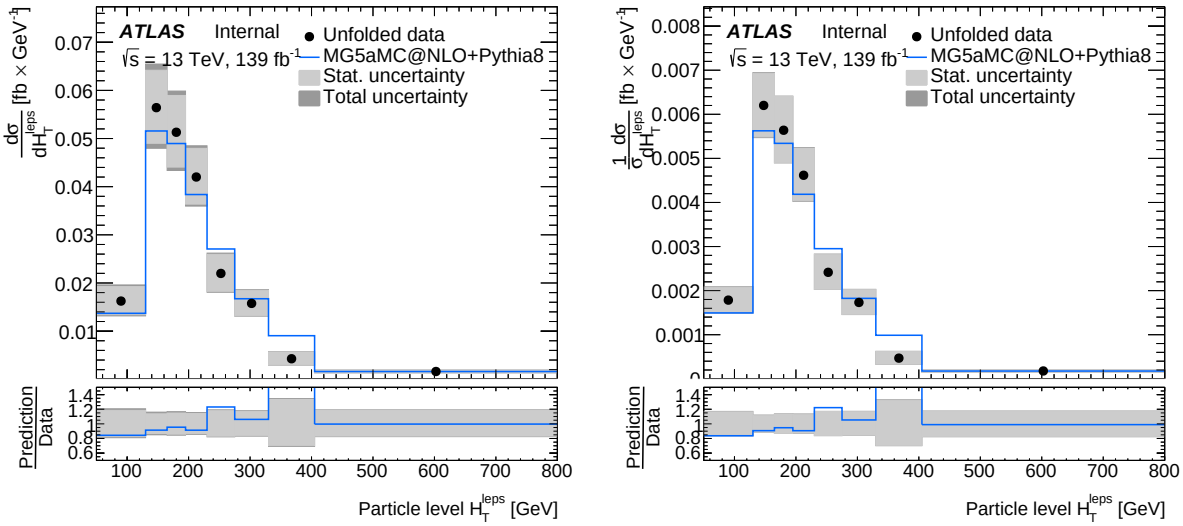

(a) **(b)**

Figure 9.31: Particle-level (a) absolute and (b) normalised differential cross-sections as a function of $H_{\mathrm{T}}^{\mathrm{leps}}$. The light-grey bands show statistical uncertainties while the dark-grey bands are the total uncertainty. The agreement with the nominal MADGRAPH4_AMC@NLO + PYTHIA8 prediction is shown in the bottom panel.

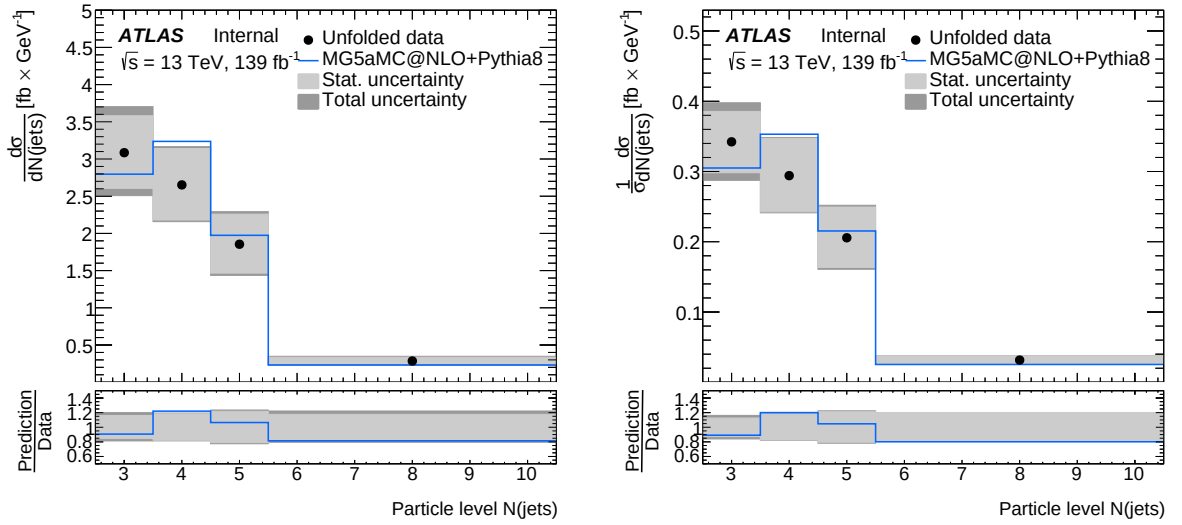

(a) **(b)**

Figure 9.32: Particle-level (a) absolute and (b) normalised differential cross-sections as a function of N_{jets}. The light-grey bands show statistical uncertainties while the dark-grey bands are the total uncertainty. The agreement with the nominal MADGRAPH4_AMC@NLO + PYTHIA8 prediction is shown in the bottom panel.

Chapter 10

Conclusions

The ATLAS detector recorded a dataset of proton-proton collisions corresponding to a total integrated luminosity of 139 fb^{-1} at the centre-of-mass energy of $\sqrt{s} = 13\,\text{TeV}$ during the LHC Run-2 period. The majority of this thesis was dedicated to the measurements of a top quark pair production in association with a Z boson using this large dataset. On the technical side, the ATLAS trigger and data acquisition system was developed in order to prepare it for higher energy and higher luminosity proton-proton collisions.

The LHC Run-2 data-taking period finished in late 2018 and a four-year period of maintenance and upgrade work took place. Significant changes were implemented in the ATLAS trigger and data acquisition system which was readied for more challenging Run-3 and Run-4 data-taking periods. As part of this transition, the monitoring of the high level muon trigger was implemented in the offline reconstruction algorithms. Additionally, the HLT validation framework was extended to include a truth-based muon efficiency monitoring tool in order to help and ensure the error-free transition to the multithreaded AthenaMT framework. The LHC Run-3 data-taking period has already begun and the ATLAS experiment is fully operational.

The physics analyses in this thesis focused on the three-lepton $t\bar{t}Z$ events which provide a good balance between the signal acceptance and background rejection. The events were selected by requiring exactly three isolated leptons in the final state (electrons or muons). Further selection criteria and techniques, including a deep neural network, were applied to efficiently discriminate between the signal and background events. Data-driven techniques were employed to estimate background processes, primarily the WZ+jets and fake lepton backgrounds, while other backgrounds were estimated from Monte Carlo simulations.

The measurement of the inclusive $t\bar{t}Z$ cross-section was presented in Chapter 8. A significant effort went into optimising the three-lepton event selection and defining the corresponding signal regions. The pseudo-continuous b-tagging approach was tested and shown to provide a significant expected improvement of up to 30% in the selection efficiency and the total uncertainty. The inclusive $t\bar{t}Z$ cross-section of $\sigma(pp \to t\bar{t}Z) = 0.99 \pm 0.05\,(\text{stat.}) \pm 0.08\,(\text{syst.})\,\text{pb}$ was measured by combining the optimised three-lepton and four-lepton events. It was found to be in good agreement with the theoretical predictions and other experimental results, and the precision was improved with respect to the previous ATLAS measurements by 38% and 20% in the statistical and systematic uncertainties, respectively. This analysis was published by the ATLAS collaboration [134].

The measurements of the differential $t\bar{t}Z$ cross-section in the three-lepton channel were discussed in Chapter 9. The profile likelihood unfolding technique was employed to perform these measurements favouring the ability to keep a coherent analysis strategy throughout, to include control regions for direct measurements of backgrounds and the ease of combining independent analyses. The differential cross-section measurements were a part of a larger effort to refine the previous $t\bar{t}Z$ analysis. The lepton reconstruction criteria were studied and a more optimal set of identification and isolation definitions were chosen. A comprehensive set of eight differential observables was selected and various configurations of the histograms associated with these observables were studied to obtain stable measurements. The unfolding technique was validated with three tests to ensure the absence of bias in the estimator. Finally, the experimental data was unfolded and the differential cross-section at particle-level was measured. The cross-sections were presented as the absolute and normalised distributions in the eight observables. The results show good agreement with the theoretical prediction of the particle-level cross-section which is well within the total uncertainty bounds. As in the previous measurements, the statistical uncertainty is still dominant, however, the overall precision is improved. For example, it was seen that the total uncertainty in the measurement of the differential cross-section of the transverse momentum of Z bosons is improved by up to 27% on average.

The measurements of the differential $t\bar{t}Z$ cross-section are ongoing and the final results are planned to be presented as the combination of the three- and four-lepton channels for most differential observables. These results can be used in future to constrain new physics effects, for instance, by performing an EFT fit to the data. This analysis will complete the measurements of the $t\bar{t}Z$ three- and four-lepton final states

using the Run-2 dataset. It is planned to be published by the ATLAS collaboration in the coming year. Looking into the future, the measurements will be possible to improve by employing a Run-3 dataset which will offer enhanced data statistics. This is especially relevant for the differential cross-section measurements as they are currently limited by the statistical uncertainty. While the Run-3 data collection period is ongoing, other interesting aspects of the $t\bar{t}Z$ process can be explored, such as the decay of the Z boson to neutrinos and combinations of the $t\bar{t}Z$ measurement with other SM processes. These measurements are being explored by the ATLAS collaboration. The two-lepton final state of the $t\bar{t}Z$ system has only been used to measure the total cross-section so far. Measurements of the differential cross-section have not been possible due to insufficient signal and background separation techniques, even when using machine learning modelling. The measurements of the $t\bar{t}Z$ process have not been exhausted and will continue to be an interesting area of research in the future.

Bibliography

[1] Sheldon L. Glashow, *Partial-symmetries of weak interactions*, Nuclear Physics **22** (1961) 579, ISSN: 0029-5582, DOI: https://doi.org/10.1016/0029-5582(61)90469-2, URL: https://www.sciencedirect.com/science/article/pii/0029558261904692 (cit. on p. 3).

[2] Steven Weinberg, *A model of leptons*, Phys. Rev. Lett. **19** (1967) 1264 (cit. on p. 3).

[3] A. Salam and J.C. Ward, *Electromagnetic and weak interactions*, Physics Letters **13** (1964) 168, ISSN: 0031-9163, DOI: https://doi.org/10.1016/0031-9163(64)90711-5, URL: https://www.sciencedirect.com/science/article/pii/0031916364907115 (cit. on p. 3).

[4] Murray Gell-Mann, *The Eightfold Way: A Theory of strong interaction symmetry* (1961), DOI: 10.2172/4008239 (cit. on p. 3).

[5] Y. Ne'eman, *Derivation of strong interactions from a gauge invariance*, Nuclear Physics **26** (1961) 222, ISSN: 0029-5582, DOI: https://doi.org/10.1016/0029-5582(61)90134-1, URL: https://www.sciencedirect.com/science/article/pii/0029558261901341 (cit. on p. 3).

[6] Peter W. Higgs, *Broken Symmetries and the Masses of Gauge Bosons*, Phys. Rev. Lett. **13** (16 1964) 508, DOI: 10.1103/PhysRevLett.13.508, URL: https://link.aps.org/doi/10.1103/PhysRevLett.13.508 (cit. on p. 4).

[7] F. Englert and R. Brout, *Broken Symmetry and the Mass of Gauge Vector Mesons*, Phys. Rev. Lett. **13** (9 1964) 321, DOI: 10.1103/PhysRevLett.13.321, URL: https://link.aps.org/doi/10.1103/PhysRevLett.13.321 (cit. on p. 4).

[8] ATLAS Collaboration, *Observation of a new particle in the search for the Standard Model Higgs boson with the ATLAS detector at the LHC*, Phys. Lett. B **716** (2012) 1, DOI: 10.1016/j.physletb.2012.08.020, arXiv: 1207.7214 [hep-ex] (cit. on p. 4).

[9] CMS Collaboration, *Observation of a New Boson at a Mass of 125 GeV with the CMS Experiment at the LHC*, Phys. Lett. B **716** (2012) 30, DOI: 10.1016/j.physletb.2012.08.021, arXiv: 1207.7235 [hep-ex] (cit. on p. 4).

[10] P. A. Zyla et al., *Review of Particle Physics*, PTEP **2020** (2020) 083C01, DOI: 10.1093/ptep/ptaa104 (cit. on pp. 5, 6, 8, 10, 91, 123).

[11] Makoto Kobayashi and Toshihide Maskawa, *CP-Violation in the Renormalizable Theory of Weak Interaction*, Progress of Theoretical Physics **49** (1973) 652, ISSN: 0033-068X, DOI: 10.1143/PTP.49.652, eprint: https://academic.oup.com/ptp/article-pdf/49/2/652/5257692/49-2-652.pdf, URL: https://doi.org/10.1143/PTP.49.652 (cit. on p. 6).

[12] CDF Collaboration, *Observation of top quark production in $\bar{p}p$ collisions*, Phys. Rev. Lett. **74** (1995) 2626, DOI: 10.1103/PhysRevLett.74.2626, arXiv: hep-ex/9503002 (cit. on p. 6).

[13] D0 Collaboration, *Observation of the top quark*, Phys. Rev. Lett. **74** (1995) 2632, DOI: 10.1103/PhysRevLett.74.2632, arXiv: hep-ex/9503003 (cit. on p. 6).

[14] Michał Czakon, Paul Fiedler, and Alexander Mitov, *Total Top-Quark Pair-Production Cross Section at Hadron Colliders Through $O(\alpha_S^4)$*, Phys. Rev. Lett. **110** (2013) 252004, DOI: 10.1103/PhysRevLett.110.252004, arXiv: 1303.6254 [hep-ph] (cit. on p. 6).

[15] ATLAS Collaboration, *Top working group cross-section summary plots June 2022*, tech. rep., CERN, 2022, URL: http://cds.cern.ch/record/2812502 (cit. on pp. 7, 9).

[16] Anna Kulesza et al., *Associated top quark pair production with a heavy boson: differential cross sections at NLO+NNLL accuracy*, Eur. Phys. J. C **80** (2020) 428, DOI: 10.1140/epjc/s10052-020-7987-6, arXiv: 2001.03031 [hep-ph] (cit. on pp. 9, 104).

[17] Andreas Helset and Andrew Kobach, *Baryon Number, Lepton Number, and Operator Dimension in the SMEFT with Flavor Symmetries*, Phys. Lett. B **800** (2020) 135132, DOI: 10.1016/j.physletb.2019.135132, arXiv: 1909.05853 [hep-ph] (cit. on p. 11).

[18] Jacob J. Ethier et al., *Combined SMEFT interpretation of Higgs, diboson, and top quark data from the LHC*, JHEP **11** (2021) 089, DOI: 10.1007/JHEP11(2021)089, arXiv: 2105.00006 [hep-ph] (cit. on p. 12).

[19] Olga Bessidskaia Bylund et al., *Probing top quark neutral couplings in the Standard Model Effective Field Theory at NLO in QCD*, JHEP **05** (2016) 052, DOI: 10.1007/JHEP05(2016)052, arXiv: 1601.08193 [hep-ph] (cit. on p. 12).

[20] J. D. Cockcroft and E. T. S. Walton, *Experiments with High Velocity Positive Ions. I. Further Developments in the Method of Obtaining High Velocity Positive Ions.*, Proceedings of the Royal Society A **136** (1932) 619 (cit. on p. 13).

[21] J. D. Cockcroft and E. T. S. Walton, *Experiments with High Velocity Positive Ions. II. The Disintegration of Elements by High Velocity Protons.*, Proceedings of the Royal Society A **137** (1932) 229 (cit. on p. 13).

[22] Lyndon Evans and Philip Bryant, *LHC Machine*, Journal of Instrumentation **3** (2008) S08001, DOI: 10.1088/1748-0221/3/08/s08001, URL: https://doi.org/10.1088/1748-0221/3/08/s08001 (cit. on p. 13).

[23] E. Boltezar et al., *Performance of the New CERN 50 MeV Linac*, IEEE Transactions on Nuclear Science **26** (1979) 3674, DOI: 10.1109/TNS.1979.4330576 (cit. on p. 13).

[24] D J Warner, *Project study for a new 50 MeV linear accelerator for the C. P. S*, tech. rep., CERN, 1973, URL: https://cds.cern.ch/record/414071 (cit. on p. 13).

[25] Study Group for CPS Improvements, *The second stage CPS improvement study: 800 MeV booster synchrotron*, Geneva: CERN, 1967, URL: https://cds.cern.ch/record/109292 (cit. on p. 13).

[26] *CERN Rapport annuel 1988*, tech. rep., CERN, 1989, URL: https://cds.cern.ch/record/1516883 (cit. on p. 13).

[27] *CERN's 25 GeV proton synchroton*, Geneva: CERN, 1960, URL: https://cds.cern.ch/record/445034 (cit. on p. 13).

[28] *The 300 GeV programme*, Geneva: CERN, 1972, URL: https://cds.cern.ch/record/104068 (cit. on p. 13).

[29] Julie Haffner, *The CERN accelerator complex. Complexe des accélérateurs du CERN* (2013), General Photo, URL: https://cds.cern.ch/record/1621894 (cit. on p. 14).

[30] L Arnaudon et al., *Linac4 Technical Design Report*, tech. rep., revised version submitted on 2006-12-14 09:00:40: CERN, 2006, URL: https://cds.cern.ch/record/1004186 (cit. on p. 14).

[31] Stephen Myers, *The LEP Collider, from design to approval and commissioning*, John Adams' memorial lecture, Delivered at CERN, 26 Nov 1990, Geneva: CERN, 1991, DOI: 10.5170/CERN-1991-008, URL: http://cds.cern.ch/record/226776 (cit. on p. 14).

[32] The ALICE Collaboration, *The ALICE experiment at the CERN LHC*, Journal of Instrumentation **3** (2008) S08002, DOI: 10.1088/1748-0221/3/08/s08002, URL: https://doi.org/10.1088/1748-0221/3/08/s08002 (cit. on p. 15).

[33] The ATLAS Collaboration, *The ATLAS Experiment at the CERN Large Hadron Collider*, Journal of Instrumentation **3** (2008) S08003, DOI: 10.1088/1748-0221/3/08/s08003, URL: https://doi.org/10.1088/1748-0221/3/08/s08003 (cit. on p. 15).

[34] The CMS Collaboration, *The CMS experiment at the CERN LHC*, Journal of Instrumentation **3** (2008) S08004, DOI: 10.1088/1748-0221/3/08/s08004, URL: https://doi.org/10.1088/1748-0221/3/08/s08004 (cit. on p. 15).

[35] The LHCb Collaboration, *The LHCb Detector at the LHC*, Journal of Instrumentation **3** (2008) S08005, DOI: 10.1088/1748-0221/3/08/s08005, URL: https://doi.org/10.1088/1748-0221/3/08/s08005 (cit. on p. 15).

[36] *LHC parameters*, URL: https://www.lhc-closer.es/taking_a_closer_look_at_lhc/1.lhc_parameters (cit. on p. 16).

[37] Werner Herr and B Muratori, *Concept of luminosity* (2006), DOI: 10.5170/CERN-2006-002.361, URL: http://cds.cern.ch/record/941318 (cit. on p. 15).

[38] ATLAS Collaboration, *ATLAS Luminosity Public Results*, tech. rep., URL: https://twiki.cern.ch/twiki/bin/view/AtlasPublic/LuminosityPublicResultsRun2 (cit. on p. 17).

[39] Joao Pequenao, *Computer generated image of the whole ATLAS detector*, 2008, URL: https://cds.cern.ch/record/1095924 (cit. on p. 18).

[40] ATLAS Collaboration, *ATLAS magnet system: Technical Design Report, 1*, Technical design report. ATLAS, Geneva: CERN, 1997, DOI: 10.17181/CERN.9O5C.VDTM, URL: https://cds.cern.ch/record/338080 (cit. on p. 19).

[41] A Yamamoto et al., *The ATLAS central solenoid*, Nucl. Instrum. Methods Phys. Res., A **584** (2007) 53, DOI: 10.1016/j.nima.2007.09.047, URL: http://cds.cern.ch/record/1069672 (cit. on p. 19).

[42] ATLAS Collaboration, *Superconducting magnet system for the ATLAS detector at CERN*, IEEE Trans. Appl. Supercond. **9** (1999) 841, DOI: 10.1109/77.783428, URL: https://cds.cern.ch/record/409763 (cit. on p. 19).

[43] J. Goodson, URL: http://www.jetgoodson.com/images/thesisImages/magnetSystems.png (cit. on p. 20).

[44] ATLAS Collaboration, *ATLAS inner detector: Technical Design Report, 1*, Technical design report. ATLAS, Geneva: CERN, 1997, URL: https://cds.cern.ch/record/331063 (cit. on p. 19).

[45] Giulia Ripellino, *The alignment of the ATLAS Inner Detector in Run-2*, PoS **LHCP2016** (2016) 196, DOI: 10.22323/1.276.0196 (cit. on p. 19).

[46] Joao Pequenao, *Computer generated image of the ATLAS inner detector*, 2008, URL: https://cds.cern.ch/record/1095926 (cit. on p. 21).

[47] Norbert Wermes and G Hallewel, *ATLAS pixel detector: Technical Design Report*, Technical design report. ATLAS, Geneva: CERN, 1998, URL: https://cds.cern.ch/record/381263 (cit. on p. 20).

[48] ATLAS Collaboration, *ATLAS pixel detector electronics and sensors*, JINST **3** (2008) P07007, DOI: 10.1088/1748-0221/3/07/P07007 (cit. on p. 20).

[49] M Capeans et al., *ATLAS Insertable B-Layer Technical Design Report*, tech. rep., 2010, URL: https://cds.cern.ch/record/1291633 (cit. on p. 20).

[50] A Miucci, *The ATLAS Insertable B-Layer project*, Journal of Instrumentation **9** (2014) C02018, DOI: 10.1088/1748-0221/9/02/c02018, URL: https://doi.org/10.1088/1748-0221/9/02/c02018 (cit. on p. 20).

[51] B. Abbott et. al., *Production and integration of the ATLAS Insertable B-Layer*, Journal of Instrumentation **13** (2018) T05008, DOI: 10.1088/1748-0221/13/05/t05008, URL: https://doi.org/10.1088/1748-0221/13/05/t05008 (cit. on p. 20).

[52] ATLAS Collaboration, *Operation and performance of the ATLAS semiconductor tracker*, JINST **9** (2014) P08009, DOI: 10.1088/1748-0221/9/08/P08009, arXiv: 1404.7473 [hep-ex] (cit. on p. 20).

[53] Vasiliki A. Mitsou, *The ATLAS Transition Radiation Tracker*, tech. rep., CERN, 2003, DOI: 10.1142/9789812702708_0073, URL: https://cds.cern.ch/record/686973 (cit. on p. 21).

[54] Adrian Vogel, *ATLAS Transition Radiation Tracker (TRT): Straw tube gaseous detectors at high rates*, Nuclear Instruments and Methods in Physics Research Section A: Accelerators, Spectrometers, Detectors and Associated Equipment **732** (2013), Vienna Conference on Instrumentation 2013 277, ISSN: 0168-9002, DOI: https://doi.org/10.1016/j.nima.2013.07.020, URL: https://www.sciencedirect.com/science/article/pii/S0168900213009960 (cit. on p. 22).

[55] A. Airapetian et al., *ATLAS calorimeter performance Technical Design Report* (1996) (cit. on p. 22).

[56] Joao Pequenao, *Computer Generated image of the ATLAS calorimeter*, 2008, URL: https://cds.cern.ch/record/1095927 (cit. on p. 23).

[57] ATLAS Collaboration, *ATLAS liquid argon calorimeter: Technical design report* (1996) (cit. on p. 22).

[58] ATLAS Collaboration, *ATLAS tile calorimeter: Technical design report* (1996) (cit. on p. 23).

[59] ATLAS Collaboration, *ATLAS muon spectrometer: Technical Design Report*, Technical design report. ATLAS, Geneva: CERN, 1997, URL: https://cds.cern.ch/record/331068 (cit. on p. 24).

[60] Joao Pequenao, *Computer generated image of the ATLAS Muons subsystem*, 2008, URL: https://cds.cern.ch/record/1095929 (cit. on p. 25).

[61] ATLAS Collaboration, *Performance of the ATLAS muon trigger in pp collisions at* $\sqrt{s} = 8$ *TeV*, Eur. Phys. J. C **75** (2015) 120, DOI: 10.1140/epjc/s10052-015-3325-9, arXiv: 1408.3179 [hep-ex] (cit. on p. 26).

[62] M. Livan, *Monitored drift tubes in ATLAS*, Nucl. Instrum. Meth. A **384** (1996), ed. by F. Ferroni and P. Schlein 214, DOI: 10.1016/S0168-9002(96)00851-0 (cit. on p. 25).

[63] T. et. al. Argyropoulos, *Cathode strip chambers in ATLAS : Installation, commissioning and in situ performance*, 2008, DOI: 10.1109/NSSMIC.2008.4774958 (cit. on p. 26).

[64] D Boscherini, *Performance and operation of the ATLAS Resistive Plate Chamber system in LHC Run-1*, tech. rep., CERN, 2014, DOI: 10.1088/1748-0221/9/12/C12039, URL: https://cds.cern.ch/record/1753173 (cit. on p. 27).

[65] Koichi Nagai, *Thin gap chambers in ATLAS*, Nuclear Instruments and Methods in Physics Research Section A: Accelerators, Spectrometers, Detectors and Associated Equipment **384** (1996), BEAUTY '96 219, ISSN: 0168-9002, DOI: https://doi.org/10.1016/S0168-9002(96)01065-0, URL: https://www.sciencedirect.com/science/article/pii/S0168900296010650 (cit. on p. 27).

[66] ATLAS Collaboration, *ATLAS level-1 trigger: Technical Design Report*, Technical design report. ATLAS, Geneva: CERN, 1998, URL: https://cds.cern.ch/record/381429 (cit. on p. 28).

[67] Peter Jenni et al., *ATLAS high-level trigger, data-acquisition and controls: Technical Design Report*, Technical design report. ATLAS, Geneva: CERN, 2003, URL: https://cds.cern.ch/record/616089 (cit. on p. 28).

[68] Joao Pequenao and Paul Schaffner,
How ATLAS detects particles: diagram of particle paths in the detector, 2013,
URL: https://cds.cern.ch/record/1505342 (cit. on p. 32).

[69] R. Frühwirth, *Application of Kalman filtering to track and vertex fitting*,
Nuclear Instruments and Methods in Physics Research Section A: Accelerators, Spectrometers, Detectors and Associated Equipment **262** (1987) 444,
ISSN: 0168-9002, DOI: https://doi.org/10.1016/0168-9002(87)90887-4,
URL:
https://www.sciencedirect.com/science/article/pii/0168900287908874
(cit. on p. 31).

[70] T Cornelissen et al.,
Concepts, Design and Implementation of the ATLAS New Tracking (NEWT),
tech. rep., CERN, 2007, URL: https://cds.cern.ch/record/1020106
(cit. on p. 31).

[71] ATLAS Collaboration, *Electron and photon reconstruction and performance in ATLAS using a dynamical, topological cell clustering-based approach*, tech. rep., CERN, 2017, URL: http://cds.cern.ch/record/2298955 (cit. on p. 33).

[72] ATLAS Collaboration, *Electron and photon reconstruction and performance in ATLAS using a dynamical, topological cell clustering-based approach* (2017)
(cit. on p. 34).

[73] ATLAS Collaboration, *Electron and photon energy calibration with the ATLAS detector using 2015–2016 LHC proton-proton collision data*,
JINST **14** (2019) P03017, DOI: 10.1088/1748-0221/14/03/P03017,
arXiv: 1812.03848 [hep-ex] (cit. on p. 33).

[74] ATLAS Collaboration, *Electron and photon performance measurements with the ATLAS detector using the 2015–2017 LHC proton-proton collision data*,
JINST **14** (2019) P12006, DOI: 10.1088/1748-0221/14/12/P12006,
arXiv: 1908.00005 [hep-ex] (cit. on pp. 33, 35, 37).

[75] ATLAS Collaboration,
Electron reconstruction and identification in the ATLAS experiment using the 2015 and 2016 LHC proton-proton collision data at $\sqrt{s}$ = 13 TeV,
Eur. Phys. J. C **79** (2019) 639, DOI: 10.1140/epjc/s10052-019-7140-6,
arXiv: 1902.04655 [physics.ins-det] (cit. on pp. 34, 82).

[76] J. Illingworth and J. Kittler, *A survey of the hough transform*, Computer Vision, Graphics, and Image Processing **44** (1988) 87, ISSN: 0734-189X, DOI: https://doi.org/10.1016/S0734-189X(88)80033-1, URL: https://www.sciencedirect.com/science/article/pii/S0734189X88800331 (cit. on p. 35).

[77] ATLAS Collaboration, *Muon reconstruction performance of the ATLAS detector in proton–proton collision data at $\sqrt{s}$ =13 TeV*, Eur. Phys. J. C **76** (2016) 292, DOI: 10.1140/epjc/s10052-016-4120-y, arXiv: 1603.05598 [hep-ex] (cit. on pp. 36, 37).

[78] ATLAS Collaboration, *Muon reconstruction and identification efficiency in ATLAS using the full Run 2 pp collision data set at $\sqrt{s} = 13$ TeV*, Eur. Phys. J. C **81** (2021) 578, DOI: 10.1140/epjc/s10052-021-09233-2, arXiv: 2012.00578 [hep-ex] (cit. on pp. 36, 37, 82).

[79] Fudong He et al., *Tagging non-prompt electrons and muons using lifetime and isolation information*, tech. rep., CERN, 2018, URL: https://cds.cern.ch/record/2632152 (cit. on p. 37).

[80] ATLAS Collaboration, *Recommended Isolation Working Points*, https://twiki.cern.ch/twiki/bin/view/AtlasProtected/RecommendedIsolationWPs (cit. on p. 38).

[81] Gavin P. Salam, *Towards Jetography*, Eur. Phys. J. C **67** (2010) 637, DOI: 10.1140/epjc/s10052-010-1314-6, arXiv: 0906.1833 [hep-ph] (cit. on p. 38).

[82] Matteo Cacciari, Gavin P. Salam, and Gregory Soyez, *The anti-k_t jet clustering algorithm*, JHEP **04** (2008) 063, DOI: 10.1088/1126-6708/2008/04/063, arXiv: 0802.1189 [hep-ph] (cit. on p. 38).

[83] ATLAS Collaboration, *Jet energy scale and resolution measured in proton–proton collisions at $\sqrt{s} = 13$ TeV with the ATLAS detector*, Eur. Phys. J. C **81** (2021) 689, DOI: 10.1140/epjc/s10052-021-09402-3, arXiv: 2007.02645 [hep-ex] (cit. on pp. 39, 82).

[84] ATLAS Collaboration, *Jet energy scale measurements and their systematic uncertainties in proton-proton collisions at $\sqrt{s} = 13$ TeV with the ATLAS detector*, Phys. Rev. D **96** (2017) 072002, DOI: 10.1103/PhysRevD.96.072002, arXiv: 1703.09665 [hep-ex] (cit. on p. 39).

[85] ATLAS Collaboration, *Determination of jet calibration and energy resolution in proton-proton collisions at $\sqrt{s} = 8$ TeV using the ATLAS detector*, Eur. Phys. J. C **80** (2020) 1104, DOI: 10.1140/epjc/s10052-020-08477-8, arXiv: 1910.04482 [hep-ex] (cit. on p. 39).

[86] ATLAS Collaboration, *Performance of pile-up mitigation techniques for jets in pp collisions at $\sqrt{s} = 8$ TeV using the ATLAS detector*, Eur. Phys. J. C **76** (2016) 581, DOI: 10.1140/epjc/s10052-016-4395-z, arXiv: 1510.03823 [hep-ex] (cit. on pp. 39, 82).

[87] ATLAS Collaboration, *Constituent-level pile-up mitigation techniques in ATLAS*, tech. rep., All figures including auxiliary figures are available at https://atlas.web.cern.ch/Atlas/GROUPS/PHYSICS/CONFNOTES/ATLAS-CONF-2017-065: CERN, 2017, URL: https://cds.cern.ch/record/2281055 (cit. on p. 39).

[88] ATLAS Collaboration, *Optimisation and performance studies of the ATLAS b-tagging algorithms for the 2017-18 LHC run* (2017) (cit. on p. 39).

[89] ATLAS Collaboration, *Secondary vertex finding for jet flavour identification with the ATLAS detector* (2017) (cit. on p. 39).

[90] ATLAS Collaboration, *Topological b-hadron decay reconstruction and identification of b-jets with the JetFitter package in the ATLAS experiment at the LHC* (2018) (cit. on pp. 39, 40).

[91] ATLAS Collaboration, *Measurements of b-jet tagging efficiency with the ATLAS detector using $t\bar{t}$ events at $\sqrt{s} = 13$ TeV*, JHEP **08** (2018) 089, DOI: 10.1007/JHEP08(2018)089, arXiv: 1805.01845 [hep-ex] (cit. on pp. 39, 40).

[92] ATLAS Collaboration, *Expected Performance of the 2019 ATLAS b-taggers*, http://atlas.web.cern.ch/Atlas/GROUPS/PHYSICS/PLOTS/FTAG-2019-005/ (cit. on pp. 40, 41).

[93] ATLAS Collaboration, *ATLAS b-jet identification performance and efficiency measurement with $t\bar{t}$ events in pp collisions at $\sqrt{s} = 13$ TeV*, Eur. Phys. J. C **79** (2019) 970, DOI: 10.1140/epjc/s10052-019-7450-8, arXiv: 1907.05120 [hep-ex] (cit. on pp. 40, 82).

[94] ATLAS Collaboration, *Performance of missing transverse momentum reconstruction with the ATLAS detector using proton-proton collisions at $\sqrt{s} = 13$ TeV*, Eur. Phys. J. C **78** (2018) 903, DOI: 10.1140/epjc/s10052-018-6288-9, arXiv: 1802.08168 [hep-ex] (cit. on pp. 41, 83).

[95] Jonathan Jamieson, *Aiming For The Top Corner: Measuring top-quark pair production in association with additional jets in highly boosted events using the ATLAS detector*, Presented 28 Feb 2022, 2022, URL: http://cds.cern.ch/record/2805713 (cit. on p. 43).

[96] Richard D. Ball et al., *Parton distributions from high-precision collider data*, The European Physical Journal C **77** (2017), DOI: 10.1140/epjc/s10052-017-5199-5, URL: https://doi.org/10.1140%2Fepjc%2Fs10052-017-5199-5 (cit. on p. 44).

[97] Andy Buckley et al., *General-purpose event generators for LHC physics*, Phys. Rept. **504** (2011) 145, DOI: 10.1016/j.physrep.2011.03.005, arXiv: 1101.2599 [hep-ph] (cit. on pp. 44, 46).

[98] Torbjörn Sjöstrand, *Jet fragmentation of multiparton configurations in a string framework*, Nuclear Physics B **248** (1984) 469, ISSN: 0550-3213, DOI: https://doi.org/10.1016/0550-3213(84)90607-2, URL: https://www.sciencedirect.com/science/article/pii/0550321384906072 (cit. on p. 45).

[99] D. Amati and G. Veneziano, *Preconfinement as a property of perturbative QCD*, Physics Letters B **83** (1979) 87, ISSN: 0370-2693, DOI: https://doi.org/10.1016/0370-2693(79)90896-7, URL: https://www.sciencedirect.com/science/article/pii/0370269379908967 (cit. on p. 45).

[100] B.R. Webber, *A QCD model for jet fragmentation including soft gluon interference*, Nuclear Physics B **238** (1984) 492, ISSN: 0550-3213, DOI: https://doi.org/10.1016/0550-3213(84)90333-X, URL:

https://www.sciencedirect.com/science/article/pii/055032138490333X (cit. on p. 45).

[101] Torbjörn Sjöstrand et al., *An introduction to PYTHIA 8.2*, Comput. Phys. Commun. **191** (2015) 159, DOI: 10.1016/j.cpc.2015.01.024, arXiv: 1410.3012 [hep-ph] (cit. on pp. 46, 73).

[102] M. Bahr et al., *Herwig++ Physics and Manual*, Eur. Phys. J. C **58** (2008) 639, DOI: 10.1140/epjc/s10052-008-0798-9, arXiv: 0803.0883 [hep-ph] (cit. on p. 46).

[103] Enrico Bothmann et al., *Event Generation with Sherpa 2.2*, SciPost Phys. **7** (2019) 034, DOI: 10.21468/SciPostPhys.7.3.034, arXiv: 1905.09127 [hep-ph] (cit. on pp. 46, 73).

[104] J. Alwall et al., *The automated computation of tree-level and next-to-leading order differential cross sections, and their matching to parton shower simulations*, JHEP **07** (2014) 079, DOI: 10.1007/JHEP07(2014)079, arXiv: 1405.0301 [hep-ph] (cit. on pp. 46, 73).

[105] Carlo Oleari, *The POWHEG-BOX*, Nucl. Phys. B Proc. Suppl. **205-206** (2010), ed. by Johannes Blümlein, Sven-Olaf Moch, and Tord Riemann 36, DOI: 10.1016/j.nuclphysbps.2010.08.016, arXiv: 1007.3893 [hep-ph] (cit. on p. 46).

[106] S. Agostinelli et al., *GEANT4–a simulation toolkit*, Nucl. Instrum. Meth. A **506** (2003) 250, DOI: 10.1016/S0168-9002(03)01368-8 (cit. on p. 46).

[107] Marilena Bandieramonte, Riccardo Maria Bianchi, and Joseph Boudreau, *FullSimLight: ATLAS standalone Geant4 simulation*, EPJ Web Conf. **245** (2020), ed. by C. Doglioni et al. 02029, DOI: 10.1051/epjconf/202024502029 (cit. on p. 46).

[108] Tomas Dado et al., *Documentation for TRExFitter*, https://trexfitter-docs.web.cern.ch/trexfitter-docs/, Accessed: 01-09-2022 (cit. on pp. 47, 49, 50, 54, 110).

[109] F. James and M. Roos, *Minuit: A System for Function Minimization and Analysis of the Parameter Errors and Correlations*, Comput. Phys. Commun. **10** (1975) 343, DOI: 10.1016/0010-4655(75)90039-9 (cit. on p. 47).

[110] Andy Buckley, Christopher White, and Martin White, *Practical Collider Physics*, 2053-2563, IOP Publishing, 2021, ISBN: 978-0-7503-2444-1, DOI: 10.1088/978-0-7503-2444-1, URL: https://dx.doi.org/10.1088/978-0-7503-2444-1 (cit. on p. 51).

[111] Volker Blobel, "An Unfolding method for high-energy physics experiments", *Conference on Advanced Statistical Techniques in Particle Physics*, 2002 258, arXiv: hep-ex/0208022 (cit. on p. 50).

[112] Peter van Gemmeren and David Malon, *The event data store and I/O framework for the ATLAS experiment at the Large Hadron Collider*, 2009, DOI: 10.1109/CLUSTR.2009.5289147 (cit. on p. 55).

[113] G. Barrand et al., *GAUDI — A software architecture and framework for building HEP data processing applications*, Computer Physics Communications **140** (2001), CHEP2000 45, ISSN: 0010-4655, DOI: https://doi.org/10.1016/S0010-4655(01)00254-5, URL: https://www.sciencedirect.com/science/article/pii/S0010465501002545 (cit. on p. 55).

[114] G A Stewart et al., *Multi-threaded software framework development for the ATLAS experiment*, Journal of Physics: Conference Series **762** (2016) 012024, DOI: 10.1088/1742-6596/762/1/012024, URL: https://doi.org/10.1088/1742-6596/762/1/012024 (cit. on p. 56).

[115] Georges Aad et al., *Performance of the ATLAS muon triggers in Run 2*, JINST **15** (2020) P09015, DOI: 10.1088/1748-0221/15/09/p09015, arXiv: 2004.13447 [physics.ins-det] (cit. on p. 65).

[116] Richard D. Ball et al., *Parton distributions for the LHC Run II*, JHEP **04** (2015) 040, DOI: 10.1007/JHEP04(2015)040, arXiv: 1410.8849 [hep-ph] (cit. on p. 73).

[117] Johannes Bellm et al., *Herwig 7.0/Herwig++ 3.0 release note*, Eur. Phys. J. C **76** (2016) 196, DOI: 10.1140/epjc/s10052-016-4018-8, arXiv: 1512.01178 [hep-ph] (cit. on p. 73).

[118] ATLAS Collaboration, *ATLAS Pythia 8 tunes to 7 TeV data* (2014) (cit. on p. 73).

[119] ATLAS Collaboration, *Measurement of the top quark-pair production cross section with ATLAS in pp collisions at* $\sqrt{s} = 7$ *TeV*, Eur. Phys. J. C **71** (2011) 1577, DOI: 10.1140/epjc/s10052-011-1577-6, arXiv: 1012.1792 [hep-ex] (cit. on p. 75).

[120] ATLAS Collaboration, *Search for supersymmetry at $\sqrt{s}$=8 TeV in final states with jets and two same-sign leptons or three leptons with the ATLAS detector*, JHEP **06** (2014) 035, DOI: 10.1007/JHEP06(2014)035, arXiv: 1404.2500 [hep-ex] (cit. on p. 75).

[121] Erich W. Varnes, *A Poisson likelihood approach to fake lepton estimation with the matrix method* (2016), arXiv: 1606.06817 [hep-ex] (cit. on p. 76).

[122] Dominik Babal et al., *Refined measurement of the inclusive and differential $t\bar{t}Z$ production cross sections at $\sqrt{s} = 13$ TeV with the ATLAS detector*, tech. rep., CERN, 2022, URL: https://cds.cern.ch/record/2800626 (cit. on pp. 77, 109, 124).

[123] G. Avoni et al., *The new LUCID-2 detector for luminosity measurement and monitoring in ATLAS*, JINST **13** (2018) P07017, DOI: 10.1088/1748-0221/13/07/P07017 (cit. on p. 81).

[124] ATLAS Collaboration, *Luminosity determination in pp collisions at $\sqrt{s}$ = 8 TeV using the ATLAS detector at the LHC*, Eur. Phys. J. C **76** (2016) 653, DOI: 10.1140/epjc/s10052-016-4466-1, arXiv: 1608.03953 [hep-ex] (cit. on p. 81).

[125] Jon Butterworth et al., *PDF4LHC recommendations for LHC Run II*, J. Phys. G **43** (2016) 023001, DOI: 10.1088/0954-3899/43/2/023001, arXiv: 1510.03865 [hep-ph] (cit. on pp. 84, 86).

[126] ATLAS Collaboration, *PMG Systematic Uncertainties Recipes*, https://twiki.cern.ch/twiki/bin/viewauth/AtlasProtected/PmgSystematicUncertaintyRecipes (cit. on pp. 84, 85).

[127] Sayipjamal Dulat et al., *New parton distribution functions from a global analysis of quantum chromodynamics*, Phys. Rev. D **93** (2016) 033006, DOI: 10.1103/PhysRevD.93.033006, arXiv: 1506.07443 [hep-ph] (cit. on p. 84).

[128] L. A. Harland-Lang et al., *Parton distributions in the LHC era: MMHT 2014 PDFs*, Eur. Phys. J. C **75** (2015) 204, DOI: 10.1140/epjc/s10052-015-3397-6, arXiv: 1412.3989 [hep-ph] (cit. on p. 84).

[129] S. Catani et al., *QCD matrix elements + parton showers*, JHEP **11** (2001) 063, DOI: 10.1088/1126-6708/2001/11/063, arXiv: hep-ph/0109231 (cit. on p. 85).

[130] Steffen Schumann and Frank Krauss,
A Parton shower algorithm based on Catani-Seymour dipole factorisation,
JHEP **03** (2008) 038, DOI: 10.1088/1126-6708/2008/03/038,
arXiv: 0709.1027 [hep-ph] (cit. on p. 85).

[131] Stefan Hoeche et al., *QCD matrix elements and truncated showers*,
JHEP **05** (2009) 053, DOI: 10.1088/1126-6708/2009/05/053,
arXiv: 0903.1219 [hep-ph] (cit. on p. 85).

[132] Stefan Hoeche et al., *A critical appraisal of NLO+PS matching methods*,
JHEP **09** (2012) 049, DOI: 10.1007/JHEP09(2012)049,
arXiv: 1111.1220 [hep-ph] (cit. on p. 85).

[133] Stefan Hoeche et al., *QCD matrix elements + parton showers: The NLO case*,
JHEP **04** (2013) 027, DOI: 10.1007/JHEP04(2013)027,
arXiv: 1207.5030 [hep-ph] (cit. on p. 85).

[134] ATLAS Collaboration, *Measurements of the inclusive and differential production cross sections of a top-quark–antiquark pair in association with a Z boson at* $\sqrt{s} = 13$ *TeV with the ATLAS detector*, Eur. Phys. J. C **81** (2021) 737,
DOI: 10.1140/epjc/s10052-021-09439-4, arXiv: 2103.12603 [hep-ex]
(cit. on pp. 85, 86, 89, 103–107, 109, 113, 114, 116, 123, 158, 164).

[135] ATLAS Collaboration,
Measurement of the production cross-section of a single top quark in association with a Z boson in proton–proton collisions at 13 TeV with the ATLAS detector,
Phys. Lett. B **780** (2018) 557, DOI: 10.1016/j.physletb.2018.03.023,
arXiv: 1710.03659 [hep-ex] (cit. on p. 86).

[136] CMS Collaboration, *Measurement of the associated production of a single top quark and a Z boson in pp collisions at* $\sqrt{s} = 13$ *TeV*, Phys. Lett. B **779** (2018) 358,
DOI: 10.1016/j.physletb.2018.02.025, arXiv: 1712.02825 [hep-ex]
(cit. on p. 86).

[137] ATLAS Collaboration, *Observation of the associated production of a top quark and a Z boson in pp collisions at* $\sqrt{s} = 13$ *TeV with the ATLAS detector*,
JHEP **07** (2020) 124, DOI: 10.1007/JHEP07(2020)124,
arXiv: 2002.07546 [hep-ex] (cit. on p. 86).

[138] Federico Demartin et al., *tWH associated production at the LHC*,
Eur. Phys. J. C **77** (2017) 34, DOI: 10.1140/epjc/s10052-017-4601-7,
arXiv: 1607.05862 [hep-ph] (cit. on p. 86).

[139] D. de Florian et al., *Handbook of LHC Higgs Cross Sections: 4. Deciphering the Nature of the Higgs Sector*, **2/2017** (2016), DOI: 10.23731/CYRM-2017-002, arXiv: 1610.07922 [hep-ph] (cit. on p. 87).

[140] ATLAS Collaboration, *Measurement of the $t\bar{t}Z$ and $t\bar{t}W$ cross sections in proton-proton collisions at $\sqrt{s} = 13$ TeV with the ATLAS detector*, Phys. Rev. D **99** (2019) 072009, DOI: 10.1103/PhysRevD.99.072009, arXiv: 1901.03584 [hep-ex] (cit. on pp. 87, 89, 93, 105).

[141] CMS Collaboration, *Measurement of top quark pair production in association with a Z boson in proton-proton collisions at $\sqrt{s} = 13$ TeV*, JHEP **03** (2020) 056, DOI: 10.1007/JHEP03(2020)056, arXiv: 1907.11270 [hep-ex] (cit. on pp. 89, 105).

[142] Giulio D'Agostini, *Improved iterative Bayesian unfolding*, arXiv preprint arXiv:1010.0632 (2010) (cit. on p. 110).

[143] Matteo Cacciari, Gavin P. Salam, and Gregory Soyez, *The Catchment Area of Jets*, JHEP **04** (2008) 005, DOI: 10.1088/1126-6708/2008/04/005, arXiv: 0802.1188 [hep-ph] (cit. on p. 110).

[144] Jeff Heaton, *Applications of Deep Neural Networks with Keras*, 2020, DOI: 10.48550/ARXIV.2009.05673, URL: https://arxiv.org/abs/2009.05673 (cit. on p. 117).

[145] Dominik Babal et al., *Measurements of the inclusive and differential production cross sections of a top-quark-antiquark pair in association with a Z boson at $\sqrt{s} = 13$ TeV with the ATLAS detector*, tech. rep., CERN, 2019, URL: https://cds.cern.ch/record/2672207 (cit. on p. 124).

List of figures

List of tables